Université de Toulouse

THÈSE

En vue de l'obtention du

DOCTORAT DE L'UNIVERSITÉ DE TOULOUSE

Délivré par Institut National des Sciences Appliquées de Toulouse

Discipline : Nanobiotechnologie

Le 6 mai 2009

Présentée et soutenue par **Adrián Martínez Rivas**

WAFER SCALE INTEGRATION OF COULOMB BLOCKADE-BASED NANOBIOSENSORS WITH MICROFLUIDIC CHANNELS FOR LABEL-FREE DETECTION OF CANCER BIOMARKERS

Jury

Alain Cazarré, UPS-LAAS-CNRS, Président
Loïc Auvray, Université d'Evry, Rapporteur
Gabor Molnar, LCC-CNRS Toulouse, Rapporteur
Claus Fütterer, Forschungszentrum Jülich GmbH, Allemagne, Examinateur
Jean-Charles Faye, INSERM-ICR, Toulouse, Examinateur

Ecole doctorale: Génie Électrique, Électronique, Télécommunications : du système au nanosystème (GEET)
Unité de recherche : Laboratoire d'analyse et architecture de systèmes (LAAS-CNRS)

Directeurs de thèse: Christophe Vieu, INSA-LAAS-CNRS,
Childérick Séverac, LAAS-CNRS

To my family, my family in law and my wife

Adrián Martínez Rivas
nanobiomex@hotmail.com

« La science la plus haute et la plus utile est la connaissance exacte et le mépris de soi-même. Ne rien s'attribuer et penser favorablement des autres, c'est une grande sagesse et une grande perfection » (Thomas à Kempis: *L'Imitation de Jésus-Christ)*

“Truly to know and despise self is the best and most perfect counsel. To think of oneself as nothing, and always to think well and highly of others is the best and most perfect wisdom” (Thomas à Kempis: *The Imitation of Christ)*

REMERCIEMENTS

Tout d'abord, je remercie grandement le Conseil National de Science et Technologie (CONACYT) du Mexique, de m'avoir octroyé la bourse d'études qui m'a permis de réaliser mon master de recherche et mon doctorat en France. Je serai toute ma vie reconnaissant envers les cadres, employés, et surtout les ouvriers et agriculteurs qui travaillent énormément et qui, grâce à leurs efforts et leur courage, m'ont permis d'obtenir l'aide financière de mon gouvernement. Je ne regrette pas, maintenant, d'avoir choisi la France pour réaliser mon doctorat parce que dans ce pays, j'ai pu avoir une autre vision du monde. J'ai découvert des choses tellement variées que je ne pourrais pas les énumérer ici. Dès que je suis arrivé en France j'ai eu l'opportunité de sentir l'accueil français, quand un couple de correspondants français m'attendait à l'aéroport de Paris avec des cadeaux pour ensuite m'inviter à dîner aux Champs Élysées pour goûter les délices de la gastronomie française. À travers la grande culture française, j'ai pu aussi mieux me rendre compte de celle de mon pays et mieux la reconnaître. J'ai pu lire les grands esprits de la vaste littérature française. Toulouse, la belle ville rose où j'ai préparé mon doctorat, où j'ai rencontré ma femme, reste dans mon cœur comme la ville où j'ai pu apprendre à mieux aimer les choses simples de la vie, mais aussi la musique classique, l'opéra, le ballet. Où j'ai pu suivre ma formation linguistique, une formation en peinture, dégustation des vins, en guitare, où j'ai pu pratiquer la course à pied, faire mon premier marathon, le vélo…. En outre, je n'oublierai jamais le sourire des belles toulousaines et beaux toulousains, les charmantes ruelles de Toulouse, ses restaurants, ses « boîtes de nuit », ses fleurs, ses violettes, son parfum, son Pont Neuf, Nougaro, sa vie culturelle, les superbes rencontres du Stade Toulousain et l'ambiance de cette dernière fois quand le Stade a rapporté le championnat de France (bouclier de Brennus en 2008). Ô Tolosa …

Ce travail de recherche a été préparé au sein du groupe nanobiosystèmes (NBS) du Laboratoire d'Analyse et d'Architecture des Systèmes (LAAS-CNRS). Je souhaite remercier M. Malik Gallab et M. Raja Chatila (directeurs successifs du LAAS, lors de mon séjour au laboratoire) de m'avoir accueilli dans ce prestigieux laboratoire.

Je remercie également mes deux directeurs de thèse. Merci à tous les deux de m'avoir accepté et encadré dans cette aventure scientifique et humaine. Je tiens à remercier Christophe Vieu d'avoir cru en moi et de m'avoir intégré dans l'équipe où il était le directeur à ce moment-là. J'ai appris beaucoup de son ouverture d'esprit, son discernement et de son humilité. Je peux dire de Childérick Séverac, que je lui suis énormément reconnaissant de m'avoir guidé et aidé sans relâche jusqu'à la fin de ma thèse (même la veille de ma soutenance) d'être resté avec moi jusqu'à 4 h du matin pour que j'eusse une présentation claire et efficace. Merci Childérick pour ta générosité envers moi et pour ton aide tant dans les situations professionnelles que personnelles.

Je tiens à remercier M. Alain Cazarré d'avoir accepté de présider mon jury, mais aussi de m'avoir donné la lettre d'acceptation pour pouvoir venir au LAAS-CNRS quand je finissais l'école d'ingénieurs à Institut Polytechnique National (IPN) du Mexique. Dans ce même contexte je remercie M. Loïc Auvray et M.Gabor Molnar d'avoir rapporté mon travail de recherche. Leurs corrections m'ont permis d'avoir un manuscrit acceptable. Je suis reconnaissant de la disponibilité de M. Claus Fütterer pour avoir été membre du jury. Son ouverture et son charisme ont permis d'avoir un débat scientifique agréable. Enfin, je remercie M. Jean-Charles Faye d'avoir accepté d'être membre du jury. Lors des discussions que j'ai eues avec lui, j'ai pu apprendre et entrevoir un côté biologique que je ne maîtrisais pas. M. Faye a été une clé dans mon travail, parce que grâce à lui, on a dirigé nos recherches vers la nanomédecine.

De quelle l'autre manière pourrais-je remercier tous les gens qui m'ont aidé au bon déroulement de mes recherches ? Je pense tout d'abord à toute l'équipe TEAM de la plateforme technologique du

LAAS, dont j'ai eu l'occasion de travailler avec la plupart des membres car j'ai pu travailler et apprendre beaucoup d'eux. Premièrement, je remercie Franck Carcenac qui m'a appris la lithographie et la microscopie électronique mais aussi le sens des rapports humains. Je remercie aussi dans la même équipe, Laurent Mazenc et Véronique Conedera qui m'ont transmis la lithographie optique, Jean-Baptiste Doucet pour la chimie et la gravure humide pour la micro et nanotechnologie, Sébastien Pinaud et Ludovic Salvagnac pour le dépôt et la technologie du vide, Laurent Jalabert et Pascal Dubreuile pour la gravure sèche. Je tiens également à remercier Pierre-François Calmon pour m'avoir fait tous les masques nécessaires à mon projet, Laurent Bouscayrol et Bernard Rousset pour m'avoir fait les oxydations et enfin René-David Colin et Samuel Charlot pour m'avoir aidé dans le montage des dispositifs. Merci aussi à tous les autres membres de l'équipe comme Emmanuelle Daran, Monique Dilhan, Monique Benoît…

Une autre équipe qui m'a permis d'aller plus loin dans mes recherches, est celle de la plateforme de caractérisation. Je remercie, dans ce cadre, Nicolas Mauran et Sandrine Assie-Souleille qui m'ont formé dans la caractérisation électrique et m'ont aidé à faire des mesures électriques précises et à obtenir de belles photos avec le microscope optique.

La grande aide que Xavier Dollat m'a fournie avec ses prototypes précis, au millimètre près, dans l'atelier mécanique a été capitale pour le bon fonctionnement des dispositifs développés, donc un grand merci.

Du fait que mon travail a été multidisciplinaire, j'ai pu apprendre pleines de choses de beaucoup de personnes. J'ai passé de longues heures avec Patrick Chinestra, de l'Institut Claudius Regaud de Toulouse (lutte contre le cancer), en faisant des expériences biologiques : il m'a initié à la biologie moléculaire, je l'en remercie vivement.

Au laboratoire de chimie et coordination (LCC-CNRS), j'ai pu faire des expériences avec des chimistes. Je remercie M. Lionel Salmon pour le temps qu'il m'a consacré et pour sa disponibilité et sa gentillesse car il m'a aidé à mettre au point la chimie de surface retenue pour l'implémentation dans mes dispositifs. Dans ce même laboratoire, j'ai pu également apprendre, plus spécifiquement, la chimie de polymères lors des expériences réalisées, je remercie à cette occasion Samuel Suhard qui m'a transmis un peu de son expérience. Merci au personnel de la bibliothèque du LAAS (Émilie, Arlette, Anne) de l'imprimerie (Christian), du magasin, de logistique…

Merci à mes amis mexicains et français avec qui j'ai pu rire et discuter : David, Montserrat, Carlos, Miguel, Marie-Pierre, Christel, merci Roahmy de nous avoir prêté ton château pour la journée mexicaine, merci Guadalupe de m'avoir hébergé à Toulouse lors de ma soutencance, merci à tous les mexiacains installés a Toulouse, mes collègues et amis du master de recherche (DEA) et du LAAS : Al señor Eric, Chloé, Chalabis, Gustavo, Michel, Mustapha …, merci Denis de m'avoir prêté la boîte pour faire les tests finaux. Merci à l'ensemble du grand groupe NanoBioSystèmes (NBS) du LAAS : À l'actuel responsable du groupe Liviu Nicu, à tous le membre du groupe qui font de la recherche de premier niveau.

Je remercie chaleureusement toute ma famille, spécialement ma mère qui m'a toujours épaulé et montré sa sagesse, son honnêteté et exemple. Même s'ils étaient loin, ils étaient près dans mon cœur. Je remercie ma belle famille en France, toujours si gentille et agréable, accueillante avec moi en France. Particulièrement Dominique, connaisseur de vins, Véronique, Léonie, Rosalie ouverts, sportifs, agréables.

Enfin un grand merci est dirigé à Valentine, ma femme, parce qu'elle m'a épaulé, soutenu et aussi supporté dans les moments difficiles lors de la rédaction du manuscrit, elle m'a même aidé à la mise en page de celui-ci. Merci d'être là, de ta patience, de ton amour et ta gentillesse.

General introduction

Nanotechnology (form the Greek nano meaning dwarf) is the creation and utilisation of materials, devices and systems through the control of matter on the nanometre length scale (less than 100nm) i.e. at the level of atoms, molecules and supramolecular structures. The term nano refers only to a scale. For example, 1nm is equal to 4 silicon atoms, 6 carbon atoms or around 10 water molecules. However, at this scale new physical phenomena appear compared with their bulk counterpart, such as lower melting temperatures, higher resistivity, higher Young's modulus or others. The experiments conducted in chapters 2 and 5 corroborate the last two properties.

Nanotechnology is an interdisciplinary approach of applied science covering (not detailing the branches): physics, mathematics, chemistry, biology, medicine, neuroscience, microelectronic engineering, electromagnetism, electronics, microfluidic engineering, materials science, informatics, robotics, ethics, philosophy and others. Hence, nanotechnology is conceived of a new multidisciplinary paradigm where there is no distance between science and technology or between science and philosophy, (see the anexe: epistemological and ethical personal opinions in nanotechnology, at the final of the thesis). In this context, nanotechnology promises to offer many improvements in the quality of life to humanity. Fig. 1 illustrates a Buckminsterfullerene C_{60} molecule (diameter size of ~.7nm) picturing sciences and technologies involved in nanotechnology.

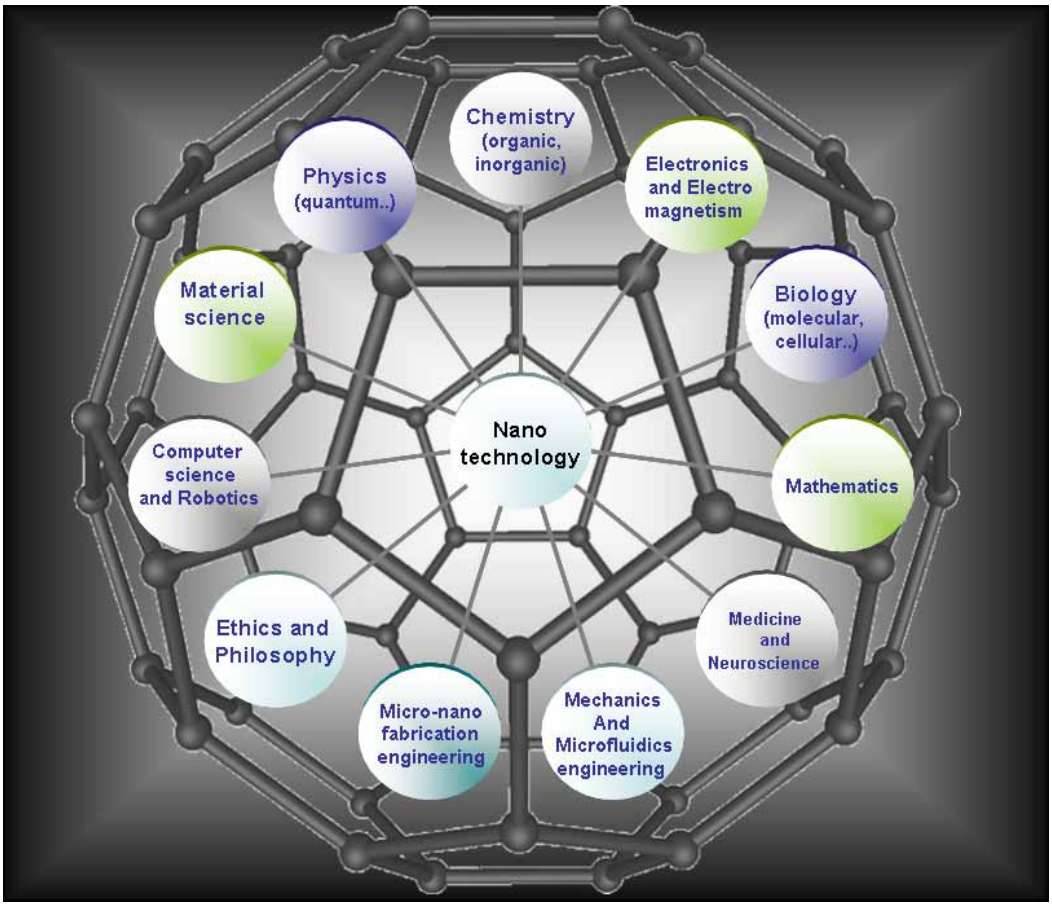

Fig.1. Buckminsterfullerene C_{60} showing some of the sciences and technologies involved in nanotechnology.

Nanotechnology has permitted revolutionary advances in technologies as diverse as electronics, information technology, material technology, adhesive, coating, or disease diagnostic and treatment. Examples of some human creations and some objects found in nature are showed in Fig. 2. In this thesis all referred as nano has a length scale < 100nm (nanoscale). Either the devices are at this scale or technological tools use at least one part at this scale.

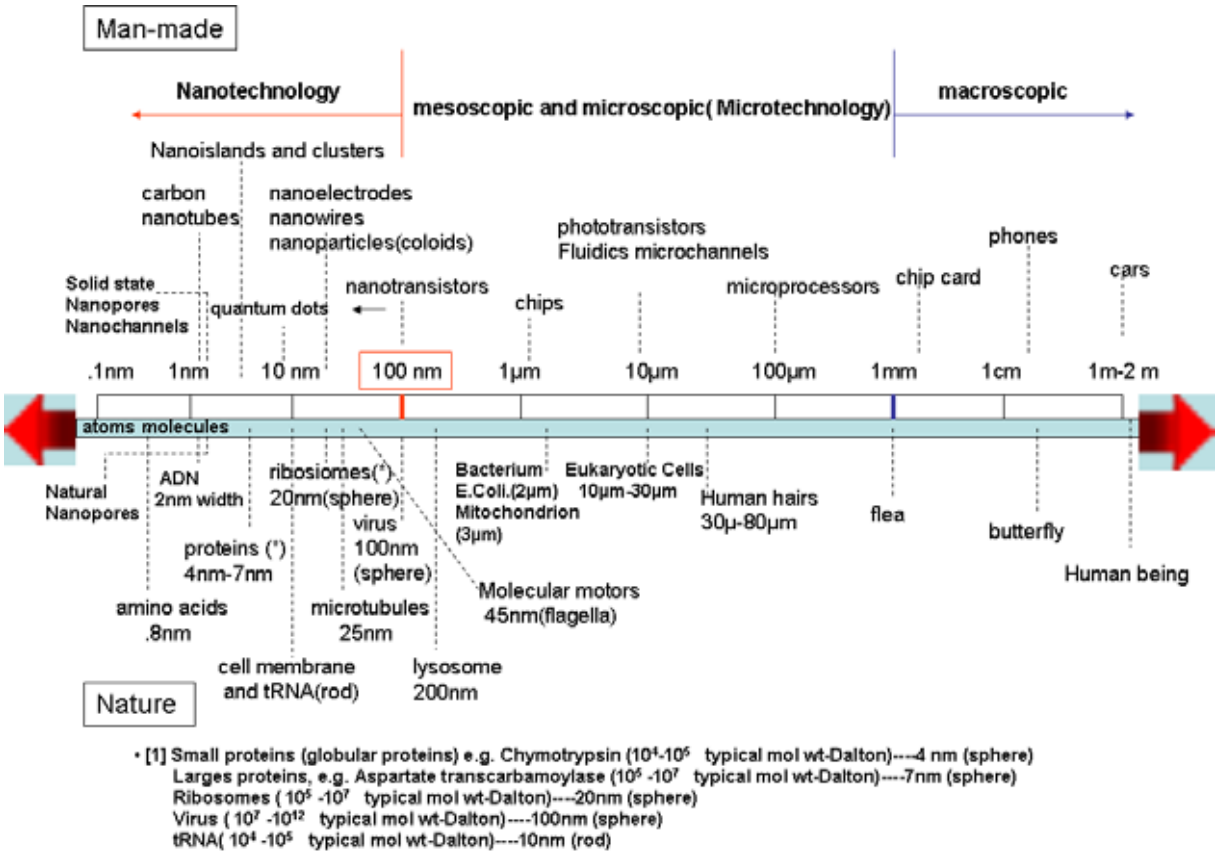

Fig.2. Scale of natural things and manmade things.

Research on biosystems at the nanoscale has created one of the most dynamic and exciting science and technology domains at the confluence of physical science, chemistry, molecular engineering, biology, biotechnology, and medicine [2] which has been named nanobiotechnology. Following this hierarchical classification, nanomedicine is an application of nanobiotechnology. Indeed, modern medicine is constantly taking advantage of the newest technology and scientific advances.

European science foundation (ESF) [3] has defined nanomedicine as “the science and technology of diagnosing, treating and preventing disease and traumatic injury, of relieving pain and of preserving and improving human health, using molecular tools and molecular knowledge of the human body. It was perceived as embracing five main sub-disciplines that in many ways are overlapping and underpinned by the following common technical issue: Analytical Tools, Nanoimaging, Nanomaterials and Nanodevices, Novel Therapeutics and Drug Delivery Systems, Clinical, Regulatory and Toxicological Issues”.

Kewal K. Jain has proposed a scheme which shows the relation between nanotechnology, nanobiotechnology and nanomedicine [4], see Fig. 3. The scheme illustrates the manner how

these fields and technologies contribute to the development of nanomedicine under the novel concept of personalised medicine.

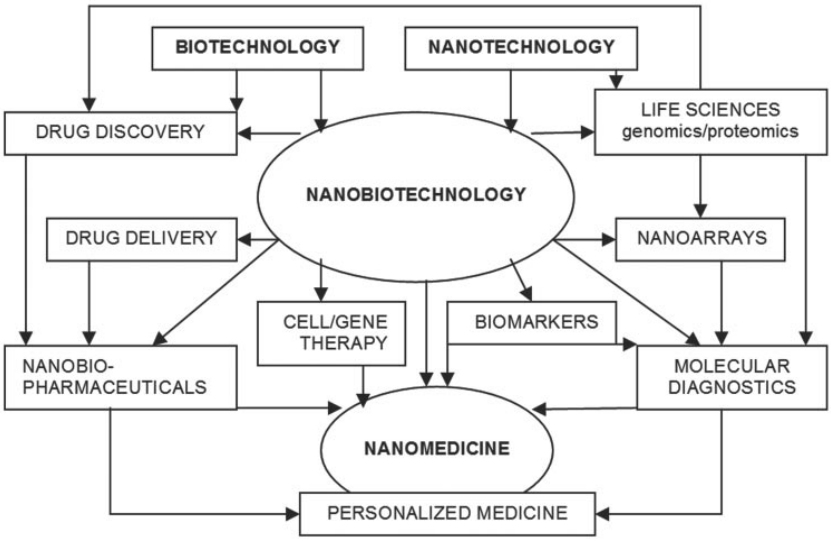

Fig.3. Relationship of nanobiotechnology to nanomedicine (Kewal K. Jain 2007).

Hence, with the research work presented in this thesis, we want to contribute to the increased development of nanomedicine by working in the domain of technology for diagnosing. Then, the purpose of the present research work is to investigate a new nanotechnological technique which enables to increase accuracy of early cancer diagnosis to reach the point of care cancer diagnostics (POC). A. Rosooly et al. proposed a methodology to reach the POC [5] illustrated in Fig. 4.

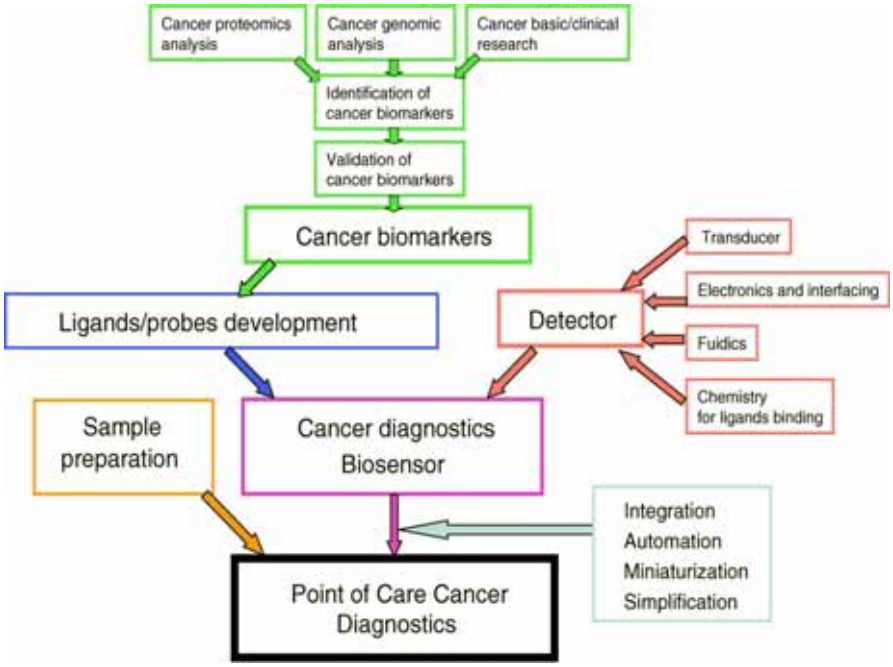

Fig.4. Illustrates the principal elements required to elaborate biosensors for point of care cancer diagnositics: POC (As appeared in: Rasooly A. et al. 2006[5]).

The different parts illustrated in the organigram of Fig. 4 are developed and described in this research work. Our purpose is to elaborate a complete integrated-high sensitive electrical

nanodevice for label-free cancer biomarkers detection, at wafer scale. Because of the written above, this work projects itself into the larger field of nanomedicine and in particular point of care of cancer diagnosis driving towards the enabling concept of personalised nanomedicine. Fig. 5 schematises the principle of the novel electrical nanobiosensor.

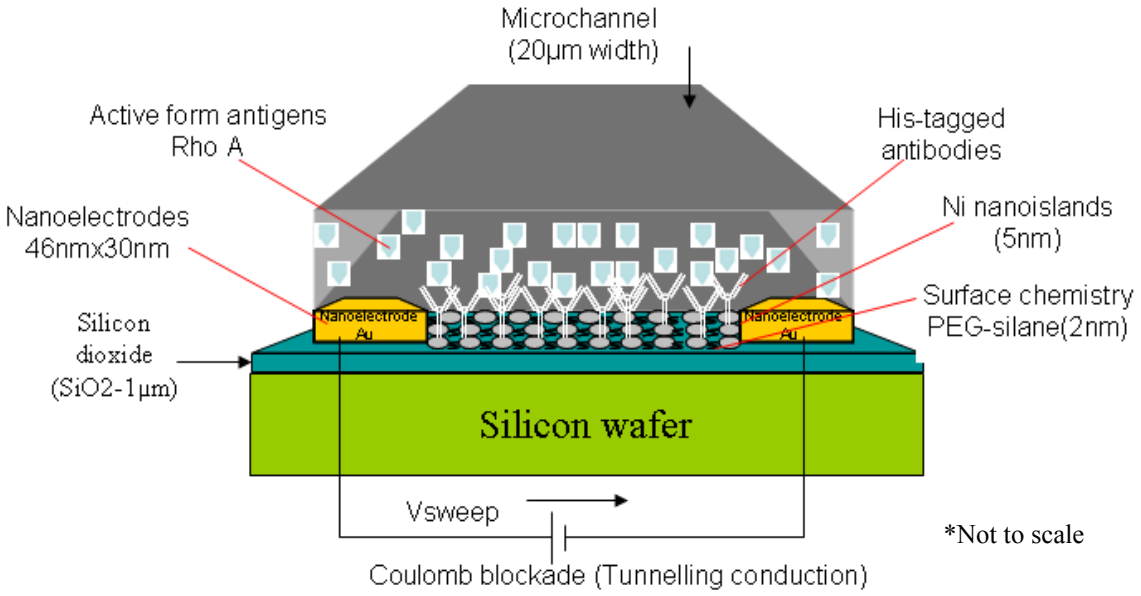

Fig. 5. Schema illustrating the principle and integration of our nanobiosensor device.

The principle is based on the variation of electrical conductivity in nanoelectrodes array due to the proteins adsorbed onto Ni nanoislands. These Ni nanoilsands (~5nm diameter) are embedded into silice (SiO_2) and placed between interdigitated nanoelectrodes devices (IND) of ~45nm width each electrode. Nanoislands are separated each other from ~2 nm. In these conditions, it is obtained a nanotransducer, based on the variation of electrical tunnelling conductivity through metal nanoislands due to the quantum phenomenon called coulomb blockade, at room temperature. Because of this phenomenon, these nanodevices are fast-response and ultrasentive to any change that can affect the tunnelling conduction, for example adsorption of proteins. Hence, his-tagged antibodies, functioning as probe are linked by coordinative bonds to the Ni nanoislands, they recognise specifically the active RhoA conformation, which functions as target, and discriminate against its inactive RhoA conformation. Finnally, an innovative methodology to realise photoPDMS-based microchannels (20µm) was developed and integrated with IND on 4 inch wafer and encapsulation with an etched PDMS-nanocomposite finalised the integration of the device.

The plan of the thesis is as follows:
In chapter 1 considering the multidisciplinarity of nanotechnology, I detail some concepts and technological developments, with the objective of being read by physicists, physicians, biologists, chemists, engineer, philosophers, and so on. Hence some concepts of molecular biology, proteomic, oncology, clinical research, cancer biomarkers, bioMEMS and medical devices, Micro-Total-Analysis Systems (µtas), lab-on-a-chip (LOC) devices and bonds found in nanotechnology and nanomedicine are described.

I describe, in detail, thje protein Rho (biomarker) used in this work. Some nanodevices used for cancer diagnosis such as carbon nanotubes, nanowires and nanoparticles are also

compared. Finally, our nanobiotechnological principle and approach for cancer diagnostics is described in detail.

In chapter 2 after remembering some micro/nano technological methodologies, elaboration of 96 cells involving 768 interdigitated nanoelectrodes devices (IND) (some times called interdigitated nanoelectrodes arrays devices: IDA or nanointerdigitated electrodes arrays devices: nIDA) by a mix and match process using UV and eBeam lithography on wafer scale is presented. Then I describe, in detail, the methodology we used to realise 96 IND with high reproducibility by using electron beam lithography (EBL) combined with typical photolithography. The electrical characterisation of our devices is conducted in bare conditions and in short-circuit nanoelectrode to estimate its conductivity.

In Chapter 3 Nickel nanoislands (~5nm) are deposited onto silicon dioxide (SiO_2) surfaces and then electrical characterisations are conducted obtaining electrical tunnelling conduction. Nanoislands are deposited between interdigitated nanoelectrodes, in entire devices. Ni Nanoislands are characterised in AFM and STEM microscopies. Coulomb blockade phenomenon is found, at room temperatures, combining nanoislands with interdigitated nanoelectrodes. Some interest applications are found by using these kinds of multitunnel junction devices, however, they will be used to reach label-free biomarkers recognition for the first time.

In chapter 4 using a quartz crystal microbalance (QCM) we validate the label-free detection of cancer biomarker binding assay interactions and recognition using the Ni nanoislands as deposited in chapter 3. We implement a surface chemistry involving an anti-biofouling coating of polyethylene glycol-silane referred as PEG-silane (< 2nm thick) to avoid non-specific bimolecular interactions. Some interesting results are found such as the fact that glycerine, used as cryogenic protectant in molecular biology, produces non-specific biomolecular interactions, in our nanobiotechnological protocol. A new protocol without glycerine has thus been validated by ELISA technique. Finally, the specific label-free detection and recognition of the active antigen conformation of RhoA, avoiding the glycerine effect, is demonstrated by quartz crystal microbalance (QCM) technology at various concentrations. This method proves the viability of the concept by implementing one of the most critical steps in nanobiosensor or protein-chip realisation, in this case by using Ni nanoislands as an anchoring surface layer enabling the detection of a specific conformation of a protein, identified as a potential cancer biomarker.

Chapter 5 is divided in three sections, the first one consists of an innovative methodology to realise photoPDMS-based microchannels which is developed and integrated with the IND on 4 inch wafer. Hence, limit resolutions in novel negative polydimethylsiloxanes (N-photoPDMS) and in positive photosensitive polydimethylsiloxanes (p-photoPDMS) for wafer scale are described for the first time. This technique permits to realise microchannels aligned onto each nanobiosensor. It is aligned, 20µm width channels onto each 7 mm X 7 mm cell, on the entire wafer.

In the second section, interconnection and bonding of 3-D polydimethylsiloxane (PDMS) microchannels on wafer scale are elaborated. PDMS is casted onto a 4 inch mould master which is elaborated on SU-8 (10 µm and 500 µm layers). A dry etching is conducted into

PDMS to define proper circular interconnecting holes (vias). I mix silica nanoparticles (20 nm) into unmodified PDMS polymer matrix to reinforce it, obtaining a PDMS nanocomposite. The advantages of using this nanocomposite are better Young modulus, better tensile and tear strength. However a better dry etching homogeneity is found in PDMS nanocomposite. Finally, pressure tubing connections are achieved and leakage pressure tests are conducted using a pressure system tool called MFCS^{R} instead of using syringe systems or peristaltic pumps that lead hysteretic and other effects. This second section is implemented as a methodology to be used for covering the PhotoPDMS based microfluidics channels of the first section.

Finally, in the third section a SU-8 mould master is used for casting a 4 inch PDMS covers. It is aligned on wafer level and an improvement on the SU-8 master mould by design offset is achieved because PDMS has an inevitable shrinkage after curing it.

Chapter 6 presents a deposition of liquid solution on each IND for multiplexed biological analysis using a spotter (called Bioplume). The bioplume tool has been developed within the nanobiosystems group and patented [4]. It is a system based on microcantilivers that permits to deposit precisely liquid spots from picolitter to femtolitter range. Therefore, the nanobiosensors devices are designed to be coupled with the "bioplume" system. The purpose is to deposit the probes biomolecules locally onto the interdigitated nanoelectrodes devices (IND) avoiding cross contamination while using less analytes. The deposition is also realised to be performed between photoPDMS microchannels described in chapter 5.

Chapter 7 presents the complete integrated high sensitive electrical nanodevices for label-free cancer biomarkers detection. The integration is performed, doing several steps on wafer level. An organigram pictured in Fig.6 resumes both the fabrication processes and the plan of the present thesis, furthermore it presents the manner we linked the developments realised in above chapters.

Firstly, marks are photopatterned to align each IND on 4 in. silicon wafer (covered with silicon dioxide layer of 1 μm). In a second step, the wafer is functionalised covalently with PEG-silane which is grafted into microchannels shape patterns made of momentary photoresist, aligning in each IND. Being the PEG-silane hydrophilic, it allows the biological compound flowing across the microchannels. It serves also as proteins repellent along the microchannels. Indeed, it avoids the non-specific biomolecular interaction in the active zone of each IND. The third step consists of depositing Ni nanoislands locally on the IND. In a fourth step, the elaboration of 768 interdigitated nanoelectrodes arrays on the entire wafer by using electron beam lithography (EBL) was conducted. In the fifth step, all nanostructures are mixed and matched with micropatterns to connect them. In the sixth step, 200 photoPDMS based microchannels (20 μm wide) aligned with IND are patterned in one step onto the 4 in wafer. Then, in the seventh step local deposition of biomolecules on the active zone of IND is proposed, after investigating the damage of the bioplumes to the IND.

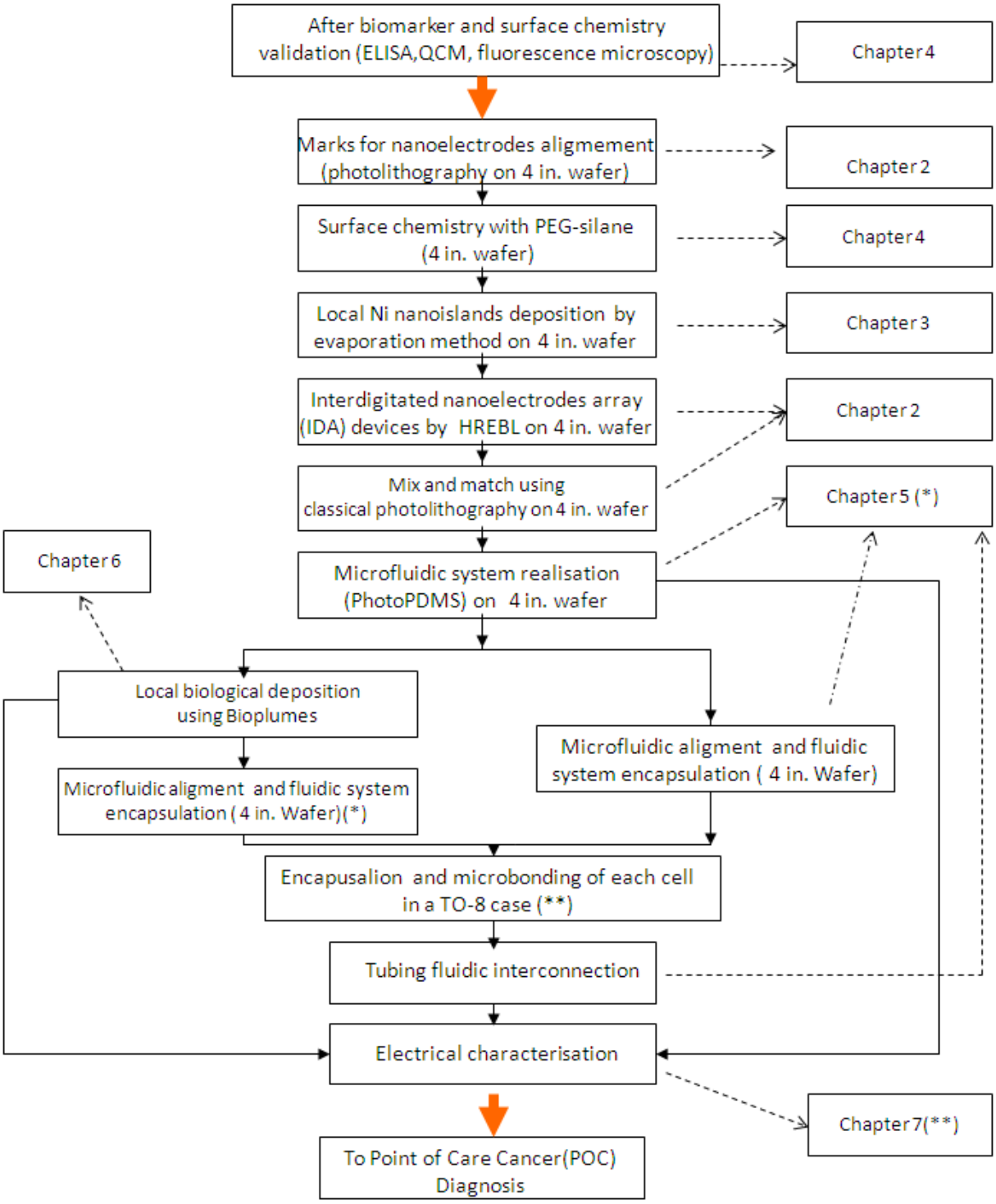

Fig.6. Organigram-planning for elaborating our integrated system and for presenting the research work in the different chapters.

Another possibility avoiding the use of local deposition (bioplumes) is by covering the photoPDMS with the flat PDMS film presented in chapter 5. See the organigram. Then, in the eighth step, cells are cut and encapsulated into TO-8 cases. Next, microbonding is conducted. In last step, interconnecting tubes are sealed to realise electrical characterisation to validate high sensitive cancer biomarkers detection in continuous biological flow and in real time (at

the time we are writing this thesis, we have detected ~100pM of the active antigen conformation of RhoA while discriminating from the inactive antigen conformation of RhoA). This integration is intended to be part of a viable Lab-on-a-chip device.

References

[1] Vo-Dinh Tuan, Protein. *Nanotechnology: Protocols, Instrumentation*, 1 ed. Human press Inc, **2005**.

[2] Roco. M., "Nanotechnology: convergence with modern biology and medicine", *Curr. Opin. Biotechn*., **2003**, 14, p. 337-346.

[3] ESF Forward Look on Nanomedicine **2005** (www.esf.org).

[4] Kewal K. Jain, "Application of nanobiotechnology in Clinical Diagnostics", *Clinical Chemistry* **2007**, 53, p. 2002-2009.

[5] Rasooly A, Jacobson J., "Development of biosensors for cancer clinical testing", *Biosens. and Bioelec,.* **2006**, 21, p. 1851-1858.

Chapter I

Clinical cancer laboratory and medical nanodevices for label-free cancer biomarkers detection

1.1 Cancer and oncology concepts

Historically, an ancient physician from Greece noticed a similarity of the swollen mass flood vessels surrounding a malignant tumour, to the form of a crab and he named the disease. Traditionally, cancer (Latin word for crab) has been thought as a genetic disease, but functionally, it is an alteration of the protein networks and signalling pathways that can produce cancer growth, tumour invasion and then metastasis [1].

Otherwise, oncology can be defined as the branch of medicine that studies cancer tumours and seeks to understand their development, diagnostic, treatment and prevention. Application of nanotechnology in cancer has been termed “nano-oncology”.

1.1.1 Cancer diagnosis

If cancer is detected at its early stages, physicians can more effectively treat it and cure it. Unfortunately, only few cancers are detected by screening programs and most are still found after patients seek medical attention, because of the tumours effects. In this context the typical route followed in the diagnostic screening, starts with an unexplained pain, bleeding or the presence of a tumour in or outer the body [2]. The patient undergoes several medical tests, hence if having the presence of tumours the patient undergoes a biopsy or fine needle aspiration to be examined under microscope by a pathologist (physician who specialises in the diagnosis of disease). However, at this early stage of cancer, a precisely diagnostic is hugely challenging, hence nowadays intense research has been dedicated. One of the intrinsic problems is the difficulty encountered by pathologist to obtain a diagnostic 100% specific and sensitive using traditional tests because these parameters are inversely related. In this context nanotechnology has an enormous impact, due to the nanometre size compared to the biological elements; the sensitivity and specificity are increased. Hence, nanomedicine offers a novel paradigm to significantly obtain advances in cancer diagnosis but also in its treatment.

1.1.2 Traditional clinical diagnosis research and cancer therapy

Diagnostics assessment is to recognise a disease process, differentiating it from others and giving it a name [2]. The first step to accomplish this assessment is to differentiate a benign from malignant growths. After realising a tissue biopsy (either surgical or fine needle aspiration), the assessment is performed by a surgical pathologist which examines the tissue and is also charged to guide the management of the patient.

The first procedure of tissue examination consists of evaluating morphologically the tumour by staining with haematoxylin and eosin (H&E). It is a visual interpretation of the H&E slide. This method, universally available, is archaic but it can be efficient and it is low cost. Nevertheless, the method needs knowledge of clinical setting such as age and sex of the patient, the anatomical site, previous histological and/or radiological findings and past surgical chemotherapy or medical intervention. As it can be noticed, in modern clinical

research, it is necessary to have a clinical diagnosis method that is sensitive, specific, and low cost. This could be possible if using nanodevices like protein nanobiochips, nanowires or the nanoelectrodes/nanoislands-based devices we propose here. In this context nanotechnology on-a-chip is emerging.

Regarding cancer therapy, nowadays most cancers are still treated with no gentle methods such as surgery to remove malignant cells, chemotherapy or radiation therapy. Chemotherapy refers to treatment of disease by chemicals that kill cells specifically those of micro-organisms or cancer. The use of chemical compounds (as drugs) to destroy tumours is mandatory in current treatment of malignancie, that is why numerals drugs are in use or are in early stages of development. However most of these drugs are not effective, as there are problems like delivery, penetration or also lowly degree of selectively. Furthermore, the most discouraging limit factor is drug resistance. For example, cancers such as prostate tumours are intrinsically resistant to most anti-tumour drugs. Ovarian carcinoma or small cell lung cancer respond to chemotherapy and often disappear "totally", returning later as drug-resistant tumours. Hence, nanotechnology has here also an important role, because for example, by using ferromagnetic nanoparticles or nanovectors such as liposomes or carbon nanotubes, it will be possible to deliver anticancer drugs specifically to malignant cells, and determine if these drugs are killing malignant cells (nowadays, it is being achieved, for instance in Dai's group, described later).

Nanotechnologists think that nanotechnologies serve as multifunctional tools that will not only be employed with any number of diagnostics and therapeutic systems, but they will change the foundations of cancer diagnostics and treatment.

1.2 Proteomic application for early detection of cancer: Biomarkers

One of the most crucial stages in cancer development is the so called metastasis (the spread of a disease from one organ to another distant organ) [4] as mentioned above the early cancer detection is important to prevent a devastating cancer development, in this context biomarkers are useful tools for cancer detection and monitoring. A biomarker is described as an entity which can reveal through its concentration measurement a normal biologic process, a pathogenic one, or pharmacologic responses to a therapeutic intervention. An alteration of a cell, metabolite or protein level can be referred as cancer biomarker. For example, prostate-specific antigen (PSA) is a biomarker and its level of expression is changed in the tumour or in blood, urine, or other body fluid of cancer patients.

Beyond early detection, the information provided by biomarkers help in sensing the status of the disease hence improving control and prevention of cancer [5]. Otherwise, proteomics is valuable in the discovery of biomarkers because the proteome reflects both the intrinsic genetic program of the cell and the impact of its immediate environment.

Proteomics technologies can be used to identify biomarkers, to monitor disease progression, and to identify therapeutic targets.

1.2.1 Proteomics analysis and proteomics technology

Proteins are folded chains of amino acids strung together by peptide bonds. If 50 amino acids are linked together, it is formed the so called peptide and if there are more than 50 linked together, it is called a protein. As writing elsewhere [6]: "Proteins are the structural and

organisational elements of the living state" and they are essential part of living organisms because they are the main component of the physiological metabolic pathways of cells [7].

Human sinthetises 20 different amino acids like histidine, cysteine, and glycine [8]. Amino acids have distinct side group with different degrees of polarity, thus water solubility. Amino acids which are non-polar and insoluble in water (hydrophobic) include pheylalanine, leucine, isoleucine, tryptophan, tyrosine, valine and histidine (in decreasing order of hydrophobicity). Histidine which has five sided ring with three carbons and two nitrogrens, is the amino acid used in this research project, because of its capacity of linking to nickel by coordinative bonds.

The vital functions of proteins are intrinsically linked to their structure and dynamic switching among different conformational states. Proteins such as: enzymes, receptor, cytoskeleton filaments, muscle myosin, and haemoglobin experience enormous conformational changes in relation to different causes. In this context, activities in living cells are performed by protein conformational dynamics, controlled by quantum mechanics (e.g. van der Waal London forces) [6], otherwise quantum states are essential of biological systems, but also in inorganic systems as demonstrated in nanotechnology. Hence, that is precisely one of the novel paradigms in nanotechnology: the couple natural-artificial comportment.

Proteomics refers to the study of structures and function of proteins, their relative abundance, function and interaction with other macromolecules in a cell or organism. Most proteins function in collaboration and interactions with other proteins and precisely one of the purposes of proteomics is to identify protein interactions.

A proteomics experiment can be split in three categories [9]:

1. Protein preparation and analysis (electrophoresis and non-electrophoresis methods).
2. Mass spectroscopy (MS) (electrospray or matrix-assisted laser desorption/ionisation).
3. Bioinformatics (the use of programs to reach large database).

Generally for the protein separation and analysis of protein mixture, there are two electrophoresis approaches. In one of them, the analysis starts purifying the proteins that could be conducted by affinity chromatography, ion exchange or subcellular fractions. Hence, two dimensional polyacrylamide gel electrophoresis (2D-PAGE) isolate single proteins to be processed by mass microscopy (MS). Other uses one dimensional gel (ID- PAGE) which allows incomplete electrophoresis separation thus it necessitates a separation technique such as high-performance liquid chromatophraphy (HPLC). Finally in non-electrophoresis methods, the complete mixture is processed to peptide; and the peptide mixture is separated by multidimensional chromatography.

Mass Spectrometry (MS) is a technique that uses a mass spectrometer to establish the molecular weight (MW) of a sample. Hence, MS is used, for example, to the identification of proteins and the establishment of their molecular weight being this technique able to determine numeral proteins in brevity of time.

1.2.2 Antibodies and antigens

Antibodies, which are also known as immunoglobulin, are the gamma globulin proteins synthesised and secreted by B-cells in the body, in response to the presence of a foreign substance, named antigen. There are five different classes of immunoglobulin (G, A, M, D

and E). Immunoglobulin G (IgG), also known as γ-globulin, has a typical molecular mass of 150kDa being the principal antibody in serum. The structure of an antibody, typically represented as the structure of an IgG molecule, consists in two heavy and two light chains each containing several domains held together by disulfide bonds. The antibody structure is illustrated in Fig. 1.1.

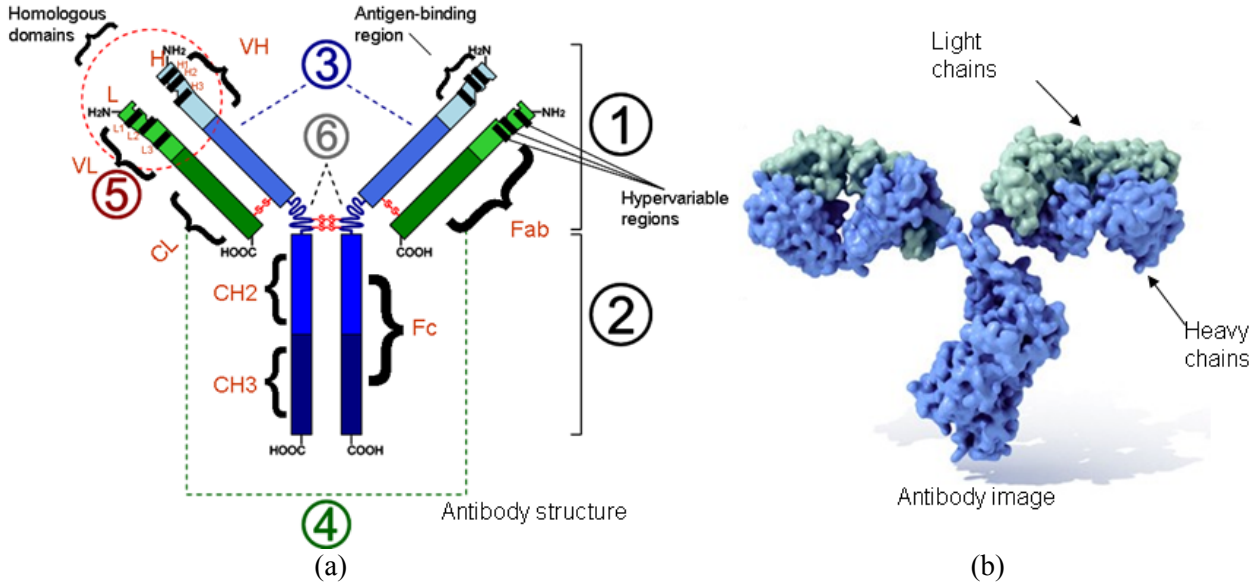

Fig.1.1. (a) Antibody structure, (b) immunoglobulin molecule from Wikipedia.com.

Parts:

1. Fragment antigen binding (Fab fragment) domain
2. Fragment crystallisable region (Fv region)
3. Heavy chain with one variable (V_H) domain followed by a constant domain (C_H1), a hinge region, and two more constant (C_H2 and C_H3) domains
4. Light chain with one variable (V_L) and one constant (C_L) domain
5. Antigen binding site (paratope)
6. Hinge regions. (-S-S- means disulfide bonds)

The interactions of antigens with antibodies form the basis of all immunochemical techniques. Then antibodies bind to antigens, most of which are proteins, polysaccharides, or nucleoproteins. The bonds between antibodies and antigens are not covalent, similar to the enzymes and substrate. The fraction of the antigen that binds to the antibody is known as antigenic determinant (or epitope) and paratope in the antibody (the antigen binding site). The only part recognised by the antibody is the epitope of the antigen. This can be mapped by using ELISA technique or proteins arrays, described later.

1.2.3 Antibody fragments

The fragment antigen binding (Fab fragment as paratope) is a region on an antibody which binds to antigens. It consists in one constant and one variable domain of each of the heavy

and the light chain. These domains form the paratope at the amino terminal end of the monomer and the two variable domains bind the epitope on their specific antigen. The fragment crystallisable region (Fc region) is the tail region of an antibody that interacts with cell surface receptors called Fc receptors and some proteins of the complement system. This property allows antibodies to activate the immune system. In IgG, IgA and IgD antibodies isotopes, the Fc region consists in two identical protein fragments, derived from the second and third constant domains of the antibody's two heavy chains and IgM and IgE regions contain three heavy chain constant domains (C_H domains 2-4) in each polypeptide chain.

1.2.4 Single Chain Variable Fragment (scFv)

It is a combination of the variable regions of the heavy and light chains of immunoglobulins, linked together with a short (usually serine, glycine) linker [10][11]. This chimeric molecule maintains the specificity of the original immunoglobulin despite the removal of the constant regions and the introduction of a linker peptide. ScFv can be created directly from subcloned heavy and light chains derived from a hybridona. ScFvs are typically used in flow cytometry, immunohistochemistry and as antigen binding domains of artificial T cell receptors.

In this thesis, we use his-tagged scFv antibody fragment immobilised onto the Ni nanoislands (~5nm diamter). The fragment is linked to the biomarker GTPase RhoA (active form of RhoA, functioning as antigen). The reason is because RhoA is found overexpressed in various tumours and because our collaborators: J.C Faye, P. Chinestra and G. Favre have recently isolated and characterised a new conformational scFv which selectively recognises the active form of RhoA [12]. Fig. 1.2 illustrates the structure of an immunoglobulin showing the antibody fragments, it was modelled using RasMol computer program (from Wikipedia).

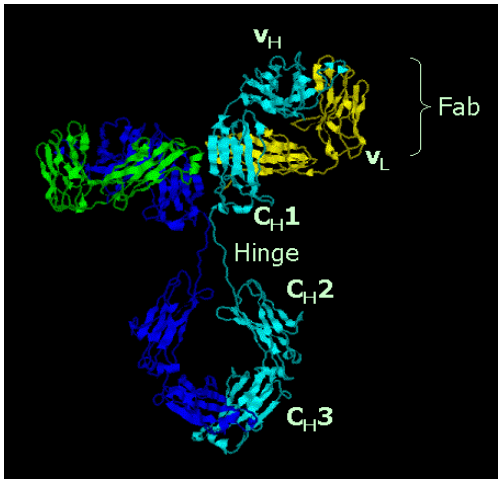

Fig.1.2. Structure of an immunoglobulin showing the Fab (RasMol) (from Wikipedia).

1.2.5 Identification of cancer biomarkers

Rho GTPases have been identified as potential cancer biomarkers [15-17], this kind of biomarker is described in next sections because the purpose of this research work is to recognise the biomarkers RhoA at high sensitivity and specificity as mentioned above.

A mentioned in the proteomic section, the 2D-PAGE coupled with MS technique have been the conventional proteomics analysis for discovering several biomarkers, however there

are numeral inherent drawbacks such as the quantity of biological compound required as starting material. Furthermore the technique is not adequate to identify low abundance of proteins. Novel techniques to improve this situation and to discover newest biomarkers are being created because a cheaper more sensitive technique with enhanced specificity is suitable and nanotechnology has the potential to improve this thereof.

1.2.6 Diagnostic immunology assays

It is an ensemble of diagnostic techniques taking advantage of the specific bonds between antibodies and antigens. This specificity has turned out to be an excellent tool in the detection of substances connected with diagnostic techniques. For example, specific antibodies for specific-wanted antigens can be performed with fluorescent label or colour-forming enzyme but also radiolabel because of this several biochemical techniques (immunoassay techniques) are used to detect the concentration of a biological substance as antigens or antibodies, typically in serum or urine. Some of these techniques, employed in biology and medicine, are Enzyme-Linked Immunosorbent Assay (ELISA) (enzyme immunoassay-EIA) or western blot (alternately, immunoblot). In this research project, we used ELISA technique thus only this biochemical technique is described here.

1.2.7 Traditional immunological techniques for biomarkers validation (ELISA)

Enzyme-Linked Immunosorbent Assay (ELISA), or Enzyme Immunoassay (EIA), is a biochemical technique used principally in immunology to detect the presence of an antibody or an antigen in a sample. Briefly, the sample that can be any body fluidic, containing a specific antibody of interest is placed in a *well* that has been conjugated with a ligand (binding protein) for that antibody. Antihuman anti-globulin antibody that has been conjugated with an enzyme is then added, it binds to the patient's antibodies and it is bound to the ligand in the well. A substrate specific for the conjugated enzyme is added giving a colour. The amount of colour is measured proportionally to the quantity of antibodies presented in the original patient sample. A typical ELISA plate consist in 96 well on an 8 x12 matrix, each well measures around 1cm in height and 0.7 cm in diameter. There are different kinds of Elisa techniques, such as indirect ELISA, sandwich Elisa, competitive ELISA and the newest Elisa renverse method & device (ELISA-R m&d). Otherwise, ELISA is not a label-free technique, it is relatively high sensitive test (pM), but false positive results could happen thus analytes such as HIV require be tested by Western Blot also [9]. In this reach work; ELISA is used to validate the different proteins functionality, before implementing the biomolecules to our devices. The simplest ELISA principle is illustrated in Fig. 1.3 and 1.4, in other section the label-free and labelled probes techniques are explained.

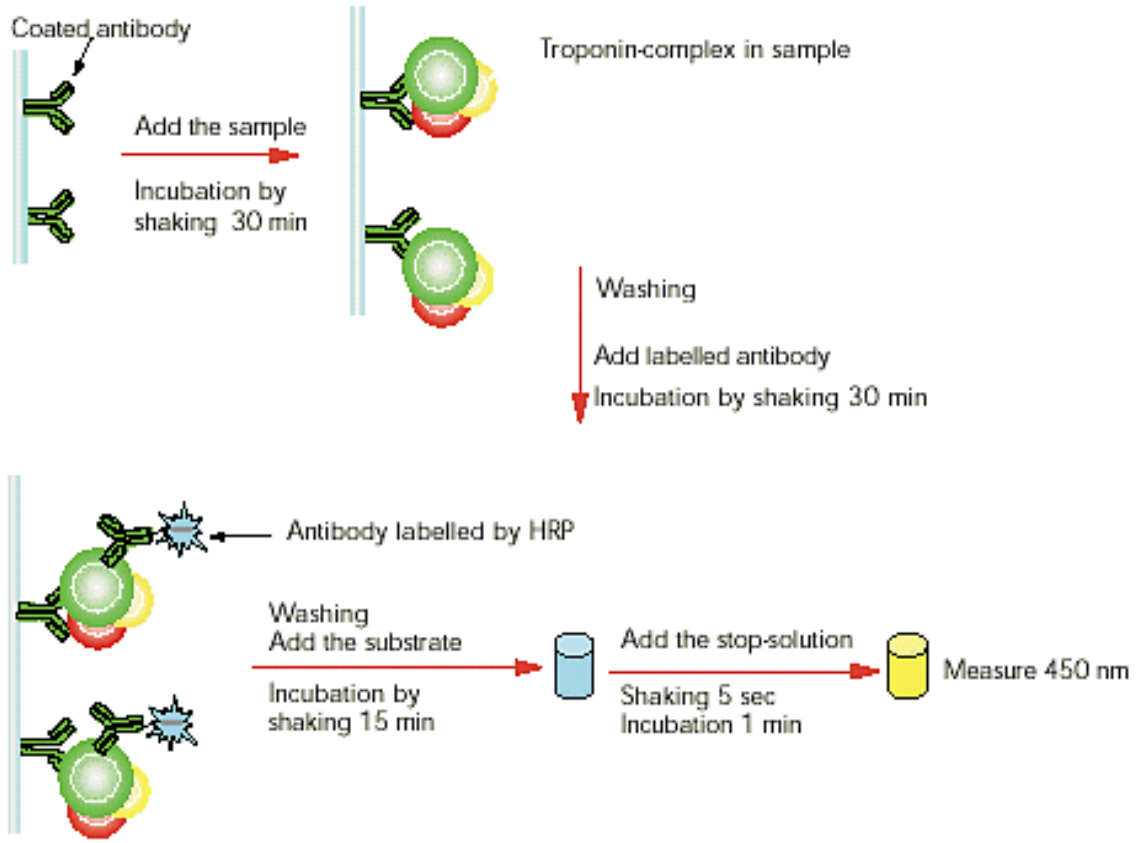

Fig.1.3. Elisa technique methodology (picture from internet of Wisconsin university).

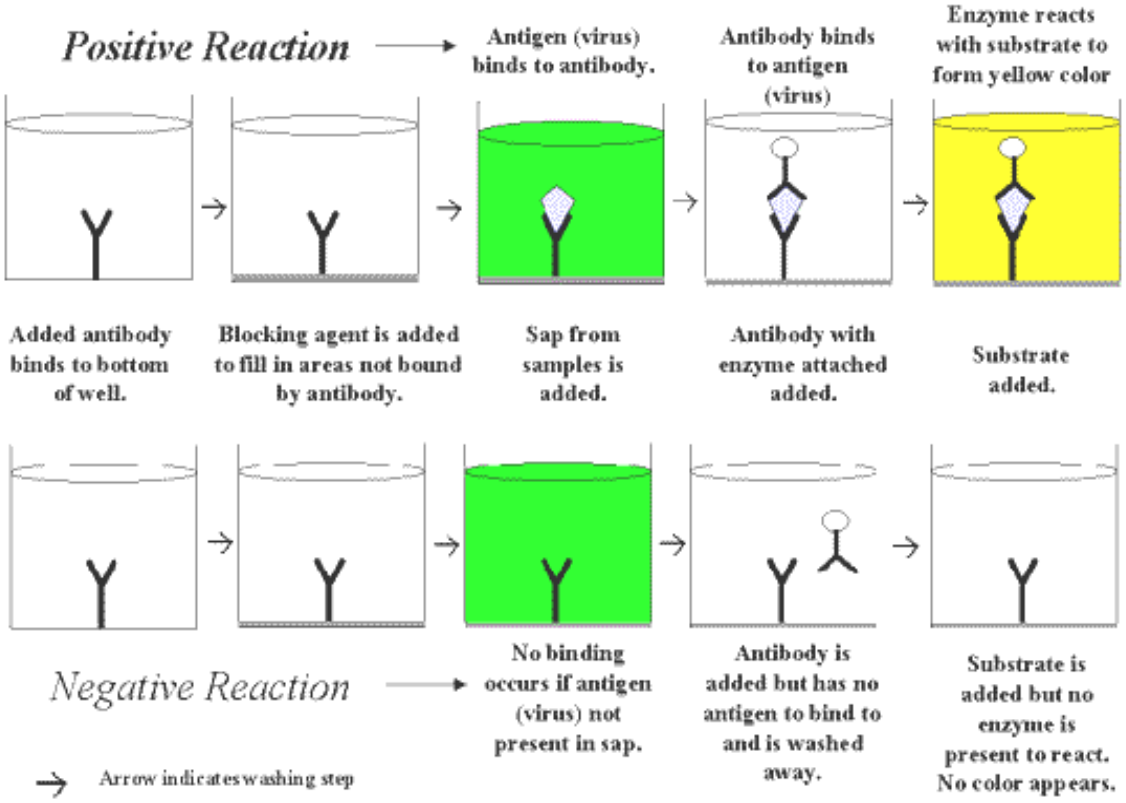

Fig.1.4. The simplest test Elisa principle (picture from internet: Wisconsin university).

1.3 The Rho GTpases

Rho stands for Ras-Homologous, the rho family of GTpases is a family of small (~21kDa) signalling G protein (more specific, a GTpase) and it is a subfamily of the Ras superfamily. Ras proteins are small monomeric GTPases (~21 kDa) that are essential in transducing growth signals from cell surface receptors to the nucleus. Briefly, Rho GTpases are molecular switches that control a wide variety of signal transduction pathways in all eukaryotic cells. The expression of some Rho family members has been found to be increased in some human cancers, and some cancer-associated mutations in Rho family regulators have been characterised too. Rho GTpases include twenty mammalian Rho GTpases: Rho (three isoforms: A, B, C); Rac (1, 2, 3); Cdc42; TC10; TCL; Chp (1, 2); RhoG; Rnd (1, 2, 3); RhoBTB (1, 2); RhoD; Rif; and TTF. How the Rho types have started to be studied?

When the first *Rho* gene was cloned in 1985, the only known members of the Ras GTpase family were the three very similar related *H-Ras*, *Ki-Ras* and *N-Ras* genes and they were identified as oncogenes mutated in human tumours. In 2001 Ras-related *Ral*, *Rap* and *Rab* genes were systematically cloned by Tavitian and colleagues, which were screening human cDNA libraries with Ras probes1. On the contrary, the first *Rho* gene was no deliberately cloned from the sea-slug *Aplysia*2. Madaule et al. identified three human homologs nowadays known as *Rho*A, *Rho*B and *Rho*C, thus several Ras experts stared studying the *Rho* genes, thinking that as *Ras* they would be oncogenes, in response to a variety of stimuli, control key signalling and structural characteristics of the cell.

1.3.1 Rho GTpases in cells tumour and cell biology

It is known that animal's cells acquire numeral diversities of forms, going from the relatively columnar epithelial cell to the complex branched structure of a neuron. Human tumours conceal multiple genetic alterations and changes in genes controlling cell growth, but also in differentiation and survival. These genetic changes include activation of oncogenes and inactivation of tumour suppressor genes; these are the reasons why cellular functions are strategic in tumourgenesis studies.

In this contextual study, the role of Rho GTpase in cells has been identified, being the regulation the actin cytoskeleton, microtubule dynamics, the ability to influence cell polarity, membrane transport pathways or transcription factor activity. As actins cytoskeleton changes are required for migratory feature of cell, in response to growth of factor stimulation or matrix interactions, studies reveal the contribution of Rho molecules to the motility and invasion of tumour cells. Clearly Rho-Family GTpases are involved in the control of cell morphology and motility in untransformed cells. In the case of metastasis tumours, on the other hand, cells develop the ability to traverse tissue boundaries, but how Rho proteins function in cell biology? Rho proteins function as a molecular switch similarly to Ras proteins and one of the most frequently activated oncogenes in human cancer is the Ras gene family.

In humans, three Ras genes have been identified: H-Ras, N-Ras and K-Ras. Rho GTpases are guanine nucleotide binding proteins which cycle between an inactive GDP-bound conformation and an active GTP-bound conformation, and they interact with their downstream targets when bound to GTP. Figure 1.5 illustrates the Rho protein cycle.

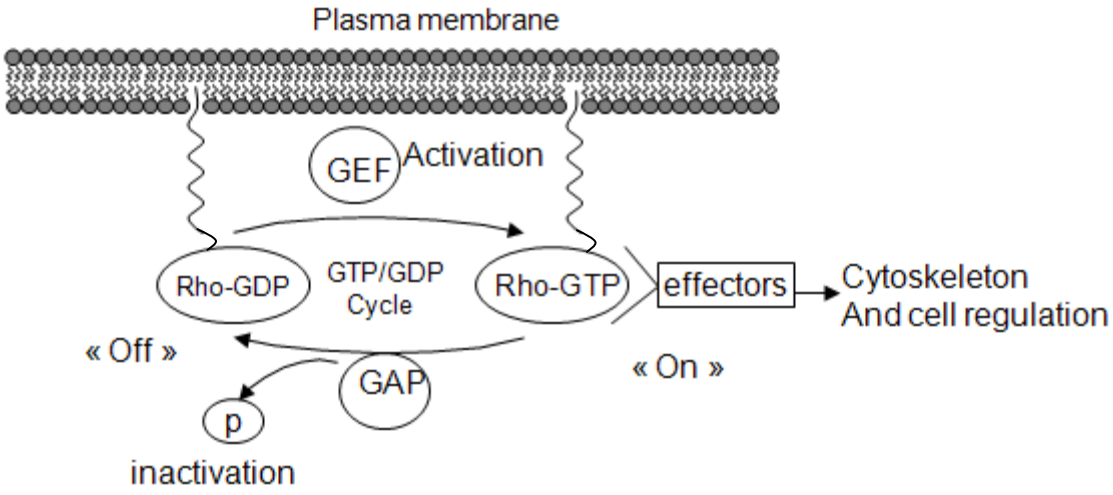

Fig.1.5. Model of Rho-protein cycle (regulation).

Fig. 1.5 shows that Rho proteins can cycle between either active (GTP-bound) conformation or inactive (GDP-bound) conformation. In the active form, they interact with one of over 60 target proteins (effectors). When bound to GDP; they can be maintained in the cytoplasm by Rho-GDP dissociation inhibitors (Rho-GDIs). The cycle is highly regulated by three classes of protein, in mammalian cells, around 60 guanine nucleotide exchange factors (GEFs) catalyse nucleotide exchange and mediate activation; more than 70 GTPase-activating proteins (GAPs) stimulate GTP hydrolysis, leading to inactivation; and four guanine nucleotide exchange inhibitors (GDIs) extract the inactive GTpase from membranes. Hence, the exchange of GDP for GTP is supported by Rho guanine nucleotide exchange factor (Rho-GEFs), and is often associated with a translocation of Rho proteins to cell membranes.

GTP-bound Rho proteins interact with numerical effectors proteins and modulate their ability to regulate the mentioned above cell feature. Finally, most Rho proteins have an ability to hydrolyse GTP to GDP and inorganic phosphate (P), which can be supported by Rho-GTpase-activating proteins (Rho-GAPs). Otherwise RND, RND2, RND/RhoE and RhoH are unable to hydrolyse GTP, and their regulation is related to the changes in proteins levels localisation, not through GDP/GTP binding.

In this thesis, the active form or conformation of RhoA (Rho GTP) is selectively detected, as this form has been identified in several tumours as described later.

1.3.2 Rho GTpase expression in tumourigenesis

As mentioned in last section, Rho are best characterised for their effects on the cytoskeleton and cell adhesion, hence these functions affect the cell migration and therefore presumably invasion and metastasis, then Rho is involved in several cancers types as detail later. Finally Rho family has been found in tumoural cells either overexpressed or downexpressed [15].

1.3.3 Rho A, B and C in cancer types implication

In specialised literature, it is found that all eukaryotes contain at least one Rho GTpase family. Some of the reasons are: RhoA are vital in the regulation of actomyosin contractility. RhoB, localised mainly on endosomes, has been shown to regulate cytokine trafficking and cell

survival, while RhoC may be more important in cell locomotion [16]. Indeed, Rho A, B and C have different functions into the cell, an it is though that the most obvious sign that there are differences in Rho functions, is found in cancer cells.

Hence, overexpressed RhoA has been indentified in several cancer cells, either highly metastatic or in which cell have defects in growth control [17]. In some tumours, Rho A has been found overexpressed such as in colon [18], breast [18], lung [18], testicular germ cell [19], head or neck squamous-cell carcinoma [20]. Otherwise, recent studies show that RhoB expression levels are decreased as the cancer progresses [17] e.g. some of our collaborators have found a loss of RhoB in lung cancer [15], it seems that RhoB may act as a negative moderator of cell survival [21]. RhoC has been found overexpresed in tumours like inflammatory breast cancer [22] [23], or pancreatic ductal adenocarcinoma [24].

In this work, Rho A is used selectively detected so that in chapter 4, a methodology and the proof of the concept are described in detail.

1.4 BioNEMS and Medical devices

MEMS and NEMS stand for micro and (nano) electrochemical systems, respectively. They refer to the integration of mechanical elements, sensor, actuators, and electronic on a common silicon substrate through micro and nanofabrication technology. Some of them are described later. MEMS are occasionally referred to as micromachines (Japan) or microsystems technology (MST) in Europe, but more importantly is that they are found in machines used for nano(micro) fabrication technology [38].

BioMEMS and BioNEMS stand for biomedical micro (nano) electrochemical systems and they are used in biomedical applications because they take advantage of the micro and nanotechnology developments and advances. BioMEMS employ a numeral of novelties, issue from areas like polymers materials, microfluidic physics, surfaces chemistries, soft fabrication technology and biocompatibility. Nowadays, based BioMEMS equipments are found in hospitals, for example, they provide improved feedback or monitoring during surgical procedures, hence they are found in the minimally invasive surgeries (MIS). Finally, BioMEMS can be implanted into the body for monitoring assignment such as cardiac rhythm or glucose in patients [9].

1.4.1 Sensor, biosensors, Micro-Total-Analysis Systems (µtas) and Lab-on-chip (LOC)

A sensor is a device that responds to a stimulus named measurand (which can be physical, chemical, biological; e.g. force, molecular interaction, etc.), it transmits a resulting impulse into a signal that carries information. Hence, sensors detect an input signal or energy and convert them to an appropriate output signal or energy. The difference between sensor and transducer is very slight, sometimes they are synonymous. Nonetheless, sensor is a more particular term, being transducer a device that performs subsequent transduction operations in a measurement or control system.

Sensors have several specifications, such as the *selectivity* which is the ability of a sensor to measure one measurand (e.g one chemical component) in the presence of others. *Sensitivity* is defined as the ratio of the change in sensor output to the change in the measurand input value. For a sensor in which the output y is related to the measurand x by equation y=f(x), the

sensitivity $S(X_a)$ at point X_a, is $S(X_a)=dy/dx_{x=xa}$. For a sensor having y =kx+b, where k and b are constants, the sensitivity is S=k for the entire measurand range. Finally, for a sensor having $y =kx^2+b$, the sensitivity is S=2kx and changes from one point to another over the measurand range. In this context, it is desirable to have a high and if possible constant sensitivity.

An ideal sensor should operate continuously without affecting its measurand, it has a high sensitivity, it is fast with a predictable response (linear or nonlinear), it has full reversible behaviour, high reliability, selectivity, compactness, high signal-to-noise ratio, immunity to environmental conditions, and is easy to calibrate. However, all the sensors are not ideal and they can affect the measurand. Finally, sensors can be passive or active and some concepts as sensor arrays, multisensors or DNA microsensor chips are commonly mentioned in bioNEMS and medical devices.

A biosensor measures living things (or virus), it has a transducer that is made to be in contact with the biological element known probe, e.g. an antibody, this element selectively recognises a particular biological molecule known target, e.g. an antibody, through a reaction, specific adsorption, or other physical or chemical processes. An ideal biosensor should neither be harmful nor deteriorate in the presence of biological substances. A concept of shape-specific recognition (or specific recognition) is commonly used to explain the high sensitivity and selectivity of biological molecules (biomolecules), especially enzyme-substrate and antigen-antibody systems. Other characteristics that have an influence in the sensor sensitivity are the size of the transducer. This is a very important characteristic in nanobiosensors, because the transducers are at the same size or even smaller than the biological elements. For example, the transducers used in this work, are nanoislands that measure ~5nm coupled with nanoelectrodes(40nm) (most proteins measured between 4nm to 20 nm).

Micro total analysis systems (μtas) and their subset devices called lab-on-chips (LOC) are the applications of a hard and soft technology fabrication, their purpose in these devices is to miniaturise them making part of a biochemical analysis. Soft technology fabrications are processes including microcontact printing (μCP), nanoimprint lithography (NIL) (all types such as UV-NIL), microtrasfer moulding (μTM), moulding in capillaries (MIMIC) or decal transfer microlithography (DTM). The Polydimethylsiloxane (PDMS) silicon is a common soft material used in these technologies, this elastomeric is used as stamp, mould, or mask. In chapter 5 of this thesis, the so called PDMS is extensively used, indeed we develop a photosensive PDMS to realise an innovative methodology to fabricate in one step several fluidic microchannels.

1.4.2 Proteins immobilisation methods for nanobiosensors

There are enormous methods to immobilise proteins onto surfaces functioning as follow: by physical adsorption (this is a non-covalent method), by interacting surfaces with hydrophobic (nitrocellulose, polystyrene) or positively charged (poly-lysine, aminosilane) surfaces, or by covalent modification onto a flat surface (chemically activated by aldehyde, epoxy, activate esters), or covalent modification into a gel coating and cross linking [26] [36]. In this work, we use the adsorption method. It is the simplest method in which the transducer is exposed to a solution of the biological active material for a periodic of time; the surface is rinsed to remove the loosely bound material. The biologically active material is then fixed on the surfaces by hydrophobic forces, of van der Waals forces, hydrogen bonds, ionic forces, or by

coordinative bonds as in our nanobiosensor's immobilisation. Different bonds found in nanobiotechnology and specifically in the nanobiosensor described in next parts.

1.4.3 Proteins biochips, labelled probes and free-label methods

Proteins biochips are based on the immobilisation of a probe (by one method described above), then a target is selectively recognised and detected by this probe. Biochemical techniques described above utilise different detection strategies which are classified as: (1) label-free methods and (2) labelled probe methods [27].

Label-free methods (in traditional clinical laboratories) include mass spectroscopy (Liotta and Petricoin, 2000), surface plasmon resonance (SPR) (Johnsson et al., 1991), atomic force microscope (AFM) (Jones et al., 1998) or quartz crystal microbalance (QCM) (Höök et al,2005).

Mass spectrometry (microarrays) uses a protein-selective surface, such as hydrophobic, ionic, or biological surfaces for immobilisation of a complex protein solution. Ions liberated from the surface by laser desorption/ionisation, go to a detector and are classified based on their mass/charge ratio. Genetic algorithms and neural network data analysis are used for data disease/non-disease data clustering analyses.

Surface plasmon resonance (SPR) detectors, on the other hand, are optical biosensors for monitoring biomolecular interactions. This technique consists of immobilising a molecule on a thin metal film, typically gold or silver. Hence, incident light is directed, at a sharp angle, to the side of the metal film opposite of the molecule and the light is reflected from the film at a certain angle. Changes to the molecule on the film such as binds of an antigen causes a modification in the metal film´s electrons, causing the angle of the reflected light vary from the original angle. Measurement of the angle of reflectance indicates a binding event between the immobilised antibody and the capture molecule.

Atomic force microscopy (AFM) is used, for example, to characterise protein microarrays, hence to observe the change and form in height of an immobilised antibody upon binding of its complimentary antigen.

Quartz crystal microbalance (QCM) is a mass sensitive machine useful for detecting a variety of analytes. Mass changes on quartz placed in the QCM due to the deposited biomolecules on surfaces. Mass is interpreted in frequency change according to the Sauerbrey equation.

These label-free based methods machines, generally require expensive and sophisticated equipment, not available in all clinics, hospitals or laboratories. Hence, these methods are useful to implement novel detection methodologies intended to be miniaturised as in present work. In this context, in this work we used a QCM in this research work for proving the antibody antigen (biomarker) concept and that will be integrated into the nanobiosensor. We will give more details about this technique in chapter 4. Fig. 1.6 schematises the principle of the described label-free based machines.

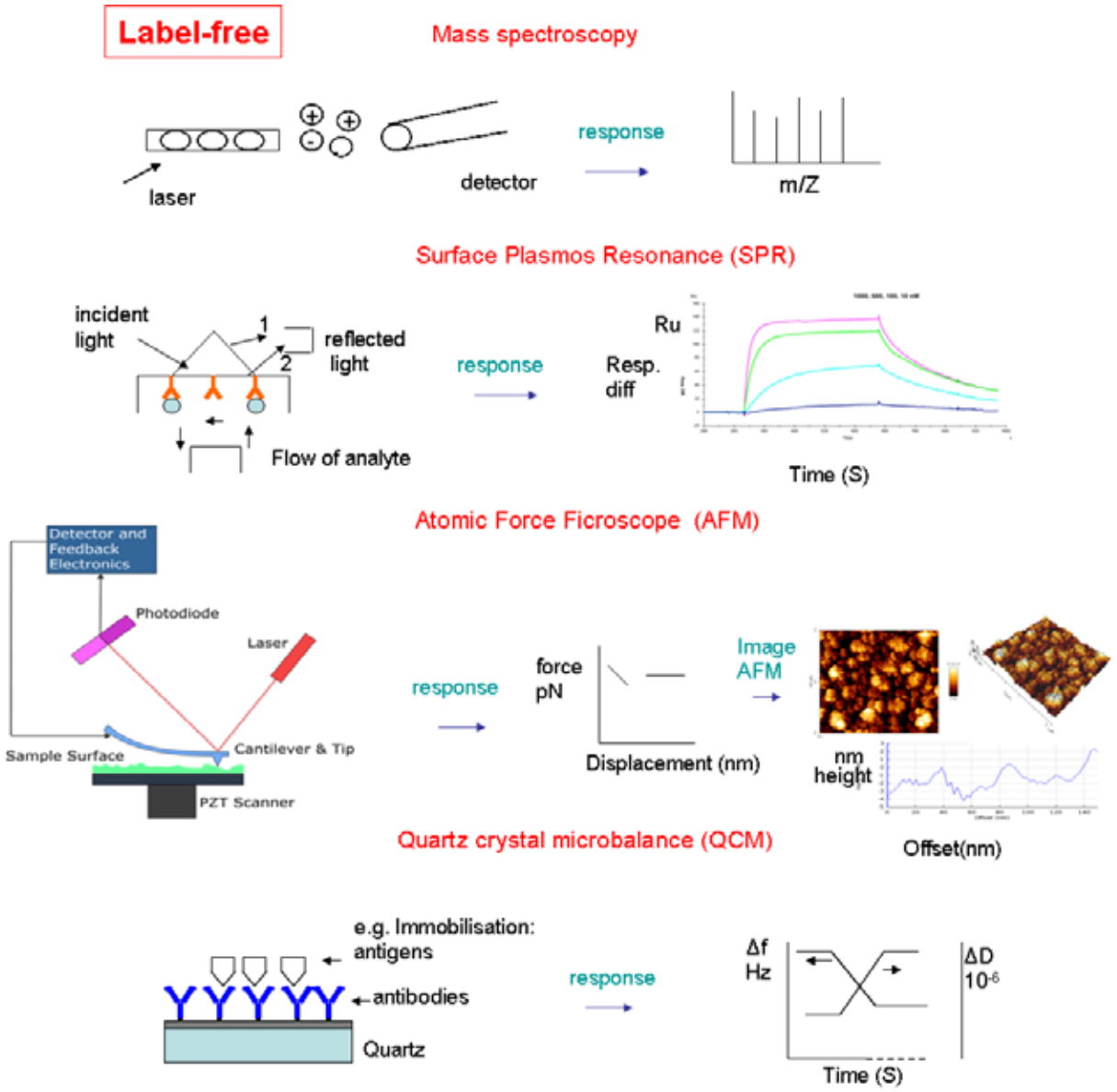

Fig.1.6. Label-free based machines.

The labelled probes methods include the use of a chromogen, fluorophor or radioactive isotope for detection of immobilised targets. The capture molecule itself could be detected directly, indirectly or by sandwich strategies. *Direct strategy* uses a labelled antibody to directly bind to the target molecule immobilised on the surface and then amplification strategies based on avidin-biotin binding increase its sensitivity. *Indirect strategies* use an immobilised antibody for capturing labelled-specific molecules from the sample. Finally, *Sandwich strategy* assay require two distinct antibodies for detection of a capture molecule. The first antibody is immobilised on the substratum, and is used to capture the molecule of interest. Then a second labelled antibody binds to the first complex allowing detection. Fig.1.7 schematises the described labelled probe methods.

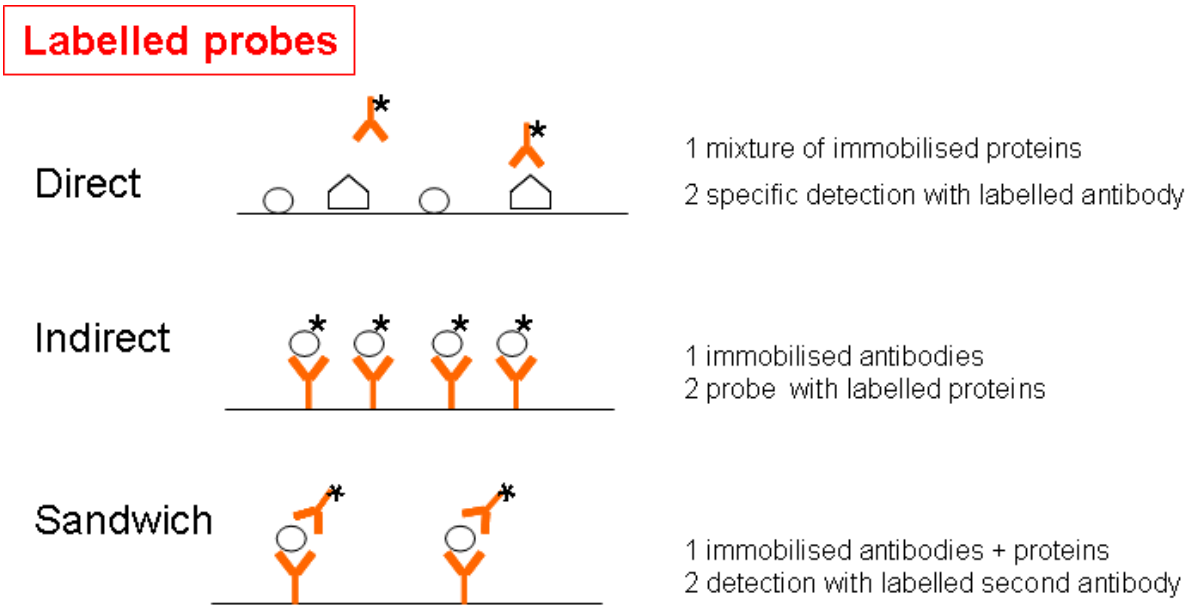

Fig.1.7. label probes techniques.

1.5 Nanodevices for nanomedicine

The purpose of nanomedicine approach is to assure a personalised medicine using nanodevices that must be more accurate and faster, more controllable, more reliable or most cost-effective to enhance the quality life of society. In this context "The most important applications of machine-phase nanotechnology are in medicine", as Freitas pointed out [28].

In this section, firstly we introduce the importance of nanotechnology in clinical laboratories, next we present some bonds used to sustain the different developments presented in this work. Next section will consist of presenting some devices to reach a more accurate and reliable diagnosis, as well as their drawbacks. Last, the approach of the novel nanodevice we developed is described.

1.5.1 Nanotechnology in clinical laboratory diagnostics

A study of cancer diagnostics or in tumours classification is more reliable in laboratories if using molecular techniques, in this context nanotechnologies can be used to improve PCR as well as non-PCR methods for rapid diagnostics. The advantages would be the use of small amount of sample, for example by using nanofludic arrays. Indeed the tests are faster, more sensitive and more selective. On the other hand, ELISA is a no label-free method employed currently in clinical laboratories, it is high sensitive (pM) but is time and quantity sample consuming, furthermore expensive, so new paradigm concepts are emerging as nanotechnology-on-chip for full chemical diagnostics system in clinical laboratories [29][30].

Some alternative label-free methods have been integrated in newest clinical laboratories, such as SPR and quartz crystal microbalance (QCM). However, I think that these tools are used just the first step for the nanotechnology-on-chip conception integration. In this context, successful results obtained from these newest nanotechnological clinical laboratories, are on

condition that other equipment like atomic force microscopes (AFM) and scanning (transmission) electronic microscopes (STEM) are used [31]. In my project, we used a SEM, a QCM, an AFM and ELISA technique to characterise the surface chemistry and the biology binding methodology just as first step towards the proof of the concept validation and integration of the nanobiosensors realisation.

1.5.2 Bonds in nanotechnology and nanomedicine

The interactions amid atoms and molecules informs the specificity of the materials and therefore of devices. Otherwise, usually unique bonds or unique molecules determine the proprieties and functions of nanostructures. Hence knowledge of bonds involved in nanodevices or in nanosystems is decisive for their functioning [32]. In nanomedicine (e.g. diagnostics), proteins are often immobilised onto a surface, being this surface heterogeneous and normally the surface contains positive and negatives charges, groups with hydrogen bonding abilities as well as non-polar regions. Hence complexity in the proteins surface exists and each and every type of protein can interact with other (bio) molecules or surfaces in a great variety of manners [33]. On the other hand, in nanotechnology, interfacial protein interacts with surfaces to assemble and construct sensors, activators and other functional components at the biological and electronic junction [34].

Here, various bonds found in nanobiotechnology and in nanomedicine are described. These bonds will permit me to explain the surface chemistry, biomolecular interactions, metallic nanoisland formations and the interactions of nanoislands with proteins. Regarding this last subject, protein-nanoislands (or clusters) interaction concept has been referred to as new artificial proteins [35], producing new paradigm in nanobiotechnology.

1.5.2.1 Van der Waals forces

Usually medium or weak bonds are of particular importance in nanotechnology. One on these kinds of bonds are the so called van der Waals bonds, in nanosystems they become important because of their cooperative effect, since usually there are many atoms bound to each other. In physics and chemistry, van der Waals forces refer to the attractive or repulsive forces between molecules (or between parts of the same molecule) other than covalent bonds, or electrostatic interaction of ions with another or with neutral molecules.

Generally, include dipole-dipole interactions, hydrogen bonding and London forces, but it is computationally convenient combine electron shell repulsion, dispersion forces and electrostatic interaction and name this ensemble van der Waals potential [7]. Van der waals forces are then essential in different domains such as in resist technology so in micro and nanolithographic technologies and for living cells, especially in proteins conformations. Indeed, van der Waals bonds are essential in hydrophobic interactions. In cells, for example, hydrophobic interactions are primary for the composition of lipid bilayer membranes, and their inclusion. Finally, van der Waals forces are important in the field of supramolecular chemistry. Through chapter 2 of this thesis, micro and nanolithographic technologies are used and in chapter 4 different kinds of biomolecules are used. Hence van der Waals bonds play an important role.

1.5.2.2 Dipole-Dipole interactions

In molecules, there are differences in electronegativity and the atoms reveal an inhomogeneous electron distribution and hence an electrical polarity of molecules is observed. Molecules with one or more dipole moments attract each other. It is a dipole-dipole interaction also called Keesom interaction (or force). These forces are not only observed in permanent dipoles since molecules with permanent dipole moment are capable of inducing a polarisation, creating a dipole moment; the energy is lower in this case. Then, dipole-dipole interactions are involved in unspecific biomolecular interactions. In nanobiotechnology, these unspecific interactions are important and nanotechnologists seek to diminish them.

In this work, the unspecified biomolecular interactions are reduced by using a surface chemistry based on an antibiofouling polymer, presented in chapter 4. Finally, an example where these Keesom interactions are important is in hydrochloric acid or water molecules. In fact, we adapt in chapter 4, precisely our surface chemistry to reduce unspecified interaction using hydrochloric acid and other chemical compounds.

1.5.2.3 Hydrogen bride bonds

It is a localised and orientated polar covalent interaction based on hydrogen atoms creating strong electronegative element bonds. These interactions are of primary importance in the supermolecular synthesis of biomoelcules.

Atoms involved in these kinds of interactions are oxygen, nitrogen or to a lesser degree sulphur. An example of this bond occurs in water. The water absorbed onto quartz surfaces of the QCM machine (used for the proof of the concept before integrating in our nanobiosensor) takes part in the signal variation. Then, there are hydrogen bride bonds that modify the required signal.

1.5.2.4 Ionic interactions

Ionic bond are also called electrovalent bond is a chemical bond that can often be formed between metal and non-metal ions (or polyatomic ions such as ammonium) through electrostatic attraction. In short, it is a bond formed by attraction between two oppositely charged ions created by electron transfer and where there are large differences in the electronegativity of atoms. One example of this is the common table salt or sodium chloride (NaCl). Electrostatic interactions like ionics are not essential in approaches derived from nanotechnology like nanoelectronics. However, in nanobiotechnology, it is common to use buffers (often with NaCl) for the amino acids or proteins manipulation, combined with detecting biological elements, and thus this can influence the biomolecules charge, so affect the selective detection in the case of a nanobiosensor. Furthermore, these interactions play an important role in the manipulation of macromolecules (proteins), supramolecular aggregates, micelles and nanoparticles in the liquid phase.

1.5.2.5 Metallic bonds

Metallic bonds take place when interactions between delocalised electrons and the metallic nuclei of metals exist. This is a strong chemical bond, essential in micro and nanotechnology

because of the numeral metals used in the different nanotechnologic processes. For example clusters or nanoislands are formed with few atoms. Metallic bonds are the origin of their formation.

The nanobiosensor, we are presenting in this work is based on Ni nanoislands (~5nm) which are deposed between interdigitated nanoelectrodes (~40nm), obtaining tunnelling phenomena and coulomb blockade, in this case to sense biomolecules for the first time. Metallic bonds explain in part the successful nanoislands realisation.

1.5.2.6 Covalent bonds

Covalent bonds are strong bonds characterised by sharing of pairs of electrons between atoms or between atoms and other covalent bonds resulting in double occupied binding orbitals. Generally covalent bonds are formed when the electronegativities of the different atoms are close. Covalent bonding includes many types of interactions, including σ bonding, π bonding, and for some researchers also metal bonds, agostic interactions, and three-centre two-electron bonds.

In chapter 4, a surface chemistry is implemented, based on PEG-silane that is covalently linked onto surfaces for avoiding non-specific interactions (reducing dipole-dipole interactions or ionic interactions).

1.5.2.7 Coordinative bonds

A covalent bond is formed by two atoms sharing a pair of electrons. The atoms are held together because the electron pair is attracted by both of the nuclei. On the other hand, *coordinative bonds* are formed when only the share of an electron pair is conducted by one of the binding partner (the ligand). Then a coordinative bond (also called a dative covalent bond) can be though as a covalent bond (a shared pair of electrons) in which both electrons come from the same atom.

Originally, a complex used to imply a reversible association of molecules, atoms or ions through weak chemical bonds, however as applied to coordination chemistry this meaning has evolved and now a complex in chemistry is used to describe molecules or ensembles formed by the combination of ligands and metal ions.

Hence, nowadays coordinative bonds are popularly used to describe coordinative complexes, especially involving metals ions. Then metal complexes (coordination compounds), include all metal compounds, aside from metal vapours, plasmas and alloys.

Coordinative bonding is usually found with metal atoms and ions because they generally present unoccupied orbitals. The metal central ion or atom (central particle) is surrounded by a sphere of several ligands and creates the so called complex (denoted also complex bonds).

Nature also uses this kind of complex bonds e.g. in the Co- or Fe-complexes of the haeme groups of enzymes [32]. Otherwise, bonds with carbon as organometallic compounds are also coordinative bonds. For example tetra-ethyl lead, once used a common anti-knock additive in gasoline (petrol).

In my project, the central part of the nanobiosensor is the binding used for detecting biomolecule interactions between Ni-nanoislands and histidine amino acid (or a protein tagged histidine), by coordinative bonds. It is a binding protein domain that exists in nature. This methodology has been used, for some time, to purify proteins in immobilised metal ion

affinity chromatography (IMAC) using metal ions. We validate the proof of the concept by using nanoislands linked by coordinative bonds to tagged proteins. Chapter 4 describes it, in detail.

1.5.3 Nanotranducers-based nanodevices for cancer diagnostics (nanodiagnostics)

Currently, sensing methods in (nano) biosensors are classified in mechanical, optical, electrochemical, electrical, or thermal [37]. *Mechanical* transducer detection is based on the change in surface stress, for example, the deflection of the free end of the microcantilever caused by the absorption of biomolecules. The two most used detection methods for *optical* biosensors are based on either a change in optical absorbance or a change in fluorescence caused by change in concentration of a particular analyte in the sensing zone of the optical sensor. The *electrochemical* detection can be *potentiometric, amperometric or conductometric*.

Potentiometric tranducer measures a change in potential at electrodes due to ions or chemical reaction at an electrode (such as an ion sensitive FET-ISFET or ChemFETs). Hence, it is able to measure a potential difference between the gate and the reference electrode in solution, or measure the change in potential converted to a change in current by a FET or a change in capacitance in low doped silicon. In this case, the gate material is sensitive to specific targets. Lieber's group, for example, has detected proteins [39], PH variation [40][41], virus [42] or cancer biomarkers [43] by using nanowires as gate in FET biosensor.

Amperometric tranducer is based on the detection of electric current associated with the electrons involved in redox processes; it has been used to detect glucose, lactase, and urea. This technique has been performed using nanoelectrodes [44]. *Conductometric* transducer measures conductance changes associated with changes in the complete ionic medium between electrodes, thus the (nano) transducer measures the change in the electrical impedance between electrodes (e.g. between 2 electrodes). The changes could be at the interface or in the bulk region and can be used to indicate biomolecular reaction between DNA, proteins, antigen-antibody reaction, or excretion of cellular metabolic elements. Conductometric detection is the technique utilised in this research work, however by using a novel methodology. Table 1.1 shows the common types of transducers and their measured properties.

Types of transducers	**Measured Property**
Electrochemical ⇢	Potentiometric , Amperometric, Voltametric
Electrical ⇢	Surface conductivity, Electrolyte conductivity
Optical ⇢	Fluorescence, Adsorption, Reflection
Mass sensitive ⇢	Resonant frequency of piezocrystals
Thermal ⇢	Heat of reaction, heat of adsorption

Table 1.1. Transducers and measured properties.

Here some basic characteristics of a (nano) biosensor are defined as: linearity, sensitivity, selectivity and the response time. *Linearity* is the maximum linear value of the biosensor calibration curve. It is the variation of the output directly with the input. Biosensor linearity

has to be high to detect considerable substrate concentration. *Sensitivity* is the value of response due to the very low concentrations. *Selectivity* can be defined as the capacity to recognise specifically an analyte amid numerous others. Finally, *time response* can be defined as the minimum time for having ~90% of the response.

Some high sensitive nanodevices or methodologies have been proposed, such as bio-barcode assay (BCA) developed by Chad Mirkin's group [48]. The system are based on magnetic nanoparticles probes with antibodies that specially bind a target of interest and nanoparticle probes that are encoded with DNA which is unique to a protein target of interest and antibodies. As an alternative, PCR on the ologonucleotide barcodes can improve its sensitivity to 3aM by coupling the BCA with PCR [49]. One limitation of BCA would be that it is necessary to prepare the DNA barcode-modified probes and magnetic probes [45].

Some others nanodevices such as gold nanoparticles [50][51], dendrimers [52], micro (nano)cantilivers [53-56], nanotubes [57-58], solid state nanopores [80][81] or recently ion channels [82] have been proposed, most of them have demonstrated detection at nM sensitivities.

In this section, we detail just Lieber's technique and Dai's technique. They have used nanowires and carbon nanotubes respectively. Sensibility of femtomolar (fM) range using nanowires has been demonstrated. However nanotechnologists thought that to next years the possibility of detecting a single (bio) molecule will be a reality. Otherwise, the devices proposed until now have some drawbacks which will be described in this section.

1.5.3.1 Nanowires for diagnosis (Lieber's group)

A nanowire is defined as a structure of nanometrical lateral size and unconstrained longitudinal size. Currently, there are different types of nanowires including metallic (Au, Ni, Pt), semiconducting (Si, InP, GaN) and insulating (SiO_2, TiO_2) and they can be either suspended, deposited or synthetised.

Electrical assays using nanowires (NW) have been employed to detect cancer marker proteins, DNA, and virus with high sensitivity and selectivity. Lieber's group, for example, in 2005, demonstrated nanowire-based field effect label-free sensors for sensing biomarkers, in aqueous solution, using functionalised antibodies, at femtomolar level [43]. They demonstrated that the use of Si nanowire gate material in the field effect transistor (FET) increase its sensitivity. The principle of detecting biomolecules, with these nanowires, is based on the change in conductivity by field effect because of liking the charge molecules on the Si nanowire surface. Conductance of the P-silicon nanowire increased (or decreased) when a protein with negative (positive) surface charge links to the antibody receptor. Opposite response was observed for an n-type (phosphorous-doped) silicon nanowire. The nanowire was capable of detecting femtomolar (mass concentration of pg/ml) of cancer biomarkers such as prostate specific antigen (PSA) (known as oncological marker in prostate cancer). Liber's group used this kind of device to detect PSA-1-antichymotryspin (PSA-ACT), cancinoembryonic antigen (CEA), mucin-1 and PSA in undiluted donkey and human serum samples. Fig 1.8 schematises the principle of these nanowires.

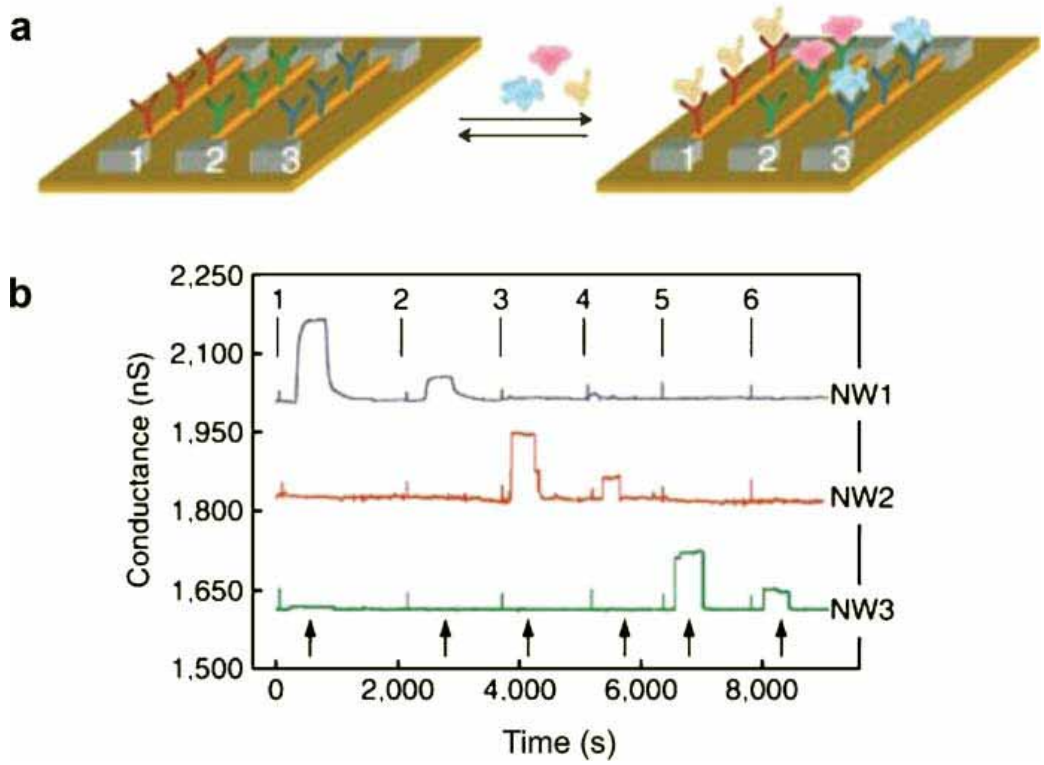

Fig.1.8. Adapted from [43][45]. Detection of multiple protein analytes using nanowires array.(a) Three silicon nanowires (NWs) to detect multiple targets, each nanowire was modified with a different antibody specific for a target. (b) Conductance versus time data recorded to detect prostate-specific antigen (PSA), carcinoembryonic antigen (CEA), and mucin-1 on p-type nanowires modified with monoclonal antibodies for PSA (NW1), CEA (NW2), and mucin-1 (NW3). Solutions were delivered to the nanowire array sequentially as follows: (1) 0.9 ng/ml PSA, (2) 1.4 pg/ml PSA, (3) 0.2 ng /ml CEA, (4) 2 pg/ml CEA, (5) 0.5 ng/ml mucin-1, and (6) 5 pg/ml mucin-1. Buffer solutions were injected at points indicated by the black arrows.

However, since nanowires are not observed spontaneously in nature and they must be produced in laboratory, a limitation of nanowire biosensors is the relatively high cost of equipment and preparation. Furthermore, it is difficult to locally align nanowires and finally to connect them. P.R. Nair et al. recently demonstrated that the nanobiosensor response is governed by the geometry of diffusion of the system based on analytic solutions [46]. They demonstrated a simple analytical model based on reaction-diffusion theory, to predict the trade-off between average response (settling) time and minimum detectable concentration for nanobiosensors, by solving Poisson-Boltzmann and reaction-diffusion equations [47]. They also demonstrated that nanobiosensors are capable of detecting bio-molecules at much lower concentrations (up to 4-5 orders of magnitude) than the classical planar sensors (ISFETs or CHEMFETs). Hence, it is well known by experience that nanowires are more sensitive to adsorbed charges e.g., DNA or proteins compared to ISFET or CHEMFET sensors [43]. However, the classical view of nanosensor response misses the kinetic part of the detection process, i.e. when a sensor is made to be in contact with the solution of target biomolecules, the time to capture a certain number of biomolecules also depends on the dimensions of the sensor affecting the nanobiosensor sensitivity.

In this context, nanoislands-based sensors (nanosphere sensors) are expected to reach higher sensitivity than nanowires-based sensors. This expectation is sustained by the demonstration of P.R. Nair et al. reported in [47] and plotted in graph of Fig. 1.9.

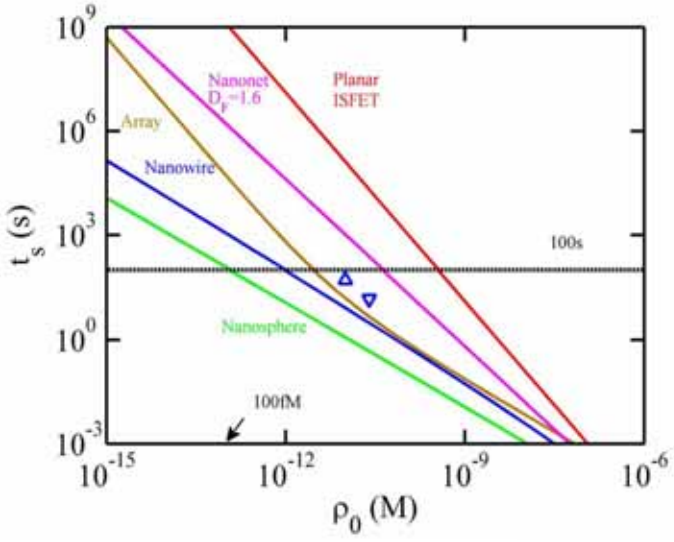

Fig.1.9. Performance limits of nanobiosensors given by $\rho_0 \sim k_D t_s^{-1/D_F}$ (adapted from [47]). The detection limits for planar sensors is much lower than that of cylindrical sensors. Uniform arrays resemble nanowire sensors at high concentrations, while at low concentrations they resemble planar sensors; the better limit detection is by using nanosphere like nanoislands.

Indeed, the number of molecules captured on the sensor surface is still unknown by using nanowires. I hope also that by using nanoislands coupled with nanoelectrodes, it will be possible to know the number of biomolecules or estimate it more precisely, because the nanoislands have the same size of the biomolecules absorbed. Hence, the linearity, sensitivity, selectivity and response time will be higher by using nanoislands (nanospheres sensors) than by using nanowires as predicted by graphs of the Fig. 1.9.

1.5.3.2 Carbon nanotubes in cancer diagnostic and therapy (Dai's group)

Carbon nanotubes (CNTs) are made of a wide variety of carbon atoms synthesised into cylinders of single or multiple layers. CNTs can have a length-to-diameter ratio greater than 1000,000 and they are classified as a single double-walled nanotubes (SWNTs) and multi-walled nanotubes (MWNTs). CNTs have been used for a great number of applications such as electrochemical sensor, memories devices, as novel composites, but also as a platform for ultrasensitive recognition of antibodies, as nucleic acid sequencer, bioseparators, biocatalysis and ion channel blockers, as Dai's group and others researcher demonstrated [59][60]. In Nanomedicine, for exemple, CNTs have been utilised as scaffolds for neural and ligamentous tissue growth for regenerative interventions of central nervous system and orthopaedic sites.

SWNTs are more preferred than MWNTs to use in biomedicine because they resemble to nucleic acid in physical dimension, and are excellent platforms for biosensing and biocompatibility, furthermore their large surface area are able to carry many biomolecules to the specific targets for sensing, sequencing and therapy [1]. Semiconductor carbon nanotubes have also been used as a FET device to detect proteins such as nanowires described above, but the detection limit has been around the nanomolar (nM) level. Fig. 1.10 shows some carbon nanotubes taken by transmission electron microscope (TEM).

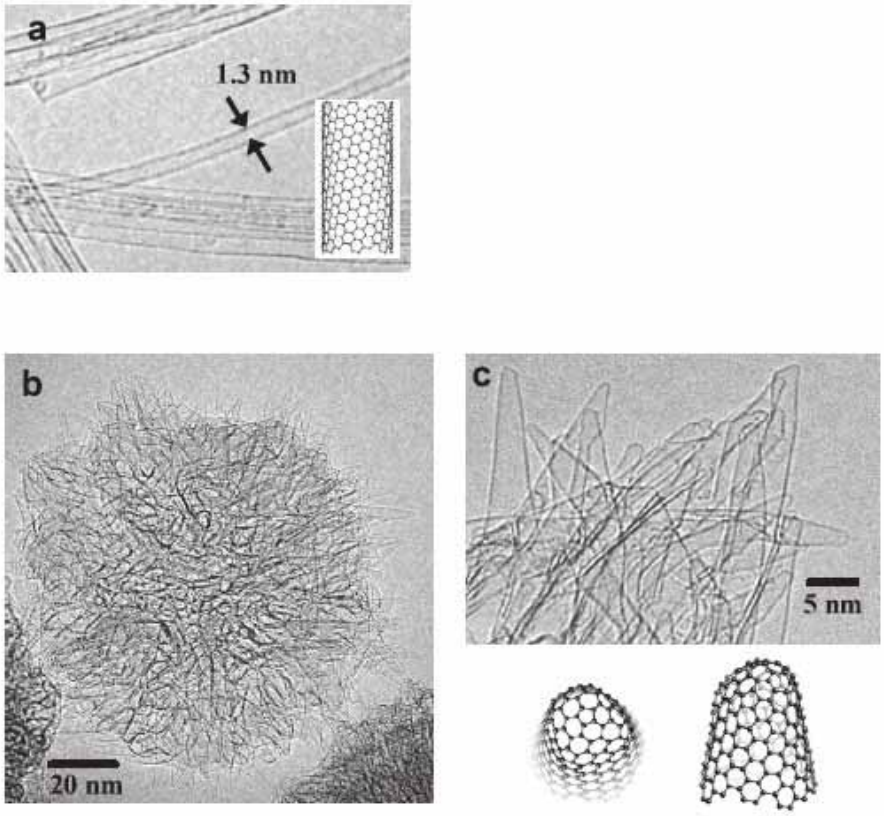

Fig.1.10. Transmission electron microscopy images of carbon nanotube (CNT) (a) and carbon nanohorn (CNH) (b), (c). Inserted illustrations are CG images of CNT and CNH respectively [62].

Recently Zhou's group [61] has integrated nanotubes into a biosensor for detection of PSA. They used n-type In_2O_3 nanowires and p-type carbon nanotubes for the detection of prostate specific antigen (PSA). To detect PSA, they modified the outside surface of the NW or SWNTs with anti PSA monoclonal antibody (PSA-AB). The surface of In_2O_3 was functionalised with 3-phosphonopropionic acid which has COOH group at one end used to immobilise PSA-AB by forming amide bonds. The SWNT surface was first functionalised with 1-purenbutanoic acid succinimidyl ester and then treated with the PSA-AB solution. They achieved to detect PSA however with a sensitivity of 5ng/ml [1]. Fig 1.11 shows the Dai's group methodology for biosensing.

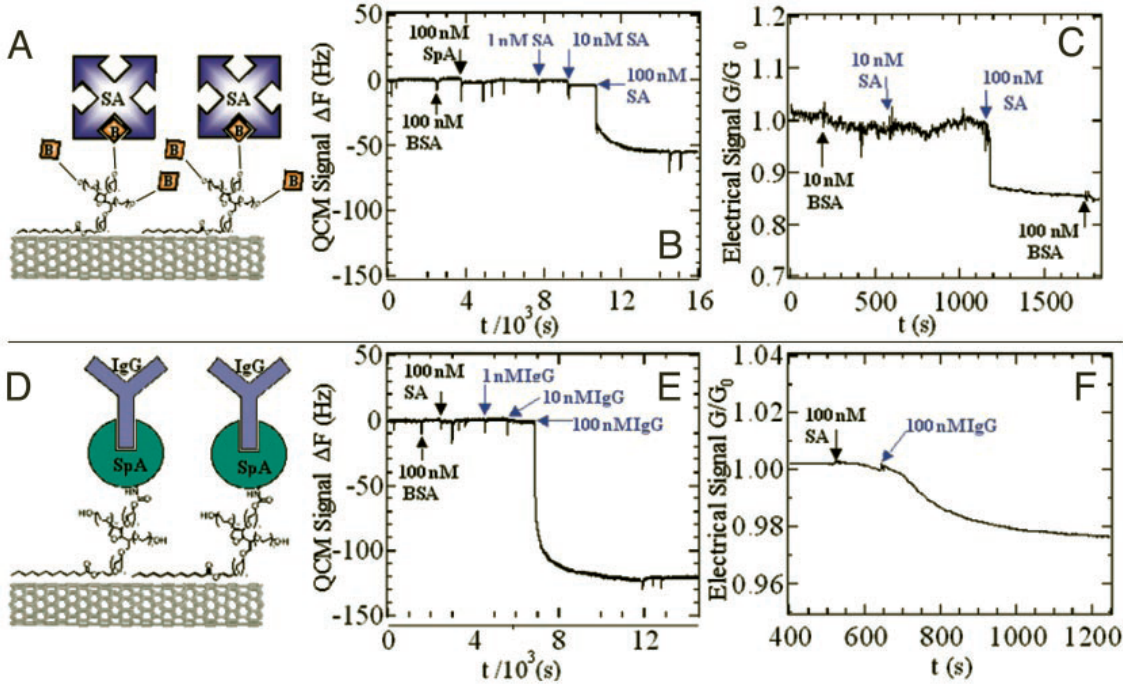

Fig.1.11. Adapted from [59]. Real-time QCM and electronic sensing of specific biological recognition on nanotubes. (*A*) Scheme for SA recognition with a nanotube coated with biotinylated Tween. (*B*) QCM frequency shift vs. time curve showing that a film of nanotubes coated with biotinylated Tween binds SA specifically but not other proteins. (*C*) Conductance vs. time curve of a device during exposure to various protein solutions. Specific binding of SA is detected electronically. (*D*) Scheme for IgG recognition with a nanotube coated with a SpA-Tween conjugate. (*E*) QCM frequency shift vs. time curve showing a film of nanotubes coated with SpA-Tween binding human IgG specifically but not unrelated proteins. Note that 10 nM IgG concentration approaches the lower detection limit of the instrument, whereas 100 nM approaches surface saturation of the sample; thus, the response does not show a full proportionality to the concentration. (*F*) Conductance vs. time curve of a device during exposure to various protein solutions. Specific binding of IgG is detected electronically (some NSB is observed for 100 nM SA, but the signal is much smaller than that of IgG).

As written above, not just diagnostic applications are important in nanomedicine, but also in therapy. Hence, some important direct application of SWNTs for cancer therapy has been described by the work of Dai's group [63], here cell were killed by laser irradiation of engulfed SWNTs raising temperatures to 70°C. Internalisation of the SWNTs was stimulated by starving the cells for folate and conjugation of the SWNTs with folic acid. These studies were conducted in artificial systems, in vitro, but modifications of this technique could make this approach an important contribution to the anti-tumour armantarium.

Several studies have demonstrated that moderate temperatures to heat, at 41°C, by laser irradiation of intracellular SWNTs increase tumour destruction. Another use of SWNTs for enhancing radiation therapy has been suggested by Yinghuai et al. [64], who have successfully attached C(2) B10 carborane cages to SWNTs which are used to increase concentration of boron in tumour cells relative to blood and other organs, resulting in sensitisation of the tumours for neutron capture therapy. Finally binding a toxin to the nanotube or laser heating would then increase the effectiveness of killing. Recently Dai's group also demonstrated a drug-delivery technique which was tested in mice [65]. Carbon nanotubes having three branches were coated with polyethylene glycol (PEG), and then they attached molecules of the anticancer drug paclitaxel to each branch. Each of the 100-nanometer-long nanotubes carried about 150 drug molecules in total.

In this research work CNTs (double-walled) were tested to be used as wires for connecting electrical circuits, thus electrical characterisations were conducted. These CNTs were brushed and positioned between the nanoelectrodes by my college; Cyril Tinguely. Nanoelectrodes were realised by electron beam lithography (EBL) described in chapter 2.

Table 1.2, summarises protein assays using nanodevices. It illustrates the analyte used, the detection limit and the references.

Assay	Analyte*	Detection limit	Ref.
Bio-barcode assay (BCA)	PSA	0.1 fg/mL(3 aM,coupled with PCR)	[48]
		1 fg /mL (30 aM, without PCR)	
BCA	ADDLs	100 aM	[66]
Colorimetric BCA	IL-2	0.5 fg/ mL (30 aM)	[67]
Fluorescent BCA	PSA	10 fg /mL (300 aM)	[68]
BCA	PSA	10 fg /mL (300 aM)	[69]
BCA on microfluidic chip	PSA	17 fg/ mL (500 aM)	[70]
Electrochemical assay using nanogold	IgG	0.5 ng /mL (3 pM)	[71]
Electrochemical assay using QDs and aptamers	Thrombin	18 pg /mL (0.5 pM)	[72]
DNA-based electrochemical assay	IgG	2 pg /mL(13 fM)	[73]
Electrochemical assay using CNTs	IgG	500 fg /mL (3 fM)	[74]
Electrochemical assay using CNTs	PSA	4 pg /mL (100 fM)	[75]
Electrochemical assay using nanocatalyst	IgG	1 fg /mL (7 aM)	[76]
	PSA	1 fg /mL(30 aM)	
Si nanowire-based assay	PSA	75 fg /mL (2 fM)	[43]
	PSA-ACT	0.32 pg /mL (3 fM)	
	CEA	100 fg /mL (550 aM)	
	Mucin-1	75 fg /mL (490 aM)	
SERS with nanoparticles	PSA	1 pg /mL (30 fM)	[77]
Fluorescence assay using dye-doped nanoparticles	IgG	1 pg /mL (7 fM)	[78]
Dual-color coincidence fluorescence assay using QDs	TNF- α	340–540 fg /mL (20-30 fM)	[79]

*Table 1.2. (adapted from [45]) shows detection limits with actual nanodevices (authors converted the units of the concentration for ease of comparison when only mass concentration or molar concentration was available in the original paper, typical detection limit by ELISA for proteins was in the pM range). PSA: prostate-specific antigen; ADDLs: amyloid β-derived diffusible ligands; IL-2: interleukin-2; IgG: immunoglobulin G; QDs: quantumn dots; CNTs: carbon nanotubes; PSA-ACT: PSA-α-1-antichymotrypsin; CEA: carcinoembryonic antigen; SERS: surface-enhanced Raman scattering; TNF- α: tumour necrosis factor-α.

1.5.3.3 Nanoelectrodes and its applications

Nanoelectrodes are defined, here, as metal electrodes with nanometric size structures (less than 100nm) in lateral and unrestricted longitudinal size (usually some microns).

Nanoelectrodes have demonstrated novel characteristics in relation to usual (micro) electrodes, such as higher mass transfer efficiency, smaller RC cell time constant, lower iR drop, higher signal-to-noise ratio and higher current density [83]. In last 20th century, the fabrication was devoted to the realisation of microelectrodes, now with development issue from nanotechnology, nanoelectrodes are being fabricated easily by, for example, electron beam lithography (HREBL) [84][85], or nanoimprint lithography (NIL) [86-88]. Some applications include electrical contact single [89][90], impedimetric biosensing [91-93], or nanobiosensors [94].

1.5.3.3.1 Nanoelectrodes for (bio) molecular connection and electrical study

There has been much interest in connecting a single (bio) molecule to elaborate the molecular electronics both in nanoelectronics and biology, or to make direct measurement of the molecules for knowing their electrical properties. One of the first solutions was using a scanning tunnelling microscope (STM) proposed by C. Joachim et al. [95] in Toulouse France. This method proved the viability of the concept by measuring the first I(V) characteristic for individual molecules. However, until now, this method is limited in controlling the substrate-molecule tip contact and there is lack of mechanical stability. One envisaged solution has been using nanoelectrodes.

1.5.3.4 Interdigitated nanoelectrodes as ultrasensitive nanobiosensor

One of the primary reasons to elaborate interdigitated electrodes structures has been to increase the length of the active zone, thus the capacitance amid these interdigitated electrodes. Hence, the first patented design, having an interdigitated structure was probably proposed in 1894 by N.Tesla [96] [97].

In 1999, W.Fritzsche et al. [98] patented an affinity sensor based on interdigitated electrodes to detect specifically molecular binding events, for the use in the field of molecular biology, especially for biosensor technology or DNA microarrays. Nowadays, nanoelectrodes are being proposed as ultrasensible sensors due to their size comparable to the biomolecules and due to the characteristics described above. Hence, interdigitated nanoelectrodes have been realised and demonstrated in our group, by L. Malaquin et al., to detect single adsorption events such as individual nanoparticles linked to biomolecules [94]. The principle [99] is illustrated in Fig.1.12.

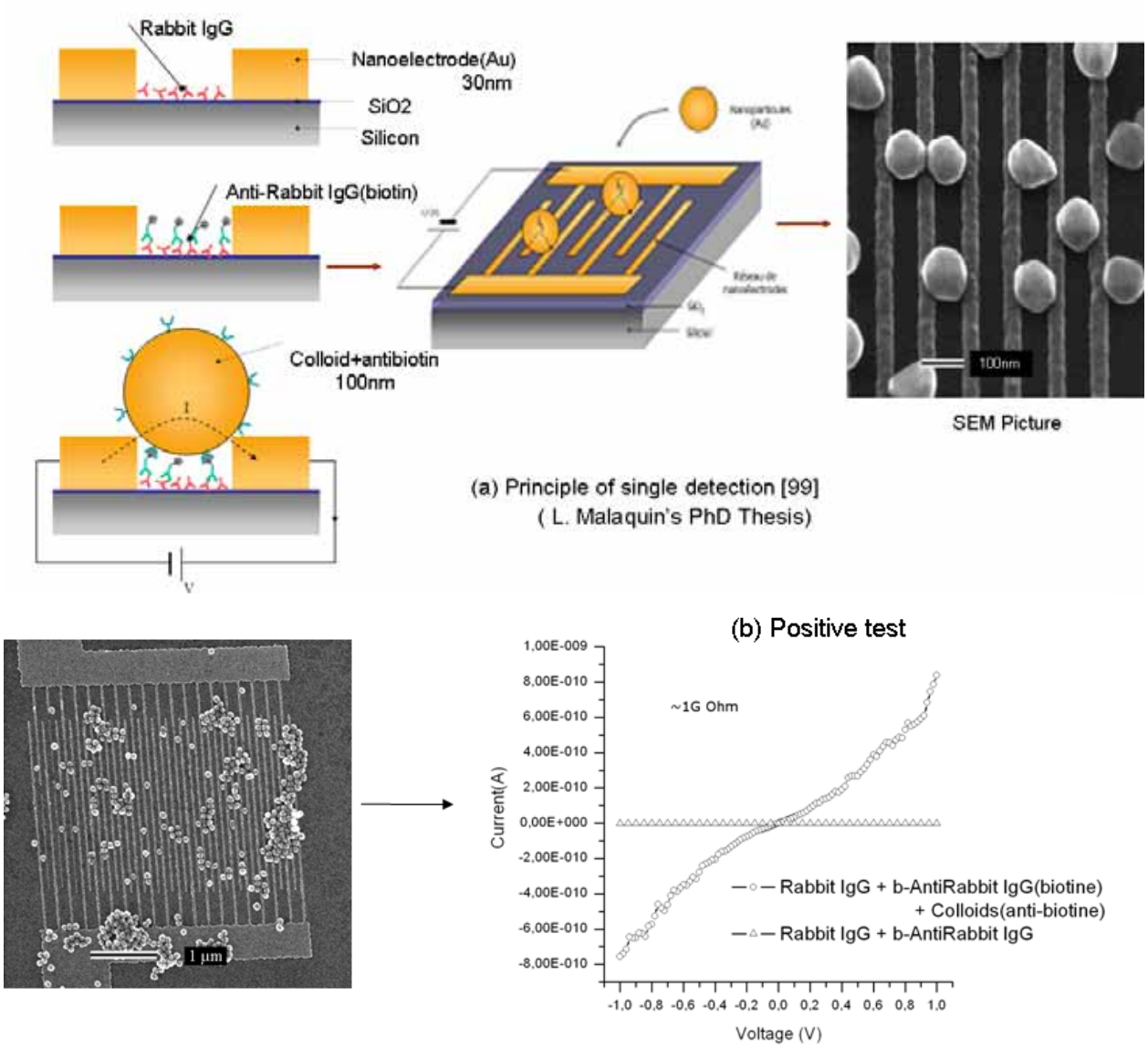

Fig.1.12. (a) Colloids (nanoparticles) deposition, (b) the positive test (L. Malaquin's PhD thesis).

Figure 1.12 (a) schematises the principle, which was to associate one biomolecular interaction to an electrical response. The couple antibody-antigen was detected using nanoparticles as markers. Hence, it is a labelled probe methodology. The first step consisted of absorbing the antibodies (probes) thus grafting biotin-tagged antibodies, and finally antibodies-tagged anti-biotin colloids are deposited (marker). Colloids had a diameter bigger than the distance between two nanoelectrodes as illustrated in Fig. 1.12 (a). In this condition, the recognition and detection were achieved by measuring a current increment. Fig. 1.12 (b) illustrates the positive test (when the recognition is accomplished).

However, in this work, only positives tests were possible and the time for one chip realisation was considerable. Indeed, only classical biomolecules were tested.

1.5.3.4.1 My project principle: ultrahigh sensitive device using nanoislands between interdigitated nanoelectrodes for label-free detection

The research turned to detecting biomolecules at ultrahigh sensitivity levels and in label-free manners. Hence, to detect the adsorption of one molecule and that be interpreted by a conductivity variation through nanoelectrodes, it is necessary to immobilise the matter between the nanoelectrodes. Otherwise, granular film has been studied for a lot of time to make single electron devices or media for high density magnetic storage (bibliography in chapter 3). My advisor Christophe Vieu had worked on this before my arrival thus he had experience on coulomb blockage phenomena and wanted to realise this by using nanoelectrodes. Firstly, I wanted to know the parameters to obtain nanoislands made of gold, because the ligand chemistry to bond to thiol-tagged biomolecules is easy to implement. At the same time, we started collaboration with a physician (oncologist): Mr. J.C Faye from Institut Claudius Regaud, to find novel ligand methods to detect biomarkers. He told us about the possibility to link proteins to nickel, being so common in the purification of proteins onto immobilised metal ion affinity chromatography (IMAC).

Then my primary research objective consisted of obtaining nanoislands made of nickel. Finally, I obtained the parameters to realise nanoislands, hence tunnelling conduction was achieved and furthermore coulomb blockade at room temperatures was achieved while depositing Ni nanoislands between interdigitated nanoelectrodes arrays. The chemistry-biology methodology for biomecular detection was implemented and validated to be integrated into our biosensors based Lab-on-chip devices.

Hence, the principle of the novel electrical nanobiosensor is based on the variation of electrical conductivity in the nanoelectrodes array, due to the proteins adsorbed onto Ni nanoislands. Ni nanoilsands (~5nm diameter) are embedded into SiO_2 and placed between interdigitated nanoelectrodes devices (IND) of 45nm width each electrode. Nanoislands are separated each other from ~2 nm. In these conditions, it is obtained a nanotransducer based on the variation of electrical tunnelling conductivity through metal nanoislands due to the quantum phenomenon called Coulomb blockade at room temperature. Because of this phenomenon, these nanodevices are fast and ultrasentive to any change that can affect the tunnelling conduction, for example, adsorption of proteins. Hence his-tagged antibodies, functioning as probe are linked by coordinative bonds to the Ni nanoislands, they recognise specifically the active RhoA conformation which functions as target, and discriminate against its inactive RhoA conformation. Finally, an innovative methodology to realise photoPDMS-based microchannels (20 μm), to inject the biomolecules, was developed and integrated with IND on 4 inch wafer, see Fig.1.13 illustrates the principle and a part of the integrated nanobiosensors envisaging a Lab-on-a-chip.

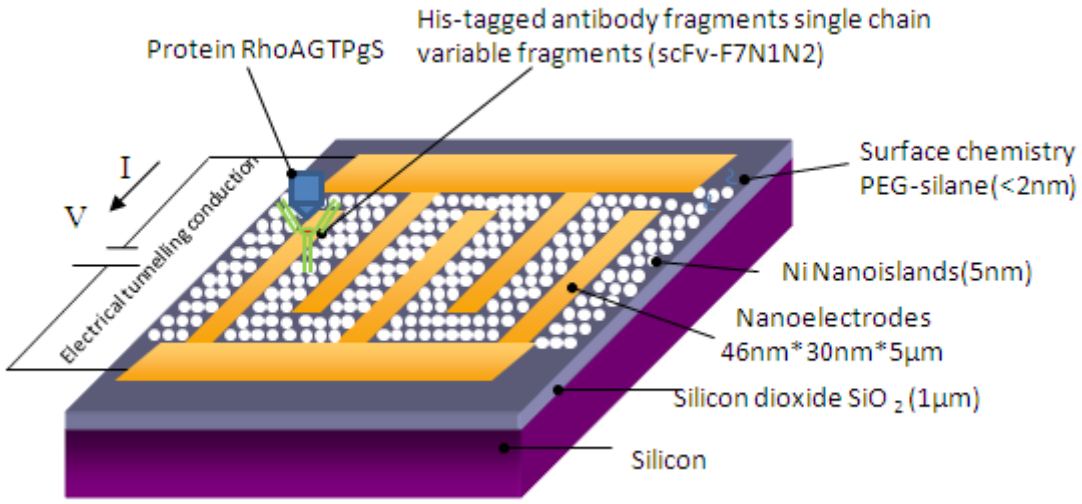

Fig.1.13. Schema illustrating the principle and integration in one nanobiosensor device.

As written in the general introduction, each part of the integrated nanobiosensor will be described in separate chapters. The organisation will be similar to scientific papers. The reason is because by this organisation planning the purpose, material, methods and results are clearly presented. Indeed, one or two papers corresponding to each chapter of my thesis are being submitted or will be submitted to an international journal.

1.6 References

[1] Challa Kumar, *Nanomaterials for cancer diagnostic*, Germany, Wiley-Vch, **2007**. 423p.

[2] Wilczynski Sharon Poltis, *Introduction to diagnosis of cancer*, chapter33, Systemic Oncology, city oh Hope National medical center, Duarte, CA, USA

[3] Garaud Jean-Claude, Roussel Guy, *Immunohistochimie en microscope photonique et électronique theorie et practique,* University of Strasbourg, **2007**, 265p.

[4] Ludwig T., "Local proteolytic activity in tumor cell invasion and metastasis", *Bioessays*, **2005**, 27, p.1181-1191.

[5] Rasooly A, Jacobson J., "Development of biosensors for cancer clinical testing", *Biosens. and Bioelec.,* **2006**, 21, p.1851-1858.

[6] Hameroff Start R., "Ultimate computing: bimolecular conscientiousness and nanotechnology", Tucson Arizona, Elsevier science Publisher B.V., **1987**, 271p.

[7] Schulz G.E., Schirmer R.H., "Principles of protein structructure", NewYork, Springer-verlag, 1, **1978**, 314p.

[8] Sivanand S. Pennadam, Keith Firman, Cameron Alexander, "Protein-polymer nano-machines. Towards synthetic control of biological processes", *Journal of Nanobiotechnology,* **2004**, 2:8, p.1-7

[9] Saliterman Steven S., "*Fundamental of bioMEMS and medical microdevices"*, Washington, Wiley-interscience, 1, **2006**, 610p.

[10] Gonzalez Oliva A., Cruz H.J., Rosa C.C., "*Immunosensors for diagnostics",* Instituto de Tecnologia Química e Biológica, Oeiras, Portugal, Biosensor Laboratory, ITQB/IBET, 27p.

[11] http://en.wikipedia.org/wiki/Single_chain_variable_fragment

[12] M Goffinet, Chinestra P, Lajoie-Mazenc I, et al., "Identification of a GTP-bound Rho specific scFv molecular sensor by phage display selection", *BMC Biotechnology,* **2008**, 8, p.1-14.

[13] Khaldeeva E.V., Budnikov G. K., "Immunosensors in biology and medicine: Analytical Capabilities, Problems, and Prospects", *Journal of Analytical Chemistry,* **2001**, 56, 10, p.886-900.

[14] Espina Virginia, Woodhouse Elisa C., "Wulfkuhle Julia et al. Protein microarray detection strategies: focus on direct detection technologies", *Journal of Immunological Methods,* **2004**, 290, p. 121-133

[15] Mazieres Julien, Antonia Teresita, Daste G., et al., "Loss of RhoB expression in human lung cancer progression", *Clin. Cancer Res.,* **2004**, 10, p.2742-2750.

[16] Wheelera Ann P., Ridley Anne J., "Why three Rho proteins? RhoA, RhoB, RhoC, and cell motility", *Experimental Cell Research,* **2004**, 301, p.43-49.

[17] Ridley A.J., "Rho proteins and cancer", *Breast Cancer Res. Treat,* **2004**, 84, p.13-19.

[18] Fritz G., Just I., Kaina B., "RhoGTphases are overexpresed in human tumors", *Int.J. Cancer,* **1999**, 19, p.682-687.

[19] Kamai T., Arai K.,Tsuji T., et al., "Overexpression of RhoA mRNA is associated with advanced stage in testicular germ cell tumor", *BJU int.,* **2001**, 87, p.227-231.

[20] Abraham M.T., Kuriakose M.A, Sacks P.G., et al., "Motility-related proteins as markers for head and neck squamous cell cancer", *Laryngoscope*, **2001**, 11, p. 1285-1289.

[21] Prendergast G.C., "Actin' up: RhoB in cancer and apoptosis", *Nat. Rev.,Cancer*, **2001**, 1, p.162-168.

[22] Van Golen K.L., Wu Z., Qiao X.L., et al., "RhoGTphase, a novel transforming oncogene for human mammary epithelial cells that partially recapitulates the inflammatory breast cancer phenotype", *Cancer Res.,* **2000**, 60, p.5832-5838.

[23] Van Golen, k.L., et al., "A novel putative low-affinity insulin-like growth factor-bonding protein, LIBC (lost in inflammatory breast cancer), and RhoC GTPase correlate with the inflammatory breast cancer phenotype", *Clin. Cancer. Rest*, **1999**, 5, p.2511-2519.

[23] Suwa H. et al., "Overexpression of the RhoC gene correlates with progression of ductal adenocarcinoma of the pranceas", *Br.J.Cancer.*, **1998**, 77, p.174-152.

[24] Zheng Gengfeng, Patolsky Fernando, Cui Yi, et al., "Multiplexed electrical detection of cancer markers with nanowire sensor arrays", *Nat. Biotechnol*., **2005**, 23, p. 1294-1301.

[25] Asch George, *Les capteurs en instrumentation industrielle*, Paris, Dunod, **2006,** 6 ed, 864p.

[26] Sze S.M., *Semiconductor sensor*, NewYork, John Wiley and Sons, Inc., **1994**, 1 ed, 550p.

[27] Espina Virginia.,Woodhouse Elisa C, Wulfkuhle Julia et al., "Protein microarray detection strategies: focus on direct detection technologies", *Journal of Immunological Methods*, 2004, 290, p. 121-133.

[28] Freitas R.A. Jr., *Nanomedicine Vol. 1: Basic capabilities,* Pilot Hill, California USA, Landes Bioscience, **1999**.

[29] Kewal K. Jain, "Application of nanobiotechnology in Clinical Diagnostics", *Clinical Chemistry* **2007**, 53, p.2002-2009.

[30] Kewal K. Jain, T*he handbook of nanomedicine*, Switzerland, Humana Press, **2008**, 403p.

[31] Kewal K. Jain, *Nanobiotechnology: Applications, Markets and Companies*, Basel Switzerland, A. Jain PharmaBiotech Report, **2004**, 334p.

[32] Köhler Michel, Fritzsche Wolfrang, *Nanotechnology: An introduction to nanostructuring techniques*, Darmstadt Germany, Wiley-VCH Verlag GmbH & Co.KGaA, **2004**, 272p.

[33] Claesson M., Blomberg Eva, Fröberg Johan C., "Proteins interaction at solid surfaces", *Advances in colloid and interface science*, **1995**, 57, p.161-227.

[34] Jeffrey J Gray, "The interaction of proteins with solid surfaces", *Current Opinion in Structural Biology,* **2004**, 14, p.110–115.

[35] Palmer Richard E., Leung Carl, "Immobilisation of proteins by atomic clusters on surfaces", *Trends in biotechnolog,* **2006**, 25:2, p.48-55.

[36] Pijanowska D.G, Torbicz.W., "Biosensor for bioanalytical applications", *Bull. Pol. Ac.: tech.*, **2005**, 53:3, p.251-260.

[37] R.Bashir, *Introduction to bioMEMS& bionanotechnology*, Purdue University, **2007**, 37p.

[38] Richards Grayson Amy c., Shawgo Rebecca s., Johnson M. Audrey, "Biomems Review: MEMS Technology for Physiologically Integrated Devices", *Proceedings of the IEEE*, **2004**, 92: 1, p.6-21.

[39] Wang Wayne U., Chen Chuo, Lin Keng-hui, et al., "Label-free detection of small-molecule–protein interactions by using nanowire nanosensors", *PNAS*, **2005**,102, p.3208-3212.

[40] Yi Cui, Qingqiao Wei, Hongkun Park, et al., "Nanowire nanosensors for highly sensitive and selective detection of biological and chemical Species", *Science (reports)*, **2001**, 293:17, p.1289-1291.

[41] Patolsky Fernando, Zheng Gengfeng, Lieber Charles M., "Nanowire-based biosensor", *Analytic Chemistry*, **2006**, p.4261-4269.

[42] Patolsky Fernando, Zheng Gengfeng, Hayden Oliver, et al., "Electrical detection of single viruses", *PNAS,* **2004**, 39, p.14017-14022.

[43] Zheng Gengfeng, Patolsky Fernando, Cui Yi, et al., "Multiplexed electrical detection of cancer markers with nanowire sensor arrays", *Nat. Biotechnol.,* **2005**,23:10, p.1294-1301.

[44] Xiaoshan Zhu, Chong H. Ahn, "Electrochemical Determination of Reversible Redox Species at Interdigitated Array Micro/Nanoelectrodes Using Charge Injection Method", *IEEE transaction on nanobioscience*, **2005**, 4:2, p.164-169.

[45] Zhang Hongquan, Zhao Qiang, Li Xing F, et al., "Ultrasensitive assays for proteins", *Analyst*., **2007**,132, p.724-737.

[46] Nair Pradeep R., Alam Muhammad A., "Screening-Limited Response of NanoBiosensors", *Nanoletters,* **2008**, 8:5, p.1281-1285.

[47] Nair Pradeep R., Alam Muhammad A., "Performance limits of nanobiosensors", A*pplied Physics Letters*, **2006**, 88, p.233120/1-233120/3.

[48] Nam Jwa-Min, Thaxton C. Shad, Mirkin Chad A., "Nanoparticle-based bio-bar codes for the ultrasensitive detection of proteins", *Science*, **2003**, 301, p.1884-1886.

[49] Nam Jwa-Min, Stoeva Savka I., Mirkin Chad A., "Bio-bar-code-based DNA detection with PCR-like sensitivity", *J. Am. Chem. Soc.*, **2004**,126, p.5932-5933.

[50] Park So-Jung, Taton T. Andrew, Mirkin Chad A., "Array-based electrical detection of DNA with nanoparticle probes", *Science,* **2002**,295, p. 1503-1506.

[51] Wang Josep, "Nanoparticle-based electrochemical DNA detection", *Analytica chimica Acta,* **2003**,500, p.247-257.

[52] Le Berre Véronique, Trévisiol Emmanuelle, Dagkessamanskaia Adilia, et al., "Dendrimeric coating of glass slides for sensitive DNA microarrays analysis nucleic acids research", **2003**, 31:16. p.2-8.

[53] McKendry Rachel, Zhang Jiayun, Arntz Youri, et al., "Multiple label-free biodetection and quantitative DNA-binding assays on a nanomechanical cantilever array", *PNAS*, **2005**, 102:41, p.14587-14592.

[54] Backmann Natalija, Zahnd Christian, Huber Francois, "A label-free immunosensor array using single-chain antibody fragments", *PNAS*, **2005**, 102:41, p.14587-14592.

[55] Fritz J., Baller M. K., Lang H. P., "Translating biomolecular recognition into nanomechanics", *Science*, **2000**, 288, p.316-318.

[56] Gupta Amit K., Nair Pradeep R., Akin Demir, "Anomalous resonance in a nanomechanical biosensor", *PNAS*, **2006**, 103:36, p.13362-13367.

[57] Li Jun, Tee Ng Hou, Cassell Alan, "Carbon nanotube nanoelectrode array for ultrasensitive DNA detection", *Nanoletters*, **2003**, 3:5, p.597-602.

[58] Barone P.W, Baik, S, Heller D.A., "Near-infrared optical sensors based on single-walled carbon nanotubes", *Nat. Mater*, **2005**, 4, p.86-92.

[59] Chen Robert J., Bangsaruntip Sarunya, Drouvalakis Katerina A., "Noncovalent functionalization of carbon nanotubes for highly specific electronic biosensors", *PNAS*, **2003**, 100:94, p.984-4989.

[60] Friddle Raymond W., Lemieux Melburne C., Cicero Giancarlo, "Single functional group interactions with individual carbon nanotubes", *Nat. Nanotechnology*, **2007**, p.1-6.

[61] Li C. Curreli, Zhou C., "Complementary detection of prostate specific antigen using In_2O_3 nanowires and carbon nanotubes", *J am. Chem. Soc*. **2005**, 127, p.1284-12585.

[62] S. Iijima, "Helical microtubules of graphic carbon", *Nature*, **1991**, 354, p.56-58.

[63] Shi Kam, N. W., Dai, H.j., "Carbon nanotubes as intracellular protein transporters: Generality and biological functionality", *J am. Chem. Soc*., **2005**, 127, p.6021-6026.

[64] Yinghuai Z., Peng A.T., Carpenter K., "Substituted carborane-appended water-soluble single-wall carbon nanotubes: New approach to boron neutron capture therapy drug delivery", *J am. Chem. Soc*., **2005**, 25, p.1483-1489.

[65] Liu Zhuang, Chen Kai, Davis Corrine et al., "Drug delivery with carbon nanotubes for in vivo cancer treatment", *Cancer Res.*, August 15, **2008**, 68: 16, p.6652-6660.

[66] Georganopoulou D.G., Chang L, Nam J.M. et al., "Nanoparticle-based detection in cerebral spinal fluid of a soluble pathogenic biomarker forAlzheimer's disease", *PNAS,* **2005,** 102:7, p.2273–2276.

[67] Nam J. M., Wise A. R., Groves Jay T., "Colorimetric Bio-Barcode amplification assay for cytokines", *Anal. Chem*., **2005**, 77, p. 6985-6988.

[68] Oh B. K., Nam J. M., Lee S. W. and Mirkin C. A., "A Fluorophore-Based Bio-Bar-Code Amplification Assay for Proteins", *Small*, **2006**, 2, 103–108.

[69] Bao Y. P., Wei T. F., Lefebvre P. A., "Detection of Protein Analytes via Nanoparticle-Based Bio Bar Code Technology", *Anal. Chem.*, **2006**, 78, p. 2055-2059.

[70] Shaikh K. A., Ryu K. S., Goluch E. D. et al., "A modular microfluidic architecture for integrated biochemical", *Proc. Natl. Acad. Sci. U. S. A.*, **2005**, 102, p.9745-9750.

[71] Dequaire M., Degrand C., Limoges B., "An electrochemical metalloimmunoassay based on a colloidal gold label", *Anal. Chem*., **2000**, 72, p.5521-5528.

[72] Hansen J. A., Wang J., Kawde A. N., **"**Quantum-Dot/Aptamer-Based Ultrasensitive Multi-Analyte Electrochemical Biosensor", *J. Am. Chem. Soc.*, **2006**, 128, p.2228-2229.

[73] Wang J., Liu G., Munge B., "DNA-based amplified bioelectronic detection and coding of proteins", *Angew. Chem., Int. Ed*., **2004**, 43, p.2158-2161.

[74] J. Wang, G. Liu and M. R., "Ultrasensitive electrical biosensing of proteins and DNA: carbon-nanotube derived amplification of the recognition and transduction events", *Jan, J. Am. Chem. Soc.*, **2004**, 126, p.3010-3011.

[75] X. Yu, B. Munge, V. Patel, et al., "Carbon nanotube amplification strategies for highly sensitive immunodetection of cancer biomarkers", *J. Am. Chem. Soc*., **2006**, 128, p.11199-11205.

[76] J. Das, Md. A. Aziz and H. Yang, "A Nanocatalyst-Based Assay for Proteins: DNA-Free ultrasensitive electrochemical detection using catalytic reduction of p-Nitrophenol by gold-nanoparticle labels", *J. Am. Chem. Soc*., **2006**, 128, p.16022-16023.

[77] D. S. Grubisha, R. J. Lipert, H. Y. Park, "Femtomolar detection of prostate-specific antigen: an immunoassay based on surface-enhanced Raman scattering and immunogold labels", *Anal. Chem.*, **2003**, 75, p.5936-5943.

[78] Lian W., Litherland S. A., Badranea H., "Ultrasensitive detection of biomolecules with fluorescent dye-doped nanoparticles", *Anal. Biochem*., **2004**, 334, p.135-144.

[79] A. Agrawal, C. Zhang, T. Byassee, "Counting single native biomolecules and intact viruses with color-coded nanoparticles", *Anal. Chem*., **2006**, 78, p.1061-1070.

[80] Saleh Omar A, Sohn Lydia L, "An artificial nanopore for molecular sensing", *Nanoletters,* **2003**, 31, p.37-38.

[81] Dekker Cees, "Solid-state nanopores", *Nat. nanotechnology*, **2007**, 2, p.209-215.

[82] Moreau Christophe J., Dupuis Julien P., Revilloud Jean, et al., "Coupling ion channels to receptors for biomolecule sensing", *Nature Nanotechnology*, **2008**, p.1-6. doi:10.1038/nnano.2008.242

[83] Wu Yunhua, Hu Shengshui, "Electrochemistry at nanolectrodes", *Indian Journal of chemistry*, **2005**, 44A, p.891-898.

[84] K. Liu, P. Avouris, J. Bucchignano, et al., "Simple fabrication scheme for sub -10nm electrodes gaps using electron beam lithography", *Appl. Phys. Lett.*, **2002**, 80, p.865-867.

[85] L. Ressier, J. Grisolia, C. Martin, et al., "Fabrication of planar cobalt electrodes separated by a sub-10 gap using high resolution electron beam lithography with negative PMMA", *Ultramicroscopy*, **2007,** 107, p.985-988.

[86] L. Montelius, B. Heidari, M. Graczyk, "Nanoimprint and UV-lithography: Mix and Match process for fabrication of interdigitated nano biosensors", *Microelec. Eng*., **2000**, 53, p.521-524.

[87] F. Carcenac, L. Malaquin, C. Vieu, "Fabrication of multiple nano-electrodes for molecular addressing using high-resolution electron beam lithography and their replication using soft imprint lithography", *Microelec. Eng.,* **2002**, 61, p.657-663.

[88] J. Tallal, D. Peyrade, F. Lazzarino, "Replication of sub-40 nm gap nanoelectrodes over an 8-in. substrate by nanoimprint lithography", *Microelec. Eng*., **2005**, 78, p. 676-681.

[89] M. A. Reed, C. Zhou, C. J. Muller, "Conductance of a molecular junction", *Science,* **1997,** 278, p. 252-254.

[90] A. Nitzan , M. A. Ratner, "Electron transport in molecular wire junctions", *Science,* **2003**, 300, p. 1384-1389.

[91] Gerwen Peter Van, Laureyn Wim, Laureys Wim., "Nanoscaled interdigitated electrode arrays for biochemical sensors", *Sens. and Actuators,* **1998**, 49, p.73-80

[92] Laureyn W., Nelis D., Gerwen P. Van, "Nanoscaled interdigitated titanium electrodes for impedimetric biosensing", *Sens. and Actuators B,* **2000**, 68, p. 360-370.

[93] Zou Zhiwei, Kai Junhai, Rust Michael J., "Functionalized nano interdigitated electrodes arrays on polymer with integrated microfluidics for direct bio-affinity sensing using impedimetric measurement", *Sens. and Actuators A,* **2007**, 136, p.518-526.

[94] L.Malaquin, C. Vieu, C. Martinez, "Interdigitated nanoelectrodes for nanoparticle detection", *Nanotechnology,* **2005**, 16**,** p.s240-s245.

[95] Joachim Christian, Gimzewski J. K., Aviram A., "Electronics using hybrid-molecular and mono-molecular devices", *Nature,* **2000**, 408, p.541-548.

[96] N. Tesla, *Electric condenser*, U.S., **1891,** Patent No. 464 667.

[97] Mamishev Alexander.V.**,** Sundara-Rajan Kishore**,** Yang Fumin**,** "Interdigital sensors and transducers*"*, *Proceding of the IEEE*, **2004**, 92:5, p.808-845.

[98] Fritzsche Wolfgang, Czaki Andrea, Michael Johann et al., *Affinity sensor for detection specific molecular binding events and use of thereof*, United States patent, **2005**, Patent No. 6,878,539 B1.

[99] Malaquin Laurent, *Dispositifs ultra-sensibles pour le nano-adressage électrique. Application a la détection de biomolécules,* Université Paul Sabatier - Toulouse III **09-06-2004**, dir. Christophe Vieu.

General references:

[100] Lahmani Marcel, Boisseau Patrick, Houndy Philippe, *Les nanosciences: Nanobiotechnologies et nanobiologie*, Paris, Belin, 1, **2007**, 1150p.

[101] Benno Krieg, Chistoph Janiak, *Chemie für Mediziner und Studierende anderer life Science*, de Gruyter, Berlin Freitburg, **2004,** 393p.

[102] Horst-Günter Rubanh, *Nanophysik und Nanotechnologie*, Germany, Teubner, **2004**, 184p.

Chapter II

Wafer scale nanoelectrode fabrication as high sensitive nanotransducers for diagnostic applications: Mix and match process

2.1 Introduction

Thanks to development issue from nanotechnology, interdigitated nanoelectrodes have been elaborated using various techniques such as nanoimprint lithography (NIL) [1-3] electron beam lithography (EBL) [4][5] or focused ion beam (FIB) [6], and they have been used in a large variety of applications, e.g. to electrical contact single molecule [7-9], in impedimetric biosensing [10-12] and recently in nano-electrochemistry [13][14] and for research in numerous fields including disease diagnostic, protein and cell engineering or to detect dopamine [15]. Laurent Malaquin previously demonstrated, in our group, that these devices are capable of sensing nanoparticles grafted with proteins at high sensitivity due to the nanometric gap between electrodes [16].

Otherwise, modern biomolecular analyses require parallel detection of multiple analytes with high sensitivity and selectivity. Hence, it is essential that large quantities of these kinds of nanobiosensors are elaborated with high degree of reproducibility. Electron lithography is a slow serial technique to produce nanostructures. It does not fit for industrialisation, however it is a convenient research tool to reach nanometre scale realisation. A potential technique that can replace electron lithography is nanoimprint lithography (NIL) used for production in parallel manner.

In this context, we present a methodology to elaborate several nanodevices onto a single cell, reproducing 96 cells per 4 inch wafer. Interdigitated nanoelectrodes devices (IND) are elaborated using electron beam lithography (EBL) thus mixed and matched with classical photolithography process, using two layers of deposited metals. The purpose is to interconnect nanostructures to microstructures at wafer level. Optimum parameters (e.g. electronic dose) are determined to elaborate IND devices on wafer scale. Electrical characterisations are performed on bare nanoelectrodes. Finally, estimation of conductivity in a nanoelectrode is conducted. The mix and match process allows us to elaborate and interconnect 768 interdigitated nanoelectrodes devices (IND) on 4 in. wafer. Interdigitated nanoelectrodes devices (IND) are used as nanobiosensors, described in a later chapter on this thesis.

Before presenting the nanoelectrode realisation, basic introduction to micro-nanofabrication techniques is given.

2.2 Basic micro-nanofabrication techniques

In this section, some techniques used in typical micro and nanofabrication are explained. However only the techniques employed to accomplish this part of the project, such as photolithography and electron lithography are presented.

2.2.1 Spin coating

In this process, a compound is dissolved in a volatile liquid solvent, poured on a wafer and the rotated at high speed. The liquid spreads, the volatile solvent evaporates and it leaves a uniform solid thin layer of the material on the sample (or wafer). Fig.2.1 (a) illustrates the spin-coating process. Fig.2.1 (b) illustrates one of the machines available in our laboratory and used in our process.

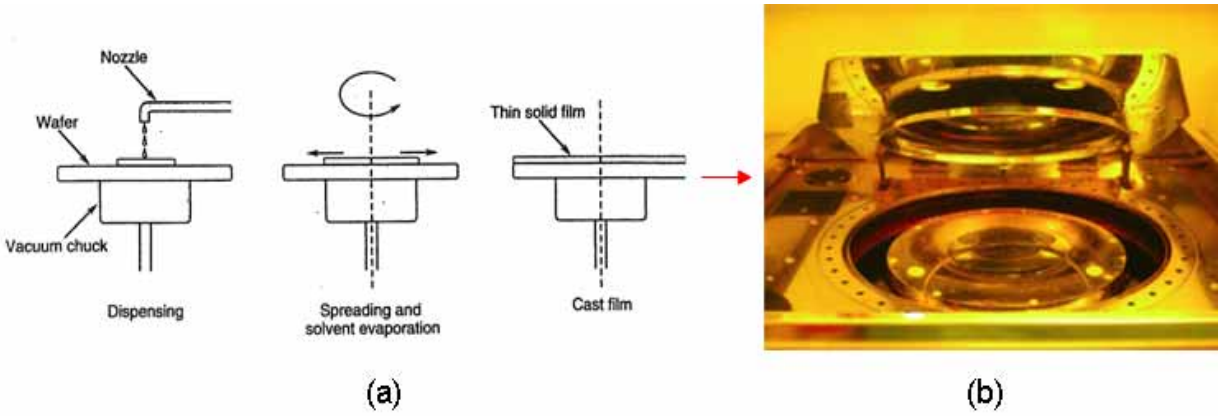

Fig.2.1. (a) Spin-coating process (picture from [17]), (b) spin-coater used at LAAS-CNRS.

The deposited thicknesses of solid films depend on the degree of viscosity and on the spin speed, hence film thicknesses could range from 100nm to even several hundreds of micrometres. The spin-coating technique is used to deposit organic materials such as the photosensitive resist or electron sensitive resist. Photosensitive resist (photoresist) is used in typical microtechnological processes. For example in chapter 5, a deposited photoresist measuring 500µm is obtained by stacking three deposited-resists. In this chapter, however the deposited photoresist films measure 2.7µm (+-10% on the edge) of thickness. Thicknesses are characterised with a mechanical profilometer KLA tencor P10.

2.2.2 Optical lithography (photolithography)

A typical photolithopgraphic process consists of producing a photomask having the desired and subsequently transferring in parallel manner those patterns onto the wafer (substrate) using an UV-light sensitive resists (*photoresist).* Nowadays, there are two photolithographic approaches: (1) *shadow photolithography*, which can be divided into contact photolithography (or contact-mode photolithography) and proximity photolithography. (2) *Projection printing* (using steppers machines). In this thesis we used shadow photolithography to mix and match with electron lithography to reach across the micrometric scale down to the nanometric scale.

Photolithographic methodology consists of spin coating a photoresist on a wafer, covering the entire wafer surface, and then the UV light passes through (exposes) a photomask directly onto the photoresist coated wafer. The photo mask or master mask (reticle) is a glass substrate with clear and opaque regions. Materials used to fabricate the masks are either soda-lime glass (transmittance from 360 nm to 2750 nm) or quartz (fused silica: transmittance from 200 nm). The choice of the material mask depends on the photosensivite material used and the

wavelength sensitivity, as we will see in chapter 5 while discussing the photoPDMS material for microfluidic applications. Concerning our process, however, the photoresist we used is sensitive to wavelength of 405 nm, and then photomasks were made of soda-lime glass.

In a photolithograhy process, typically photoresist has to react to the exposing radiation so that a replication of patterns of the mask is left in the resist [18] and have to protect the underlying material during subsequent processes, typically etching, ion implantation or lift-off. Photoresists have two basic forms: Negative and Positive. *Negative* photoresist reticulates during radiation exposure so that the exposed resist is not removed in the development process (a special solvent removes the unexposed areas, in this case) leaving an inverse image of the mask in the resist. *Positive* resist is broken down during radiation, so exposed areas can be easily removed in the development process step (a special solvent removes the exposed areas in this case). Then positive image of the mask is obtained in the photoresist. Fig.2.2 illustrates the photolithographic process and the two resist types.

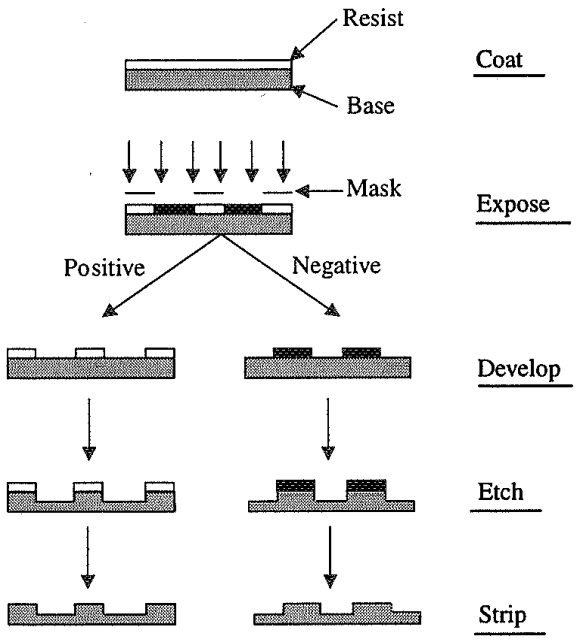

Fig.2.2. Schematic representations of the photolithographic process (picture from [19]).

The theoretical resolution capability (minimum size of the individual photopatterned elements of shadow photolithography) consists of equal lines and spaces of width b, is given by:

$$R = b_{\min} = \frac{3}{2}\sqrt{\lambda\left(s + \frac{d}{2}\right)} \qquad \text{Eq. [1]}$$

Where, b_{min} is the minimum feature size transferable, s is the gap between the mask and the photoresist surface, λ is the wavelength of the exposing radiation and d is the photoresist thickness. If we used in our processes: λ= 405 nm, s= ~40μm, and d =2.7 μm, then R equals ~ 6 μm.

From this equation we observe that to improve resolution, it is necessary to have shorter wavelength, smaller gaps and thinner resist layers.

2.2.3 Lift-off processing

It is a technique where a negative image of the required metal pattern is formed in resist on the wafer before the metal deposition step. After depositing the metal (e.g. by evaporation), the resist is removed taking the unwanted metal with it. Lift-off process is used both to elaborate microstructures (photolithography) and nanostructures (electron lithography).

There are reversible photoresist, in which the transfer form (positive to negative) is realised at the final process by curing the original positive resist. Reversible photoresist are best adapted to use with lift-off. The reason is that the patterns obtained with this kind of resist are not enough vertical and allow the solvent to enter and remove the undesired metal. In this thesis, the AZ5214 reversible resist is used.

2.2.4 Electron beam lithography (EBL)

The first use of e-beam lithography (EBL) was to elaborate masks (or reticle) that would be used with optical lithographic method [18]. Now, EBL is used for [20]: (1) the elaboration of mask in the use of optical steppers or proximity x-ray lithography, (2) as tool for direct writing on wafers. The cost of an e-beam is high but a higher resolution is obtained than that obtained by photolithography. The reason is that e-beam uses electrons and electron wavelength is much shorter than that of the photons used in photolithography method as could be anticipated from equation [1].

In e-beam lithography, an electron source produces an important quantity of electron that are accelerated either electrostatically or magnetically to form a beam into a vacuum column chamber. The beam can be a round spot or an adjustable rectangular spot, using special systems described elsewhere [18]. The beam is directed against a resist-covered wafer. However in this case the resist is sensitive to electrons. There are positive and negative electron-resists. In a *positive resist*, molecules are broken and in a *negative resist* molecules are polymerised, in a similar way than for photolithographic technique. Then chemicals compounds for developments are used to remove either the regions of the resist that were exposed to an electron beam in the case of a positive resist or those that were not exposed in the case of a negative resist. Fig. 2.3 illustrates the patterns writing by e-beam lithography and the two electron-resists types.

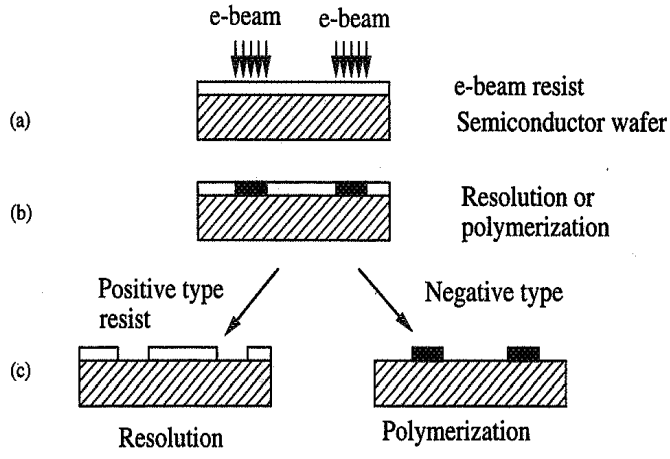

Fig.2.3. Patterns wrote by e-beam, (a) resist exposure, (b) molecules go away (positive) or polymerised (negative); (c) chemical compounds used to remove molecules of the positive or negative resins. (Image from [20]).

Fig. 2.4 shows the e-beam writer used in this work (LAAS-CNRS clean room facility) which is a Raith 150 (Germany). It is a direct electron-beam writer for R&D applications to produce patterns down to 50 nm. Some principal features are (from Raith.com): Beam energy selectable between 200V to 30kV, selectable writing field sizes between 0.5 to 800 µm, 6 inch laser interferometer stage with electrostatic chuck and automated sample levelling using 3 point contact piezo-electric devices, flexible dual PC with patterns generators (GDSII) and flexible graphical editor. Magnification from 20 to 900000 times and its software accepts several format editors.

Details of the electron resist and parameters used in our development process are given later.

Fig.2.4. E-beam Raith 150 (picture from Raith.com).

2.2.5 Film deposition method: Evaporation

The evaporation method is used in this work to depose the different metals. In evaporation method, the metal is taken from a hot source (the crucible) to a substrate. A schematic of this system is shown in Fig. 2.5.

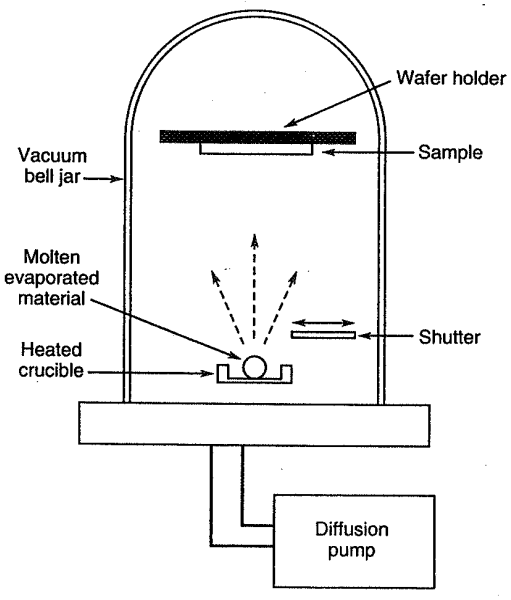

Fig.2.5. Schematic of an evaporation system (picture from [17]).

Evaporation systems contain a vacuum chamber, a pump, a holding frame for the samples, a crucible and a shutter. A sample of the material is placed in the crucible and the chamber is evacuated at around 10^{-6} Torr. A tungsten filament is used to heat the crucible and to evaporate the material from the crucible onto the sample surface or wafer surface. The film thickness is determined by using a crystal quartz microbalance.

Since the material is evaporated from the crucible, evaporated films have shadowing effects causing poor step coverage. On the other hand, poor step coverage is suitable to reach easily a lift-off so the chemical compound can go under the protected areas and remove the undesirable element. However, by using evaporation technique, non-uniform thickness are obtained, then only thin film metals can be evaporated because the evaporated metals have residual stress and are disordered [17]. Evaporation technique is well suited to our needs because in the case of nanostructures realisations, the thickness of the deposited metals is under 30 nm and in the case of contact pads showed later in this chapter, the thickening of the pads with 1 µm gold (for wire bonding purposes) is not affected by shadowing effects because the micropads measure 400µm x 400µm and are much wider that they are thick. Fig.2.6 shows a Veeco 770 machine used in this research work.

Fig.2.6. Evaporation system (Veeco 770) at LAAS-CNRS.

2.3 Fabrication of devices by mix and match lithography process

In this section, a methodology to realise 768 interdigitated nanoelectrodes devices (IND) on 4 inch wafer scale is presented. The technique to accomplish this, is a combination of photolithography with electron lithography, called mix and match process.

The use of micromarks realised by photolithography was crucial to align and realise 96 cells, carrying each cell 8 IND which are, in a second step, elaborated by electron lithography.

Four-inch silicon wafers covered with 1µm of SiO_2 realised by thermal oxidation were used. The photolithographical process to realise the mentioned marks was realised using a reversible photoresist (AZ5214, Clariant), using the process presented in the next table 2.1.

Typical AZ5214 process
*Spin-coating 3ml of AZ5214 was spin-coated at 1000 tr/min, during 30 s *Soft cure 105 °C for 55 s *Exposure Machine MA -150 Suss Microtec at 20 mW/cm, during 2.7 s * Post exposure bake 105 °C during 55 s *Exposure to inverse the resist type (transparent mask) Machine MA -150 Suss Microtec, at 20 mW/cm, during 12 s * Development AZ developer/water (1:1 in volume) during 30 s *Hard bake 105 °C during 10 s

Table 2.1. Protocol for photoresist AZ5214 realisation.

To depose Ti/Au-10nm/20nm in thickness, onto the mask patterns the above mentioned Veeco 770 evaporator was employed. Titanium is necessary to assure the adherence of the subsequent gold deposition because gold is not enough rough to assure a homogenous adherence if depositing it, directly onto the silice. The metals were deposited at a deposition rate of 20 Å/S. The lift-off step was realised into a baker containing acetone for 5 min. To accelerate the lift-off realisation, ultrasonic agitation at 135 kHz was applied on the baker during 5 min.

Fig. 2.7 pictures a 4 in. wafer process carrying 96 cells which measures each one 7 mm x 7 mm, there is also a close-up of one cell and two marks on the right. These marks are inverted-L shape, measuring 5µm in width and 22 µm in length. The reason for using this kind of shape is because vertical and horizontal lines are needed by the eBeam writer to calculate the centre of each mark which serves to align each IND. To do this, a vertical line is realised by the Raith 50 (before realising each IND) in the middle of the horizontal part of each L mark and a horizontal line is realised in the middle of the vertical part of the same L mark. See Fig. 2.7 (a).

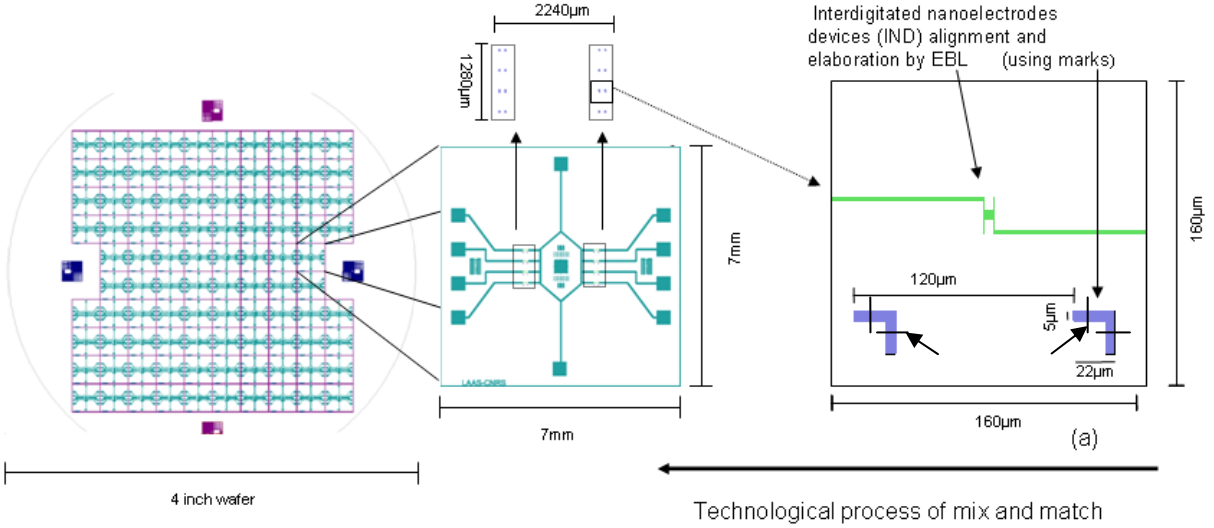

Fig.2.7. Mix and match in 4 in. wafer (left) showing enlargement of one cell (middle) and two alignment marks (right).

Each cell has 16 marks which allow aligning and elaborating 8 IND in each cell. In Fig. 2.7 an arrow, on the bottom of the images, indicates that the process starts by elaborating the marks, to subsequently make a mix and match until reaching the required 4 in. wafer integration.

In chapter 6, we will propose the use of a cantilever-based spotter device, combined with our nanotechnological development that permits to deposit precisely liquid spots from picolitter to femtolitter range. The interest in using this system is to deposit in parallel and locally the probes onto the active zone of the interdigitated nanoelectrodes devices (IND). Therefore, we designed each cell's interdigitated nanoelectrodes devices (IND) to fit with the space distance between each cantilever (360 µm). We had then, to adapt each writing field size of our eBeam writer to fit with the distance of each IND (360 µm) so the writing field size is 160 µm x 160 µm. In each cell (7 mm x 7 mm) there are 14 writing fields (2240 µm) horizontally and 8 writing fields (1280 µm) vertically. It is an important point, because eBeam is a serial technique and there is an interest in minimising the work time by reducing the total number of writefields, Figure 2.7 illustrates also the size of a cell (160 µm).

The design of interdigitated nanoelectrodes devices for electronic lithography was realised using the CLEWIN software. The same software was used for the photolithography layers, described in next part.

In eBeam lithography, electrons are accelerated at high voltage against the material sensitive to electrons thus electrons tend to scatter to the neighbourhood, these effects are known as proximity effects and they are important in electronic-beam lithography. These proximity effects cause variation in the width of the exposed nanopatterns because of the density of other close patterns [21][22]. Finally proximity effects are responsible of poor yields reproduction. To compensate for these effects, the IND devices were lengthened (20 µm) as illustrated in Fig. 2.8 (b). When the IND were not lengthened, the proximity effect caused non homogenous size reproduction of IND.

Fig. 2.8 illustrates the design of the IND with a zoom on the nanoelectrode in Fig. 2.8 (c). These devices resemble a comb. Each nanoelectrode was designed to be 40 nm in width and 5 µm in length. Each device has a total of 36 nanoelectrodes with 18 nanolectrodes in each side of 140 nm pitch.

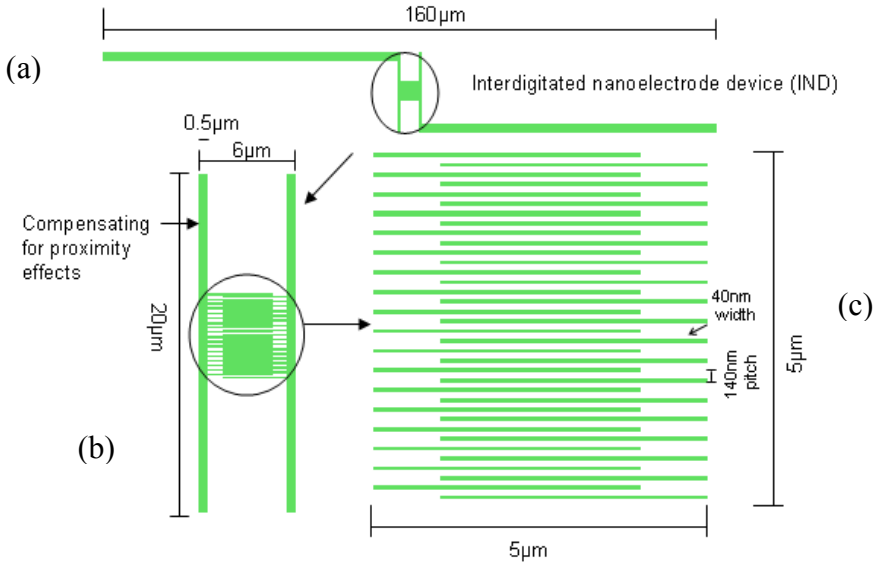

Fig.2.8. Nanoelectrode array design and compensation for proximity effects.

When simple lines represented the nanoelectrodes in Clewin software, all nanoelectrodes were not successfully obtained (after lift-off step, some nanoelectrodes appeared cut) and the proximity effects were visible, then nanoelectrodes are less wide in the border than in the middle. See Fig. 2.9 (a), in this case the dose is designated as single pixel line (cm). After deposition of Ti/Au-10nm/20nm we obtained nanoelectrodes having 30 nm in width. However, when the nanoelectodes were drawn having a 40nm width, a better yield was obtained. Furthermore, the devices were lengthened to compensate for the proximity effects, see Fig. 2.9 (b). In this case the electronic exposure dose is designated by area (cm^2) thus nanoelectrodes are wider (~46 nm width). The width depends on the electronic dose value, as discussed later.

In both cases of the Fig.2.9, the nanoelectrodes were elaborated by the e-beam writer, as follows: PMMA (996 k molecular weight, 30g/l) was spin coated at 3000rpm for 30s, on 4 inch silicon wafer with previously discussed marks. The PMMA film thickness measures 140 nm (films were characterised with a mechanical profilometer, model KLA Tencor p10). Finally, the wafer carrying the PMMA film was baked at 170°C for 1min. PMMA functions as positive type resist.

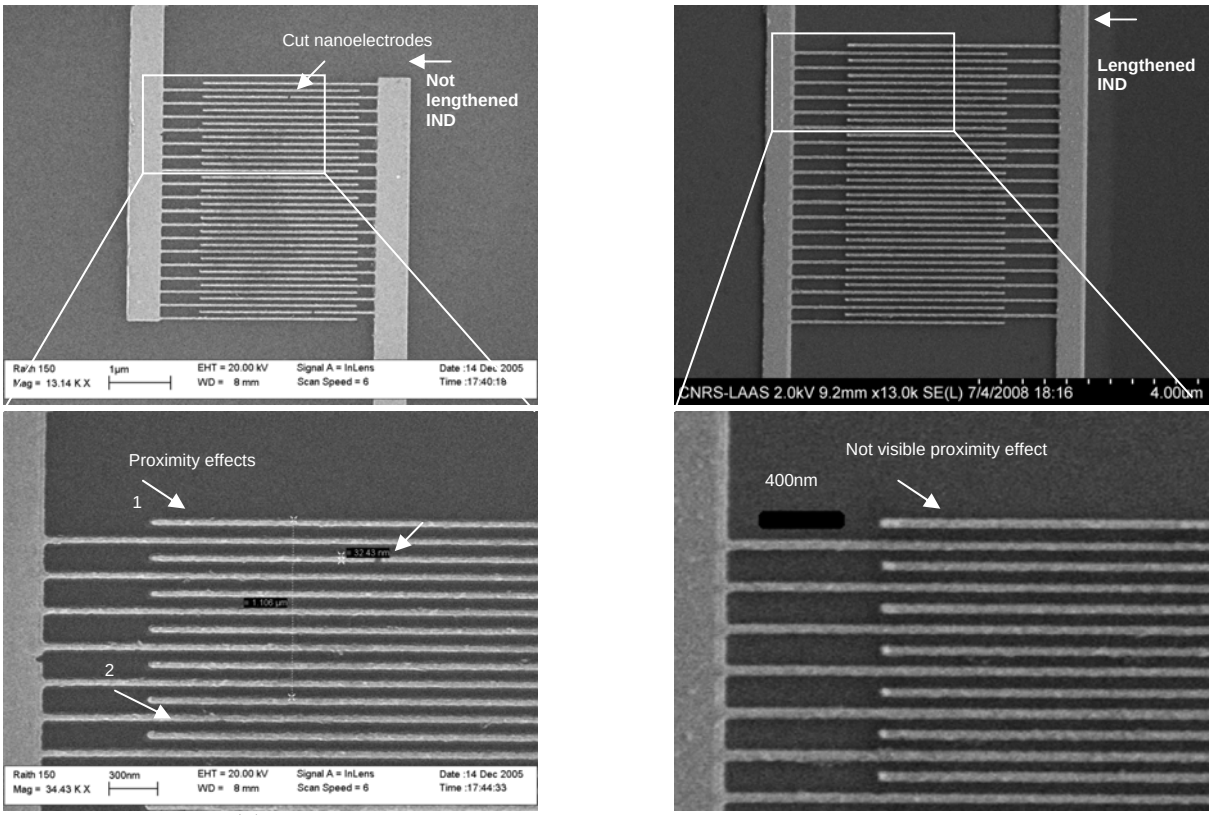

Fig.2.9. Lengthened IND (b) compared to no lengthened IND (a) observing in this case proximity effects.

A dose study was conducted to know the optimum dose and to be able to reproduce nanoelectrodes over the entire 4 in. wafer. To do this, 350µC/cm^2 dose was used as the base dose, and then a column of IND was constructed, multiplying the base dose by a factor which varied from 0.5 to 1.20 (by steps of 0.05) as illustrated in Fig.2.10.

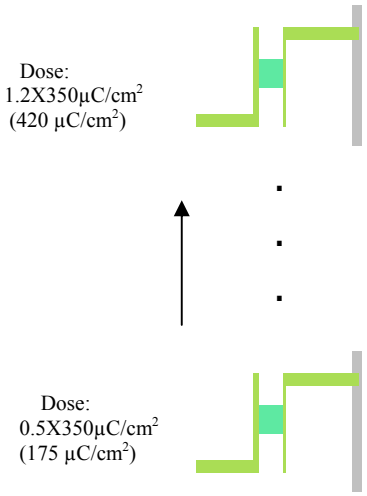

Fig.2.10. Column arrangement for determination of the optimum dose.

The development of the nanostructures was realised in a baker during 45s, containing methyl isobutyl ketone (MIBK)/Isopropanol(IPA), at 1:3 in volume. The IND were observed directly by the Raith 150. We observed that the smallest electronic doses produced non homogenous thickness nanopatterns in the PMMA film (dark spots lines) depicted in Fig. 2.11 (a). In this case variation can be of 50 % between one nanoelectrode and other. Contrary, the highest electronic doses produced wide nanopatterns in PMMA film thus in this case the nanoelectrodes, after metal deposition and lift-off process, would be wider. See Fig.2.11 (b).

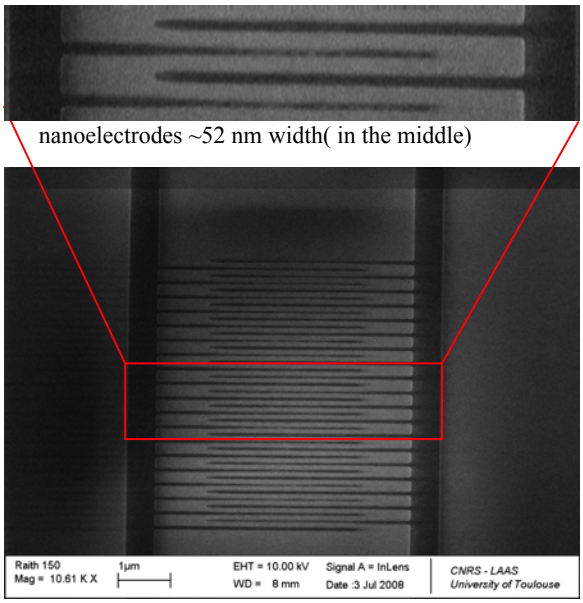

(a) Electronic dose: 0 .5x 350µm/cm2 (175 µm/cm^2)

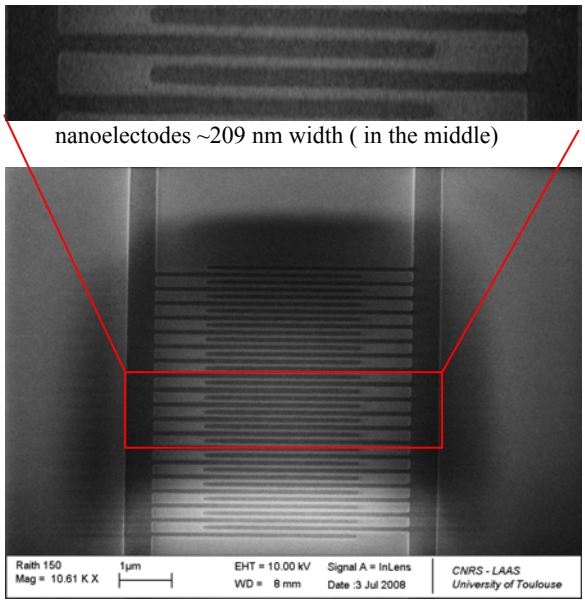

(b) Electronic dose: 1.2 x350µm/cm2 (420µm/cm^2)

Fig.2.11. PMMA-IND development (a) thin, non homogenous nanopatterns (b) Largely wide nanopatterns.

It is important to note that observing the results of the developments in a scanning microscope alter slightly the width of the developed nanolectrodes for any ulterior metal deposition and

lift-off. This study can not therefore give information of the final width of the nanoelectrodes but allows comparing the influence of the smallest doses with that of the highest doses.

For comparison of the arranged nanoelectrodes in the above column of Fig. 2.10, zooms of the 15 nanoelectrodes are illustrated in Fig. 2.12 with the smallest doses on the bottom and the highest doses at the top of the column. The electronic doses, from 385 μm/cm^2 to 262 μm/cm^2 appear to be more homogenous in shape. Furthermore, nanoelectrodes' width to pitch ratio for these doses are compatible with the subsequent metal deposition and for a successful lift-off process. At smaller doses, the nanoelectrodes become inhomogeneous while at higher doses, the width to pitch ratio becomes incompatible with the lift-off process producing short circuits between electrodes.

Ulterior lift-off tests revealed that the optimum dose for our IND is around 280 μm/cm^2 yielding the desired nano-electrode width of 40 nm.

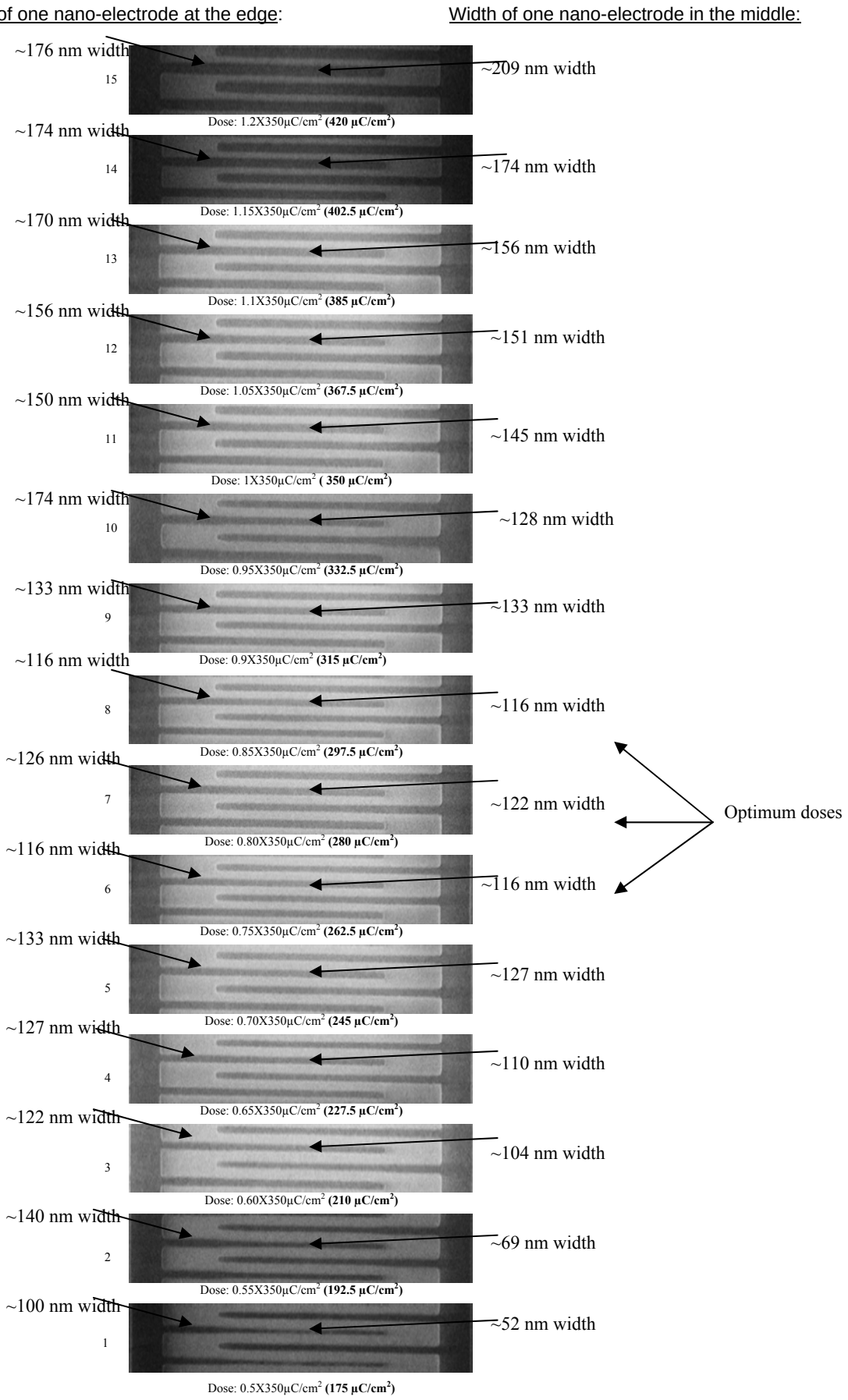

Fig. 2.12. Part of whole column of PMMA-IND development as a function of the dose.

After the previous study, we were able to realise the IND in wafer scale. We spin-coated the PMMA using the same parameter described above. Table 2.2 presents the main exposure parameters used in our process: base dose, write field, working area, voltage, beam current and working distance. Note that as nano-electrodes were designed to be 40 nm in width and as they were designed as surface area, the exposure parameters for single pixel lines are zero.

Design	
GDSII file:	C:\RAITH150\User\Franck\GDSII\Adrian\07-03-2007\masqueModificationpeignes7-03-2007Franck.gds
GDSII structure:	TestDeDose
GDSII layer(s):	2-3
Writefield size:	160*160 µm²
Working area:	(0,-80) to (1600,400) µm
Coordinates	
Stage (x, y, z):	(1.805269, 11.088445, 16.405)
Global (u, v, w): * used *	(0.000002, 0.5, 7.5)
Local (u, v, w):	(0, 0, 0)
Column parameters	
Voltage:	20 kV
Aperture:	30 µm
Beam current:	143 pA
Magnification:	625 x
Working distance:	7.751 mm
Exposure parameters	
-- Areas --	
Step size:	10 nm
Dwell time:	2.448 µsec
nominal Dose:	350 µC/cm²
calculated Dose:	350.064 µC/cm²
-- Single Pixel Lines --	
Step size:	0 nm
Dwell time:	0 µsec
nominal Dose:	0 pC/cm
calculated Dose:	0 pC/cm
-- Single Dots --	

Table 2.2. Parameters used to elaborate IND in wafer scale by Raith 150.

The alignment of the IND was realised using the above marks placed in each cell and using four marks designed at the border or the wafer, see Fig. 2.13. The electronic exposure in our eBeam writer took ~4 hours. In these conditions an automatic alignment and exposure for each cell on the entire wafer were possible.

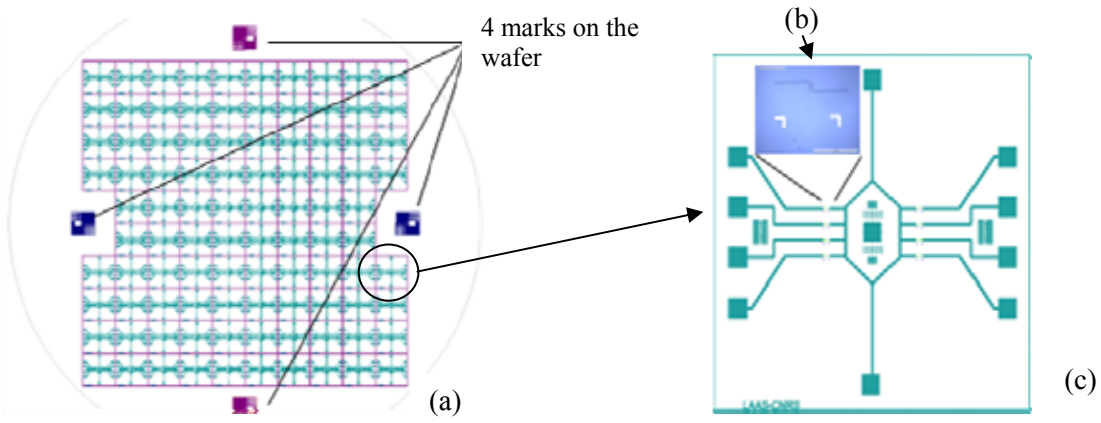

Fig. 2.13. (a) 4 in. wafer illustrating 4 marks to align the IND, (b) one IND to be connected with subsequent photolithographic processes, (c) Mix and match allows connecting the micropads to IND.

The development was realised in a baker during 45 s, containing methyl isobutyl ketone (MIBK)/Isopropanol(IPA), at 1:3 in volume. Deposition of Ti/Au-10nm/20nm followed this development.

Next technological step was the connection of the IND using two subsequent photolithographic processes known as "mix and match". Mix and match allowed us to connect micropads to the IND (nanostructures) and obtain 96 cells. Fig. 2.13 (b) illustrates, in detail, this first photolithographic process which is similar of that illustrated in Fig. 2.7. Each cell contains the 8 IND distributed in two columns, each IND is connected to one pad which serve as ground (common) and to other micropad which is used for the positive bias polarisation (there are 10 pads totally).

To realise the first photolithographic process, the AZ5214 photoresist process of table 2.1 was conducted. Then, a deposition of Ti/Au-10nm/20nm was conducted, finally the lift-off process was realised in a bake containing acetone. A schema illustrating the mix and match process in one IND is pictured in Fig. 2.14. It illustrates a cross section view of the process after metal deposition. Finally, a second photolithographic step was conducted to elaborate a thickening of gold (1µm thickness) and to obtain a good contact between gold of nanostructures and gold of microstructures. Note that the thickening metal deposition exceeds the second deposition emplacement to assure Au-Au contact between nanostructures and microstructures. The thickening is necessary to elaborate microbondings in each cell.

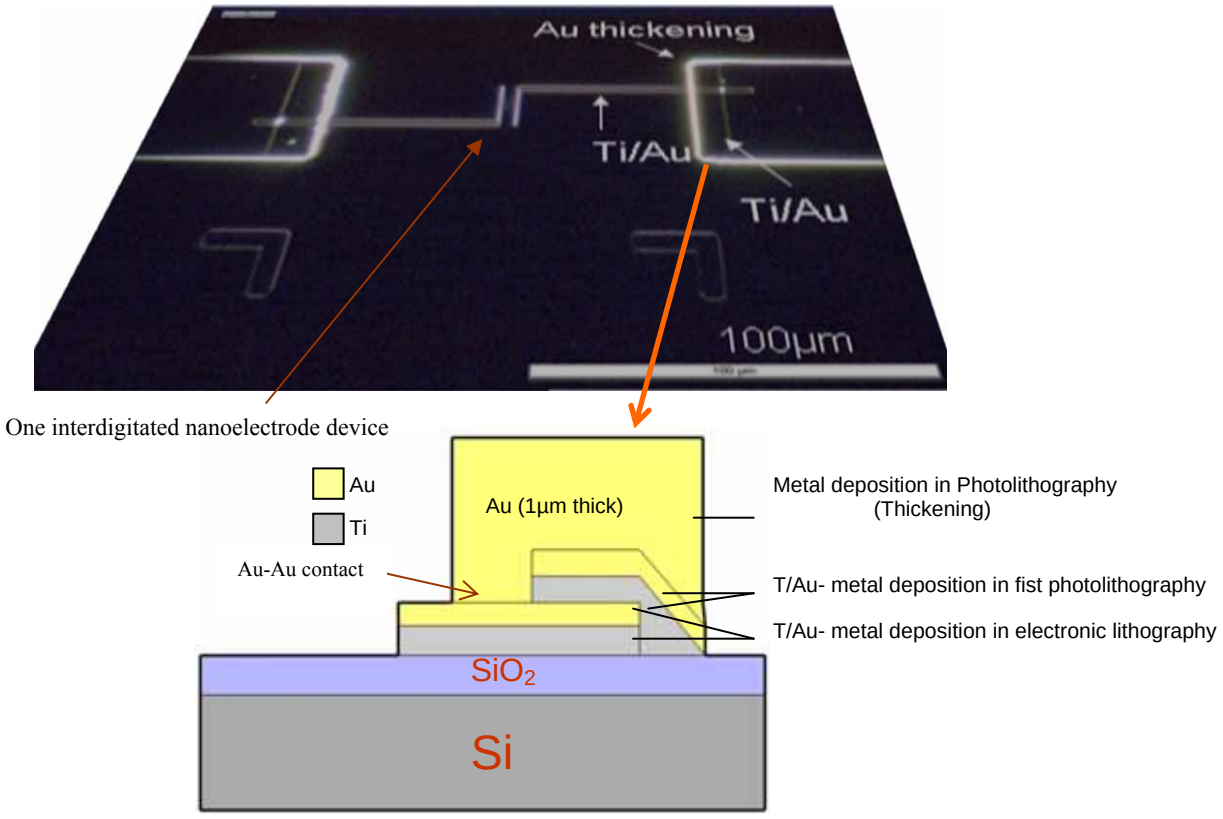

Fig. 2.14. Cross section of the connecting area between the nanostructures and the microstructures of the mix and match process.

Fig. 2.15 depicts optical and SEM images of a cell (7 mm x 7 mm). SEM image was taken by an ultra-high resolution scanning electron microscope FE-SEM Hitachi S-4800, a close-up of

one interdigitated nanoelectrode device and a unique nanoelectrode measuring 46 nm (electronic dose: 262.5 µC/cm^2) are shown.

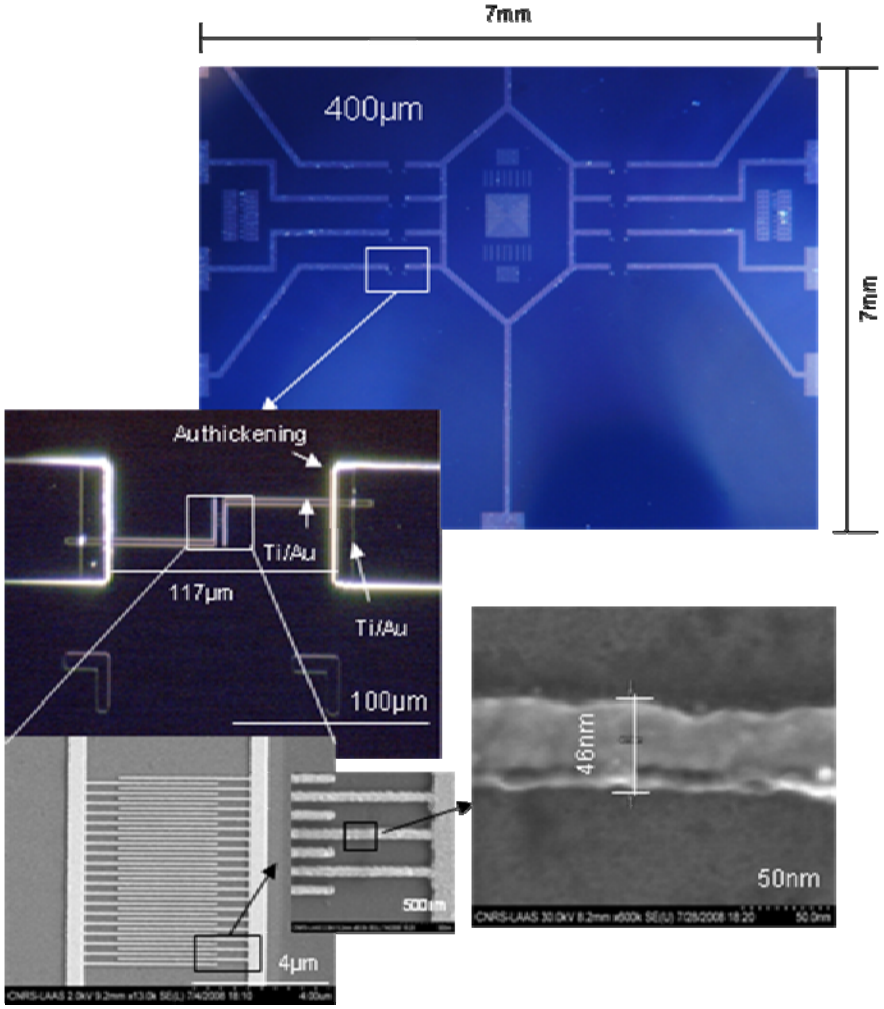

Fig.2.15. Mix and match process on one cell. Zoom of one nano-electrode.

2.4 Characterisation of the devices

Mix and matches in a complete 4-in. wafer level are pictured in Fig.2.16 in where 768 IND were elaborated.

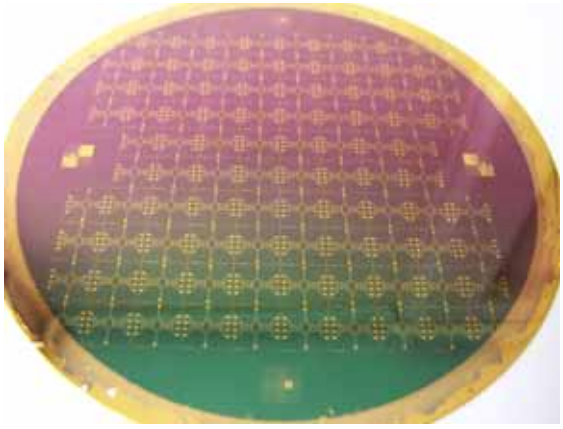

Fig.2.16. View of the full 4-inch wafer containing 796 IDA devices in 96 cells.

Two types of characterisation were performed on the resulting devices over the whole wafer. First, a SEM characterisation to visualise and measure the resulting device structures at different zones of the wafer. Second, electrical characterisation at different zones of the bared devices was evaluated.

2.4.1 SEM characterisation

Fig. 2.17 pictures SEM images and zooms on the interdigitated nanoelectrode devices (IND) at four edges and in the centre of the wafer. The electronic dose used, in whole wafer, was 297μC/cm^2, what explains this range of the nanoelectrode widths.

As explained in the introduction, the Veeco 770 evaporator produces shadowing effects yielding poor step coverage. Despite this deposition problem, it was possible to increase the yield on the nanoelectrode realisation by decreasing the rate metal deposition form 20 Å/S down 2 Å/S. A possible reason is that coalescence in the metal is not enough rapid, thus the metal is deposited (enters) easier into the apertures.

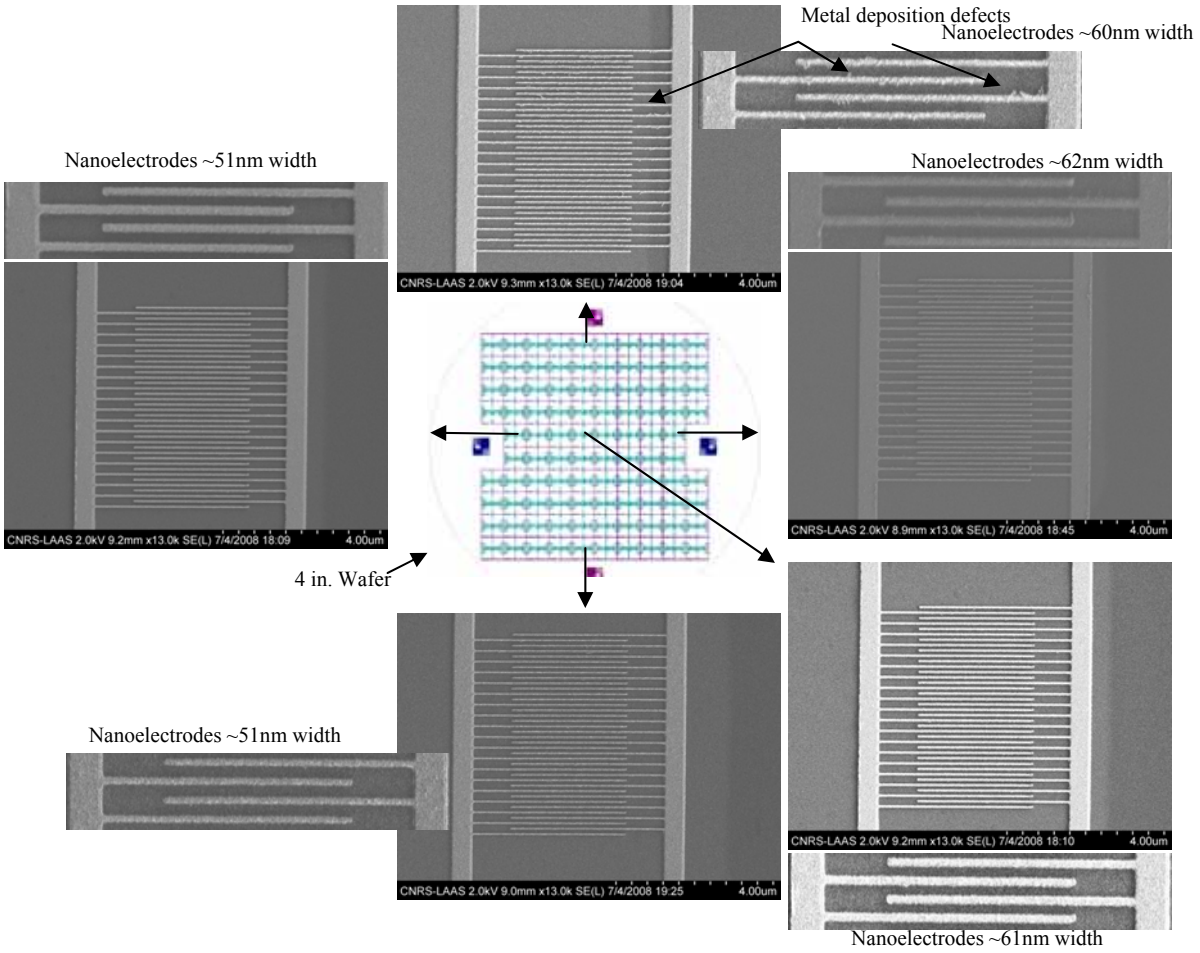

Fig. 2.17. IND variation in 4 in. wafer level. Some defects found at the top of the wafer.

These pictures revealed that some nanoelectrodes had defects at the wafer top side (from flat wafer side in the bottom.

Variations in nanoelectode widths were also found. For example nanoelectrodes obtained on the left and on the bottom of the wafer are ~51nm in width. At the top, in the middle and

on the right, nanoelectrodes are ~ 61 nm in width. However, 97% of them bear a resemblance, all of them are proper.

There are 768 IND in 4 in. wafer, and 97% proper IND were obtained at the final mix and match process thus considering the deposition method; this yield is acceptable.
Fig. 2.18 depicts a proper IND with nanoelectrodes width of 61 nm +-10% due to the above mentioned effects.

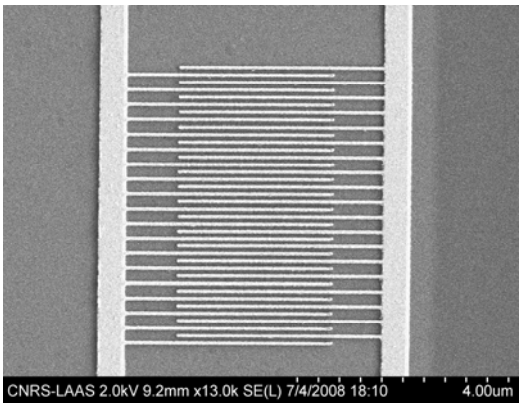

Fig.2.18. Proper interdigitated nanoelectode device ~61nm width each electrode (dose: 297μC/cm^2), obtained in the centre of the wafer.

2.4.2 Electrical characterisation of bare devices

In proper IND, elaborated on SiO_2 (dielectric constant of 3.7), the current passing between the interdigitated nanoelectrodes, is of the order of few femto amperes (fA) obtaining resistances of TOhm range.

Otherwise, as written in general introduction, at the nanometre scale some material properties change. Hence a metallic nanostructure below 1μm presents higher resistivity (in some nanostructures for exemple nanowires, the resistivity could decrease due to the surface scattering [19]). In any case there is a difference from its counterpart bulk metal. The resistivity of a gold bulk metal is ~2.5 μOhm.cm at 23°C, this resistivity could increase a hundred of times in a metallic nanostructure [23].

To know the resistivity in one nanoelectrode, intentionally a short circuited nanoelectrode was fabricated, thus an electric characterisation was conducted using a Cascade Microtech connected to a Keithley 4200-SCS. Classical four-point collinear probe method was used to determine the nanoelectrode resistivity. See fig. 2.19.

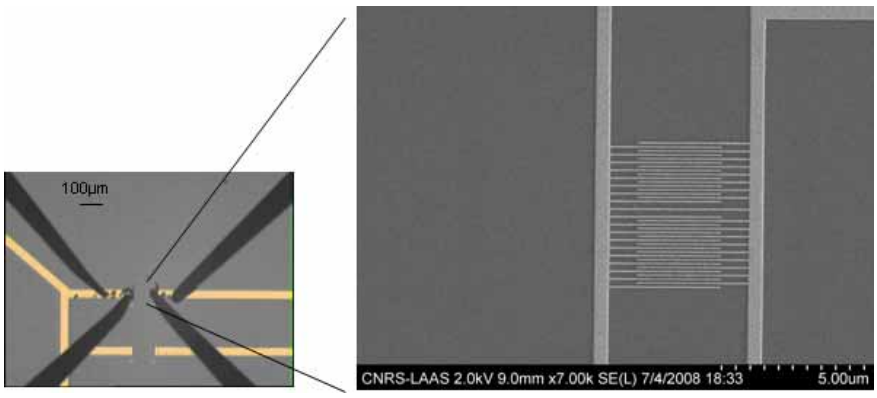

Fig.2.19. Four-point collinear probe method and SEM picture of the short circuited nanoelectrode.

A current was swept from 0A to 50µA with steps of 1µA, in the short-circuited nanoelectrode, finding for each step a potential difference, and calculating for each value a resistance of 6.7 kOhm. See Fig.2.20.

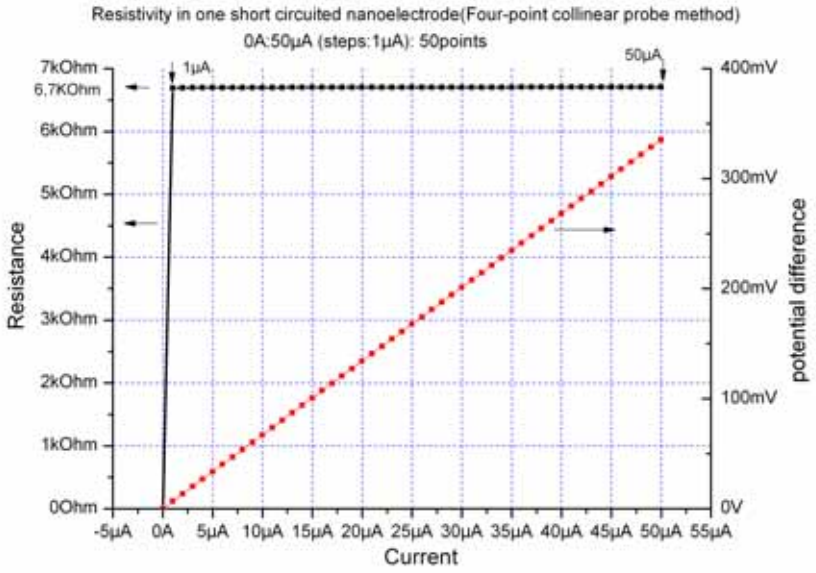

Fig.2.20. Electical response of a bare short-circuited nanoelectrode.

Considering that the length of the nanoelectrode as 4µm and the cross sectional area defined as width x thickness as 46 nm and 20 nm (Ti/Au-10nm/20nm) respectively, the obtained resistivity is around ~230µOhm.cm at 23°C. This is orders of magnitude higher than the resistivity of a bulk gold metal. As expected, since resistivity increases in metallic nanostructures due to the increased surface scattering which plays an enormous role in nanostructures. At this scale the polycrystalline metal is modified thus there are defects which can modify the mean free path of electrons and then if the nanostructures are smaller than the mean free path of electrons (a few nanometres in metals), the motion of electrons is modified or interrupted due to collision with the surface [19].

2.5 Conclusions

In this chapter we demonstrated the elaboration of interdigitated nanoelectrode devices (IND) on entire 4 in. wafer by using a mix and match process with high reproducibility. 97% successful IND were elaborated at wafer level (4 in wafer). The technique consisting in mixing and matching patterns realised in photolithography and in electronic lithography. The strategy was to use write field alignment marks placed in each cell and the 4 wafer alignment marks placed at the edge of the wafer to align and realise the IND.

We were able to compensate for the proximity effects that are inevitable when using EBL. This compensation was achieved by lengthening the devices connections. Then a dose study was conducted by constructing an IND column. Thanks to this study we were able to find the optimum electronic dose for the entire wafer level. However, due to our deposition technique, some defects and width variations of nanoelectrodes were found. In spite of this drawback, we increased the yield by lowering the metal deposition rate. Each cell was successfully encapsulated into TO-8 case as Fig.2.21 illustrates

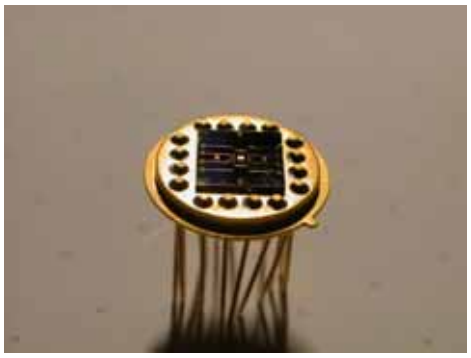

Fig.2.21. One cell with IDA devices encapsulated, into a TO-8 case.

Finally, in properly formed devices (bare IND, what means without nanoislands or biomolecules deposited between their gaps some electrical characterisation were realised). Electrical characterisations in proper IND gave TOhm values, demonstrating good insulating properties of the SiO_2 between nanoelectrodes. The estimation of the resistivity in one short circuited nanoelectrode was also conducted. This permitted us to corroborate that resistivity in metallic nanostructures is a hundred time higher that in bulk gold. This value will be use when comparing the devices after depositing nano-islands between the gaps of interdigitated nanoelectrodes. In fact, we will see in chapter 3, that at certain conditions, nanoislands could produce short-circuits and this will be avoided.

2.6 References

[1] Montelius L., Heidari B., Graczyk M., "Nanoimprint and UV-lithography: Mix and Match process for fabrication of interdigitated nano biosensors", *Microelec. Eng*., **2000**,53, p.521-524.

[2] Carcenac Franck, Malaquin Laurent, Vieu Christophe, "Fabrication of multiple nano-electrodes for molecular addressing using high-resolution electron beam lithography and their replication using soft imprint lithography", *Microelec. Eng.,* **2002**, 61, p.657-663.

[3] Tallal J.,. Peyrade D, Lazzarino F., "Replication of sub-40 nm gap nanoelectrodes over an 8-in. substrate by nanoimprint lithography", *Microelec. Eng*., **2005**, 78, p. 676-681.

[4] Liu K., Avouris P., Bucchignano J., et al., "Simple fabrication scheme for sub-10nm electrodes gaps using electron beam lithography", *Appl. Phys. Lett.*, **2002**, 80, p.865-867.

[5] Ressier L., Grisolia J., Martin C., et al., "Fabrication of planar cobalt electrodes separated by a sub-10 gap using high resolution electron beam lithography with negative PMMA", *Ultramicroscopy*, **2007,** 107, p.985-988.

[6] Errachid A., Mills C.A., Pla-Roca M., et al., "Focused ion beam production of nanoelectrodes arrays" *Mater. Sci. and Eng. C*, **2008**, 28, p. 777 -780.

[7] Reed M. A., Zhou C., Muller C. J., et al.,"Conductance of a molecular junction", *Science,* **1997**, 278, p. 252-253.

[8] Fritzsche Wolfgang, Böhm Konrad, Unger Eberhard, et al., "Making electrical contact", *Nanotechnology,* **1998**, 9, p. 177-183.

[9] Nitzan Abraham**,** M. A. Ratner Mark A.**, "**Electron Transport in Molecular Wire Junctions", *Science,* **2003**, 300:5624, p.1384-1389.

[10] Gerwen Peter Van, Laureyn Wim, Laureys Wim, "Nanoscale interdigitaed electrode arrays for biochemical sensors", *Sensor and Actuators B*, **1998**, 49, p-73-80.

[11] Laureyn W., Nelis D., Van Gerwen P., "Nanoscale interdigitated titanium electrodes for impedimetric biosensing", *Sensor and Actuators A, **2000***, 68**,** p. 360-370.

[12] Zhiwei Zou, Junhai Kai, Michael J. Rust, et al., "Functionalized nanointerdigitated electrodes arrays on polymer with interdigitated microfluidic for bio-affinity sensing using impedimetric measurement", *Sensor and Actuators A,* **2007**,136, p.518-526.

[13] Finot Eric, Bourillot Eric, Meunier-Prest Rita, et al., "Performance of interdigitated nanoelectrodes for electrochemical DNA biosensor", *Ultramicroscopy,* **2003,** 97, p. 441-449.

[14**]** Xiaoshan Zhu, Chong H. Ahn, "Electrochemical determination of reversible redox species at interdigitated array micro/nanoelectrodes using charge injection method", *IEEE Trans. on Nanobioscience, **2005**, 4:2, p-164169.*

[15**]** Daehli Skjolden L. H., Spegel C., Emnéus J., L. Montelius. Conf. MNE **2007**

[16**]** Malaquin Laurent, Vieu Christophe, Martinez Camilo, et al., "Interdigitated nanoelectodes for nanoparticles", *Nanotechnology,* **2005**, 16, p. S240-S245.

[17] Sze S.M., *Semiconductor sensor*, NewYork, John Wiley and Sons, Inc., **1994**, 1, 550p.

[18**]** Browman Ron, Griffin James, potter Dick, et al., *Advanced VLSI Fabrication,* Scottsdale USA, Integrated circuit corporation (ICE), **1995**, 600p.

[19**]** Cao GuoZhong, *Nanostructures and Nanomaterials: Synthesis, properties and applications*, London, imperial college press **2004**, 1, 433p.

[20**]** Yoshio Nishi, Robert Doering, *Handbook of semiconductor manufacturing technology*, Marcel Dekker, NY, **2000**, 1157p.

[21] Shu-Fen Hu, Ching-lung Sung, "Proximity effects of electron beam lithography for single-electron transistor fabrication" , *applied physic letters*, **2004**, 85:17,p.3893-3895.

[22] Goodberlet James G., Hasting J. Todd, Smith Henry I., "Performance of the Raith 150 electron-beam lithography systems", *J.Vas.Sci. Technol.,* **2001**, B 19(6), p.2499-2503.

[23] Fallou Michel, *Résitivité des métaux*, Techniques de l´ingénieur, **1988,** p**.** K710-1.

Chapter III

Wafer scale Ni nanoislands deposition and coulomb blockade mutitunnel junction devices at room temperature

3.1 Introduction

Over the last 40 years, ultrathin metal films, also called granular metal films, based on nanoislands (grains) have been studied [1]. They consist in metallic grains, embedded in an insulating surface like silicon dioxide (SiO_2). Electrical conductivity of granular films has been understood and explained [2-6]. Hence, nanoislands have been used for the elaboration of single electron transistor (SET) explained by Likharev Konstantin K. using orthodox theory [7]. Otherwise there are numerous deposition methods to elaborate nanoislands and to obtain discontinuous metal films, such as thermal evaporation [8-12], liquid metal ion source emission [13-14], sputtering [15], or low energy cluster beam deposition [16][17]. Electrical conduction by tunnelling effect, described in this chapter, has been observed in granular metal films. However the tunnelling conduction and coulomb blockade (CB) phenomena have been generally characterised and observed at temperatures lower than the room temperature (<300 K) [18-21], being a drawback for some applications. Recently, CB has been observed at room temperature but these devices have been characterised with a scanning tunnelling microscope (STM) [22], so the applications are limited to the use on vacuum environment, and obviously not for biomedical applications as we propose.

Otherwise, research of ferromagnetic granular films based on Ni, Co or Fe (nanoislands) has been performed [23-27] and some theories have been proposed [28-33] since the early tunnel junction measurements of Jullière [34]. Recently, the research of ferromagnetic granular films has been intensified, mainly after the discovery of the giant magnetoresitance (GMR) in thin films [35][36] (in fact, since 1972 the concept of giant magnetoresitance has been used and proved in granular Ni films, before the discovery of GMR in thin films [28]). Since then, an interest in studying ferromagnetic nanoislands has been grown in scientific community [37] and it has been found a spin-dependent tunnelling transport in these nanoislands [38], presenting superparamagnetism [39]. Novel phenomena have been found in granular films, such as tunnel magnetoresistance (TMR) [40], giant Hall effect (GHE) [41], giant electroresistance (GER) [42]. Indeed, some applications are envisaged, mainly for the future molecular electronics, for ultrahigh-density magnetic recording media to reach the range of 1 Tb/in^2 [43], for spin-based devices (spintronics) or magnetroelectonics [44] or for novel single electron transistors (SET) [45] [46] derived from coulomb blockade.

In this chapter, Ni nanoislands (~5nm) are deposited by thermal evaporation. Then, tunnelling electric conduction through Ni nanoislands is obtained. Ni nanoislands are deposited between interdigitated nanoelectrodes, obtaining Coulomb blockade at room temperature.

However, in this chapter, first some concepts are briefly introduced, such as nucleation, vacuum, tunnelling electric conduction, tunnel junction, double junction tunnel, nanoislands, multiple tunnel junction and coulomb blockade.

3.1.1 Nucleation modes

To deposit ultrathin films at nanometre scale; i.e. to form nanosislands, the initial nucleation is very important. Three basic nucleation modes have been observed [47]:

(1) Island or Volmer-Weber growth
(2) Layer or Frank-van der Merwe growth
(3) Islands-layer or Stranski-Krastonov growth.

Fig. 3.1 illustrates the three modes of nucleation in the film growth. An *island (Volmer-Weber)* growth occurs when the atoms or molecules are more strongly attracted and bonded to each other than to the surface (involving metal bonds described in chapter 1). If subsequent growth is formed, then islands are coalesced to form a continuous film. It is precisely the regime used in this chapter to elaborate Ni nanoislands to find tunnel conduction and coulomb blockade phenomena.

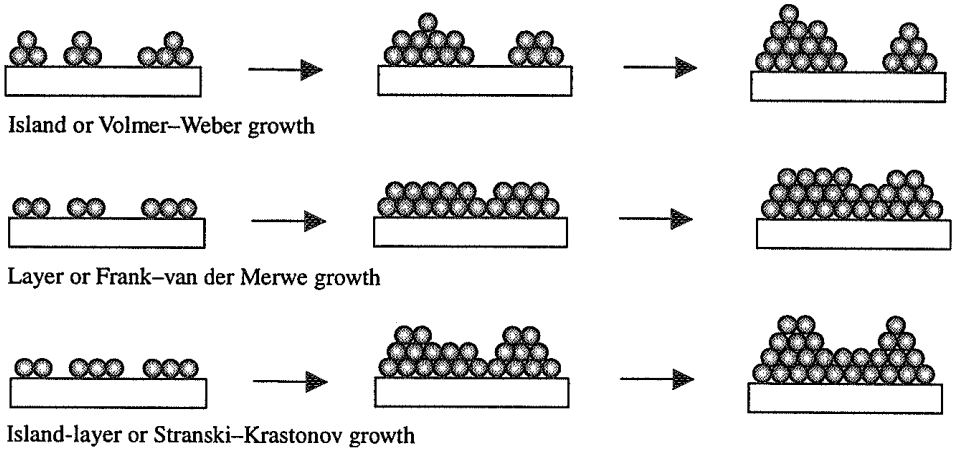

Fig.3.1. Schematic illustrating the three basic modes of nucleation in the film growth (picture from [48]).

Contrary to island growth is the *layer (Franck-van der Merwe)* growth, where the atoms or molecules are more strongly attracted and bonded to the surface that to each other. In this case a continuous film is formed just before the second deposited layer appears. The last nucleation mode illustrated in the Fig. 3.1, is the *islands-layer (Stranski-layer)* growth which is an intermediate mode between the layer growth and island growth. In this mode, the stress is involved during the film formation or nuclei formation.

3.1.2 Fundamental of heterogeneous nucleation (island or Volmer-Weber growth)

Here, islands growth is described in detail because it is the closest regime that fits with our Ni nanoslands realisation.

A heterogeneous nucleation process is formed when one material is formed on another material. If an island growth on a planar solid substrate is considered, and if it is assumed that growth species in the vapour phase strike the surface, then growth species diffuse and aggregate, forming a nucleus which has a shape like illustrated in Fig. 3.2.

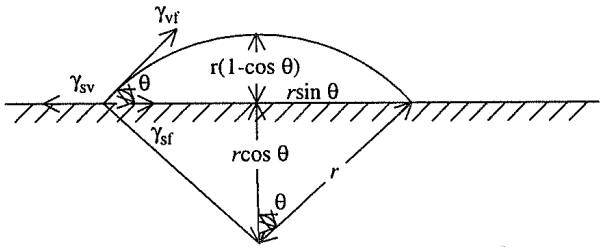

Fig.3.2. Heterogeneous nucleation process, picture from [48]).

In heterogeneous nucleation, Gibbs free energy decreases and the interface energy increases. In these conditions, chemical energy, ΔG, is completely changed, and is associated with the formation of heterogeneous nucleus, thus ΔG is given by (from [2]):

$$\Delta G = a_3 r^3 \Delta\mu_v + a_1 r^2 \gamma_{vf} + a_2 r^2 \gamma_{fs} - a_2 r^2 \gamma_{sv} \qquad \text{eq. [1]}$$

r is the nucleus mean dimension, $\Delta\boldsymbol{\mu}_{\mathbf{v}}$ is the change of Gibbs free energy per unit volume, $\boldsymbol{\gamma}_{\mathbf{vf}}$ is the surface or interface energy of vapour-nucleus, $\boldsymbol{\gamma}_{\mathbf{fs}}$ is the nucleus-substrate and $\boldsymbol{\gamma}_{\mathbf{sv}}$ substrate-vapour interface. The geometric constants are written:

$$a_1 = 2\pi(1-\cos\theta); a_2 = \pi\sin^2\theta; a_3 = 3\pi(2-3\cos\theta+\cos^2\theta) \qquad \text{eq. [2]}$$

Contact angle (θ) is defined by Young-dupré equation:

$$\gamma_{sv} = \gamma_{fs} + \gamma_{vf}\cos\theta \qquad \text{eq. [3]}$$

This concept is important and useful in nanotechnology, mainly to characterise the contact angle (angle at which a liquid/vapour interface meets the solid surface). Contact angle permits to know the degree of hydrophobicity or hydrophilicity of a surface. The principle is found in some commercial machines to characterise directly the contact angle of the surfaces. A machine using this principle is presented in chapter 4 to verify the proposed surface chemistry.

If the nucleus is larger than a critical size (r^*), it is stable. The critical energy ΔG^* and the r^* are given by (after substituting all geometric constants of eq. 2), from [48]:

$$r^* = \frac{2\pi\gamma_{vf}}{\Delta G_v}\left\{\frac{\sin^2 * \cos\theta + 2\cos\theta - 2}{2-3\cos\theta+\cos^3\theta}\right\} \qquad \text{eq. [4]}$$

$$\Delta G^* = \left\{\frac{16\pi\gamma_{vf}}{3(\Delta G_v)^2}\right\}\left\{\frac{2-3\cos\theta+\cos^3\theta}{4}\right\} \qquad \text{eq. [5]}$$

The first term refers to the value of the critical energy barrier for homogenous nucleation, and the second refers to a wetting factor. For nanoislands growth, synthesis of nanoparticles or quantum dot deposited onto a substrate, the contact angle must be larger than zero, i.e. θ >0 and less than 180°. Heterogeneous nucleation is referred to as islands growth or Volmer-Weber growth, and then, the Young-dupré equation becomes [48]:

$$\gamma_{sv} < \gamma_{fs} + \gamma_{vf} \qquad \text{eq. [6]}$$

If the deposition does not wet the substrate at all ($\theta = 180^{\circ}$), the nucleation is a homogenous nucleation. Finally, for layer growth, the deposit wets the substrate completely and then the angles value equals zero (the same conceptual phenomenon functions for a simple drop of water formed on a surface), in this case the corresponding young dupré equation becomes:

$$\gamma_{sv} = \gamma_{fs} + \gamma_{vf} \qquad \text{eq. [7]}$$

These concepts are commonly used in the thin film scientific community.

3.1.3 Basic vacuum introduction

The evaporation method described in chapter 2, is the technique employed here to deposit the Ni nanoislands. Generally, in the evaporation technique, some concepts are utilised, as vacuum or mean free path. Indeed, most films deposition and processing are performed in a vacuum. A *vacuum* is a volume space that is essentially "empty" of matter, ideally there are not molecules, thus any matter but normally there are (a philosophical paradigm studied since Blaise Pascal). The vacuum is necessary to permit, ideally, to the deposited atoms and molecules to impinge only the surface. Then, in a vacuum chamber a low pressure exists comparing to that of the atmosphere. Pressure has Pascal as unit of measure (international system) but historically it is used the Torr or mbar. Finally, *mean free* path is the average distance than a molecule travels before striking another molecule.

3.1.4 Tunnelling effect and Coulomb blockade phenomenon

Tunnelling effect is a phenomenon predicted by quantum physics, that "violates" the principle of the classical physics, because a particle passes through a potential barrier or impedance that is higher than its kinetic energy. Fig. 3.3 schematises the tunnelling effect (quantum physics) in comparison with the classical physics.

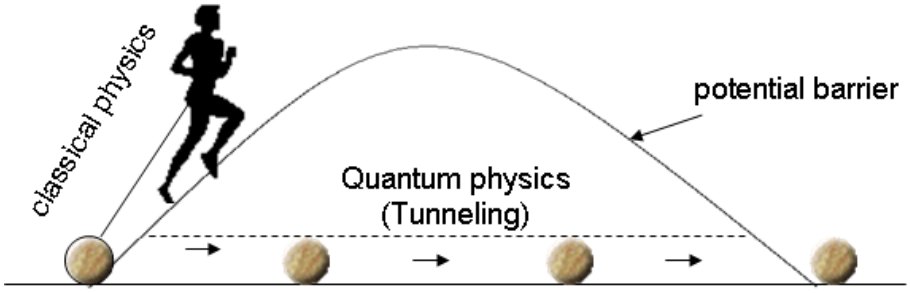

Fig.3.3. Comparing tunnel effect (quantum physics) with classical physics.

A **tunnel junction** is formed when two conductors are separated by a potential barrier, generally an insulator but thanks to its physical and geometrical arrangement, a charge is able to penetrate this barrier by tunnelling effect, hence there are charge effects. These effects are the base of all the charge electronics thus the molecular electronics. Phenomenological speaking, the tunnel junction is a duality: capacitor/resistance which means that a junction tunnel is neither a capacitor nor a resistance but both of them, without being both at the same time. Similar to wave/particle duality of wave-corpuscular theory. Fig. 3.4 illustrates a tunnel junction, and its phenomenological electrical model.

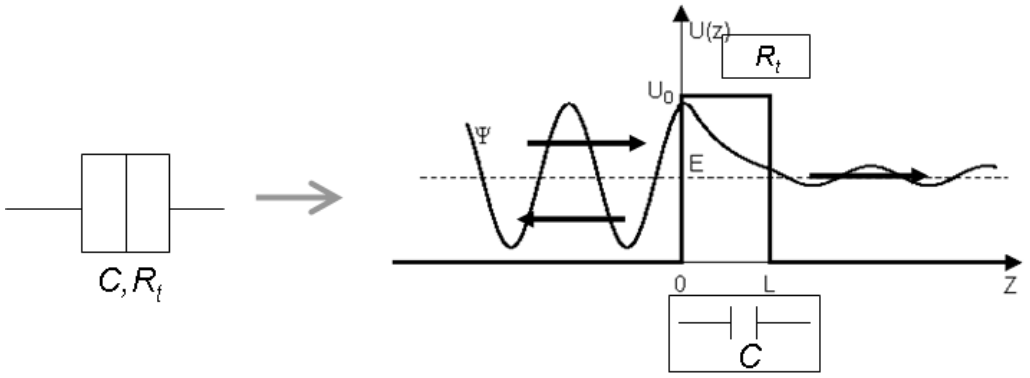

Fig.3.4. A junction tunnel (capacitor/ resistance duality).

On the other hand, in *electrical tunnelling conduction* exists a probability for an electron on one side of a barrier to reach the other side, this probably is characterised by the state function obeying the Schrödinger wave equation given by:

$$i\hbar \frac{\partial \psi(r, t)}{\partial t} = \hat{H} \psi(r, t) \qquad \text{eq. [8]}$$

Where Ψ (r,t) is the wave function of the electron. The modulus square of the state function $|\Psi|^2$ determines the probability density to observe a particle in space. The potential barrier is characterised by its transmission coefficient T. It is an important parameter given by:

$$T = \frac{(2K\kappa)^2}{(K^2+\kappa^2)^2 \sinh^2(2a\kappa) + (2K\kappa)^2} \qquad \text{eq. [9]}$$

$$\text{Where } K = \sqrt{\frac{2mE}{\hbar^2}} \qquad \text{eq. [10]}$$

$$\text{And } \kappa = \sqrt{\frac{2m}{\hbar^2}(V_o - E)} \qquad \text{eq. [11]}$$

T depends on the height potential barrier (V_o) (U_o in Fig. 3.4) and its width 2a (L in Fig.3.4).

Tunnelling electric conduction involves a charge transport through an insulation medium separating two conductors which are closely separated (nanometre separation, that is why it is know as nanoscopic phenomenon). In this case the tunnel resistance is inversely proportional to the barrier transmission coefficient thus T decreases exponentially with the thickness of the insulation medium [45].

Scanning tunnelling microscope (STM) employed to image single molecules or to manipulate atoms or molecules is based on the concept of this tunnelling quantum phenomenon. See Fig.3.5.

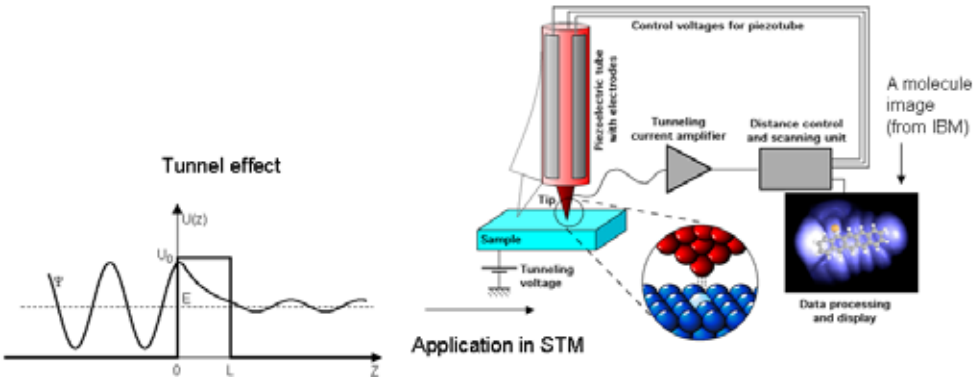

Fig.3.5. Tunnel effect, an application in scanning tunnelling microscope (STM)(adapted from Wikipedia.com).

3.1.5 Double junction tunnel and multiple tunnel junctions

From the written above, a *double tunnel junction* is created when two tunnel junctions are closely positioned in series. It this case, island concept emmerges and for obtaining a tunnelling electrical conduction, a nanoisland is necessary. Then a *nanoisland* is an integral nanoconductor zone, coupled electrostatically but insulated galvanically. Fig. 3.6 illustrates the double junction. It illustrates the nanoislad concept and its electrical scheme where n_1 is the number of electrons penetrating the first junction, by tunnel effect, and entering the island. n_2 is the number of electrons, penetrating the second junction, by tunnel effect, and exiting the island. Then, total number of electrons is $n=n_1-n_2$. If C_1, Rt_1, V_1 and C_2, Rt_2, V_2 are the capacitance, resistance and potential of the junction one and two respectively, q_0 is initial charge in the island (it is a non-integer value due to parasitic capacitances or impurities close to island) thus the charge in junction one is $q_1=C_1V_1=n_1e$, and the charge in junction two is $q_2= C_2V_2=n_2e$, finally the total charge becomes $q=q_2-q_1+q_0=-ne+q_0$. The total potential is $V_b=V_1+V_2$, if $V_1=C_2V_b+ne/C_1+C_2$ and $V_2=C_1V_b-ne/C_1+C_2$. The electrostatic energy stored in the double junction is $E_c= q_1^2/2C_1+ q_2^2/2C_2$ or $E_c= C_1C_2V_b + (ne)/2C_1+C_2$.

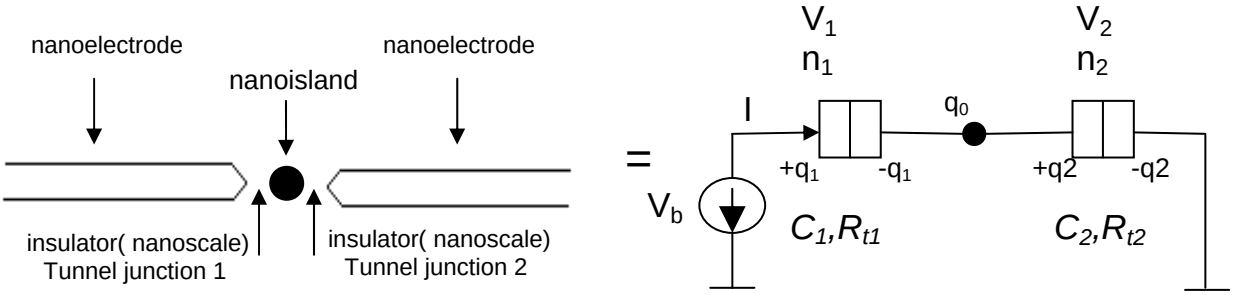

Fig.3.6. One double junction schema and its electrical circuit.

These systems have been investigated both theoretically by M. Likharev [7] and experimentally, for example, by M. Devoret [45]. It is now well established that the Coulomb repulsion in such nanometric islands plays a crucial role and can inhibit tunnelling across the different junctions. The charging energy (E_c) of the island can be expressed as $e^2/2C$ where e is the electron charge and C is the capacitance of the island. Thermal agitation (thermal energy) is expressed as k_BT where k_B is Boltzmann constant, T is absolute temperature.

If thermal energy is below this electrostatic (charging) energy ($k_BT << e^2/2C$), tunnelling effect is reduced and then no current can flow through the device, this phenomenon is

described as **Coulomb blockade effect**. A schema of an ideal symmetrical double junction (when $C_1Rt_1=C_2Rt_2$) is illustrated in Fig. 3.7(a), in where at low bias, there is zero conductance regime. The voltage range where the current is blocked is called the **Coulomb gap**; it goes from $-e^2/2C$ to $e^2/2C$. For strongly not symmetrical double tunnel junction (e.g. $C_1Rt_1>>C_2Rt_2$) the I(V) characteristic exhibits staircases at lower temperatures as illustrated in Fig. 3.7(b). When the temperature of the devices increases, the staircase and the coulomb gap features are smoothed because the $K_BT>> E_c$, nevertheless to observe tunnelling effects, it is necessary that $E_c >>K_BT$ (otherwise thermal fluctuations avoid single-electron effects). Then, to observe tunnelling effects, at room temperature, it is necessary that the nanoislands are of nanometric size.

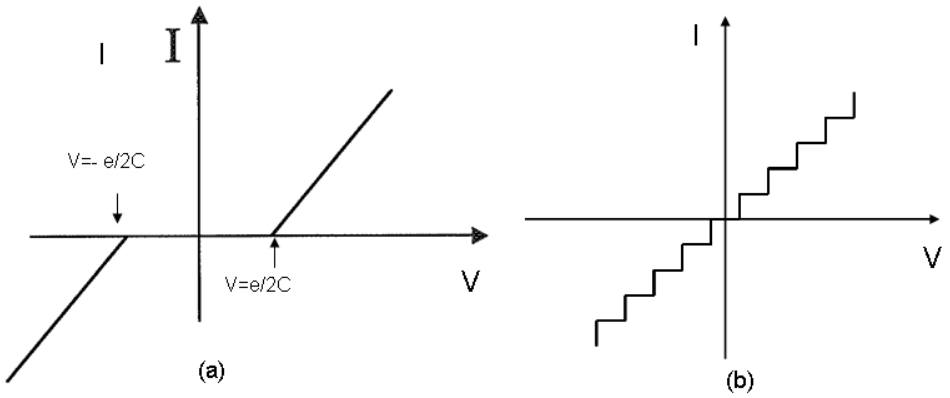

Fig.3.7. Characteristics of (a) ideal symmetrical double junction ($C_1Rt_1=C_2Rt_2$), (b) ideal asymmetrical double junction ($C_1Rt_1>>C_2Rt_2$).

Likharev [7] has calculated the E_c and island's self capacitance (C) as a function of the island diameter (barrier thickness of 2nm). Curves are presented in Fig.3.8.

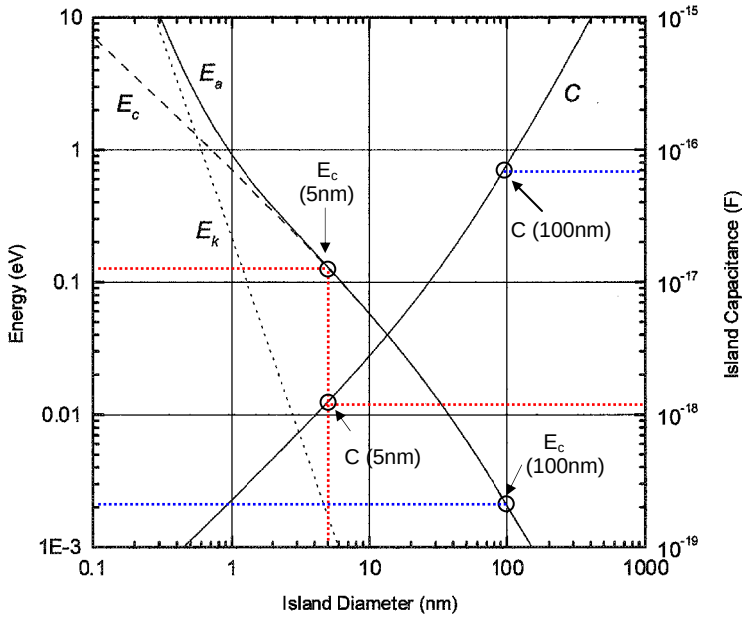

Fig.3.8. Charging energy (Ec), Single-electron energy addition (Ea), Electron kinetic energy (Ek) and islands self capacitance (C) as a function of the island diameter (with island round, barrier thickness of 2nm and dielectric constant $\varepsilon_r=4$,). Adapted from [7].

If we consider that Ec > $5k_BT$ to observe tunnelling effects, at room temperature, and if we would have an island with 100nm in diameter, the charge energy would be of the order of ~1 meV (see Fig.3.8.). Then to observe tunnelling effects, the experimental temperature would be at 10K. On the contrary, if the nanoisland is of the order of 5 nm, its charge energy is more than 100 meV (see Fig.3.8) and tunnelling effects are observable at room temperature. We can conclude that to observe tunnelling effects, it is necessary that the (metallic) islands be below 6 nm, and have a tunnel junction thickness of ~2 nm. Finally, from the Fig.3.8, the 5nm island has a self capacitance of ~10^{-18} F (1aF) and a 100nm island has a self capacitance of ~10^{-16} F (100aF).

To observe single-electron effects at room temperature, a practical double tunnel junction using an STM was employed by Graf H. et al. [22]. A schema is pictured in Fig. 3.9(a). In this experimental work, a double tunnel junction is formed. One tunnel junction corresponding to a UHV-STM (omicron micro-STM) was placed above Co nanoclusters (nanoislands) and the other tunnel junction corresponding to a thin film of Al_3O_3 (1nm-2nm thick). Fig. 3.9(b) shows the I-V plots taken at room temperature. It demonstrates the dependence of the coulomb blockade gap width on the Co nanoclusters size. Plots characterise the I-V of three Co nanoclusters sizes (4.1nm, 3.0nm, and 3.5nm). They concluded about the fact that if the nanoclusters size decreases the coulomb gap widens, what it means that the nanoislands' (nanoclusters') self-capacitance decreases and the charging energy increases. We observe that Coulomb blockade behaviour is characterised by low capacitance tunnel junction and an important resistance in the low-voltage region of the non-linear I (V) curve.

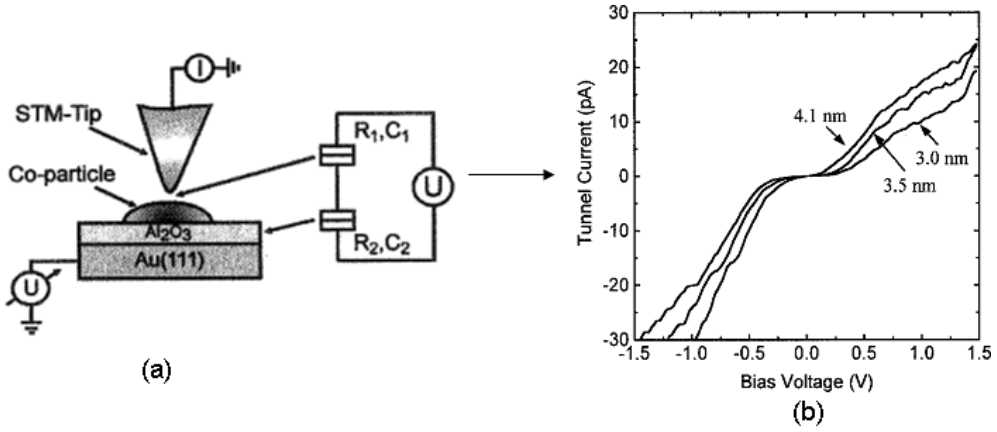

Fig.3.9. (a) Experimental work of a double junction with a STM, (b) I-V plots for 3 nanoislands sizes [22].

Concerning our experimental devices, the electrical conduction through the nanoelectrodes will involve many multi tunnel junctions (MTJ), having numerous disordered Ni nanoislands with size variations. It has been found that in this case, the staircase features vanish and MTJ feature resembles to double tunnel junctions [51].

*A **Multi-Tunnel-Junction (MTJ)*** consists in numerous tunnel junctions arranged in series and parallel way. In these devices coulomb blockade effect have been found mainly at temperatures lower that the ambient temperature. However, because of its complexity, the application of the orthodox theory for describing its electrical conduction requires also computational techniques such as SIMON code. Then, **Coulomb blockade** (Coulomb charging) occurs when the contact resistance is larger than the resistance of nanostructures used to make the contact and when the total capacitance of the nanoislands (nano-objects) is so small (capacitances down 1 aF) that adding single electrons requires significant charging

energy. Fig. 3.10 illustrates a multiple tunnel junction schema used in a Monte Carlo simulation [52], its electric schema representation [53] and an experimental MTJ [51].

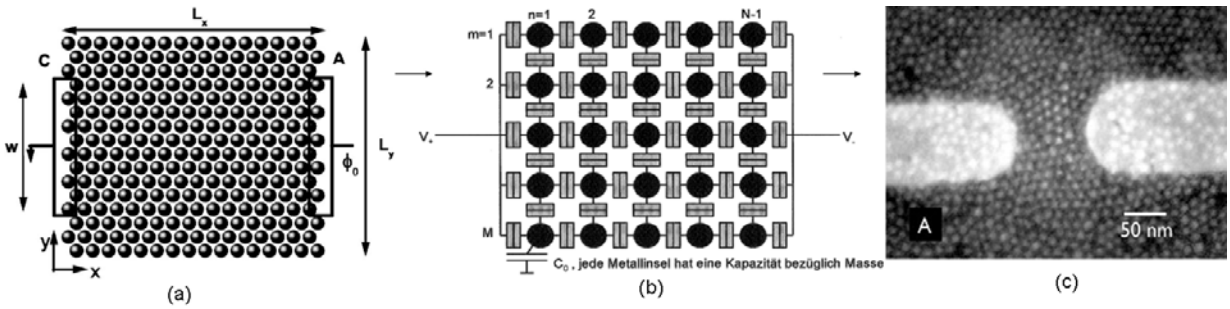

Fig.3.10. Simulation by Monte Carlo method [52], electric schema representation [53], a practical MTJ [51].

The practical MTJ pictured in Fig. 3.10 (c) was used to characterise spin dependant electron transport in 10-nm cobalt islands, its I-V characteristic is illustrated in Fig 3.11(a). Coulomb blockade is found, at a temperature of 2K, however for higher temperatures the curves become non-linear, near zero bias. At 70K the phenomenon disappears and at 300K the I-V is linear, with a resistance of 100kOhm.

My advisor Christophe Vieu et al. demonstrated in 1998 coulomb blockade phenomena up to 200 K [14] and a non-linear current voltage characteristic up to room temperature (~297K). See Fig. 3.11 (b). Finally, MTJ structure are more preferable electrically than a simple double-junction because MTJ reduce co-tunnelling (co-tunnelling generally leads to undesirable leakage current) and MTJ are also robust against offset charge effects [58].

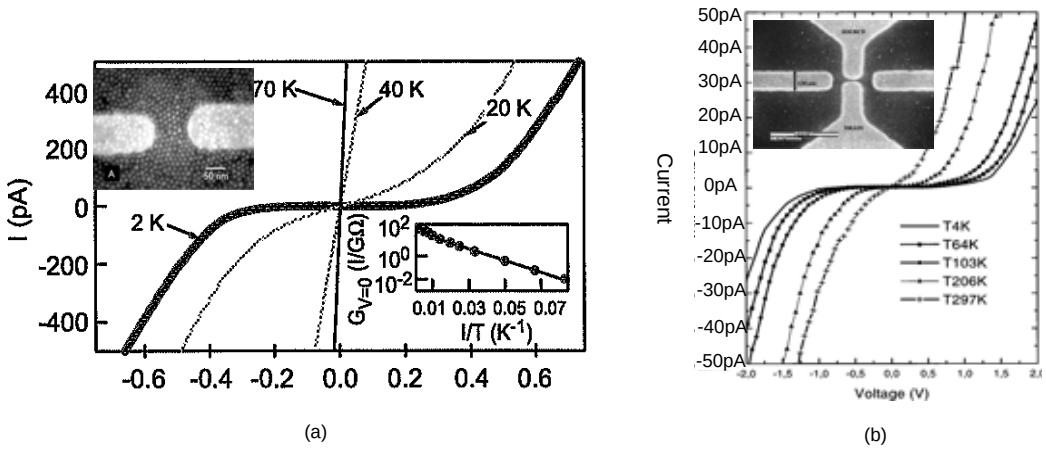

Fig.3.11. (a) is the I-V of the MJT, adapted from [51], (b) I-V in a SET, adapted from [14].

3.1.5.1 Ferromagnetic nanoislands

In the case the nanoislands are made of ferromagnetic metals like Fe, Co or Ni, other phenomena take place in tunnel junctions, such as tunnel magnetoresistance (TMR) [40] due to the spin dependant tunnelling conduction. As written in the introduction, the potential applications are in spintronics, spin-FET or magnoelectronics [44]. A non-ferromagnetic metal such as copper ("normal metal") has the same number of electron with up and down spins, thus it has non net magnetisation and its Fermi level is unpolarised [54]. In the case of ferromagnetic metals such as Co, Fe, Ni (3d), there is a splitting between the up and down

spin states called “exchange splitting”, thus it exists a spin imbalance [54]. Similar to semiconductors, in which there are majority carriers and minority carriers (electrons and holes) a ferromagnetic metal has up-majority spins and down-minority spins. See Fig. 3.12.

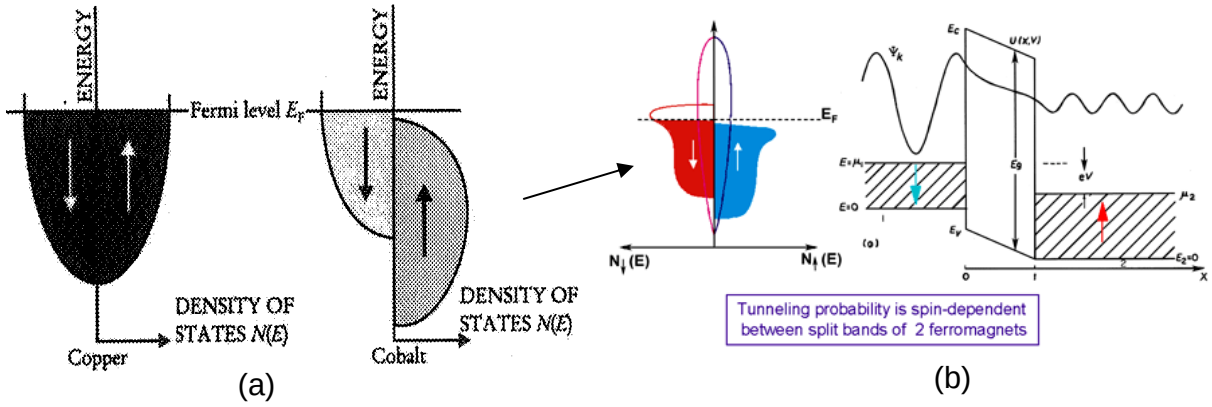

Fig.3.12. (a) Density of states N(E) in copper and cobalt, from [54], (b) Spin- dependant tunnelling in ferromagnetic metals (from Hitachi global storage, Inc).

An interesting application of the double junction tunnel or MTJ is in single electron devices (SET) explained by K. Likharev [7] with orthodox theory in which single electron tunnel effects are involved. These effects were demonstrated for the first time in granular metal films [61][62]. In the case of a SET using a not ferromagnetic island, two electrodes are closely positioned in series, functioning as drain and source respectively, thus another electrode is placed between the drain and source (called gate). It controls the potential thus the charges and the quantity of electrons passing through the nanoisland(s). Some practical works have been reported [18, 45]. Figure 3.13 illustrates a SET with a not ferromagnetic nanoisland and its electrical circuit.

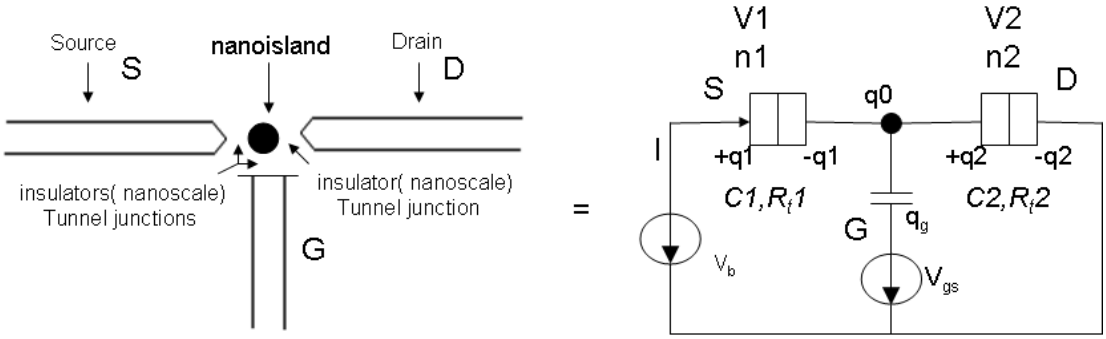

3.13. Schematic and electrical schemas of a typical SET.

In these devices, coulomb oscillations appear. Coulomb oscillations, explained by the statistical thermodynamics, are current oscillations due to the discreetness of the current flow. This current is modulated by the gate tension and then to observe coulomb oscillations, a graph is constructed by setting the drain current in the ordinate and the gate voltage in the abscissa.

When using a ferromagnetic nanoisland between the drain and source, the manipulation of single electrons is possible without using a gate but by using an external magnetic field [63]. In these Spin-SET devices, giant magnetoresistance has been observed, known as magnetoresistance of granular magnetic metal film (GMMF) [29], demonstrated by

Berkowitz et al. and Xiao et al [64][65]. Then the resistance decreases when an external magnetic field is applied since the field aligns the magnetic moment of the nanoisland(s). Works are reported mainly in Valet, Fert et al. [4][38].

In my work, however, I have used Ni nanoislands with the purpose of using Ni-histidine (amino acid) bonding, for attaching biomolecules to these metallic islands as a novel based methodology nanobiosensor realisation. We have not specially investigated the magnetic field effects expected in these kinds of tunnel junction devices made of ferromagnetic nanoislands such as spin dependent transport. However, I think that the devices I elaborated could lead to interesting experimental observations in the field of spinelectronics or spintronics.

3.2 Methods, material and experimental section

I wrote in chapter 1, that the first experience was to investigate parameters to obtain nanoislands made of gold, because Au nanoislands are easier to observe by scanning transmission electronic microscopy (SEM) and because from this study I would infer the parameters to obtain Ni nanoislands. We deposited Au on SiO_2 surfaces, using a Precision Etching Coating System (Model 682 PECS®) for Scanning Electron Microscope (SEM), Transmission Electron Microscope (TEM) and Light Microscope (LM) applications. The deposition observation was realised using a scanning transmission electron microscope (STEM) CM20-Philips. A typical image of nanoislands realisation, just before coalescence, (Volmer-Weber growth) is showed in different images of Fig 3.14. Fig. 3.14(c) shows a typical nucleation mode when a layer starts being formed (Islands-layer or Stranski-Krastonov growth). The Au nanoislands appear as small circular bright dots (3nm-5nm) in Fig. 3.14(a), or bigger bright dots (30nm-50nm) in Fig. 3.14(c). There is a part of SiO_2, in Fig. 3.14(b), where there are no Au nanoislands.

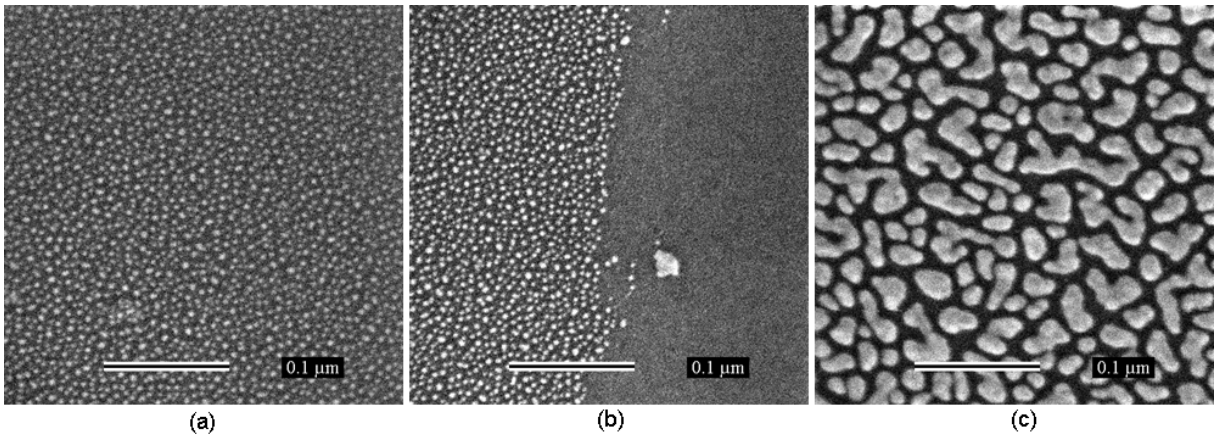

Fig.3.14. (a) Au depositions, (b) 0.7nm thick, (c) 1.6nm thick deposition.

In Fig. 3.14(a), a layer of nominal 0.7nm thickness was deposited at 4KeV ion beam energy and a 101µA ion current. In Fig. 3.14(b) we used the same parameters but one part of the surface (SiO_2) was covered with a piece of SiO_2 to verify the deposition properness. Fig. 3.14 (c) has a nominal 1.6 nm thickness at 4KeV ion beam energy and a 101µA. From these pictures we observe that, it is difficult to control the nucleation growth since the coalescence is made rapidly if few nominal nanometre depositions are subsequently deposited. However,

the study permitted us to infer that the optimum parameters to obtain nanoislands, separated each other from few nanometres, could be between 0.7nm and 1.6nm thickness deposition.

We wanted to realise nanodevices at wafer scale, and one of a disadvantage of the PECS is that just samples with 2.5 cm x 2.5 cm size can be entered, and only samples of 4 mm X 4 mm size could enter to (STEM) CM20-Philips. At this time our laboratory acquired an ultra-high resolution scanning transmission electronic microscope in which was possible to enter 4 in. wafers, so we decided to investigate the nucleation realisation using thermal evaporation. This technique available at LAAS, allowed us to enter 4 in. wafer to have at the same time 100 devices.

Hence, thermal evaporation method was employed to elaborate the Ni nanoislands. It is the same machine used in chapter 2: Veeco 770 thermal evaporator. On a silicon sample covered with 1µm (SiO_2) realised by thermal oxidation, was deposited ~1nm nickel at a pressure of ~10^{-6} mbars (~10^{-6} Torr) and a rate deposition of 0.2nm/s (optimum parameters determined after numerous tests). Nanoislands were observed by ultra-high resolution scanning electronic microscopy FE-SEM (Hitachi S-4800). Figure 3.15 pictures a typical image of a thin layer of Ni (nominal thickness of 1nm). The Ni nanoislands appear as small circular bright dots, exhibiting in average diameter of ~5 nm with a separation below ~ 2nm.

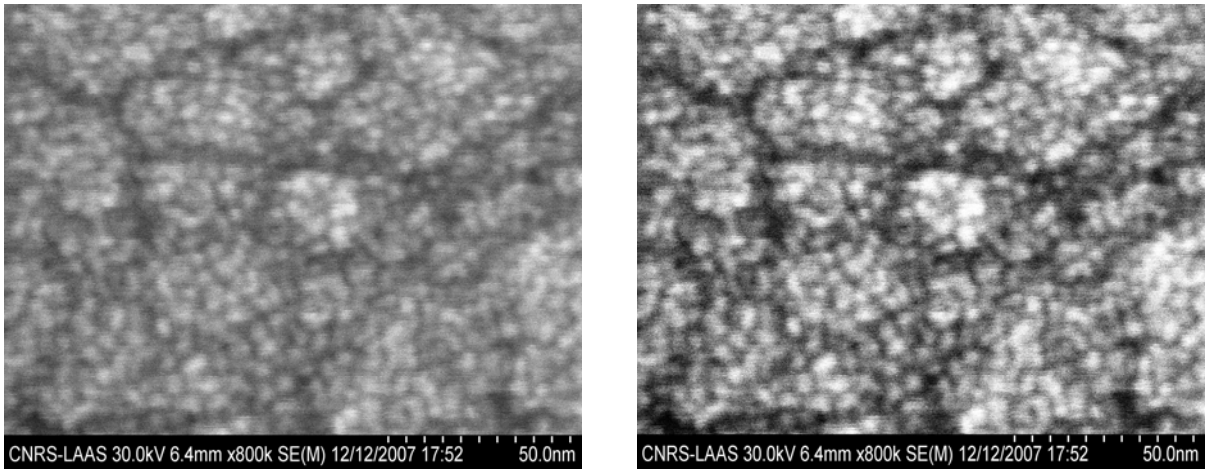

(a) (b)

Fig.3.15. (a) high resolution SEM image showing a typical Ni granular film deposited on SiO_2 (Ni nanoislands ~5nm), (a) treated SEM image for better contrast.

Atomic force microscopy (AFM, JPK nanowizard II, intermittent mode) was also employed for inferring from the morphology of these Ni films. The picture allowed us to characterise the Ni nanoislands height and to observe a homogenous deposition. A typical AFM image is shown in Fig.3.16. From the images, the Ni islands density deposition is very high and the height of the islands is below 5nm.

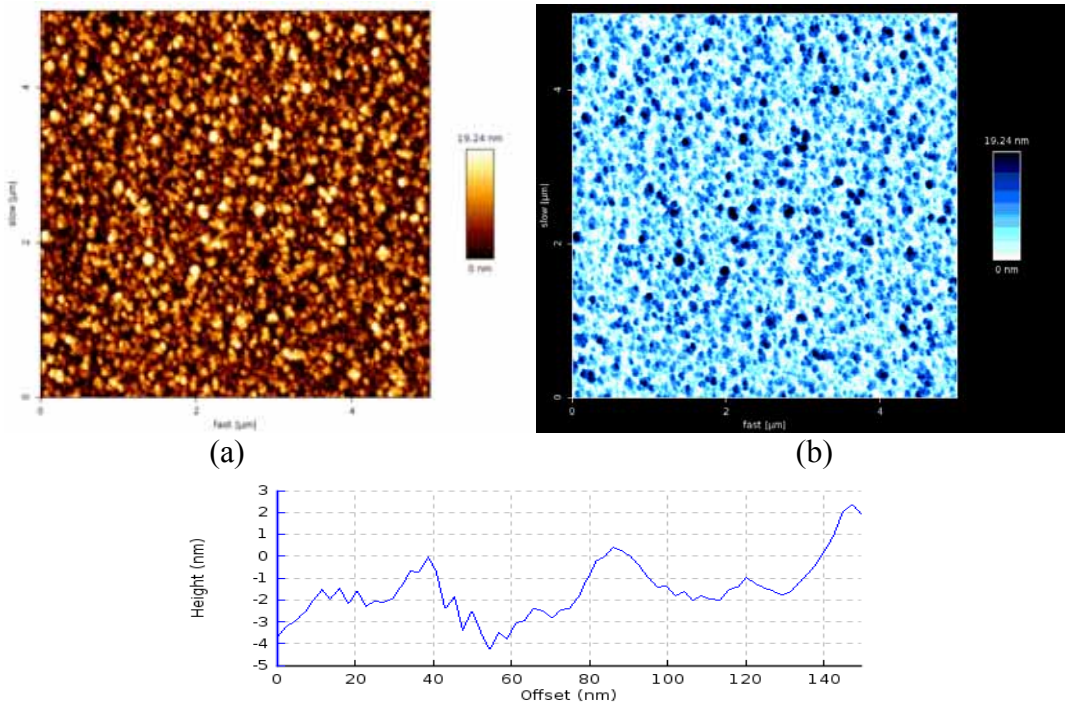

Fig.3.16. (a) AFM image showing Ni of ~5 nm in height, (b) image with inverted colours (for better appreciation).

Both SEM and AFM characterisations indicate that for this kind of nominal thickness (~1nm), the Ni film exhibits a 3D growth (Volmer-Weber growth) with a high density of islands just before coalescence. These films are excellent candidates for Coulomb blockade devices because of their size and their separation, being possible to observe tunnel effect at room temperature as demonstrated in the introduction section (see curves of Fig. 3.8).

3.3 Results and discussion

After Ni islands deposition between interdigitated nanoelectrodes, it was possible to measure the current flowing through the device at room temperature (RT). To do this, we used metallic probes of a Cascade Microtech station connected to a Keithley model 4200SCS. This machine measures current with a noise smaller than 10 fA. This kind of machine is necessary because our Multitunnel Junction devices (MTJ) present high resistances (~10^{10} Ohm), thus low current levels need to be detected.

Having fabricated full 4 in. wafers carrying 768 interdigitated nanoelectrodes devices (IND) on each wafer, some measurements were conducted but only a few are presented here and are the most representative. However, before characterising IND, we were interested in observing directly the electrical conduction through the Ni nanoislands, thus two electrical probes of the cascade station were positioned on the surface of a granular Ni deposition film. Note that, the distance between the 2 probes is larger than the typical size of the nanoislands. A plot is showed in fig.3.17. The voltage was swept between -2V and 2 V with increments steps of 5mV.

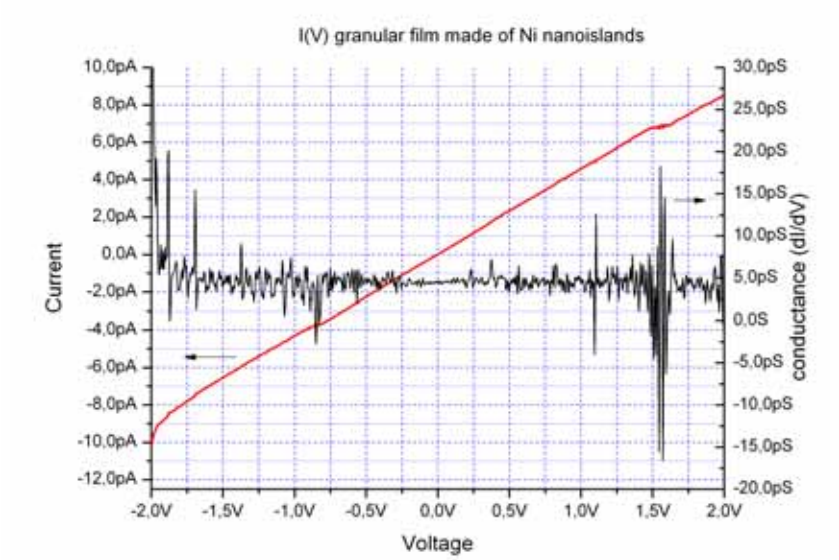

Fig.3.17. I (V) characteristic of a tunnelling electrical conduction thought Ni nanoislands. Conductance in siemens on the left (steps of 5mV:801 points).

The I(V) characteristic of the Ni granular film is linear and its electrical conductance is in the order of 10pS. This value is consistent with tunnel conduction through the different islands. However, because of its configuration, where there are not electrodes on the surface, there is not defined conduction path and then it is not possible to observe coulomb blockade effects.

Otherwise, we observed in this experience, an illumination sensitivity of the Ni deposition to the light. These effects are pictured in Fig. 3.18. The applied voltage bias was kept initially at 2V to reach the time stabilisation of the current flow I(t). We observed high reproducible current variations when the light of the optical microscope was turned off and turned on. See Fig. 3.18. When turning off the lamp, flowing current decrements rapidly (curve lowers) thus the current recovers its initial value in some seconds**.** When turning on the lamp, the opposite effect is similar, thus the current rapidly increases (curve rises), it is also stabilised in some seconds. Note that the microscope lamp is a halogen type that takes 2 seconds to be turned off and on. Another experience consisted of turning off and on subsequently the lamp (see the close-up on the right). The transient current are very reproducible for this condition (white illumination) with $\Delta I = \sim 1$ pA.

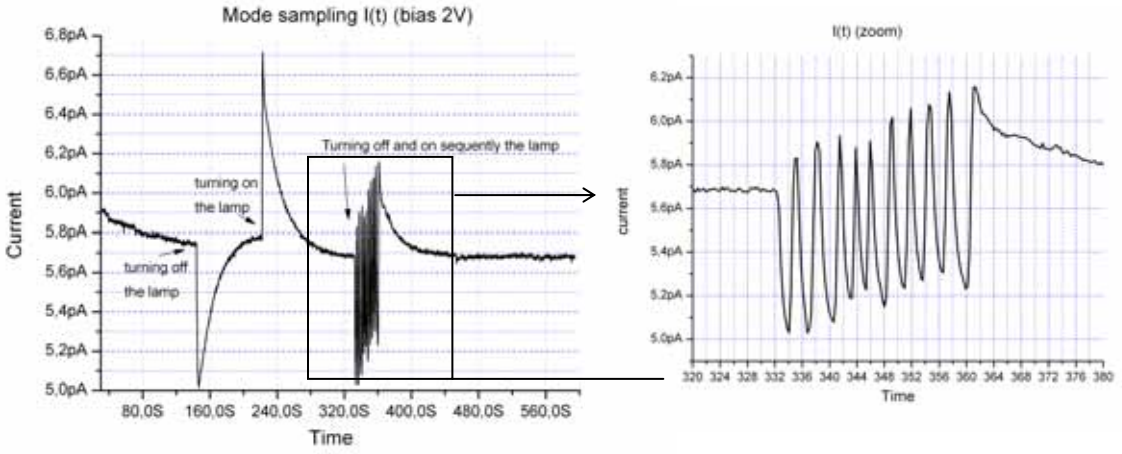

Fig.3.18. I(t) to know the current time stabilisation on Ni nanoislands tunnelling current. It shows also the influence of the light.

Other experience consisted of using a commercial laser pointer (<1mW, 630nm-680nm) to illuminate the granular film while flowing current though it (the laser was turned on and off manually). The excitation was performed at ~15 cm distance. Rapid and highly reproducible transient current responses are found. Two close-ups are pictured in Fig. 3.19. In the first transient current of Fig. 3.19 (a), the laser was turned on and off. The second wide transient current of the same figure is due to the fact that the laser was maintained in on condition for ~8 seconds. Another close-up is showed in the bottom, see Fig. 3.19 (b), in this case the pointer laser was turned on and off sequently and manually.

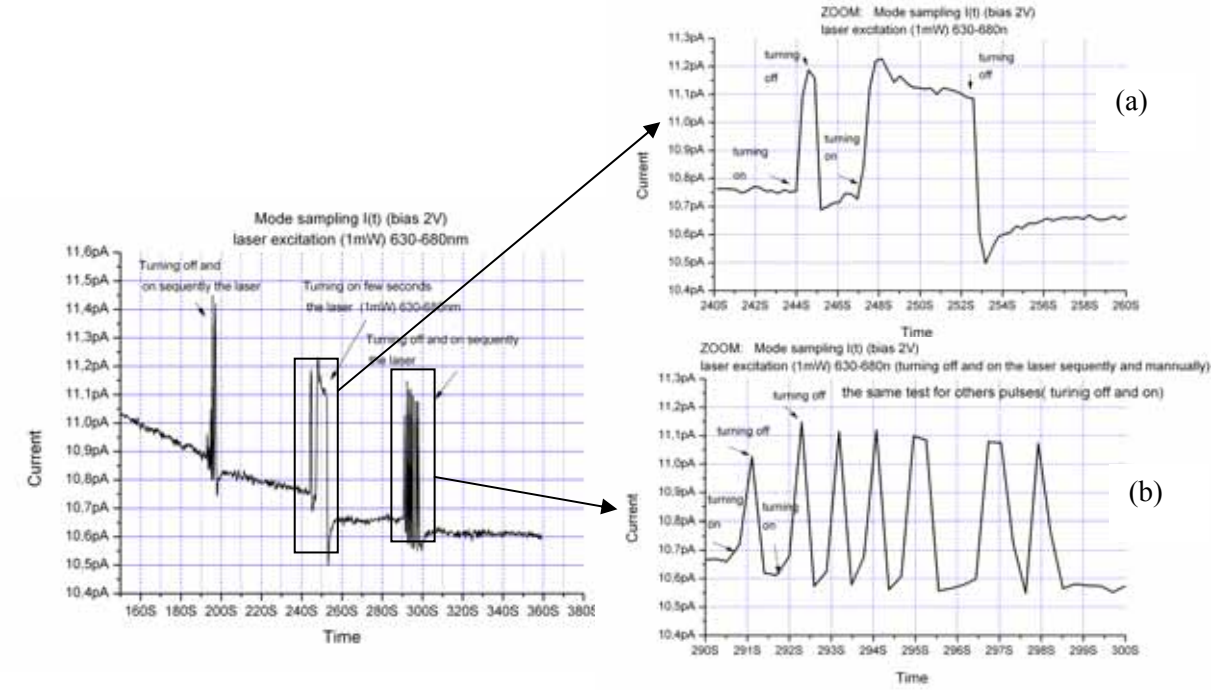

Fig.3.19. Ni nanoislands tunnelling current, with laser pointer excitation.

Lasr experience using the laser to excite the granular film while flowing current though it, consisted of turning on and turning off the laser in periodically manner. (Intervals periods in on and off conditions of around 8 s, performed manually). It is a reproducible response as Fig. 3.20 shows.

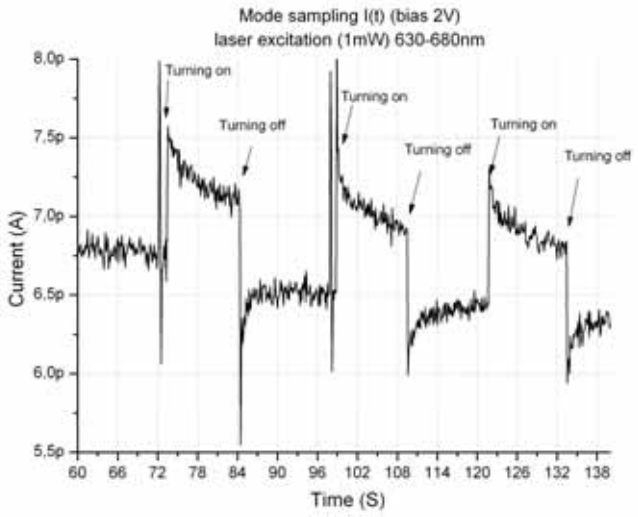

Fig.3.20. Ni nanoislands tunnelling current, with periodic laser pointer excitation.

The origin of this interesting phenomenon is unexpected and it is not understood. We think that charges induced by light are involved in the SiO_2 around the Ni nanoislands. The first graph (Fig. 3.18) (white illumination with halogen lamp, so various wavelengths) has a transient current behaviour, perhaps due to charges. The current reponses reproduce the response of the lamp (2 seconds). However when the device is excited with a unique wavelength (between 630nm-680nm), the transient gaps have different behaviour since its response is fast in both directions (modulating the current). This characteristic has a resemblance to photodetector response (photodiodes or phototransistor) which is rapid and high sensitive (not quantised yet) and apparently without leakage current (or extremely low).

Certainly other phenomena due to photon-electron are involved in these ferromagnetic nanoislands. More investigation is necessary, for exemple experiments to investigate the spin-charge dependant transport [64][65]. This is beyond the scope of this thesis, so we focused just on the observation of Coulomb blockade phenomenon, at room temperature.

To investigate the coulomb blockade phenomenon, we fabricated the IND as demonstrated in chapter 2. However, Ni nanoislands were deposited before the elaboration of nanoelectrodes. The reason is because when doing the contrary, that is first the elaboration of nanoelectrodes and after the Ni nanoisland deposition, the Ni nanoislands nucleation and growth are affected by the nanoelectrodes, resulting in short-circuit devices (the devices were characterised electrically before and after deposition). Fig.3.21 illustrates the typical Ni nanoisland deposition after nanoelectrodes fabrication.

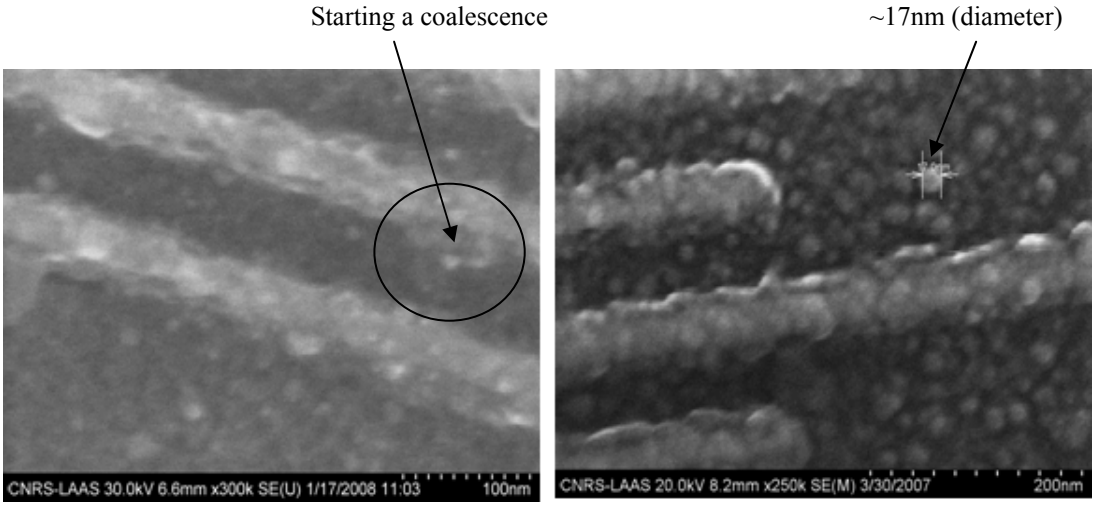

Fig.3.21. (a) SEM image of Ni nanoisland deposition on IND (1 nm thick), (b) Ni nanoislands deposition on IND (2.5nm thick and ~17nm diameter).

From the Fig. 3.21(a), we observe that if depositing on the nanoelectrodes, previously prepared, coalescence starts being formed close to nanoelectrodes (nominal nanoislands thickness deposition of 1nm). Fig. 3.21 (b) is a typical image in which a more important deposition is conducted. In this case 2.5nm thus the nanoislands measure ~17nm.

These kinds of depositions are not useful for our purposes because in the first case we obtained a short-circuit and in the second case the islands are big to observe tunnelling effect. The solution was to deposit Ni at 1nm nominal thickness, before elaborating the nanoelectrodes.

To elaborate nanoelectrodes at wafer level, we employed the same procedure described in chapter 2. The alignment marks, pictured in Fig. 3.22(a), are used to align and realise the 768 IND devices on an existing Ni nanoislands film. Fig. 3.22(b) depicts SEM images of a classical IND device. It illustrates one interdigitated nanoelectrode device and a magnification of one nanoelectrode, with 40nm in width and a 60 nm of gap between the nanoelectrodes. Finally, optical image and its corresponding electronic microscopy magnification illustrate a rectangular spot, revealing emplacement of the Ni nanoislands deposition after the lift-off process.

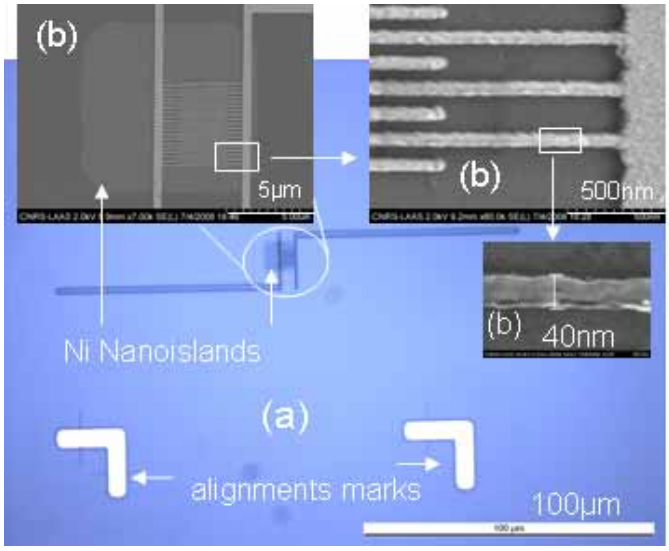

Fig.3.22. (a)(b) Optical and SEM images of an interdigitated nanoelectrode device elaborated on a previous deposited granular Ni film.

Magnification of one nanoelectrode is pictured in Fig. 3.23, in which there are Ni nanoislands measuring mostly ~5nm (there are some nanoislands measuring 3nm or 4nm). It is possible to produce the nanoislands having a high homogeneity, all of them are deposited in the interdigitated nanoelectrodes emplacement (the picture has a slight white square spot illustrating the Ni granular film deposition emplacement on the right).

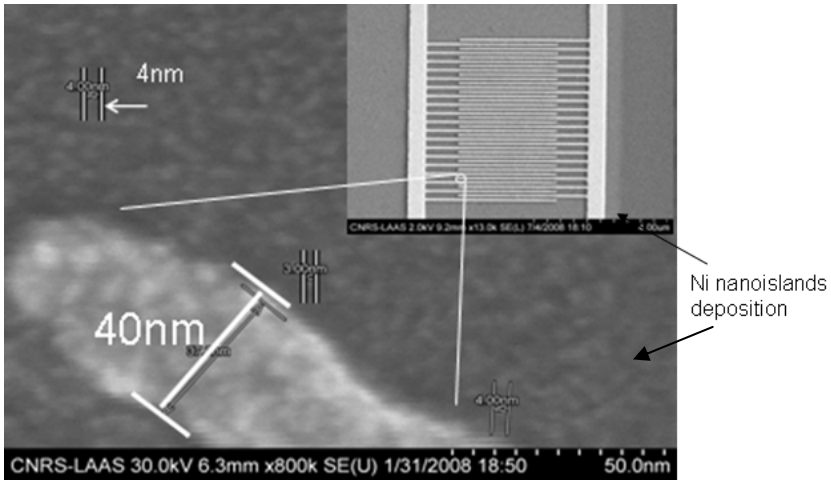

Fig.3.23. Magnified view of a single nanoelectrode by SEM (40nm width) showing the Ni nanoislands, picture illustrates one 4nm Ni island.

Fig. 3.24 shows a 4 in wafer carrying 96 cells, each cell has 8 IND, and then each 4 in wafer has exactly 768 IND. The final connections, realised photolithography, were to connect the IND devices using mix and match process as demonstrated in chapter 2. This figure depicts also the magnification of one cell measuring 7 mm X 7 mm. It illustrates the pads to connect directly the probes of the cascade equipment coupled to Keithley analyser. The electrical characterisations were conducted at room temperature.

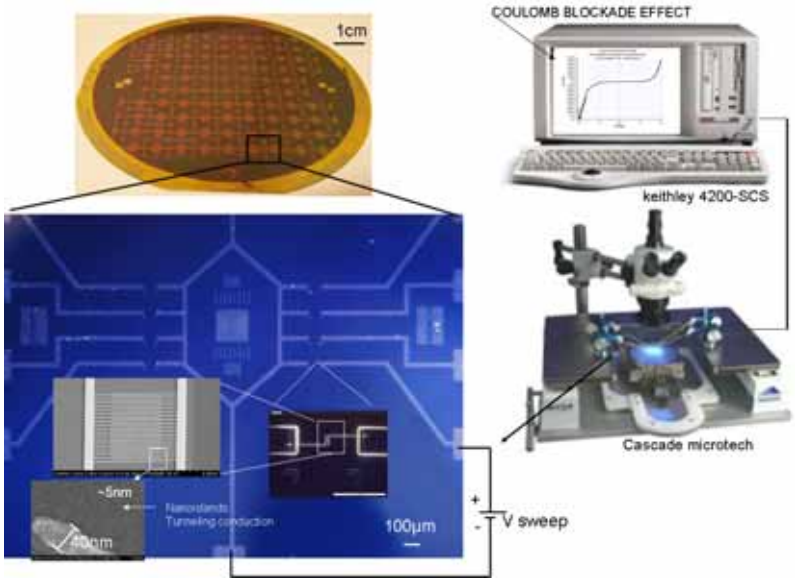

Fig.3.24. Wafer scale realisation of IND presenting Coulomb blockade phenomena at room temperature and the cascade microtech coupled to a keithley 4200-SCS used to characterise the devices.

An example of one electrical characterisation at room temperature is illustrated in Fig. 3.25. Voltage was swept between -3V and 3V with increment steps of 25mV (240 steps). A clear Coulomb gap between -400mV and 400mV can be observed in the conductance plot (derivative dI/dV). The conductance (dI/dV) is plotted in relation to the voltage swept.

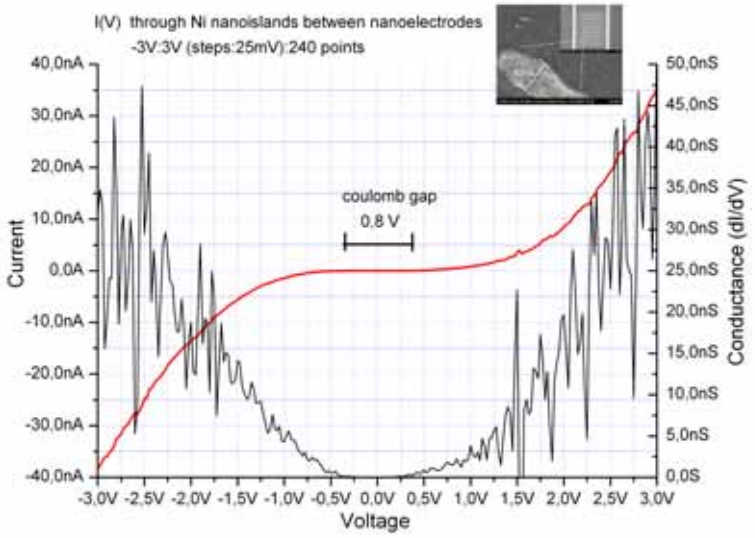

Fig.3.25. I-V showing Coulomb blockade at room temperature through Ni nanoislands (4nm-5nm) deposited between interdigitated nanoelectrodes devices (IND).

This characteristic is exactly what it is expected for multitunnel junction devices (MTJ) with islands having a charging energy larger than the thermal energy at room temperatures (25meV). From a schematic evaluation, a coulomb gap of 800 mV (-400 mV to 400 mV) gives a typical capacitance of 0.2 aF and a charging energy of ~400 meV which is large compared to the thermal agitation (~16 times the K_BT). For comparison, we assimilate this capacitance to the self capacitance of one isolated spherical Ni island as $C_s=2\pi\varepsilon_o\varepsilon_r d$ where ε_r is the average static relative permittivity between SiO_2 ($\varepsilon_{r=}$ 3.7), which is the insulator surrounding each island and air (ε_r= 1), d is the islands diameter (5nm), ε_o is the vacuum permittivity ($8.8541878176\times 10^{-12}$ F/m ($C^2/N\times m^2$). Then, for a Ni island (5nm diameter) with ε_r=2.35, we found C=0.65 aF. It is in good agreement with the value extracted from our experience. If we calculate the mutual capacitance between islands, the expression becomes $C_m=2\pi\varepsilon_o\varepsilon_r d^2/s$ where s is the separation between neighbouring islands. For s=2 nm thus C_m =.16 aF which is also in quite good agreement.

We thus conclude, from these experiments, that our interdigitated nanoelectrodes devices having Ni nanoislands deposited between them behave as classical multitunnel junction devices. Since the charging energy of these 5 nm islands is quite high, the coulomb blockade effects can be observed at room temperature. The charging, as calculated from the coulomb gap gives a value of several hundred of meV, corresponding to coupling interdots capacitances on the order of 0.2 aF. These values of capacitances agree with the size of the Ni islands (5nm). However, these values as well as the current levels were observed vary from device to device, for example, for some devices their current can reach 10 nA at 2V, see Fig. 3.25 or it can be smaller for devices having a larger coulomb gap as Fig. 3.26 illustrates. In this device, the current reaches 600 pA at 2V (it is obtained with a huge amount of acquisition points). This variability is attributed to sensibility of the devices to exact positions the conduction islands between the nanoelectrodes. The variability can be observed while comparing Fig. 3.25 and Fig.3.26, which correspond to normally identical devices. Hence, RT coulomb blockade effect is observed in two cases but the current levels as well as the coulomb gaps are not the same. These variations can be as large as 100 %.

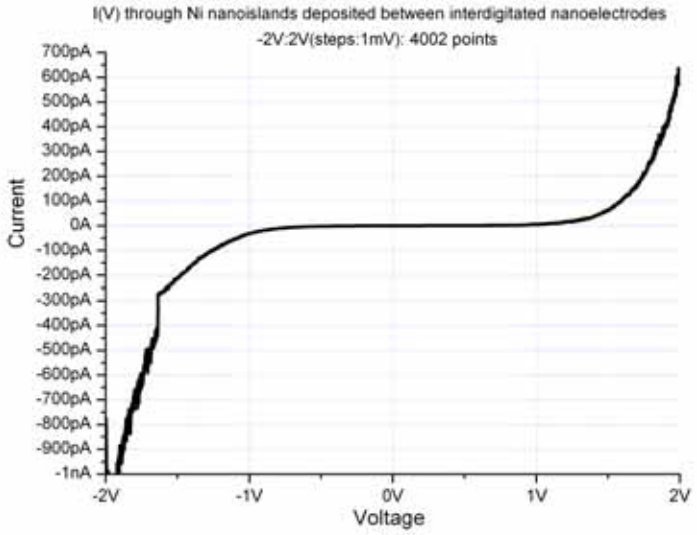

Fig.3.26. I-V showing Coulomb blocakade at room temperature through Ni nanoislands (~5 nm) deposited between interdigitated nanoelectrodes devices (IND).

In fig. 3.27 we present a magnified view of the conductance near zero voltage, corresponding to graph of Fig.3.26. The graph definitely demonstrates a Coulomb blockade of the tunnel current at room temperature. Its conductance near zero voltage is less than 5 picoSiemens (5pS).

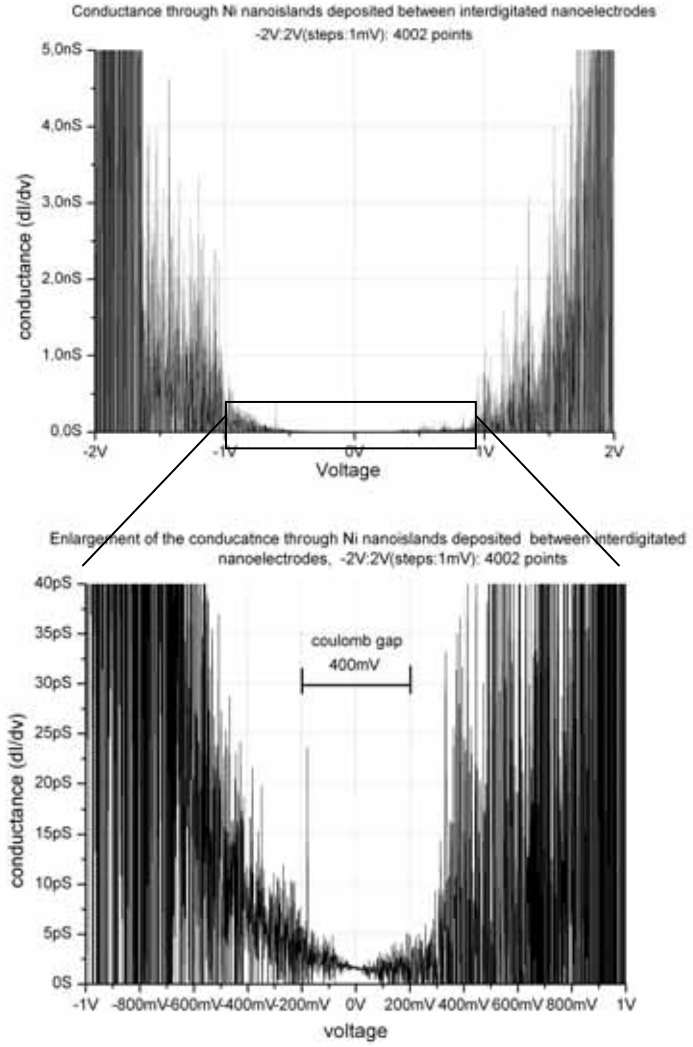

Fig. 3.27. Conductance of the Coulomb blockade effect illustrated in Fig.3.26 (obtained with a huge amount of acquisitions points). Close-up between -1V and 1V.

3.4 Conclusions

In this chapter we have characterised the electrical conduction through interdigitated nanoelectrodes with nanometric size Ni islands deposited between their gap. Most of the fabricated devices (a systematic statistical analysis has not been performed) exhibited a Coulomb blockade effect at room temperature. The conduction is therefore interpreted as single electron charge transport from island to island. The configuration of the islands is highly disordered with dispersion in their diameter and separation. This disorder changes the tunnel resistance and the capacitance associated to each tunnel junction. Moreover, the interdigitated configuration of the nanoelectrodes is such that multiple conduction paths are probably achieved and conduct the current in parallel. However, it is anticipated that due to the resistivity of the induction mechanism changes in the local environment of the island (charges, variation ε of conduction and lowering the tunnel barrier due to molecular

adsorption) these devices can be exploited to molecular detection purposes. The bimolecular adsorption on Ni nanoislands will be described in chapter 4 and the integrated devices will be described in chapter 7.

Otherwise, in these experiments two observations have been made. Firstly, these devices are sensitive to light, probably due to the charge injection in the dielectric surrounding each nanoisland moderating the single electric transfer rate (a deep study is suitable). This observation indicates us that special care on the illumination at the final device must be taken to avoid that the detection signal be disturbed by detrimental fluctuations of the flux of photons in the environment. Secondly we have observed large fluctuations (Coulomb gap and conduction at large voltages from device to device). This means that the electrical signal can not be absolute (for example, defining a current threshold and discriminate subsequent biomolecule adsorption events), then it needs to rely on the comparison of the I(V) curve before and after biomolecules adsorption and interactions, at a fixed voltage beyond the coulomb blockade region (e.g. 2 V). In these conditions, the current needs to be measured before the incubation of the analyte and then compare its value at the same voltage after the biological reaction.

3.5 References

[1] Sheng Ping, Abeles A. "Voltage-induced tunnelling conduction in granular metal at low temperatures", *Physical Review Letters*,**1971**, 28:1,p.34-37.

[2] Hill R.M, Coutts T.J., "charge transfer in discontinuous thin and cermet films", *Thin Solid Films,* **1976**, 41, p.201-212.

[3] Tománek D., Mukherjee S., Bennemann K.H., "Simple theory for the electronic and atomic structure of small clusters", *Physical Review B*, **1983**, 28:2, p. 665-673.

[4] Mullen K., Ben-Jacob E., Jaklevic R.C., "I-V characteristics of coupled ultrasmall-capacitance normal tunnel junction", *Physical Review B*, **1988**, 37:1, p.98-105.

[5] Fulton, T.A., Gammel P.L., Dunkleberger L.N., "Determination of coulomb-blockade resistance and observation of the tunnelling of single electrons in small-tunnel-junction circuits", *Physical Review Letters*, **1991**,67:22, p.3148-3151.

[6] Janes D.B, Konlagunta V.R., "Electronic conduction through 2D arrays of manometer diameter metal clusters", S*uperlattices and Microstructures,* **1995**, 18, p.275-282.

[7] Likharev Konstantin K, "Single electron devices and their applications", *Proceding of the IEEE*, **1999**, 87:4, p.606-632.

[8] Gangopadhyay S., Handjipanayis, Dale B., "Magnetic prorperties of ultrafine iron particle", 45:17, *Physical Review B*, **1992**, 45:17, p.9778-9787.

[9] Andres R.P., Datta S., Dorogi M, et al., "Room temperature coulomb blockade and coulomb staircase from self-assembled nanostructures", *J.Vac.Sci.Technol.A*, **1996**, 14:3, p.1178-1183.

[10] Sang H., Ni G., Lu J., et al., "Preparation and structural characterization on nanostructured CoAg granular films", *J.Vac.Sci.Technol.B, **1997***,15:4, p. 1456-1459.

[11] Tan Y.T., Kamiya T., Durrani Z.A.K., et al., "Room temperature nanocrystalline silicon single-electron transistors", *Journal of Applied Physics*,**2003**, 94/1,p.663-637.

[12] Hosoya H., Arita M., Nishio H., "Single-electron transistor properties of Fe-SrF_2 granular films", *Material Science and Enginnering*, **2008**, 147, p.100-104.

[13] Vieu C, Gierak J., David C., et al., "Gold nanograins deposited from a liquid metal ion source", *Microelectronic Engineering*, **1997**, 35, p.349-352.

[14] Vieu C, Pepin A, Gierak J., et al., "Coulomb blockade devices fabricated by liquid metal ion source droplet deposition", *J. Vac.Sci.Technol.B*, **1998**, 16:6, p.3789-3794.

[15] Yi J.B., Zhou Y.Z., Ding J., et al., "An investigation of structure, magnetic properties and magnetoresitance of Ni film prepared by sputtering", *Journal of Magnetism and Magnetic Material*, **2004**, 284, p.303-311.

[16] Parent F., Tuaillon J., Stern L.B., "Giant magnetoresistance in Co-Ag granular films prepared by low-energy cluster beam deposition", *Physical Review B*, **1997**, 55:6, p.3683-3687.

[17] Dumas-Bouchiat F., Nagaraja H.S., Rossignol F., "Cobalt cluster-assembled thin films deposited by low energy cluster beam deposition: Structural and magnetic investigation of deposited layers", *Journal of Applied Physics*, **2006**,100, p.064304-1(8).

[18] Mejias M., Lebreton C., Vieu C.,et al., "Fabrication of coulomb blockade devices by combination of high resolution electron beam lithography and deposition of granular films", *Microelectronic Engineering*, **1998**, 41/42, p.563-566.

[19] Lebreton C., Vieu C., Pepin A., et al., "Coulomb blockade effect through a 2D ordered array of Pd islands obtained by colloidal deposition", *Microelectronic Engineering*, **1998**, 41/42, p.507-510.

[20] Cordan A.S, Golzené A., Hervé Y. et al., "electron transport in metallic dot array: effect of broad dispersion in tunnel junction dimensions", *Journal of Applied Physics*, **1998**,84:7, p.3756-3763.

[21] Pépin A, Vieu C., Mejias M., "Temperature evolution of multiple tunnel junction devices made with disordered two-dimensional arrays of metallic islands", *Applied Physics Letters*,**1999**, 74:20, p.3047-3049.

[22] Graf H., Vancea J., Hoffman H., "Single electron tunnelling at room temperature in cobalt nanoparticle", *Applied Physic Letters*, **2002**, 80:7, p.1264-1266.

[23] Moodera J. S., Kinder R. Lisa, Wong M. Terrilyn, et al., "Large magnetoresitance at room temperature in ferromagnetic thin film tunnel junctions", *Physical Review Letter*, **1995**, 74:16, p.3273-3276.

[24] Dong X.L., Zhang Z.D., Jin S.R.,et al., "Characterization and magnetic properties of Fe-Co ultrafine particles", *Journal of Magnetism and Magnetism Materials*, **2000**, 210, p.143-149.

[25] Fonseca F.C., Goya G.F., Jardim R.F., Murillo R, Carreño NLV, Longo E, et al., "Superparamagnetism and magnetic properties of Ni nanoparticles embedded in SiO_2", *Phyics. Review B* , **2002**, B66,p.104406-1(5).

[26] Koch S.A., Velde R.H., Palasantzas G, et al., "Magnetic versus structural properties of Co Co nanoclusters thin films": A magnetic force microscope study, applied physics letters, **2004**, 84:4, p.556-558.

[27] Skomski R., Zhang J., Sessi V., "Substrate-controlled growth and magnetism of nanosize Fe Clusters on Pt", *Journal of Applied Physics*, **2008**,103, 07D519-1(3).

[28] Gittleman J.I., Goldstein Y., Bozowski S., "Magnetic properties of granular nickel films", *Physical Review B*, **1972**, 5:9, p. 3609-3620.

[29] Helman J.S., Abeles B., "Tunnelling of spin-polarized electrons and magneto resistance in granular Ni films", *Physical Review Letters*, **1976**, 37:21, p.1429-1432.

[30] Barzilai S., Goldstein Y., Barberg I., et al., "Magnetic and transport properties of granular cobalt films", *Physical Review B*, **1981**, 23:4, p.1809-1817.

[31] Ferrari E.F., da Silva F. C.S., Knobel M., "Theory of giant magnetoresistance in granular alloys", *Physical Review B*,**1999**, 59:13, p.8412-8415.

[32] Yang Rong, Zhang Wei, Song W.J., "Theory of giant magnetoresistance of magnetic granular films", *Journal of Applied Physic*, **1998**, 84:4, p.2044-2047.

[33] Braig Stephan, Brouwer Piet W., "Rate equations for coulomb blockade ferromagnetic leads", *Physical Review B*, **2005**, 71, p.195324-1(9).

[34] M. Jullière, *Phys. Review Lett.* 54 (**1975**) 225.

[35] Baibich M.N., Broto J.M, Fert A., "Giant magnetoresitance of (001)Fe/001)Cr magnetic superlattices", *Physical Review Letters*, 1988, 61:21, p.2472-2475.

[36] Binasch G., Grünberg P., Saurenbach F., et al., "Enhanced magnetoresistance in layered magnetic structures with antiferromagnetic interlayer exchange", *Physical Review B*, **1989**, 39, p.4828 -4830.

[37] Takahashi S., Maekawa S., "Effect of coulomb blockade on magnetoresistance in ferromagnetic tunnel junctions", *Physical Review letters*, **1998**, 80:8, p.1758-1761.

[38] Schelp L.F., Fert A., Fettar F., et al., "Spin-dependent tunnelling with coulomb blockade", *Physical Review B*, **1997**, 57:10, p.R5747- R5750.

[39] Frydman A., Kirk T.L., Dynes R.C., "Superparamagnetism in discontinuous Ni films", *Solid State Communications*, **2000**, 114, p.481-486.

[40] Chang Ching-Ray, Lo Kuo-Hung, "Giant magnetoresistance in granular array". *J. Appl. Phys.,* **1996**, 80:12, p. 6888-6893.

[41] Pakhomov A. B., Yan X., Zhao B., "Giant Hall effect in percolating ferromagnetic granular metal-insulator films", *Applied Physics Letters*, **1995**, 67:23, p. 3497-3499.

[42] Zhuravlev M. Ye., "Sabirianov R.F., Jawal S.S., Giant electroresistance in ferroelectric tunnel junctions", *Physical Review Letters*, **2005**, 94,p. 075401-075406.

[43] R. Skomski, J. Zhang, V. Sessi (K. Kern's group), "Substrate controlled growth and magnetism of nanosized Fe clusters" *Journal of Applied Physics*, **2008**, 103, p. 07D519-1 (3)

[44] E Prinz Gary A., "Magnetoelecgtronics", *Science*, **1998**,282, p.1660-1663.

[45] Devoret Michel H., Esteve Daniel, Urbina Cristian, " Single-electron transfer in metallic nanostructures", *Nature*, **1992**, 360,p.547-553.

[46] Averin D.V., Likharev K.K., "Coulomb blockade of single-electron tunnelling, and coherent oscillations in small tunnel junction", *Journal of low Temperature Physics*, **1986**, 62, p.345-373.

[47] Venables J A, Spiller G D T, Handbücken M., "Nucleation and growth of thin films", *Rep. Prog. Phys.* **1984**, 47, p. 399-459.

[48] Cao GuoZhong, *Nanostructures and Nanomaterials: Synthesis, properties and applications*,London, imperial college press, **2004**, 1, 433p.

[49] Davis P.C.W., "Quatum tunnelling time", *Am. J. Physic,* **2005**,73, p.23-27.

[50] Brasseur Vincent, Thomas Kairet, *Le blocage de coulomb et le transistor à un électron*, cours in University catholoque de louvain, **2001-2002**, 35p.

[51] Black C.T., Murray C.B, Saldstrom R.L., et al., "Spin-dependent Tunneling in self-assembled cobalt-nanocrystal supperlatices", *Science*, **2000**, 290. p. 1131-1134.

[52] Kechratos D., Trohidou K.N., "Correlation between tunnelling magnetoresistance and magnetization in bipolar-coupled nanoparticles arrays", *Physical Review B*, **2002**, B71, p.054416-1(8)

[53] Franz Kreupl, thesis: *Coulomb-Blocakade bei Raumtemperatur in selbstorganisieren Arrays von Pt-Clustern*, der Fakultät für Physik, Universität Regensburg, **1998,** Pr. Dr, H . Hoffman.

[54] Prinz Gary A., "Spin-polarized transport", *Physical Today*, **1995**, p.58-63.

[55] Margeat Olivier, Thesis: Effect de taille et de surface sur les proprietés physiques de nanoparticules superparamagnétiques, **2005,** Dir. Chaterine Amiens et Bruno Chaudret.

[56] Hunter Eliza, Fendler Janos H., "Exploitation of localized surface Plasmon resonance", *Advanced materials*, **2004**, 16:19, p.1685-1706.

[57] Kravets, V. G., Poperenko L.V., Yugelevych I.V., et al. "Optical and magneto-optical properties and magnetorefractive effect in metal-insulator CoFe-Al_2O_3", *Journal of Applied Physics*, 2005, 98, p.043705-1 (7).

[58] Mizuta Hiroshi, Müller Heinz-Olaf, Tsukagoshi Kazuhito, "Nanoscale coulomb blockade memory and logic devices", *Nanotechnology* , **2001**, 12, p.155-159.

[60] Fulton T.A., Gammel P.L., Dunkleberger L.N., "Determination of Coulomb-blockade resistances and observation of the tunneling of single electrons in small-tunnel-junction circuits", *Phys.Rev.Lett.***1991**, 25, p.3148-3151.

[61] Giaever I, Zeller H.R, "superconductivity of small tin particles measured by tunnelling", *Phys.Rev.Lett. **1968**,*26, p.1504-1507.

[62] Lambe J. Jaklevic R.C.,"Charge quantization studies using a tunnel capacitor", *Phys.Rev.Lett. **1969**,*25, p.1371-1575.

[63] J. Barnas, and A. Fert, "Magnetoresistance Oscillations due to Charging Effects in Double Ferromagnetic Tunnel Junctions", *Phys.Rev.Lett. **1998**,* 80, p.

[64] Michel Marso, Peter Javorka, Peter Kordos "Spin and Charge: Spintronics Electrical and Optical Properties of Quantum Structures and Devices" *Forschungszentrum Jülich*.

[65] H. Wang, S. Mitani K., Takanashi, and H. Imamura, "Numerical simulation of spin accumulation and tunnel magnetoresistance in single electron tunnelling junctions with a nonmagnetic nanoparticle*", Physical Status Solidi (b)*, **2007**, 244 (12),P.4443-4447. *Fulton T A, Dolan G. J., "Observation of single-electron charging effects in small tunnel junctions", *Phys. Rev. Lett.*, **1987**, 59, p.109-112.

Chapter IV

Label-free cancer biomarker recognition by nickel nanoislands using quartz crystal microbalance

4.1 Introduction

In this chapter, we present a methodology for label-free detection of cancer biomarker binding assay interactions and recognition using a similar deposition of Ni nanoislands as in chapter 3. His-tagged (scFv)-F7N1N2 is the antibody fragment which is directly immobilised by coordinative bonds, onto evaporated ~5 nm nickel islands (Ni nanoislands) deposited on the surface of quartz crystal microbalance. Biomarker GTPase RhoA is investigated because it is found overexpressed in various tumours (bibliography in chapter 1) and because our collaborator: Patrick Chinestra, Jean-Charles Faye and Gilles Favre (from Claudius Regaud Institute) recently isolated and characterised a new conformational scFv capable of selectively recognising the active form of Rho [1].

The elaboration of ultrasensitive nanobiotransducers while avoiding the non-specific adsorption and conserving the proteins conformation is crucial. We implement the corresponding surface chemistry involving an anti-biofouling (protein repellent) coating of polyethylene glycol-silane referred as PEG-silane (<2nm thick) to avoid non-specific bimolecular interactions. Glycerine, used as cryogenic protectant in molecular biology, produces non-specific biomolecular interactions, in our nanobiotechnological protocol. A new protocol without glycerine has thus been validated by ELISA technique. Finally, the specific label-free detection and recognition of the active antigen conformation of RhoA, avoiding the glycerine effect, at various concentrations is demonstrated by quartz crystal microbalance (QCM) technology. This method proves the viability of the concept by implementing one of the most critical steps in nanobiosensor or protein-chip realisation, in this case by using Ni nanoislands as an anchoring surface layer, enabling the detection of a specific conformation of a protein identified as a potential cancer biomarker.

4.1.1 Quartz crystal microbalance (QCM)

For validating the biomolecular interaction and the specific recognition, we used a quartz crystal microbalance (QCM-D). This technology permits the determination of an additional mass per unit area by measuring the frequency shift of the mechanical resonance of a quartz crystal. Hence, this technique developed in the 90's by Rodahl and coworkers, enables the quantification of deposited masses at the surface of the quartz crystal and the characterisation of the viscoelastic properties of thin adsorbed films. Thanks to the simultaneous measurement of the dissipation D, the QCM-D provides additional information about the structural state of the adsorbed films. QCM technology is particularly well adapted for the development and validation of biofunctionalised surfaces or protein chips applications [2]. Currently, the resolution in frequency is in the range of 0.2 Hz (in liquid) corresponding to a mass resolution of around 3.5 ng/cm^2 [3].

4.1.2 PEG-silane based surface chemistry

PEG stands for polyethylene glycol, it is a biocompatible polymer used as "biological" passivating surface film. PEG has a structure characterised by hydroxyl groups at either end of the molecule, its formula is HO-$(CH_2CH_2O)_n$$CH_2CH_2$-HO. PEG is a linear and neutral molecule available in numerous weights and soluble in numerous organic solvents. Furthermore, PEG has been used in a lot of biochemical and biomedical applications including tissue engineering, mainly because of its antibiofouling characteristic (property to reject proteins) [4][5]. Finally, as this polymer is not toxic, it is one of the few synthetic polymers in food, cosmetics or pharmaceuticals [6].

Regarding the property of the PEG known as protein repellent, there have been some approaches to explain the PEG inertness. For example Andrade and de Gennes considered theoretically the proteins resistance, by taking ideas from the colloid stabilisation [7]. Their postulation was that the water molecules in hydrated PEG chains have a tendency to move as the protein approaches. Then, PEG inertness is explained by a thermodynamic approach, in which there is increment in steric repulsion due to the removal of water. However, their approach does not provide a complet explanation of the high repellent property involved in PEG. Contrary, Sheth and Lecknand (1997) [8] published that PEG is not inert, and it can bind proteins on certain conditions. They grafted monolayers of M_r 2000 methoxy terminated thus streptavidin was deposited on the surfaces and they measure the molecular forces between the streptavidin and PEG by a surface force apparatus. It seems that these bounds are concerned with the arrangement in the polymer configuration or a change in PEG. At low compressive loads, the molecular forces were repulsive. However when higher compressive loads were applied to press the proteins into the polymer, the molecular forces turned out to be attractive.

In this chapter we demonstrate that silane terminated PEG (PEG-Silane) can absorb organic compounds such as glycerine, this effect named "glycerine effect" produces non-specific bimolecular interactions, so it is imperative to avoid glycerine in our experiments.

PEG is not a universal repellent to avoid non-specific interactions but if taking care of some situations, it is a good protein repellent, then it is necessary to consider various phenomena taking place in the couple polymer-protein such as the competitive interactions or the PEG configurational entropy. The protein repellent property has not been yet completely explained, but what is a fact, is the ability of PEG to control biofouling (the strong tendency of organisms or proteins to physically be adsorbed to synthetic surfaces).

Otherwise, silicon and silicon-based (e.g., silica, glass) materials most commonly used in bioMEMs and bioNEMs have to be passivated to obviate the non-specific interactions for maintaining the regulation of biofouling and its biocompatibility. One of the most efficient materials to do this is precisely the PEG. Several techniques have been proposed to electrostatically link PEG onto surfaces, using for instance, Poy(L-lisine) g-poly(ethylene glycol) referred as PLL-g-PEG [9]. Nevertheless, the bonding is weak and the immobilised polymers do not permanently remain on surface due to physical or chemical changes. On the contrary, covalent grafting of PEG is a most effective way of creating a more stable film on surfaces.

Sharma et al. developed nanostructured PEG films using covalently attached PEG-silane onto silicon or silica surfaces, using different methods [10]: one on them consists of coupling

PEG-silane in solution and the other consists of vapour deposition of ethylene oxide to grow PEG on the surface.

In this work, we have adapted the PEG-silane process in solution phase. The film is a monolayer of ~1.6 nm covalently grafted onto the surface as Fig. 4.1 (a) illustrates. Fig 4.1 (b) gives the variation of the PEG thickness depending on the graft concentration.

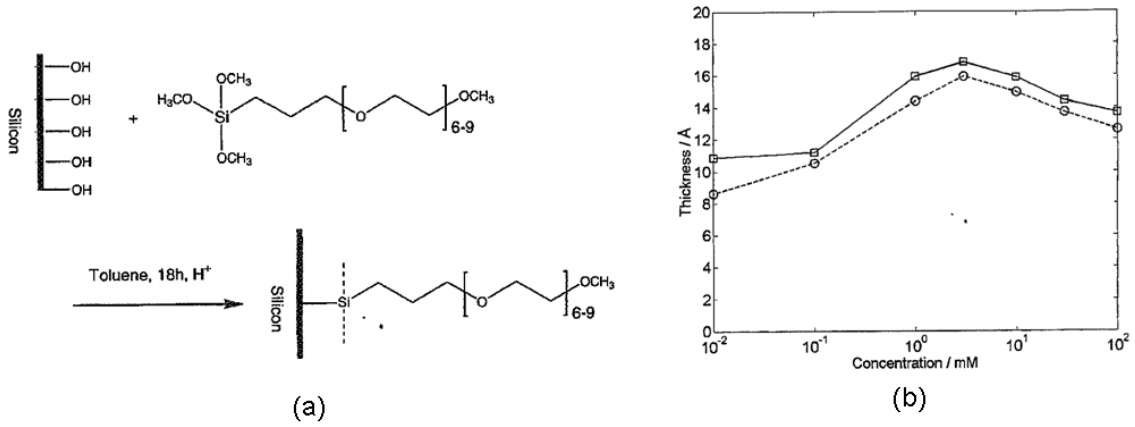

Fig.4.1. Schematic representation of the PEG-silane covalently grafted onto silicon, (b) Reponses of X-ray reflectivity (full line) and XPS (dashed line) giving a comparison of calculated thickness, depending on the graft concentration (images from [10]).

4.1.3 Proteins purification by Ni-NTA

A purification method developed by Porath and coworkers [11] has been used for some time. It consists of binding proteins onto immobilised metal ion affinity chromatography (IMAC). The purification is possible because of the affinity the proteins with exposed amino acid cysteine or histidine side chains have for metals, such as Ni^{2+}, Co^{2+}, Zn^{2+}, Cu^{2+} and Mn^{2+}[12] through coordinative bonds. The nitrogen in the imidazole core histidine of 6His-tagged proteins binds to Ni^{2+} cations. The dissociation constant is ~10^{-13} M in the case of His Ni-NTA at pH 8 [13]. The typical dissociation constant in most antibody binds are from 10^{-6} M to 10^{-9} M (weak to high affinity), however weaker that the avidin-biotin (K_D of 10^{-15} M [14]).

In this work, we take benefit of this principle by using the very thin layer of Ni exhibiting nanoislands (chapter 3) as a surface chemistry for attaching His-tagged antibody fragments for the ligand-binding assays. Fig. 4.2 schematises the commonly used Ni-NTA, bonded to His-tagged proteins.

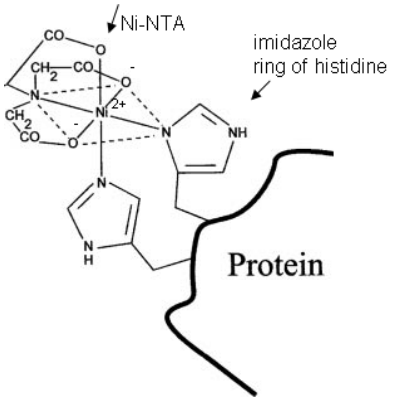

Fig. 4.2. Ni-NTA bonding to His-tagged proteins. (Adapted from [12]).

4.2 Methods, material and experimental section

The different measurements were made using a QCM-D (Q-sense E4, Sweden), shown in Fig. 4.3. Quartz with SiO_2 50nm thick film (Q-sense, Sweden) were covered with 1µm silicon oxide (SiO_2) using plasma-enhanced chemical vapour deposition (PECVD), in our clean room facility. We used a fluorescence microscope (Olympus IX70).

(a) (b)

Fig. 4.3. (a) Q-sense E4, (b) some quartz and the metal piece where they are positioned (from: q-sense.com).

4.2.1 Anti-biofouling coating

For many application purposes related to micro and nanobiosensors, silicon oxide surfaces are used due to their compatibility with silicon technology. We have thus optimised a chemical protocol on this type of surfaces and then we employed quartz crystals covered with a silicon oxide thin layer. During the experiments, we rapidly noticed that the biomolecules of interest for our work (antibody fragments and proteins) exhibited some unwanted interactions with those SiO_2 surfaces. We therefore tested several passivation methods to avoid these non-specific adsorptions. We came to a decision on using 2[methoxy (polyethyleneoxy) propyl] trimethoxy silane (Gelest), a silane conjugated polyethylene-glycol chain (henceforth referred as PEG-silane) (Mw 460–590), because of its biocompatibility and its covalent binding onto SiO_2 as written above. This kind of PEG has already been used in nanostructured PEG-films preparation for silicon-based BioMEMS [15].

To prepare the surfaces, PEG-silane molecules and concentrated HCl were mixed in toluene in a clean glass beaker with 100µl PEG-silane, 40µl HCl and 50ml of toluene (~3mM of PEG silane). The beaker was then placed in a sonicator for 1 min and its content was transferred to another clean glass beaker. A 1.5cm-diameter quartz covered with a 1µm thick SiO_2 PECVD-deposited layer was immersed during 2 h and washed sequentially with toluene, ethanol and finally de-ionised water (each step during 2 min). This protocol generates an ultrathin PEG-silane layer on the surface with a thickness comprised between 1nm and 1.8 nm [10] see Fig 4.1(b).

The final quartz surface, after this film fictionalisation process, is schematised in Fig. 4.4.

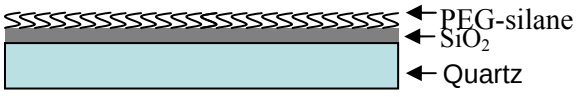

Fig. 4.4. Schematic representation of a quartz functionalised with an anti-fouling PEG-silane coating.

In chapter 3, we introduced the concept of contact angle to characterise the degree of hydrophobicity or hydrophilicity of a surface. We used this technique to corroborate the presence of the covalent PEG-silane on our surfaces. We used a contact angle meter, called Digidrop$^{(R)}$ (GBX, France). A water drop was deposited on the silicon dioxide to compare its angle before and after PEG grafting. To attach the PEG covalently on the surfaces, it is necessary that the surfaces are proper and have hydroxyl layer on the silicon as Fig. 4.1 (a) illustrates. What it means that the surfaces need to be cleaned, to do that we used a mixture of ethanol and water (1:1 in volume) which was poured on a glass beaker containing the 4 in. wafer. Then, ultrasonic agitation during 2 min (35 kHz) was applied. To create a hydroxyl layer, we used piranha solution (H_2O_2:H_2SO_4, 2:5 (v/v)) for 5 min., followed by rinsing with de-ionised (DI) water and applying ultrasonic agitation during 2 min (35 kHz). After the formation of the hydroxyl layer, the water angle contact measure ~10°, but after grafting the PEG-silane the water contact angle measure ~37°. This value is consistent with the values of the contact angle depending of PEG concentration demonstrated by Papra et al. [10]. We can conclude that the PEG is grafted onto our surfaces and from the contact angle and Papra et al. paper, we have a PEG-silane measuring ~1.6nm (A characterisation using ellipsometer or X-ray reflectivity [10] can corroborate it). A typical water contact angle on PEG-silane is pictured in Fig. 4.5 which illustrates the way of the angle is estimated by the Digidrop software.

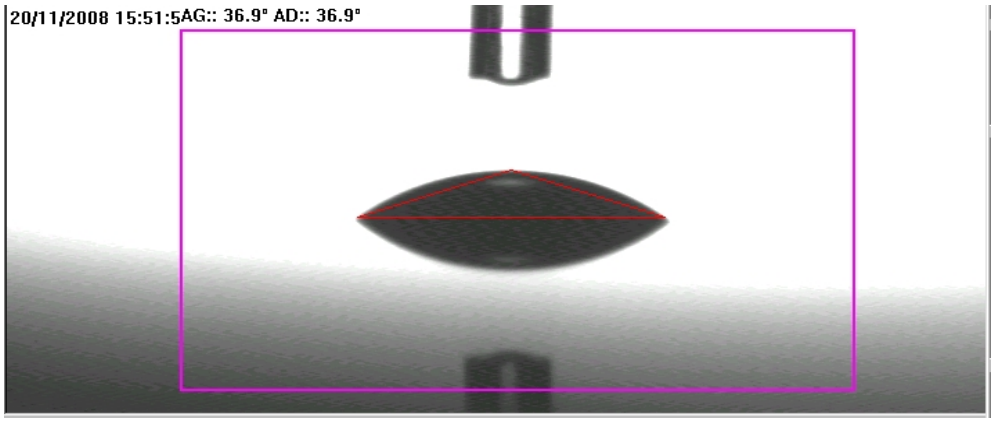

Fig.4.5. Water drop formed on a silica surface treated with PEG-silane exhibiting a typical contact angle of 37°.

Some characterisations using Raman spectroscopy technique were conducted. This technique permits to know the organic molecules present on a surface, because the frequency of light scattered is modified based on the structure of the molecular bonds of the chemical compounds. Raman scattering spectra were used in the range of 800 cm^{-1} to 3500 cm^{-1}. A resonance was observed at 1154 cm^{-1}, corresponding to COH and at 2328 cm^{-1} corresponding certainly to OH [16]. These kinds of characterisations including the X-ray reflectivity to know the film thickness have been reported [10].

Finally, the experiences reported until now to covalently graft the PEG-silane had been done under nitrogen, during 18h and using toluene anhydrous. Concerning our experiences, we demonstrated that the protocol can work by doing the experiences during 2h and without the use of nitrogen. Furthermore we did not use toluene anhydrous but normal toluene.

However, the bakers are covered avoiding the contact with air. In chapter 7 we will present the integration of our devices, and we will graft PEG-silane in certain parts of the wafer, the other parts of the same wafer are protected with a photoresist. Furthermore we will characterise the water angle of PEG-silane of surfaces after photolithographic or electronic steps, with the objective of demonstrating the effectiveness of this covalently grafted PEG-silane.

4.2.2 Nickel nanoislands deposition

As presented in chapter 3, different techniques exist for depositing nanoislands such as sputtering or vacuum evaporation. The sputtering method was disregarded because we wanted the deposition process not to damage the PEG coating, which would not have been the case due to the ionic bombardment of the surface in sputtering method.

We used then the Veeco 770 thermal evaporator machine as in last chapter. It was evaporated onto the PEG-silane surfaces 1 nm thick film of nickel at a pressure of ~10^{-6} mbars at room temperature (RT) (we had observed that the PEG is not modified when leaving it under vacuum). The Ni films morphology was confirmed by high resolution scanning electron microscopy SEM (Hitachi S-4800). A typical image of the deposited film is shown in Fig. 4.6. The Ni nano-islands appear as tiny bright spots, a statistical analysis of the observed nanoislands indicated an average diameter of 5 nm.

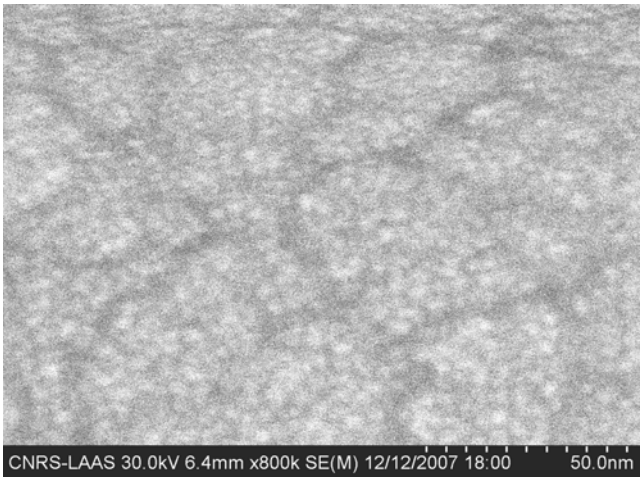

Fig.4.6. High resolution SEM image of a granular Ni film (1nm nominal thickness) deposited by thermal evaporation on a SiO2 surface.

As in the last chapter, this characterisation of the thin Ni film was confirmed by Atomic Force Microscopy (AFM) using in air, the intermittent contact mode of a JPK system (NanoWizard® II, Germany). A typical image is shown in Fig. 4.7. The height analysis also indicates an average dimension of ~5 nm. Both images (SEM and AFM) indicate that there are some spaces between the Ni nano-islands. In our process, those Ni islands will attach the antibody fragments through Ni-Histidine interaction. We think that this kind of morphology is profitable for minimising the possible denaturation of adsorbed proteins on the surface because the nanoislands are separated from ~2nm thus the biomolecules are ideally separated also to each other from ~2nm. It was reported that when small nanoislands or nanoclusters are

used, the chances for protein denaturation can be minimised [14]. The reason is because the nanoislands size is comparable to biomolecules and the tertiary structure can be less modified.

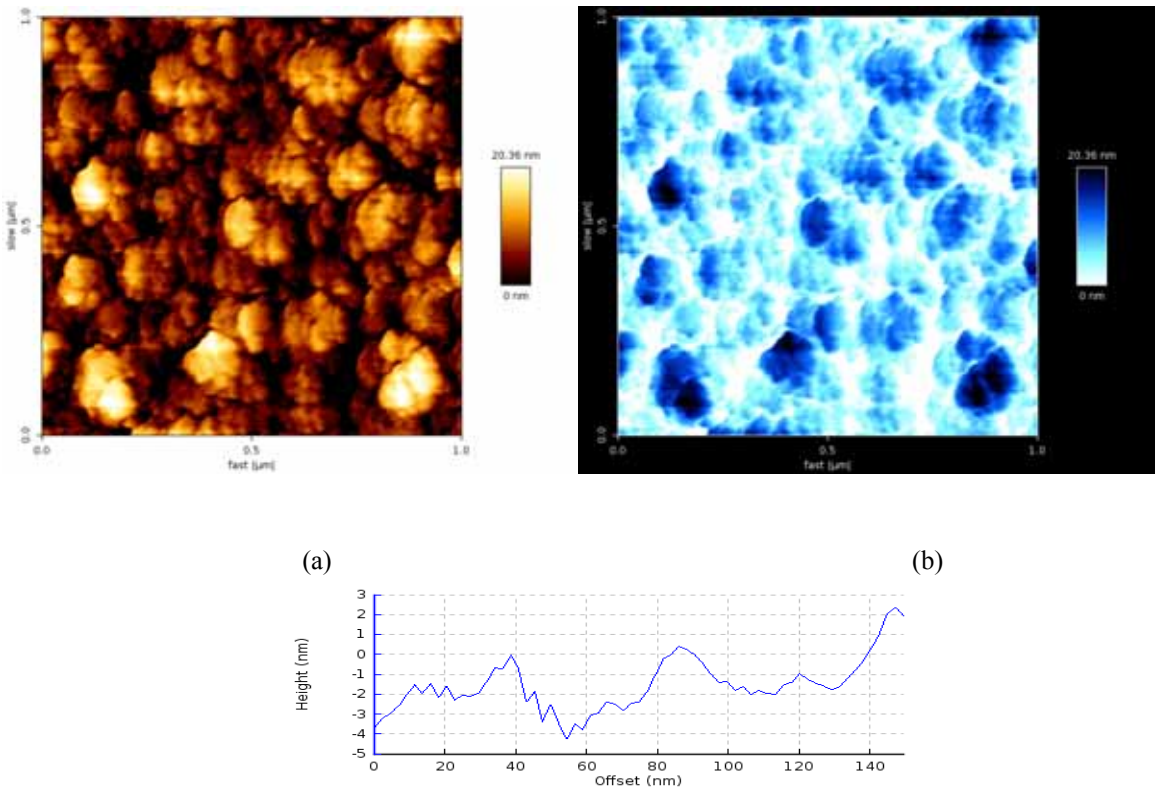

Fig.4.7. (a) AFM image of a granular Ni film (1nm nominal thickness) deposited by thermal evaporation on SiO2 surface. (b) inverted picture (for better appreciation).

The final surface of the Quartz crystal used for the QCM experiments is depicted in Fig. 4.8.

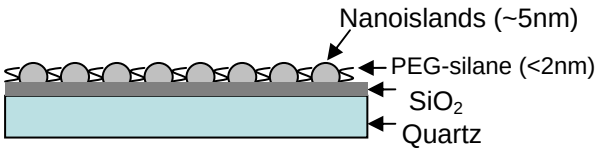

Fig.4.8. Schematic representation of a quartz functionalised with an anti-fouling PEG-silane coating and 5nm size Ni nanoislands.

4.2.3 Biomolecules purification

The production and purification of soluble single-chain antibodies was performed at the Claudius Regaud Institut (ICR) in Toulouse France as follows: TG1 *E coli* strain harboring the pHEN F7N1N2 plasmid was grown in 100 mL of LB medium containing ampicillin (100 µg/mL) and 2% of glucose at 37°C. At a proper concentration (OD_{600} =0.6-0.8), the culture was centrifuged at 3,3 x g for 10 minutes. Bacteria were once more suspended in LB medium containing ampicillin (100µg/ml) and incubated in a 0.1 mM IPTG overnight at 30°C. Bacteria were harvested, re-suspended in 50 mM NaH2PO4, pH 7.5, 300 mM NaCl, 10 mM imidazole (1/10 of the culture volume). Then bacteria were sonicated during 30 minutes. The cell lysate was centrifuged at 17,500 x g during 15 minutes. The supernatant containing the

scFvs were concentrated on 1ml of 50% slurry Ni-NTA agarose (Qiagen) at 4°C by shaking for at least two hours. After washing with 50 mM NaH2PO4, pH 7.5, 300 mM NaCl, 10 mM imidazole, bound scFvs were eluted by 50 mM NAH2PO4 pH 7.5, 300mM NaCl, 250mM imidazole.

Recombinant GST fusion RhoA protein was expressed and purified from protease deficient strain (*E.coli* BL21). Bacteria were grown at 37°C in 1 liter of LB medium containing ampicillin (100 µg/ml) until an OD_{600} = 0.6-0.8 was reached. Protein expression was induced for overnight incubation in 0.1mM isopropyl-β-D-glactopyranoside (IPTG) at 20°C and cells were harvested. Bacteria pellets were frozen at -20°C for 15-20 minutes, and subsequently re-suspended at 4°C in 50 mM Tris-HCl, pH7.5, 150 mM NaCl, 5 mM $MgCl_2$ and triton X100 0,1% at 1:10 of the original culture volume. Cells were incubated by using ice for 30 minutes, sonicated five rounds for 15 sec each one. Lysate was centrifuged at 12,500 x g for 30 minutes at 4°C. The GST-RhoA containing supernatant was purified by using Magnet GSTTM protein purification system (Promega) according to the manufacturer instructions.

All purified recombinant proteins were applied to PD-10 desalting columns (GE Healthcare) equilibrated with HEPES 10 mM pH 7.5, 150 mM NaCl, 5 mM MgCl2 to remove glutathione and imidazole.

Samples were analysed by SDS-PAGE and Coomassie blue staining, and then stored at 4°C for short term storage or - 70°C with 15% glycerin for long term storage.

Finally, for Rho GTP loading, recombinant GST-RhoA purified by using glutathione beads, was loaded with 0.1mM of GDP or GTPgS in Hepes 10 mM, 150 mM NaCl, 5 mM MgCl2 at 37°C for 1 hour.

4.2.3.1 ELISA tests

HisGrab^{TM} Nickel Coated 96-Well Plates (PIERCE) were incubated during 1 h at RT with 100µl of purified scFv F7N1N2 (6µg/ml) in PBS. The wells were washed 3 times with PBS Tween 0.05% and 100µl of purified GST-RhoA loaded with GDP or GTPgS, were added at appropriate concentrations in PBS, 5mM MgCl2. After 1 h of incubation at RT, the wells were washed 3 times and incubated by using anti-GST-HRP conjugate (GE Healthcare, RPN1236). The immuno-reaction was developed using 3, 3', 5,5'-tetramethylbenzidine (PIERCE, 34022), stopped by adding 1M sulfuric acid and we measured the results using an ELISA reader (Multiskan Labsystems) at OD= 450nm.

4.3 Results and discussion

To validate the surface chemistry for preventing non specific adsorption, we used 0.5µM of 6His-tagged green fluorescent proteins (GFP) (biomolecules from Claudius Regaud institute), onto the different quartz surfaces *(quartz-SiO_2, quartz-SiO_2-PEG-silane)* before and after nanoislands deposition. Firstly, QCM was used to corroborate the PEG-silane effectiveness as anti-biofouling. We prepared 2 quartz, one having on surface 1µm silicon nitride (Si_3N_4) and the other having 1µm Silicon dioxide (SiO_2), both insulators films deposed by PECVD.

Fig 4.9 demonstrates the effectiveness of the PEG-silane grafted on Si_3N_4 and SiO_2. Biological compounds were injected onto four quartz at the same time. First, hepes buffer was injected to stabilise the signal, at 15min the 6His-tagged GFP was injected onto four quartz, once more at 22min. Hepes buffer was injected into four quartz to remove the not absorbed

biomolecules. Clearly, quartz 1 (Si_3N_4 PEG-silane treated) and quartz 3 (SiO_2 PEG-silane treated) display not frequency shift, however both in not treated Si_3N_4 and not treated SiO_2 the frequency shifts are ~25 Hz (variation at 15 min).

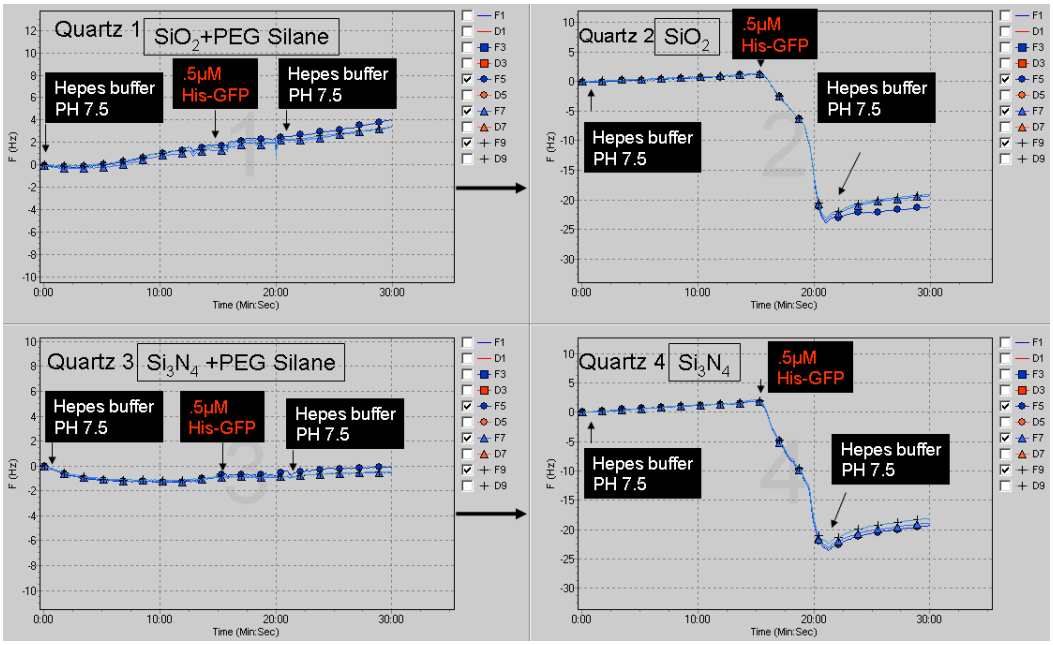

Fig 4.9. Graphs illustrating the PEG-silane effectiveness.

After incubation of the GFP, the surfaces were analysed by fluorescence microscopy. Fig. 4.10(a) corroborates that the PEG coating acts as an efficient anti-biofouling layer preventing the adsorption of proteins. Conversely, on the virgin SiO_2 film the adsorption is considerable, see Fig.4.10 (b) which is a classical homogenous adsorption onto SiO_2. Last fluorescence figure (c) illustrates an adsorption onto quartz treated PEG-silane. It is clear that the presence of Ni nanoislands change the repartition of the proteins on the surface compared to SiO_2 surfaces. It is of course not possible to obtain any molecular scale information by using simple fluorescence characterisations but the role of the different layers is clearly identified. The PEG-silane coating is an efficient anti-biofouling layer between the Ni nanoislands while these latter induce a robust linkage to the surface on specific sites.

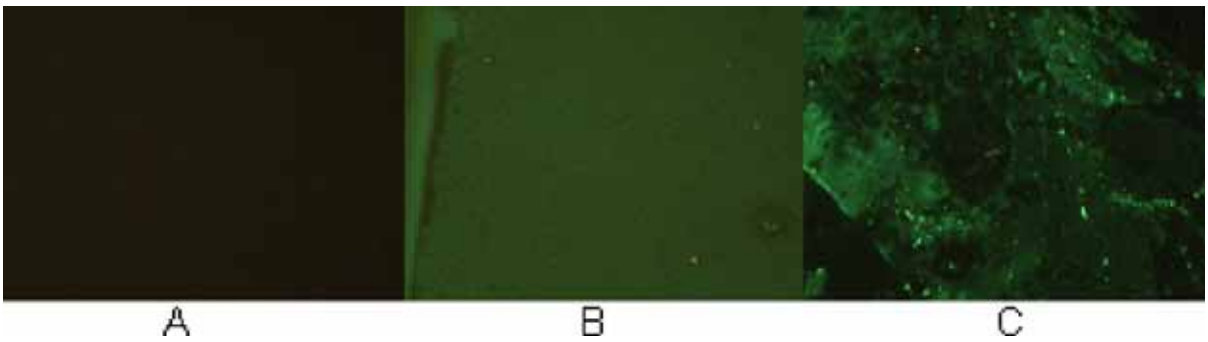

Fig.4.10. Fluorescence microscopy characterizations of the adsorption of 6His-tagged green fluorescent proteins (GFP), onto the different quartz surfaces. (A) PEG-silane, (B) SiO_2, (C) PEGsilane+ Ni nanoislands.

The first attempts to detect the specific interaction of RhoA proteins with probe molecules selective to their active form by QCM using quartz crystals treated with PEG and Ni nanoislands failed. During these experiments, we identified an unexpected adsorption of glycerin on both SiO_2 surfaces and PEG coated surfaces. We thus conclude that minimizing the quantity of glycerin (glycerol) as a cryogenic protectant for proteins storage was mandatory for our experiments. This called glycerine effect, not noticed in traditional ELISA tests, turned out to mask completely the specific proteic interaction we wanted to investigate by QCM. We have thus determined the maximum glycerin percentage compatible with a convenient storage of the proteins and reliable QCM signals. As can be seen in Fig. 4.11, the incubation of a solution containing a ratio of 0.2 % (in volume) of glycerin in HEPES buffer does not induce any significant frequency shift on quartz-SiO_2 coated with PEG and generates only a small variation of 1 Hz on virgin SiO_2 quartz. Conversely, higher glycerin contents (1% or 10%) were found to induce significant unspecific adsorption events on both types of surfaces (see figure 4.11).

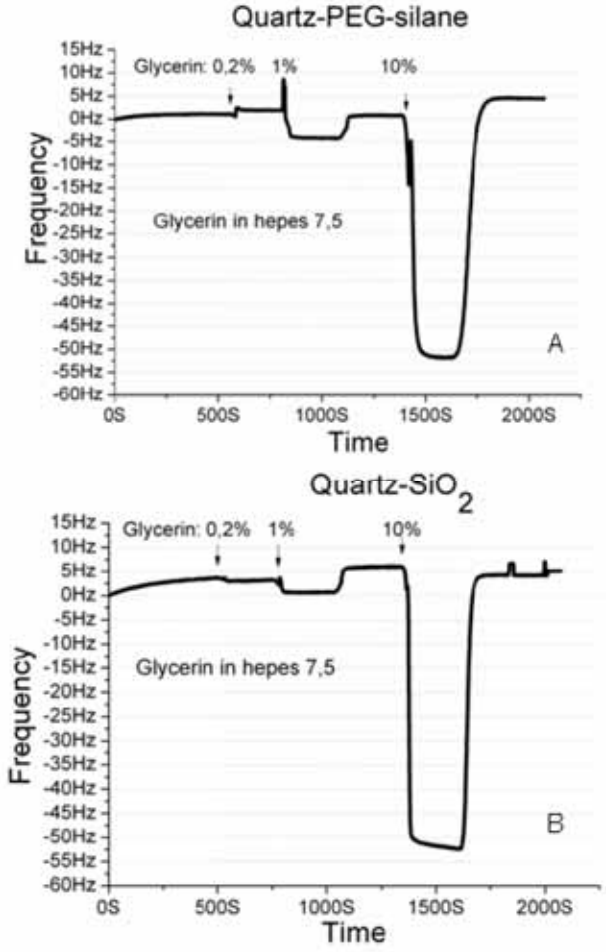

Fig.4.11. QCM signals obtained after the incubation of a solution of glycerin diluted in HEPES buffer at various concentrations (percentage in volume). (a) quartz-SiO_2 coated with PEG (b) virgin quartz-SiO_2.

When there was a percentage of glycerin higher than 0.2 % mixed with the biomolecules of interest, the QCM signals exhibited a response comparable to those of figure 4.11. To avoid this bias, the glycerin content in our solutions was kept below this level.

In the biomarker detection, experiments we used as a probe molecule His-tagged antibody fragments single chain variable fragments (scFv-F7N1N2) that bind selectively to the active antigen conformation RhoA, referred to RhoAGTPgS with respect to the inactive antigen conformation of RhoA referred to RhoAGDP [1]. To verify the ability of this purified scFv to bind nickel atoms while keeping its specificity for the active form of RhoA, an ELISA test was conducted as follows: Ni-NTA microplates were coated with scFv-F7N1N2. Specific interactions were measured by adding serial dilutions of GST-RhoA loaded with GDP or with GTPgS. The amount of GST-RhoA linked to the scFv was measured after adding an anti-GST-HRP conjugate. Fig.4.12 presents the results of these ELISA experiments demonstrating the selectivity of our probe molecule to the active form of RhoA proteins and the good discrimination with respect to the inactive conformation of the same protein.

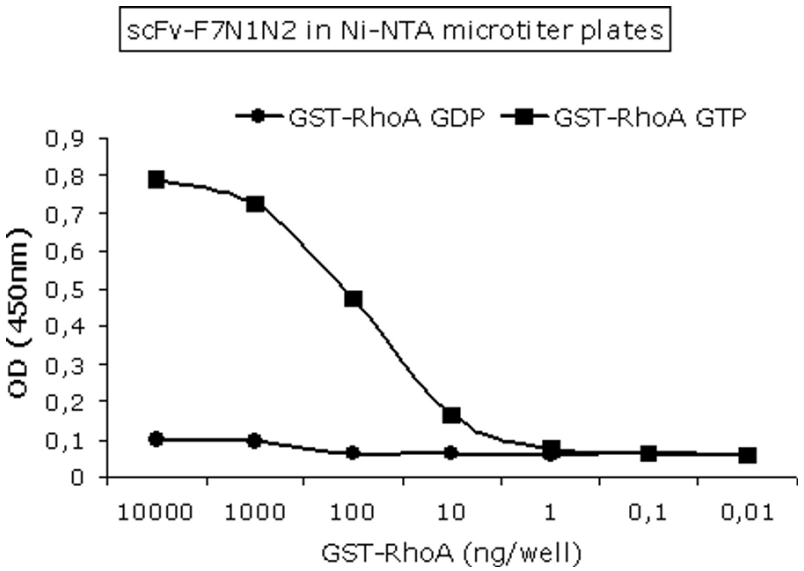

Fig.4.12. ELISA tests showing the selectivity of the selected probe molecule (His tagged scFv-F7N1N2) to the active conformation of RhoA proteins (RhoA GTPgS) compared to the inactive conformation (RhoA GDP) of the same protein.

QCM experiments were finally performed at a flow rate of 60 mL/min on quartz-SiO_2 coated with PEG and equipped with Ni nanoislands. Firstly, Hepes buffer 10mM, NaCL 150mM plus 5mM of $MgCl_2$ was injected onto two similar independent quartz. Quartz 1 was used to detect the active form of RhoA (RhoA GTPgS) and quartz 2 to detect the inactive form of RhoA (RhoA GDP).

The results are depicted in Fig. 4.13. At step 1, a 40µg/ml (Mw 55kD) solution of (scFv-F7N1N2) was injected into both fluidic channels. A frequency variation of around 70 Hz was observed in both quartz, revealing the adsorption of the probe molecules on the surface covered with Ni islands. HEPES buffer was then injected for removing loosely bound molecules and for stabilising the QCM signal. At step 2, a solution of RhoA GTPgS at 4µg/ml (Mw 45kD) was injected onto quartz 1 and a solution of RhoA GDP at 4µg/ml (Mw 45kD) onto quartz 2. In both quartz, it was difficult to observe any specific adsorption. We thus decided to increase the surface density of probe molecules grafted on the Ni nanoislands and incubated at step 3 a 200µg/ml (Mw 55kD) solution of scFv-F7N1N2 that was injected into both fluidic channels.

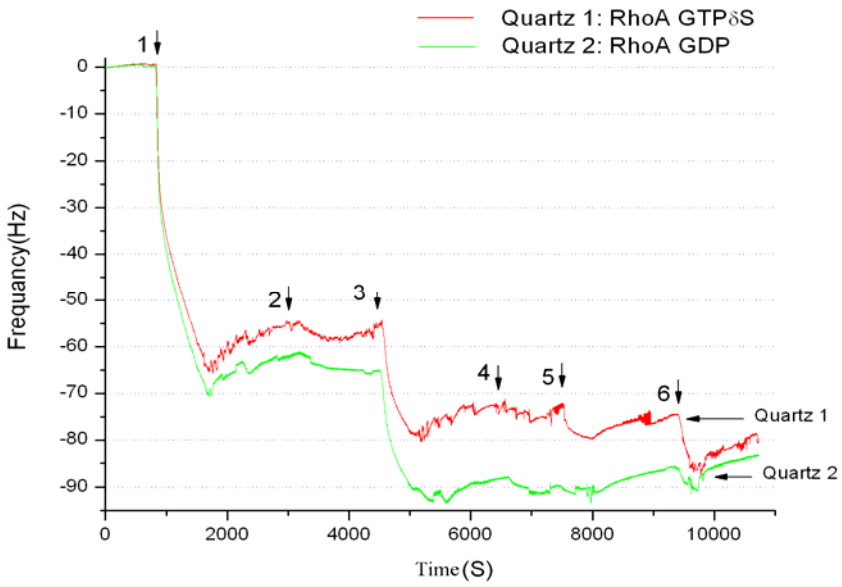

Fig.4.13. QCM Frequency variations of two identical quartz (SiO_2/PEG/Ni nanoislands) subjected to different incubation steps.

An additional low frequency shift of ~25 Hz was observed in both reaction chambers which confirms that the surface was not initially saturated with probe molecules. At step 4, we injected the same concentration of RhoA proteins as at step 2 (4µg/ml) of active and inactive antigens respectively into quartz 1 and quartz 2. A slight frequency shift is observed but cannot be distinctly attributed to a significant stable adsorption on the surface. We then increased the concentration of antigens up to 20µg/ml (step 5) and 40 µg/ml (step 6) of active and inactive antigens, respectively, for quartz 1 and quartz 2. In these cases a clear adsorption signal was recorded in quartz 1 (7Hz at step 5 and 10 Hz at step 6) while no trace of a clear adsorption could be noticed on quartz 2 (see Fig. 4.14 for a better appreciation of the frequency shifts).

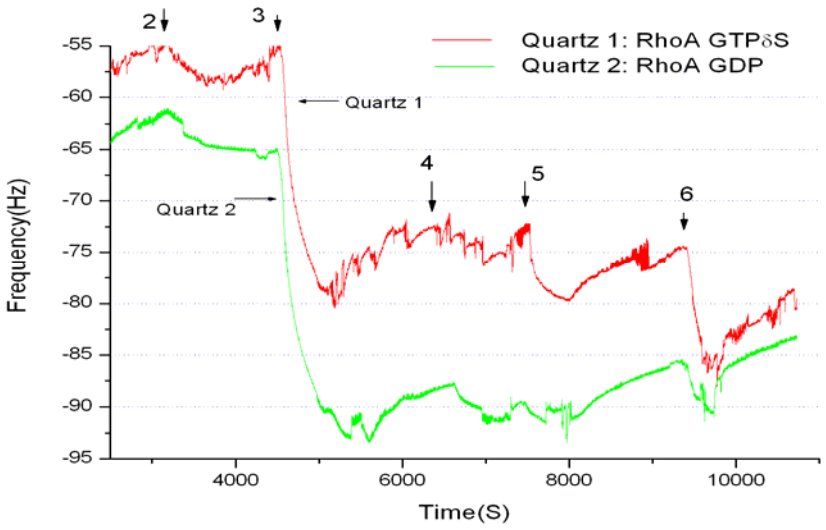

Fig.4.14. Enlarged view of figure 8. Note that at step 5 and 6, the active form of RhoA protein was injected into Quartz 1 and the inactive form of this protein was injected in Quartz 2 (step5 20 µg/mL, step6 40 µg/mL).

The clear difference between the response of Quartz 1 and Quartz 2 indicates that the label-free detection of RhoA proteins in their active conformation can be achieved in our Ni nanoislands deposition in conjunction with the implemented surface chemistry, this by QCM analysis. Hence, this result turned out to be possible only on quartz crystals equipped with nanometric nanoislands of nickel.

4.4 Conclusions

In this chapter, we have implemented a surface chemistry involving an anti-biofouling coating of polyethylene glycol-silane (PEG-silane) (< 2nm thick) onto a SiO_2 thin film combined with the deposition of 5nm size Ni islands. This specific surface chemistry on SiO_2 surfaces turned out to be suitable for attaching probe molecules (antibody fragments) to the Ni islands through Histidine tags. The nanoscale roughness developed by the nanoislands turned out to improve the selectivity of the detection of the conformation of RhoA proteins on these surfaces. Indeed, through QCM analysis we have shown the possibility of a label-free detection of RhoA biomarkers which can discriminate the active and inactive conformations of this protein. We found that glycerin, often used as a cryogenic protectant in molecular biology protocols, produces non-specific biomolecular interactions. A new protocol without glycerin has thus been developed and validated by ELISA technique. This work proves the viability of the concept by using Ni nano-islands as an anchoring surface layer enabling the detection of a specific conformation of a protein identified as a potential cancer biomarker.

This biomolecule detection conjugated with a surface chemistry is the basis to be integrated into the nanobiosensors presented in this thesis. As demonstrated in chapter 3 the Ni nanoislands will be deposited between interdigitated nanoelectrodes. These integrated devices will be used to detect the proteins of interest through conductance variations. Finally, these Multiple Tunnel Junction (MTJ) devices are expected to exhibit high sensitivity or ultralow limits of detection, comparable to nanowire based FET sensors [17]. The advantages will be label-free detection and less analytic product used (close to nanolitter), as it will also have an integrated microfluidic system (demonstrated in chapter 5).

4.5 References

[1] Goffinet M., Chinestra P., Lajoie-Mazenc I., Medale-Giamarchi C., Favre G., Faye J.C., “Identification of a GTP-bound Rho specific scFv molecular sensor by phage display selection”, *BMC Biotechnology*, **2008**, 8, p.1-14.

[2] Richter R, Aydin D., “Quartz Crystal Microbalance with Dissipation monitoring (QCM-D)”, *Practical course in biophysical Chemistry*, Heidelberg University

[3] Höök F, Rudh M, “Quartz crystal microbalances (QCM) in biomolecular recognition”. *BTi* Journal , **2005**.

[4] Kannan Balaji, Castelino Kenneth, Frank Chen Fanqing et al.,“Lithographic techniques and surface chemistries for the fabrication of PEG-passivated protein microarrays”, *Biosensors and Bioelectronics*, **2006**, 21, p.1960-1967.

[5] Sheeny Lan, Mandana Veiseh, Miqin Zhang, "Surface modification of silicon and gold-patterned silicon surfaces for improved biocompatibility and cell patterning selectivity, biosensors and bioelectronics", *Biosensors and Bioelectronic*,**2005**,p.1697-1708.

[6] Sharma Sadhana, Popat Ketul C., Desai Tejal A., *Design and biological applications of nanostructured poly(ethylene Glycol) Film*, USA, **2006**, 500p.

[7] Andrade J., Hlady V., *Adv.Polym. Sci.*, **1986**, 79, 1, p.39-1(26).

[8] Sheth S., Leckband D., "Measurement of attractive forces between proteins and end-grafted poly(ethylene glycol) chains", *Proc. Natl. Acad. Sci*., USA, **1997**,94, p.8399.

[9] Ning-ping Huang, Roger Michel, Janos Voros, "Poy(L-lisine)g-poly(ethylene glycol) layer on metal oxide surfaces: Surface-analytical characterization and resistance to serum and fibrinogen Adsoption", *Langmuir*, **2001**,17,p.489-498.

[10] Papra A, Gadegaard N, Larsen N., "Characterization of Ultrathin poly (ethylene glycol) Monolayers on silicon substrates". *Langmuir,* **2001**, 1, p.1457-1460.

[11] Porath, J., Carlsson, J., Olsson, I., et al., "Metal chelate affinity chromatography, a new approach to protein fractionation", *Nature,* **1975**, 258, p.598-599.

[12] Hainfeld James F., Liu Wenqiu, Halsey Carol M. R., "Ni–NTA–Gold Clusters Target His-Tagged Proteins", *Journal of Structural Biology,* **1999,**127**,** p.185-198.

[13] Schmitt, J., Hess, H., and Stunnenberg, H. G. "Affinity purification of histidine tagged proteins", *Mol. Biol. Rep.*, **1993**, 18, p.223–230.

[14] Palmer RE, Leung C. "Immobilisation of proteins by atomic clusters on surfaces".*Trends in biotech*, **2006**; 25:p.48-55.

[15] Kannan Balaji, Castelino Kenneth, Chen Fanqing Frank, Majumdar Arum. "Lithographic techniques and surface chemistries for the fabrication of PEG-passivated protein microarrays", *Biosensors and Bioelectronics*, **2006**, 21, p.1960-1967.

[16] Kozielski Marek et al., "The Raman scattering study of selected polyoxyethyleneglycols", *Journal of Molecular Liquids*, **2003**, 11: p.1-5.

[17] Zheng Gengfeng, Patolsky Fernando,Cui Yi, Cui Yi, Wang U Wayne, Lieber M. Charles. "Multiplexed electrical detection of cancer markers with nanowire sensor arrays", *Nat. Biotechnol.*, **2005**,23:10,p.1294-1301.

Chapter V

Innovative microfluidic system methodology for Lab-on-chips applications at wafer scale

5.1 General introduction

Microfluidic systems are applied in modern medical analysis, environmental monitoring and several fields of research and applications e.g. for detection and separation of proteins [1], for single cell analysis [2], in biochemical and clinical analysis [3], as portable microfluidic platforms for diagnosis of cancer [4], or in drug discovery [5]. Hence the importance in making microfluidic systems has increased in the last two decades, mainly for the realisation of viable lab-on-a-chip (LOC) [6] and hybrid integrated nanodevices [7].

The most common materials used to fabricate microchannels are silicones like polydimethylsiloxane (PDMS). These elastomeric materials are easy to cast with properties like impermeability to water, non toxicity to cells or permeability to gases [8]. Furthermore, PDMS-based elastomers have an UV optical transparency from 240nm to 1100nm wavelength and an elastomeric property with a tunable Young's modulus: typical value can range from 750 kPa to 4MPa [9]. However, because of its chemistry, PDMS elastomers cannot be photopatterned directly to elaborate complex microfluidic systems. In this context, new processes to obtain photoPDMS are indispensable.

On the other hand, one of the most delicate steps in the micro/nano fluidic system design and development is the realisation of tubes interconnection and device packaging [10]. Finally, there is an inevitable shrinkage problem encountered in PDMS when curing it [11]. In this chapter, I overcome these three bottlenecks as follows:

Firstly, a negative photodefinable polydimethylsiloxane (N-photoPDMS) covalently bonded on wafer surfaces; reaching a resolution of 20 µm at wafer level is presented. Next, an optimisation process for positive photodefineable polydimethylsiloxane (P-photoPDMS) reaching a resolution of 60 µm, is conducted. To show that both photoPDMS processes can be applied to the fabrication of lab-on-chips devices, 192 microchannels (20µm width) have been aligned on the interdigitated nanoelectrode devices (IND) at wafer level. Mechanical properties after cross-linking in N-photoPDMS are presented. These two processes are low-cost and are conceived for rapid prototyping. Indeed, these two complementary methodologies can be adapted to a large number of applications.

Secondly, interconnection of 3-D microfluidic system on 4 in. wafer scale is presented. An etching is performed in both unmodified PDMS and in a PDMS nanocomposite material specifically elaborated. We obtain faster and more homogenous rate etching in this kind of PDMS nanocomposite. Finally some pressure tests are conducted in this microfluidic device.

Thirdly and finally, modification in the master mould is conducted to compensate for the inevitable shrinkage when curing a PDMS. A study is presented, and some perspectives are proposed to formulate a more exact shrinkage ratio equation.

Because of this planning, this chapter is divided into three sections, as if they were three

small chapters, but described in interdependent manner, so these sections will have their own reference section. The three sections are part of an innovative microfluidic methodology to be integrated in our nanobiosensor device.

Microfluidic engineering and technology are not described here, but there are several references proposed throughout this chapter and some general references are [22] [23].

5.2 PHOTOPDMS FOR MICROCHANNELS FABRICATION

In the literature, a negative photodefinable polydimethylsiloxane (N-photoPDMS) was developed by Lötters et al. [12], based on a commercial polysiloxane bearing methacrylate groups and 2,2-dimethoxy-2-phenyl acetophenone as photoinitiator. It is the closest method compared to our N-photoPDMS we present here, however the photoinitiator is not easy to dissolve at ambient temperature and the crosslinking had to be performed in absence of oxygen. Dow Corning commercialises a PDMS that can be photopatterned but only after several steps and for thicknesses between 6µm and 50µm [13]. The basic chemistry consists in hydrosilylation reactions which are facilitated in the presence of a photoreagent under UV irradiation. Nonetheless, this methodology still necessitates a soft baking before UV treatment followed by post-exposure baking to finish the synthesis of the material. Others authors have presented non commercial polysiloxanes that are UV-sensitive, but these imply specific syntheses [14].

On the other hand, a positive photodefineable polydimethylsiloxane (P-photoPDMS) was described last year by Papautsky et al. [15], using the popular Sylgard 184 in a clever process. Mixing the polymer with benzophenone which functions as photoinhibitor, they showed that this led to the inhibition of the crosslinking process under the irradiated zones. The exposure was performed at <360nm wavelength implying the use of expensive high resolution chrome masks (transmittance from 200 nm). The limit resolution for these two photoPDMS types was not presented.

Collaboration with chemists from LCC-CNRS and IMRCP-CNRS at Toulouse France was established, because they had been developing the N-photoPDMS and by that time, we were adapting the P-PhotoPDMS. Then, we started working together with Mrs. Anne-Françoise Mingotaud and Mr. Samuel Suhard to reach the resolution limit in these two types of photoPDMS, and mainly to apply them to functional devices, like those we are presenting in this thesis.

In this context, firstly we present here, the N-photoPDMS methodology. A negative photopatternable polydimethylsiloxane (N-photoPDMS) covalently bonded on surfaces by grafting acrylates moieties is presented. Next, a commercial PDMS containing methacryloyl groups is mixed with Irgacure 2100 as photoinitiator, leading to 20µm resolution on wafer level. The mechanical properties of N-photoPDMS are assessed by piezorheometry too.

We also present an improvement of the P-photoPDMS process to reach 60µm on wafer scale. We use benzophenone acting as photoinhibitor as described by Papautsky et al. [15] but with UV peak absorption at ~360nm (4-Dimethylaminobenophenone). At this wavelength, we can use low cost masks (soda lime glass with transmittance from ~360nm).

To validate an application in functional LOCs devices, we aligned 192 microchannels (20µm) on previously demonstrated wafer scale realisation of 768 interdigitated nanoelectrodes devices (IND) [16] serving as nanobiosensors which were described in detail in chapter 2.

5.2.1 Methods, material and experimental section

RMS 083 and acryloxypropyltrimethoxysilane were purchased from ABCR, Sylgard 184 was purchased from Dow Corning. Irgacure 2100 was given by Ciba. Toluene was purchased from Sigma-Aldrich and methylisobutylketone (MIBK) from Honeywell. Crystalline benzophenone was purchased from Sigma-Aldrich and 4 inch silicon wafers were oxidised with SiO_2 (1µm) in our clean room facility.

5.2.1.1 Negative photoPDMS fabrication

To enhance polymer adhesion on SiO_2 surfaces, a wafer was first treated by O_2 plasma (140 Watts) for 30 min., and was immersed immediately in water to generate Si-OH moieties and finally dried under vacuum and placed under argon. For the chemistry functionalisation, 50 ml of toluene were added followed by addition of 2.5 ml acryloxypropyltrimethoxysilane, this allows sticking covalently the polymer.

In a second step, a degassed mixture containing RMS-083 and Irgacure 2100 as the photoinitiator (2% w/w) was used. RMS-083 is a copolymer of dimethyl and methacryloxypropylmethyl siloxane. The percentage of methacrylate monomer units lies between 7 % and 9 % and its kinematic viscosity is in the 2000-3000 cSt range corresponding to a molecular weight in the 40000 g. mol^{-1} range. Schema 5.1 illustrates the chemical pathways, showing the binding of acrylate functions to the wafer, followed by the photocrosslinking of the siloxane polymer which at the same time links it to the surface of the wafer.

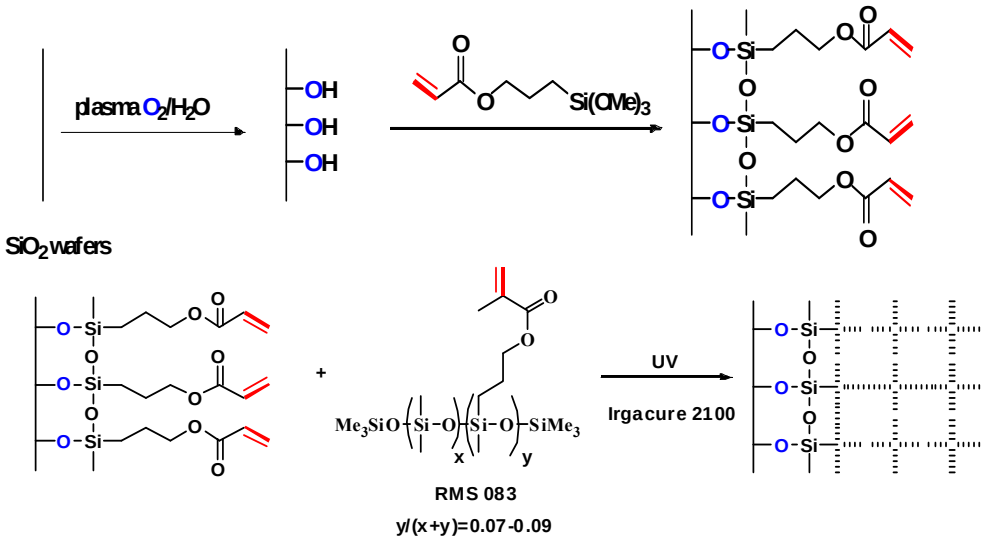

Schema5.1. Chemical steps in the synthesis of N-photoPDMS grafted onto Si/SiO2 wafers.

Next, the compound was spin-coated on 4 in. silicon wafer (oxidised with SiO_2 layer, 1µm thick) at 2000 rpm to obtain a layer of PDMS with a thickness of 26 µm (measured with a mechanical profilometer P15 model). We used a low cost chrome mask made of soda lime glass carrying some periodical patterns to determine the resolution in photoPDMS and two microchannels, see Fig.5.2.1. Mask was positioned, using an EVG 620 machine, above the spin-coated PDMS wafer, maintaining a gap of 50 µm between the mask and the wafer to avoid touching the uncured photoPDMS. The exposure step was conducted in an EVG 620

machine (350-450nm, 75mW/cm²), during 1 minute. No adjustment of the machine was necessary and no purge of the system was used before irradiation. Development was performed in methylisobutylketone (MIBK): isopropanol (IPA), 1:1 in volume, during 3 minutes.

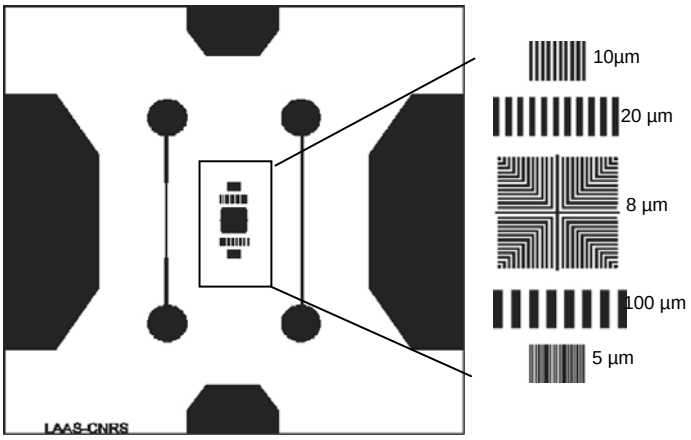

Fig.5.2.1 Design of one cell (7mm x 7mm) for N-photoPDMS tests. Close-up of periodical lines to determine the limit resolution (on the right).

Fig. 5.2.1 illustrates one cell of the 96 designed on 4 in. wafer. As in this case N-photoPDMS is used, the patterns are protected (black patterns) as pictured in the figure. On the centre, there are lines and space periodical patterns of various dimensions for the resolution determination and two microchannels with 50µm and 20µm width, with circular (500µm diameter) as inlets-outlets. Each cell has also four patterns on the side, once opened they are used to make microbondings, after encapsulating each cell on TO-8 cases as illustrated in next part.

5.2.1.2 Positive photoPDMS fabrication

To enhance adhesion on wafer surfaces, simple treatment by O_2 plasma (300W) for 3 min was applied by a Tepla model 300 plasma machine. We used 4-dimethylaminobenzophenone as photoinititiator, with a UV peak at 360 nm. Sylgard 184 was mixed in a 10:1 w/w ratio with its curing agent and degassed for 10 min to remove the formed bubbles. A 3% w/w solution of the benzophenone in toluene was added. As in this case a P-photoPDMS is used, the chrome low cost mask carries no protected patterns as Fig. 5.2.2 pictures.

The p-photoPDMS was spin-coated at 2000 rpm to obtain ~26 µm of PDMS thickness on the 4 in. wafer (measured with a mechanical profilometer P15 model), the exposure step was conducted in an EVG 620 machine (350nm-450nm, 75mW/cm²) during 10 minutes, maintaining a gap of 70 µm between the mask and the wafer, to avoid touching the uncured photoPDMS. After that, a post-exposure baking was performed in an oven at 80°C during 5 min. Finnally, development was performed in methylisobutylketone (MIBK): isopropanol (IPA), 1:1 in volume, during 5 minutes.

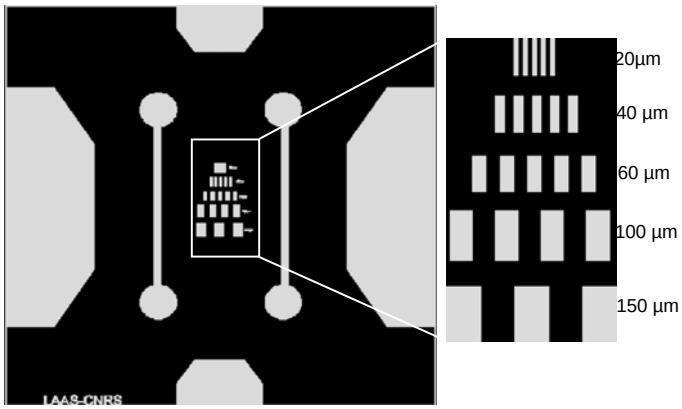

Fig.5.2.2. Design of one cell (7mm X 7 mm) for P-photoPDMS tests. Close-up of periodical lines to determine limit the resolution (on the right).

5.2.1.3 Mechanical measurements

The complex shear modulus G = G' + iG'' of the sample was measured as a function of frequency with the piezo-rheometer developed these last years for studying the rheological properties of polymers [17], liquid crystal elastomers [18] and uniaxial magnetic gels [19]. The principle of this apparatus consists of applying a small strain ε to the sample by means of a piezoelectric ceramic vibrating in the shear mode, and measuring the amplitude and the phase φ of the shear stress σ transmitted through the sample using a second piezoelectric ceramic. The complex shear modulus of the sample is given by the stress over strain ratio $G = \sigma/\varepsilon$. The sample has an elastic response when the strain and the stress are in-phase (φ = 0), and a viscous response when the strain and the stress have a phase difference φ of 90°. For a viscoelastic sample, the phase difference φ is in between 0° and 90°.

In practice, the compound is placed between two glass slides, each of which is stuck to one of the ceramics. G was determined for frequencies ranging from a few 10^{-1} Hz to a few 10^{3} Hz. The applied strain ε was very small ~10^{-4}, and the validity of the linear response checked experimentally.

5.2.2 Results and discussion for N-photoPDMS

Using the procedure described above, it was possible to assess the limit of resolution attained with N-photoPDMS. Fig. 5.2.3 shows the patterns designed after development the N-photoPDMS. The line-shape patterns were opened and allowed us to determine a resolution because they are periodically arranged. As shown in figure 5.2.3 (b), 20µm resolution is reached at wafer level and the thickness of the N-photoPDMS used in these experiments is 27 µm. Reproducible and proper microchannels were obtained.

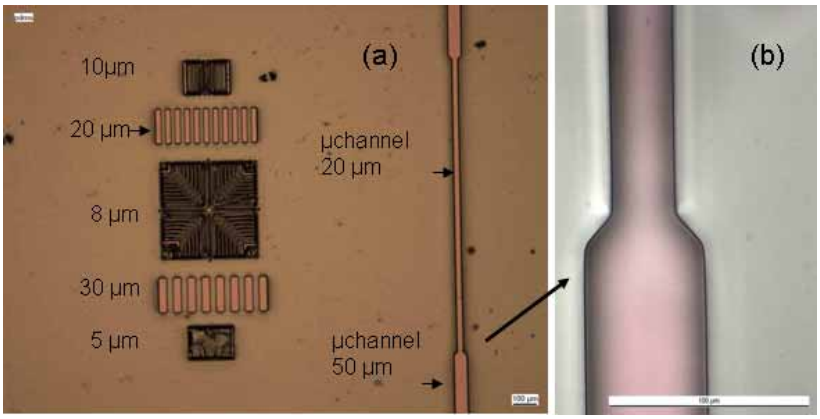

Fig.5.2.3. (a) N- PhotoPDMS showing limit resolution, (b) Enlarged channel illustrating excellent and proper 20µm, 50µm channels, exposure time of 1 min.

Periodical patterns measuring 5µm, 8µm and 10µm were not successfully developed as Fig. 5.2.3 (a) illustrates. From 20µm width, patterns were properly developed on wafer level, thus alignments on wafer scale for lab-on-chips application can be accomplished.

The same process was also used by our collaborators, in the elaboration of a system incorporated in a microactuator, obtaining cavities of 500 µm in width for 125 µm in height. Hence, it is possible to use this N-photoPDMS for several thicknesses requirements. Fig. 5.2.4 demonstrates that this method can be used to elaborate either large patterns or small micrometric ones. In some cases, isolated patterns as small as a few micrometers, were clearly obtained, pictured in figure 5.2.4 (d).

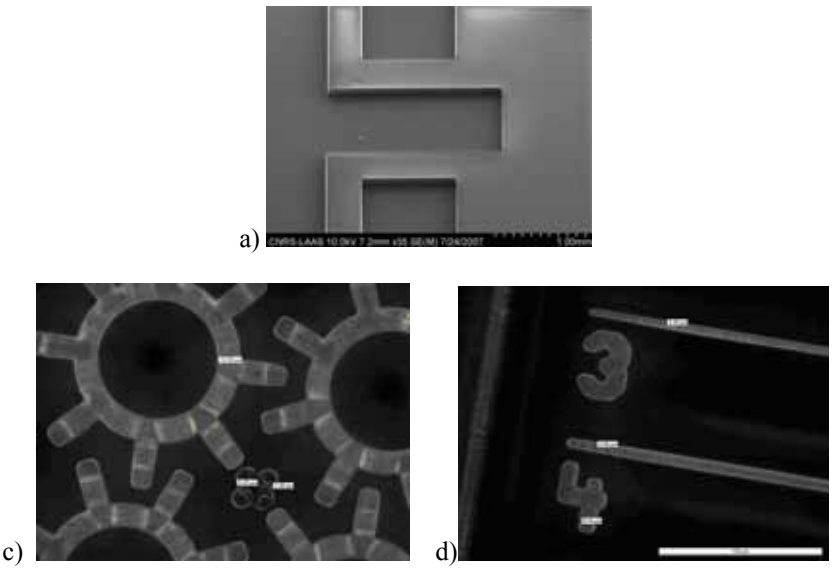

Fig.5.2.4. (a) Square-shape cavities (1mm x 1mm x 125µm). (b) Notched wheels (internal diameter: 85µm, with 13µm width, and 27µm thick). (c) Lines of 3µm and 4 µm width.

5.2.2.1 Process optimisation in N-photoPDMS

The N-photoPDMS process was optimised by examining the effect of the UV exposure time. One minute was determined as the optimum time. To do this, different parts of the wafer were irradiated using the same EVG 620 aligner machine, increasing from 30 s to 300 s by steps of 30s.

The minimum gap between the wafer and the mask we were able to use was 50µm, to avoid a contact between the mask and the uncrosslinked polymer. After finishing the process, a study of the mechanical properties was conducted by piezorheometry, this study was performed by our collaborator at Institut Charles Sandron in Strasbourg France. This method has the advantage of being a technique specifically designed for thin films characterisation. The results obtained on a 100 µm thickness sample are shown in Fig. 5.2.5. The curves obtained are typical of a solid such as chemical gel or elastomer with a constant storage modulus and a loss modulus that can be seen at high frequencies. Thus, the material is gel-like with a Young's modulus of 0.45 MPa (assuming E = 3G'), which is slightly lower than Sylgard's which is usually described between 750kPa up to 4MPa.

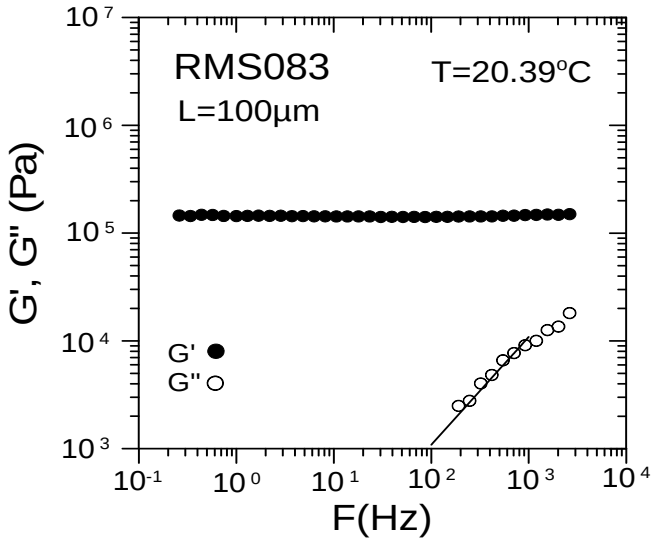

Fig.5.2.5. Determination of mechanical properties of N-photoPDMS RMS083 by piezorheometry. The straight line represents the terminal behaviour of G'' (G'' ~ F).

5.2.3 Results and discussion for P-photoPDMS

The limit of resolution for P-photoPDMS was also determined. Fig. 5.2.6 shows the patterns after development. As in the complementary N-photoPDMS technique, the line-shape patterns were opened and allowed us also to determine a resolution. Proper microchannels were obtained at wafer level.

Periodical patterns measuring 20 µm and 40 µm were not successfully developed as Fig. 5.2.6 (a) illustrates. Patterns of 60 µm width were developed on wafer level. In this case, the limit resolution is not as high as in N-photoPDMS. However by using this kind of photoPDMS, it is not necessary to perform a surface chemistry to enhance adhesion of the P-photoPDMS. Furthermore, the P-PhotoPDMS keeps its Young's modulus (Sylgard 184 Young modulus) as shown in the literature.

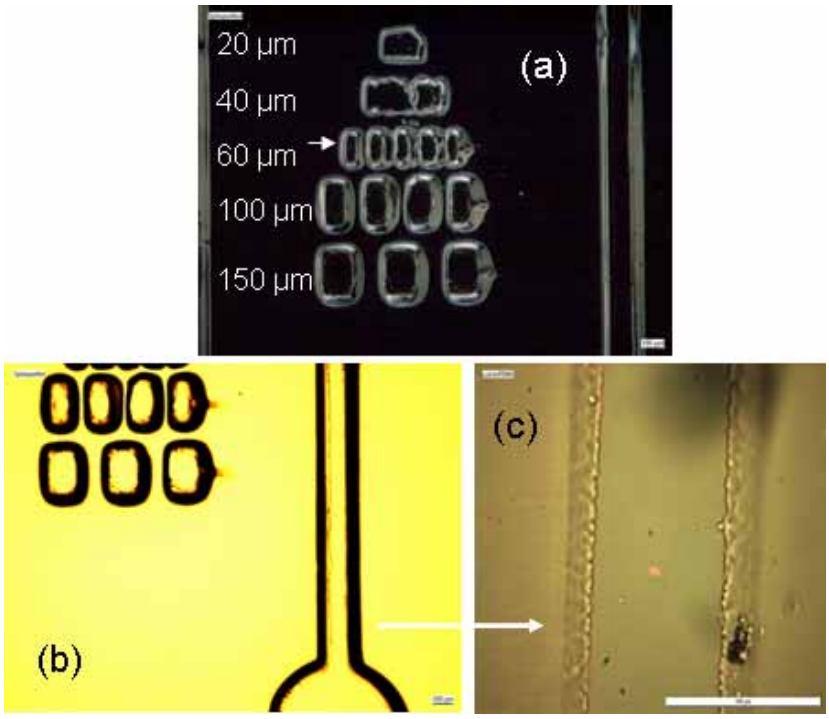

Fig.5.2.6. (a) Optical dark field image of the P-PhotoPDMS showing its limit resolution, (b) enlarged channel, (c) proper 80µm channel, exposure time of 10 min.

5.2.3.1 Process optimisation in P-photoPDMS

The P-photoPDMS process was also optimised by examining the effect of the UV exposure time. To do this, different parts of the wafer were irradiated using the same EVG 620 aligner machine, increasing from 120 s to 1200 s, by steps of 120 s. Ten minutes were determined as the optimum time. If less time of exposition is used, some patterns are not properly developed and if it is exposed for more time, the patterns appear bigger after development and it is not possible to determine the limit resolution.

The minimum gap between the wafer and the mask we were able to use was 70 µm, to avoid a contact between the mask and the uncrosslinked polymer. Mechanical properties were not conducted in this case since they are already described in the literature.

I tested several similar PDMS, for example, the RTV615 from GE Bayer silicones purchased from AB Chimie Sarl France or DMS-V35 purchased from GELEST. In these kinds of silicones, the irradiated parts remain uncured because they contain vinyl group which react with benzophenone radicals [15]. However these two types of PDMS did not work as the Syligard 184 did. Probably the quantity of the vinyl termination in the Sylgard can be the reason but perhaps because of other parameters found in each silicone. A table comparing the RTV 615 and the Sylgard 184 is presented in this chapter (section three).

5.2.4 Wafer scale microfluidic realisation for viable LOCs

Figure 5.2.7 shows two complete cells of the 96 elaborated in the wafer. They are made of N-photoPDMS and P-photoPDMS, respectively.

Images demonstrate that these two complementary techniques can be used to a large variety of applications, for example if an acrylate-based surface chemistry is not possible to used on

the wafer surface, P-photoPDMS is more convenient. Otherwise, if a higher resolution is required, the use of N-photoPDMS is more convenient. We decided to use N-photoPDMS to demonstrate a viable application.

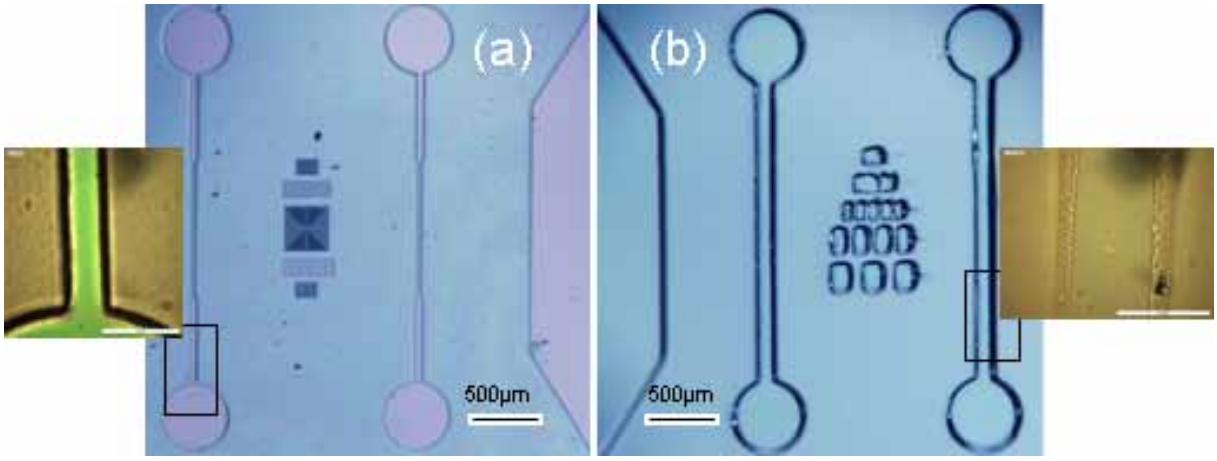

Fig.5.2.7. (a) Optical image of one cell realised by using N-photoPDMS, (b) Optical image of one cell realised by using P-photoPDMS.

To demonstrate and application, microchannels were then aligned on 768 interdigitated nanoelectrodes devices (IND), previously demonstrated in chapter 2.

Then, subsequently two N-photoPDMS microchannels (20µm) were aligned on each of the 96 cells (7 mm X 7 mm). We remember that each cell has two columns containing four IND (and 4 micropads measuring 400 µm x 400 µm on each side to be used for electrical characterisations of the device), see Fig.5.2.8. Well defined N-photoPDMS microfluidic channels (20 µm) fabricated and aligned in one step at wafer level can be seen on this figure. Apertures on each cell side can be used for microbondings step.

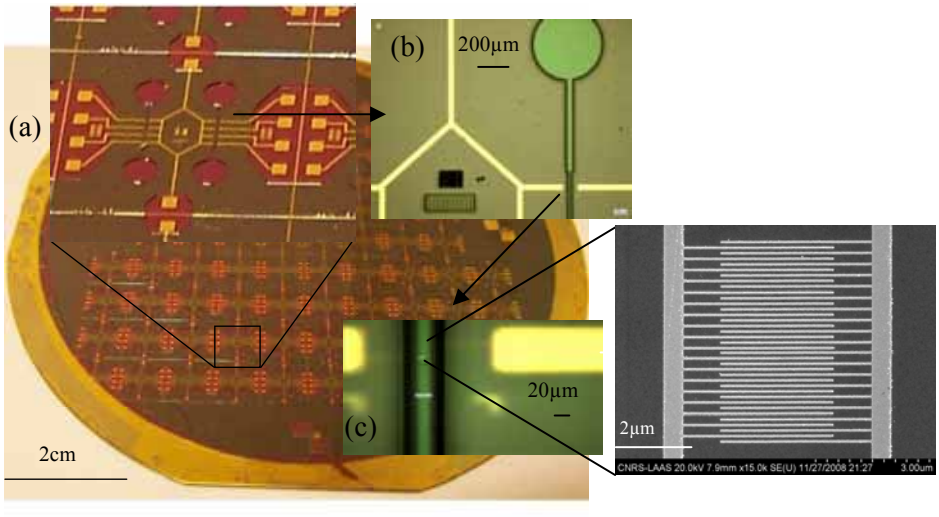

Fig.5.2.8. N-PhotoPDMS alignment on wafer scale for functional LOCs applications, (a) close-up showing excellent alignment in each 7mmx7mm cell, (b)(c) Close-up of microchannels successfully aligned and a SEM image of one IND (45nm width each electrode).

The 96 cells of the 4 inch wafer containing N-photoPDMS-aligned microchannels (20 µm width) were cut and some of them encapsulated in TO-8 cases. See Fig.5.2.9, these functional nanobiosensors devices (encapsulated and integrated with microfluidic channels) have been successfully characterised electrically, presenting electrical tunnel conduction and coulomb blockade, at room temperature as demonstrated in chapter 3. Then our devices based on multitunnel junction conductivities are almost already to be used to detect, at high sensitivity, cancer biomarkers.

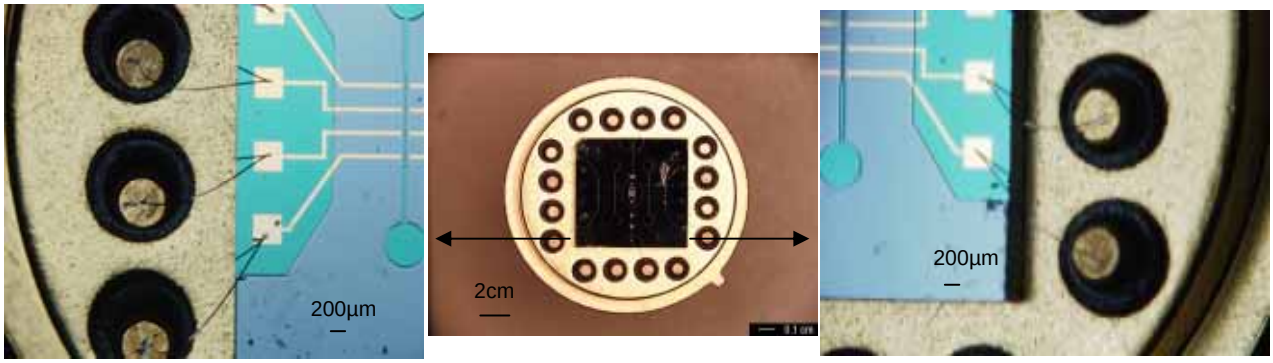

Fig.5.2.9. (a) one cell (7 mm X 7 mm) encapsulated in TO-8 case showing microbonding into the apertures realised by using N-photoPDMS.

Microfluidic channels developed by N-photoPDMS are useful to guide the biological flow to be analysed. A full encapsulated cell is pictured in Fig. 5.2.10. It shows also both microchannels on the right picture and microbondings.

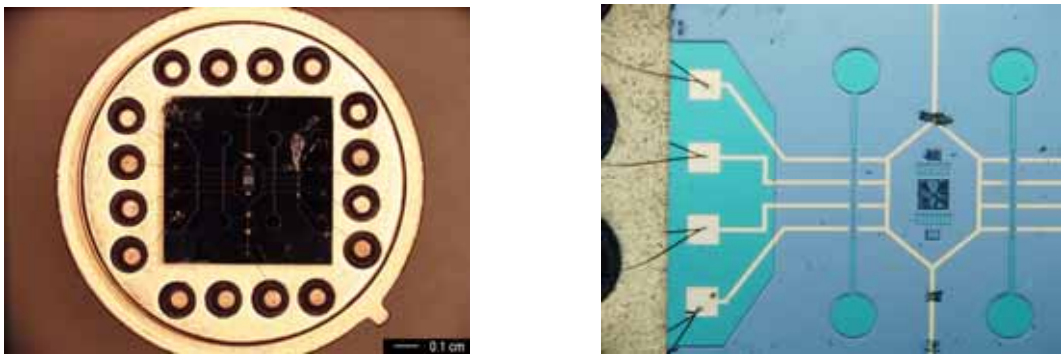

Fig.5.2.10. One cell encapsulated in TO-8, on the right a cell showing microbondings and both microchannels properly aligned on IND.

5.2.5 Conclusions

In the present section, we have presented two kinds of photoPDMS to realise complex microfludic devices.

One of these kinds of photoPDMS is negative type which was named N-PhotoPDMS. It was bonded covalently on surfaces, reaching a resolution of 20 µm to make microchannels on 4 in. wafer. In a second step, mechanical characterisations of N-photoPDMS were performed by piezorheometry technique.

We have also improved the development in the other positive type photoPDMS, named P-

photoPDMS. It allowed us to use chrome low cost patterned mask and principally we were able to reach a resolution of 60µm on wafer scale.

We have demonstrated possible applications by aligning 192 microchannels (20 µm) on a previously demonstrated wafer scale realisation of 768 interdigitated nanoelectrodes devices (IND) serving as nanobiosensors, that are part of the project we are presenting in this thesis. These cells were firstly cut and encapsulated into TO-8 cases. Secondly microbondings were successfully performed on the apertures elaborated by N-photoPDMS.

Finally, these multitunnel junction devices will be used to detect, at high sensitivity, cancer biomarkers by a biology and chemistry presented in chapter 4 (submitted [20]). However before presenting the complete integration and biological validation, we present, in this chapter, the methodology we will follow to encapsulate and interconnect the photoPDMS-based microchannels.

5.2.6 References

[1] Dou Y. H, Bao N., Xu J. J., Meng F., Chen H. Y., "Separation of proteins on surface-modified poly(dimethylsiloxane) microfluidic devices", *Electrophoresis*, **2004**, 25, p.3024-3031.

[2] Wheeler A. R., Throndset W. R., Whelan R. J., Leach A. M., Zare R. N., Liao Y. H, et al., "Microfluidic device for single-cell analysis ", *Anal. Chem.,* **2003**, 75, p.3581-3586.

[3] Shaikh K.A., Ryu K. S., Goluch E. D., Nam J. M., Liu J., Thaxton C. S., et al., "A modular microfluidic architecture for integrated biochemical analysis", *PNAS*, **2005**, 102(28), p.9745-9750.

[4] Pilarski L. M., Adamia S., Pilarski P. M., Prakash R., Lauzon J., Backhouse C. J., "Improved diagnosis and monitoring of cancer using portable microfluidics platforms", Proc. Inter. Conf. on MEMS, NANO and Smart Systems (ICMENS'04), *IEEE*, **2004**, p.340-343.

[5] Dittrich P. S., Manz A., "Lab-on-a-chip: microfluidics in drug discovery", *Nature Reviews Drug Discover,* **2006**, 5, p.210-218.

[6] Mitchell P., "Microfluidics-downsizing large-scale biology", *Nature Biotechnology*, **2001**, 19, p.717-721.

[7] Brunner C., Ernst K. H., Hess H., Vogel V., "Lifetime of biomolecules in polymer-based hybrid nanodevices", *Nanotechnology*, **2004**, 15, p.S540-S548.

[8] Sia S. K, Whitesides G. M., "Microfluidic devices fabricated in poly(dimethylsiloxane) for biological studies", *Electrophoresis*, **2003**, 24, p.3563-3676.

[9] McDonald J. Cooper, Whitesides George M., "Poly(dimethylsiloxane) as a material for fabricating microfluidic devices", *Accounts of Chemical Research*, **2002**, 35 (7), p.491-499.

[10] N. S. Korivi, L. Jiang, "A generic chip to word Fluidic interconnect system for microfluidic devices",*39th Southearn Sympsium on System Theory IEEE*, Macon GA, **2007**.

[11] Seok Woo Lee. Seung S. Lee, "Shrinkage ratio of PDMS and its alignment method for the wafer level process", *Microsyst. Technol.*, **2008**, 14, p.205-208.

[12] Lötters J. C., Olthuis W., Veltink P. H., Bergveld P., "Polydimethylsiloxane, a photocurable rubberelastic polymer used as spring material in micromechanical sensors", *J. Micromech. Microeng*. **1997**, 7, p.64-67.

[13] Patternable Silicones for Electronics, Product Data Sheet, Dow Corning (**2005**).

[14] Pouliquen L., Coqueret X., *Macromol. Chem. Phys.*, 1996, 197, 4045-4060.
Chen J., Vaino A.R., Smith R.L., Collins S.C., *J. Polym. Sci. A*, **2008**, 46, 3482.

[15] Bhagat Ali Asgar S., Jothimuthu Preetha and Papautsky Ian, "Photodefinable polydimethylsiloxane (PDMS) for rapid lab-on-a-chip prototyping polydefinable*", Lab. Chip.*, **2007**, 7, p.1192-1197.

[16] Martinez Rivas Adrian, Séverac Childérick, Carcenac Franck, Saya Daisuke, Nicu Liviu, Vieu Christophe, "Wafer scale deposition of liquid solution on interdigitated nanoelectrode devices for high sensitive multiplexed biological analysis", *Abstract MNE conference*, **2008**.

[17] D. Collin, P. Martinoty, *Physica*, **2003**, A 320, 235.

[18] D. Rogez, G. Francius, H. Finkelmann, P. Martinoty*, Eur. Phys. J. E*, **2006**, 20, 369.

[19] D. Collin, G. Auernhammer, O. Gavat, P. Martinoty, H. Brand, Macromol. *Rapid Commun.*, **2003**, 24, 737.

[20] Martínez Rivas Adrián, Chinestra Patrick, Favre Gilles, Pinaud Sébastien, Séverac Childérick, Faye Jean-Charles, Vieu Christophe, "Label-free cancer biomarkers detection using nickel nanoislands and quartz crystal microbalance", *Nanomedicine: Nanotechnology, Biology and Medicine*, summited **2008**.

[21] S. Suhard, P. Fau, B. Chaudret, S. Sabo-Etienne, M. Mauzac, A.-F. Mingotaud, G. Ardila-Rodriguez, C. Rossi, M.-F. Guimon, Chem. Mat, *accepted*, 2008.

[22] Tabeling P., *Introduction à la microfluidique*, ed. Belin, **2003**.

[23] Colin S., *Microfluidique*, *ed.* Hermes Science publications, **2004**.

5.3 INTERCONNECTION AND BONDING MICROFLUIDICS

One of the most delicate steps in the micro/nano fluidic systems design and development is the realisation of tube interconnections but also device packaging [1]. One of the reasons is the dimensional incompatibility in connecting micro or nano-scale devices to macro-scale devices. Indeed, mechanical problems and leakage fluidic are important bottlenecks in the system. Several approaches proposed for packaging and interconnect fluidic devices using PDMS have been proposed [2-7] and recently some robust systems too [8][9]. However, the holes for connecting tubes are not proper to avoid leakage problems, and the systems are not intended for a parallel alignment and realisation of inlets and outlets on wafer scale.

In this second section of this chapter, we present the realisation and interconnection of 3-D microfluidic systems on 4 in. wafer scale. To do that, SU-8 master mould is elaborated by stacking two layers of 10µm and 500µm. Next, PDMS is poured onto the 4 in. master mould which allows obtaining PDMS with ~480 µm thick and residual thin PDMS films (~20 µm) on the inlets-outlets emplacement. Physical etching method is used then to remove these residual films. Finally, we obtain proper circular inlets-outlets interconnecting holes.

On the other hand, as written in the introduction section the polydimethylsiloxane (PDMS) is the silicone material most often used in microfluidic systems, however this unmodified PDMS (called also pristine PDMS) has some disadvantages e.g. absorption of organic solvents, poor electroosmotic flow (EOF) or poor mechanical strength [10]. The reinforcement of elastomers like PDMS is especially important for some applications because some physical properties like modulus, tensile strength or tear strength increase (characteristics recently summarised by H.Zou et al. [11]). To reinforce elastomers, chemists often use nanoparticle fillers as fumed silica. One method is called blending; this method consists of directly mixing nanoparticles with elatomers. We used this simple method to reinforce our PDMS and to obtain a PDMS nanocomposite by mixing silica nanoparticles into PDMS to improve its mechanical properties.

Otherwise, a few works have been reported to etch pristine PDMS [12-14] and there have not been works dedicated to the etching of PDMS nanocomposite to elaborate apertures (vias) for tube interconnections and packaging realisation on 4 in. wafer. Here, we show also that homogeneity and rate etching involved in PDMS nanocomposite increases, compared to unmodified PDMS.

Finally, we use typical plasma method to bond a PDMS film on glass wafer, this permits us realise pressure characterisations. We propose also another chemical compound we elaborated, to bond the PDMS onto the glass wafer if it is not possible to use the common plasma method. Hence, this section will enable us to encapsulate the microchannels made of photoPDMS, and to bond the interconnecting tubes to inject the biological flow to be analysed.

5.3.1 Methods, material and experimental section

5.3.1.1 SU-8 photoresist process

First, we present here the elaboration of the 4 in. mould. All designs were realised in CleWin and printed onto transparent glass masks (low cost) using a direct-laser based generator machine for masks fabrication (Heidelberg DWL 200L, Germany).

To fabricate the mould, two layers were used which allow obtaining a homogenous PDMS film of ~480 µm thick and thin PDMS films of ~20µm thick placed in interconnecting tubes emplacement. In these conditions, this methodology prevents us from using a glass capillary to punch the PDMS after casting it, as reported elsewhere [3], because by punching it is not possible to obtain proper holes apertures that avoid leakage. Furthermore, it is not a parallel method for 4 in. wafer realisation.

The methodology followed here consisted in doing first the 10µm thickness process. Then, SU-8 3005 (Microchem Corp) was spin coated at 900 rpm, soft cure was conducted at 65°C during 60s. The exposure was performed in a Suss Microtec MA-150 (100mJ).The post bake was accomplished at 95°C during 3 min. and the wafer was developed in PropyleneGlycolmono MethylEther Acetate (PGMEA), followed by rinsing in isopronanol (IPA). Finally a hard bake was conducted at 125°C during 1min.

SU-8 (10µm thick) defines microchannels in each cell. Microchannels are 10µm height, 10µm width in the middle and 50µm width on the border. Fig. 5.3.1 schematises in 3D the two SU-8 processes. The design has four circle-shape patterns to define inlet and outlet interconnection holes. The design has also four rectangular-shape patterns which serve to realise microbondings after being opened as in the case of photoPDMS. In the middle, the design has several lines, in this case, employed as moiré method (interference patterns) to realise alignments in each cell.

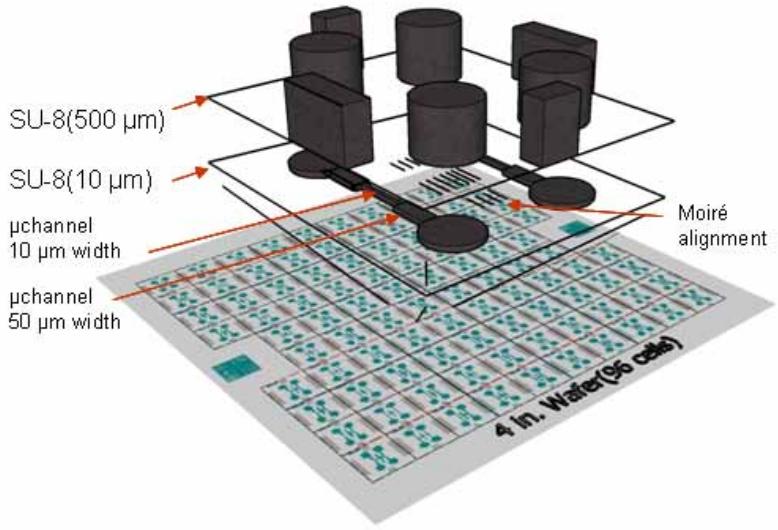

Fig. 5.3.1. Schematic 3D illustration of one cell to define microfluidic patterns in SU-8 on two layers of different thicknesses for wafer scale.

A second SU-8 (500 µm) layer on SU8-3050 was then deposited. To improve adherence between the two layers, oxygen plasma was applied for 2 min at 1000 W with a Tepla model 300 plasma machine. The process consists of depositing three layers of SU-8 3050 photoresist (Microchem Corp). They were spin coated at 800 rpm during 30 s and cured at 95°C for 3h each deposition. To depose the three layers, a fully automated photoresist coater-developer machine (EVG-120) was employed. This machine ensures a homogenous SU-8-master mould thickness. The alignment and exposure were performed in the same Suss Microtec MA-150 used for 10µm process. The post exposure bake was done at 95°C during 5 min. Next, the SU-8 was developed in PGMEA and rinsed with isopronanol (IPA). Finally the hard bake was preformed at 125°C. See Fig. 5.3.1.

Part of the final 4 in. wafer mould is presented in Fig. 5.3.2 (a), (b). Fig. 5.3.2(b) was taken

by an ultra-high resolution scanning transmission electronic microscope FE-SEM (Hitachi S-4800).

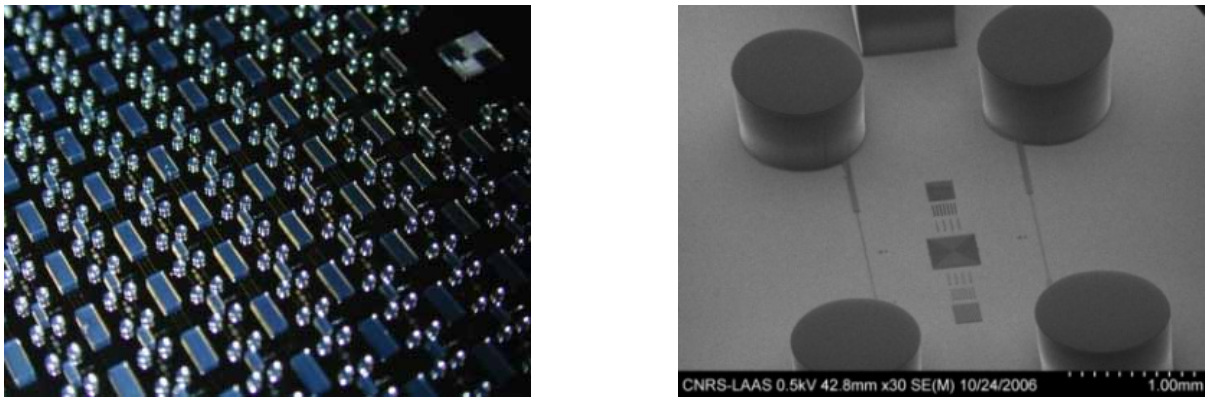

(a) (b)

Fig. 5.3.2. (a) View of the full 4 in. SU-8 mould showing an alignment mark at the top (right), (b) SEM photograph of one cell showing both SU-8 (10μm) and SU-8 (500 μm) processes.

5.3.1.2 Casting process

Unmodified PDMS (sylgard 184), from Dow Corning Corp, was obtained by mixing 10:1 in volume ratio with its curing agent. To obtain the PDMS nanocomposite, silicon dioxide amorphous nanoparticles were mixed directly (fumed silica of 20nm purchased from GELEST$^{(R)}$) at 8% in weight (wt) with unmodified PDMS. We degassed both silicones for 10 min to remove the bubbles.

For the casting process, the 4 in. master mould was positioned in a flat aluminium piece we realised which ensures its stability. After pouring the PDMS, it was covered with a glass wafer. A press was fabricated; it allowed us to obtain a homogenous thickness PDMS layer. The press has two metal plates that provide uniform force onto the stack (optimum force has not yet been determined). Both types of PDMS were cured during 4h at 100°C. Fig.5.3.3 illustrates the mentioned press, the SU-8 master mould and the glass wafer to cover the stack.

Fig.5.3.3. Press for curing the silicon for obtaining a homogenous film thickness.

5.3.1.3 PDMS Etching

After curing the PDMS, an etching was realised. To do this an Aviza technology Omega 201 machine as Inductively Coupled Plasma Reactive Ion Etching (ICP-RIE) was used with a $SF6/O_2$ (3:1) gas mixture at 80W RF platen 500W RF Coil and 20 mTorr. In these conditions an etching was performed in the 20 µm thick residual PDMS films formed at the top of inlets-outlets emplacement on the SU-8 master. The etching rate was around 330 nm/min. This allowed us to obtain 96 cells with proper circular opened holes at the same time, with the intention of been aligned and integrated into the nanobiosensor developed in this thesis.

Excellent opened patterns and good uniformity was successfully obtained on all the 4 inch wafer .See Fig. 5.3.4.

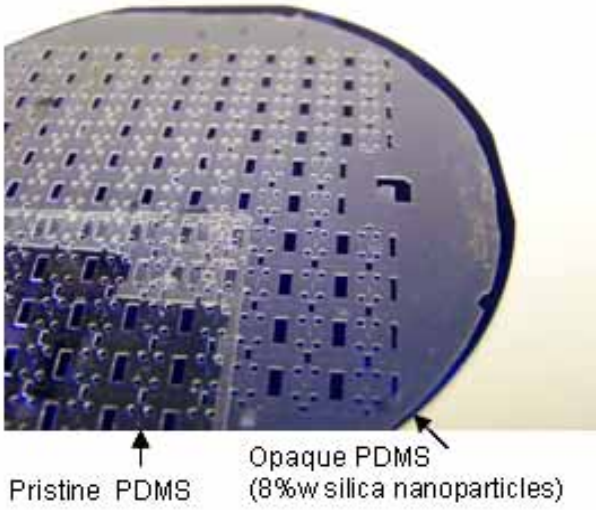

Fig.5.3.4. etched PDMS at wafer level (96 cells of 7 mm x7 mm each one).

Fig. 5.3.4 illustrates an etching performed in both thickness-homogenous unmodified PDMS and PDMS nanocomposite. Otherwise, PDMS nanocomposite (opaque PDMS) contains silica nanoparticles at 8% wt. The so-called opaque PDMS film can nevertheless be aligned because visible light passes through it.

Both kinds of PDMS had the same thickness and the same etching parameters were used. Nevertheless, we observed faster and homogenous etching rate for PDMS nanocomposite thus successfully etching in entire PDMS nanocomposite was obtained. On the contrary, we were not able to obtain an etching in the entire 4 in. unmodified PDMS. Images of Fig. 5.3.4 corresponding to unmodified PDMS illustrate just a part of etched PDMS which was obtained at the border of the 4 in. wafer (in the centre of the unmodified PDMS, was not properly etched).

Thermal stability enhancement in PDMS nanocomposites [11] due to inorganic nanoparticles into polymer matrix probably explains the etching improvement. Indeed, nanoparticles have a huge surface to volume ratio, thus they experience more important contact area with the fluorine-based plasma gas used to etch this polymer. Finally, gas transport properties change in PDMS nanocomposites as solubility, diffusivity, permeability [11] and definitely they participate in the improvement etching rate. We think that other parameters can be involved in this improvement. Hence, a deep study would be suitable.

A single cell is pictured in Fig. 5.3.5 (a) and (b), optical images show proper interconnecting holes in PDMS nanocomposite. Fig. 5.3.5 (b) (PDMS placed on a blue wafer

that explains the blue colour) was taken by a Hirox digital video-microscope. Note that etching in micro channels realisation (10µm height and 50µm width) is even observable (small picture on the right).

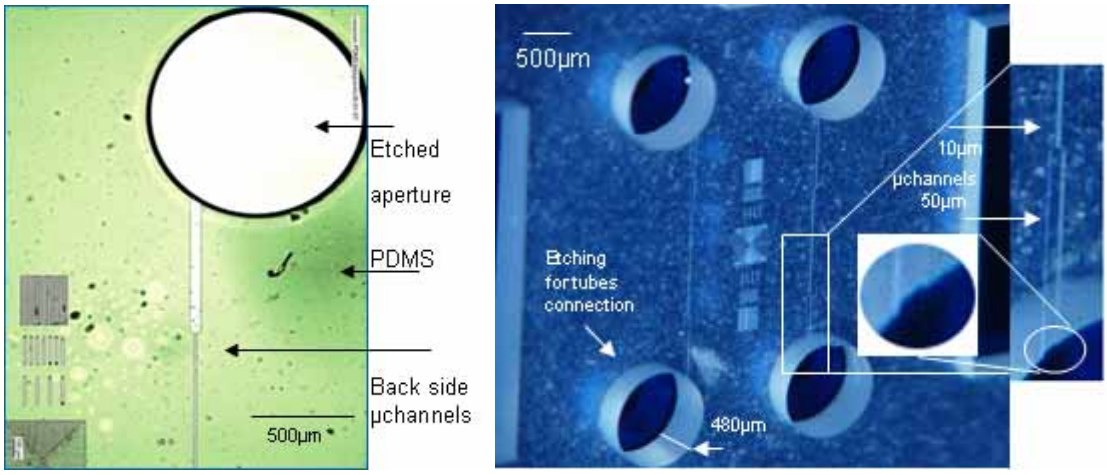

Fig.5.3.5. (a) PDMS etched for circulars holes, (b) One 3D 7mm X 7 mm cell showing µchannels and etched apertures.

5.3.2 Results and discussion

To interconnect microfluidic systems I used FEP® Teflon tubes (O.D. 1.02mm and I.D. 0.5mm) Flangeless TM FEP Fittings for 1/16 OD (Upchurch Scientific, purchased from Cluzeau info lab. France). The microfluidic system is conceived to be connected to a flow control system, a syringe system, a peristaltic pump or a dedicated pressure tool (Fluigent®). To do this connection, tubes (I.D. 500µm, O.D. 1mm), finger, tight fittings, and ¼-28 Coned Finger tight were purchased (Upchurch Scientific).

I tested several adherent resists to seal the tubes into the PDMS emplacement, for example the E505 from Epotecny® France, and the N-008 from Cluzeau info lab. France and they did not work because they were either too viscous or not enough viscous to maintain the tubes into the holes. Finally, the E501 resist model from Cluzeau info lab. France was used since it had the optimum parameters to reach our purpose. Fig. 5.3.6 (a) pictures four sealed tubes in a 7 mm x 7 mm cell. Tubes were sealed at the same time by using a polymer piece we fabricated. These tubes can serve as inlet and outlets connexions.

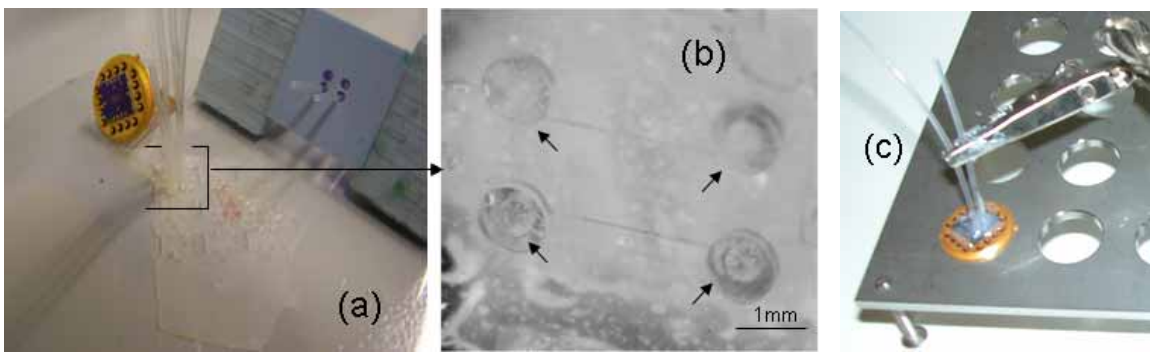

Fig.5.3.6 (a) Four FEP tubes sealed. (b) Close-up of 4 tubes sealed. (c) Interconnection of two tubes in a TO-8 case.

Each PDMS cell can be aligned and encapsulated in TO-8 cases as part of the integrated nanobiosensor we present in this thesis as illustrated in 5.3.6 (c). Originally, each PDMS cell had been conceived to integrate microchannels and interconnecting holes (at that time, photoPDMS had not been developed) then the cells had been intended to be aligned directly on the interdigitated nanoelectrodes devices (IND). Nevertheless in our final integration, each PDMS cell will serve us just to maintain the tubes and to encapsulate the photoPDMS-based microchannels. Thereof, we use in this design and technological process to conduct pressure tests.

To realise these tests, some PDMS cells were cut and bonded on a 4-in transparent glass wafer by using three adherent methods. First, we used the typical plasma method to create hydroxyl functional groups, employing a Tepla model 300 plasma machine. The second technique consisted of using a UV-curable resist purchased for Epotecny^{R} France. The resist is the OAD393 sensitive from 250 nm to 400 nm with a peak absorption at 365nm. To bond one cell, irradiation at 70 mW/cm^2 for 2 min (standard NUV) was used. Finally I elaborated an acrylic-based (HEMA) adherent compound mixed with a photoinitiator that has an UV peak at 360 nm (the same photoinitiator used in P-photoPDMS). The HEMA based adherent compound is biocompatible for our biological applications; this is the reason why we employed this adherent resist too.

5.3.2.1 Pressure system tools

To determine the leakage pressure in PDMS microfluidic system, that is the maximum working pressure it can stand, some tests were conducted with a pressure tool system called MFCS which stands for MicroFluidic Control System (Fluigent®). The system was conceived and fabricated at Institute Curie in France [15]. MFCS regulates pressure with feed-back control and allows a precise pressure control (steps: 16 μbar) maintaining a stable flow in microfluidic and nanofluidic systems. This system avoids plug effects or unwanted hydrostatic flows obtained with peristaltic or syringe systems as Fütterer et al. reported [16]. Furthermore, in this microfluidic system, tubes are not in direct contact with the push pressure (driven pressure*)* tubes. Fig. 5.3.7 illustrates the differences between the MCFS and a typical syringe pump.

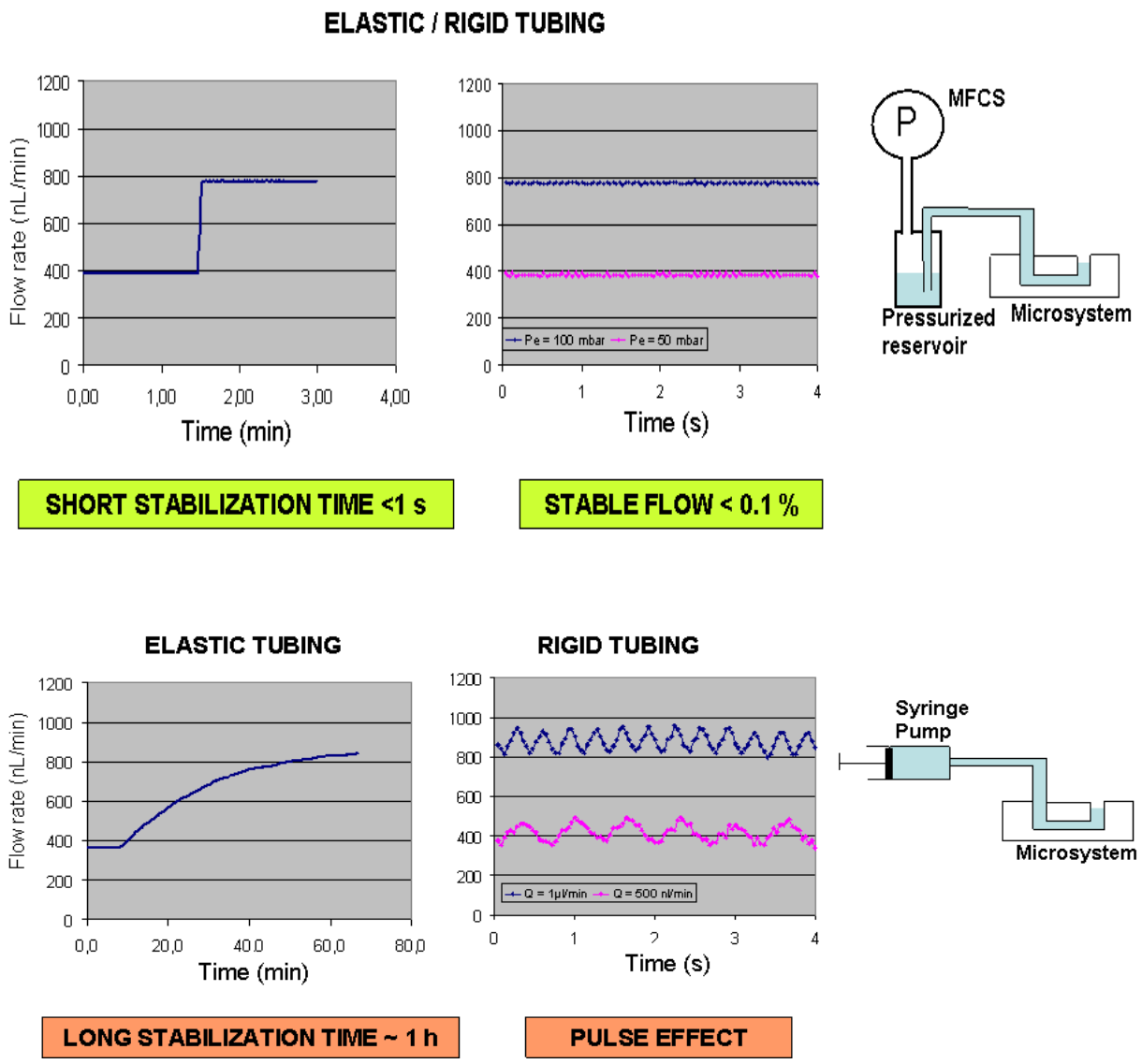

Fig.5.3.7. Images from Fluigent® comparing the pressure tool system (MCFS) and a simple syringe.

5.3.2.2 Interconnection pressure tests

One sealed tube was connected to the MCFS as Fig. 5.3.8 pictures. Pressure was imposed, starting from 10 mbar and then raised gently to the maximum pressure the system can supply (1.2 bars). After 3 minutes operating at this pressure, a leakage was observed at side of the microchannels but not around the proper holes. From these experiments we concluded that our PDMS interconnects can stand a pressure up to 1.2 bars if using the acrylic-based (HEMA) adhesive resist, we elaborated, as well as if using the other adherent methodologies presented here.

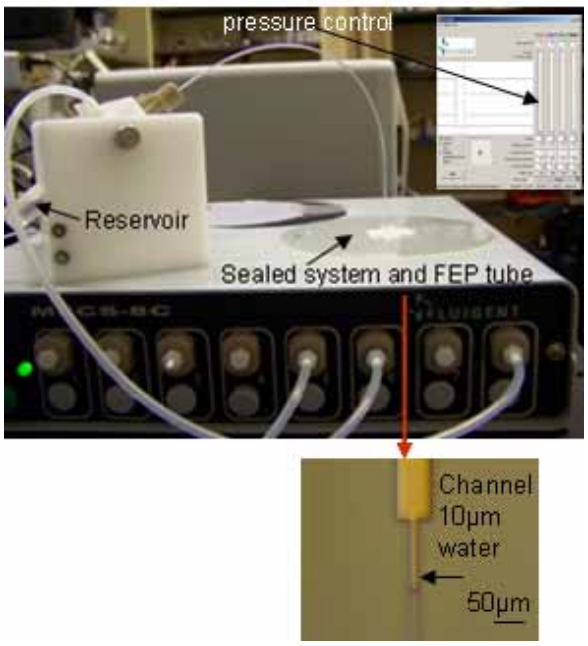

Fig.5.3.8. One cell PDMS connected by tubes to MFCS for pressure tests realisation.

It is formulated the fluidic resistance (hydrodynamic resistance) for a rectangular channel with low aspect ratio [17] as:

$$R = \frac{12\mu L}{wh^3}\left[1 - \frac{h}{w}\left(\frac{192}{\pi^5}\sum_{n=1,3,5}^{\infty}\tanh\left(\frac{n\pi w}{2h}\right)\right)\right]^{-1}$$

We have channels of one part with 2 mm length (L), 50µm width (w) and 10 µm height (h), and another part of the same channel measuring L = 1mm, w=10µm, h=10µm. The water dynamic viscosity µ is $1x10^{-3}$Pa.s. If calculating, we obtain an important resistance of $\sim 10^{16}$ Pa.s/m^3 for these values. Otherwise a single channel contains ~1nL. The volume flow Q is a function of the external applied pressure difference P, and the resistance R, so we have Q=P/R [15][17]. A maximum pressure driven P=1.2 bars (120kPa) has been applied, thus we obtain Q=1µl/min, and a mean velocity of 370000µm/s. We infer from these results that leakage occurs after some minutes of flow, because of the size of the channels (10µm width).

This demonstrates that for 10µm-width channels, our technology enables to induce a significant flow without leakage. To perform successful typical biomedical applications, we think that our system is adequate because we do not need a pressure as high as 1.2 bars. Epoxy resist was not used for reinforcing the PDMS bonding with the wafer glass. However this system could be encapsulated in a TO-8 case using the mentioned epoxy resist to reinforce the device and obtain a more robust device.

5.3.3 Conclusions

We have shown in the present section (interconnecting development) of this chapter, the use of two different levels processes of SU8 fabrication. These processes have been combined with a PDMS dry etching to obtain proper apertures to connect tubes.

Wafer scale etching on PDMS was improved by using silica nanoparticles embedded into unmodified PDMS (pristine PDMS) obtaining a PDMS nanocomposite in which a few pressure tests were performed by using pressure tool system (MFCS). This kind of pressure system avoids typical effects obtained with other systems.

Finally, this technological development will be not intended to integrate microfluidic channels but to encapsulate the previous photoPDMS-based microfluidic channels, thus each cell of the 96 cells of the 4 in. wafer will contain open interconnecting holes. This technique can be adapted also to realise more complex 3-D microfluidic systems based lab-on-chip.

5.3.4 References

[1] Naga S. Korivi, Li Jiang, "A generic chip to word Fluidic interconnect system for microfluidic devices",*39th Southearn Sympsium on System Theory IEEE*, Macon GA, **2007**.

[2] Hofmann O., Niedermann P., Manz A., "Modular approach to fabrication of three-dimensional microchannel systems in PDMS-application to sheath flow microchip"**,** *Lab on a Chip*, 1,**2001**, p.108-114.

[3] Li Shifeng, Chen Shaochen, "Polydimethylsioxane Fluidic Interconnects for microfluidic systems", *IEEE Transations on Advanced Packaging*, 2**003**, 26, p.242-247.

Shifeng Li et al. "Disposable polydimethylsiloxane/silicon hybrid chips for protein detection", *Biosensors and Bioelectronics*, 21, **2005**, p. 574-580.

[4] A. V. Pattekar and M. V. Kothare, "Novel microfluidic interconnectors for high temperature and pressure application", J. *Micromech. Microeng.* **2003**, 13, p.337-345.

[5] Christensen A. M., Chang-Yen D. A., Gale B., "Characterization of interconnects used in PDMS microfluidic systems", J. *Micromech. Microeng*. **2005**, 15, p.928-932.

[6] Han Ki-Ho, Frazier A. Bruno, "Reliability aspects of packaging and integration technology for microfluidic systems"*IEEE Trans. Device Materials Reliab.*, **2005**, 5, p.452-457.

[7] Plecis Adrien, Chen Yong, "Fabrication of microfluidic devices based on glass-PDMS technology", *Microelectronic Engeneering* ,84, **2007**, p.1265-1269.

[8]. Murphy E. R, Inoue T., Sahoo H. R., Zaborenko N., Jensen K. F., "Solder-based chip-to-tube and chip-to-chip packaging for microfluidic devices" , *Lab on a Chip*, **2007**, 7, p.1309-1314.

[9] Mair D. A., Geiger E., Pisano A P., Fréchet JM. J., Svec F, "Injection molded microfluidic chips featuring integrated interconnects" *Lab on a Chip*, **2006**, 6, p.1346-1354.

[10] Sia S. K, Whitesides G. M., "Microfluidic devices fabricated in Poly(dimethylsiloxane) for biological studies ", *Electrophoresis,* **2003**, 24, p.3563-3676.

[11] H. Zou, S. Wu, J. Shen, "Polymer/silica nanocomposites: Preparation, characterization, properties, and applications, *Chem. Rev.,* **2008***, 108* (9), p. 3893-3957
S. S. Ray, M Okamoto, *Prog. Polym. Sci.,* **2003**, *28*, 1539.

[12] M. E. Vlachopoulou, A. Tserepi, N. Vourdas, E. Gogolides, K. Misiakos, "Patterning of thick polymeric substrates for the fabrication of microfluidic devices", *Journal of Physics: Conference Series*, **2005**, 10, 293-296.

[13] J. Garra, T. Long, J. Currie, T. Schneider, R. White, M. Paranjape, "Dry etching of polydimethylsiloxane for microfluidic systems", J. *Vac. Sci. Techno Al.*, **2002**, 20 (3), p.975-982.

[14] D. Szmigiel, K. Domanski, P. Prokaryn, P. Grabiec, "Deep etching of biocompatible silicone rubber", M*icroelectronic Eng*., **2006**, 83, p.1178-1181.

[15] Fütterer C., *MicroFludics Control System: User manual*, *Fluigent MFCS software*, **2006**.

[16] Fütterer C., Minc N., Bormuth V., Codarbox JH., Laval P., Rossier J., Viovy J. L., 'Injection and flow Control in Microchannels, *Lab on a Chip*, **2004**, 4, p.351-356.

[17] Beebe D. J., G. A. Mensing, G. M. Walker,"Physics and applications of microfluidics in biology", *Annu.Rev. Biomed.Eng*, **2002**, 4, p.261-286.

5.4 COMPENSATION OF MISALIGNMENT IN POLYDIMETHYLSILOXANE (PDMS)

As written in the introduction section, shrinkage is an inevitable phenomenon due to a thermal expansion occurred when curing classical PDMS. This shrinkage produces deleterious misalignment when patterned-PDMS films are aligned at wafer level. Few works have reported this problem. However in a recent published paper, Seok Woo and Seung S. Lee [1] studied the shrinkage ratio concerning curing PDMS conditions like temp/time or thickness of the PDMS. They proposed a solution for diminishing the PDMS shrinkage, consisting in elaborating the master mould with an offset. By doing this offset, patterns appeared bigger than the patterns where the PDMS is supposed to be aligned, so it is necessary to take in consideration the shrinkage ratio of the PDMS. They concluded in their paper, that shrinkage ratio increases linearly with the PDMS curing temperature and the mixing ratio of diluents, however the ratio implication relating the curing agent used in PDMS is complicate to be determined.

In present final section of this chapter, we adapt the solution proposed above, thus the design of the photomask carrying the patterns had been drawn with offsets. To do this a previous study of the shrinkage ratio at a fixed temperature is conducted.

As written in the interconnection part of this chapter (second section), we will use the PDMS film (480µm) to encapsulate, guide and bond the interconnecting tubes. Hence, in this section we use the PDMS film just for carrying open circle-shapes used to interconnect the tubes and for injecting the biological flow to be tested, because the microchannels will be generated by a UV exposure of a positive photoPDMS layer and thus directly aligned on 4 in. wafers.

5.4.1 Measurement of the misalignment due to PDMS shrinkage

First, we used the mould decribed in the second section of this chapter. This mould was designed with patterns that fit in the mix and match process at 4 in. wafer level, developed in chapter 2. PDMS was obtained by mixing 10:1 in volume ratio with its curing agent. The curing temperature was 100° C for one hour. After peeling off the PDMS, it was aligned manually onto the 4 in. wafer which had previous mix and match processes. To know the required shrinkage ratio, it is not necessary to align precisely the PDMS patterns onto the wafer, because once positioned the PDMS film, we can compare the measurements taken for each cell with a reference (part of a mix and match made of gold). Measures were taken from left to right. Fig.5.4.1 pictures just three circles-shape patterns, each one corresponding to a different cell, clearly “moving” to left due to the shrinkage (distance between two circles is 7 mm which is the distance between two cells).

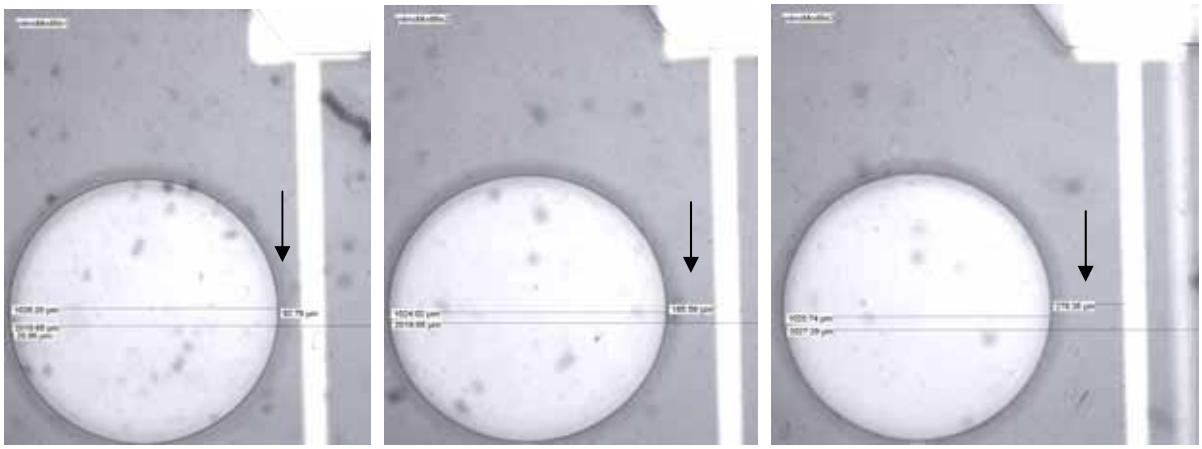

Fig. 5.4.1. Alignment of PDMS using unmodified and first SU-8 master mould to determine the shrinkage ratio.

From the pictures, we observe that the variation between one cell and other (separated by 7 mm) is ~100 µm. Measures from left to right between the circle-shape patterns and the gold pattern, is 99 µm the first, 185 µm the second and 278 µm the third. Measures values were taken in the 10 horizontal cells of the 4 in. wafer level. This variation is constant and it is the same in vertical direction (for 10 cells too).

5.4.1.2 Improvement on the SU-8 mould master by design offsets

Seok Woo and Seung S. Lee [1] formulated the shrinkage ratio as:

$$\frac{1}{L}\times d\times 100=\frac{1}{L}\times\frac{1}{L}\sum_{i=1}^{4}d_i\times 100$$

Where d is the average value of d_i and L is the distance from the centre of the wafer. See Fig. 5.4.2.

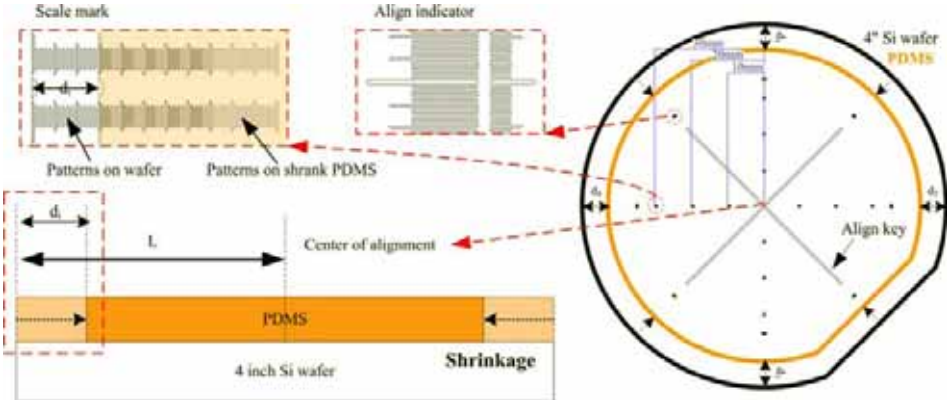

Fig.5.4.2. Image from [1], schematising the method to determine the shrinkage ratio.

Taking our parameters we find a shrinkage ratio percentage of: $\frac{1}{50mm}\times 500\mu m\times 100=1\%$.
We modified then, the design by augmenting 100µm vertically and horizontally the distance between two patterns of two cells.

5.4.1.3 Results and discussions

We used the modified master mould (design offsets) to prepare another PDMS film but now just having circle-shape patterns as illustrated in Fig.5.4.3.

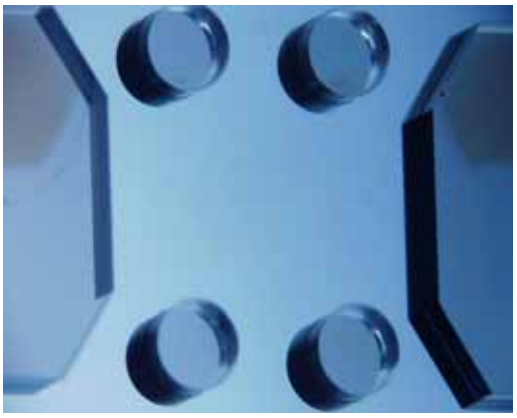

Fig.5.4.3. Optical image of one cell in the 4 in. SU-8 master mould.

PDMS was obtained by mixing 10:1 in volume ratio with its curing agent as described above. The curing temperature was 100° C during one hour. After peeling off the PDMS, the second step consisted of aligning manually the PDMS film to the same 4 in. wafer which had a mix and match process. Fig. 5.4.4 pictures just the first three optical images of the alignment.

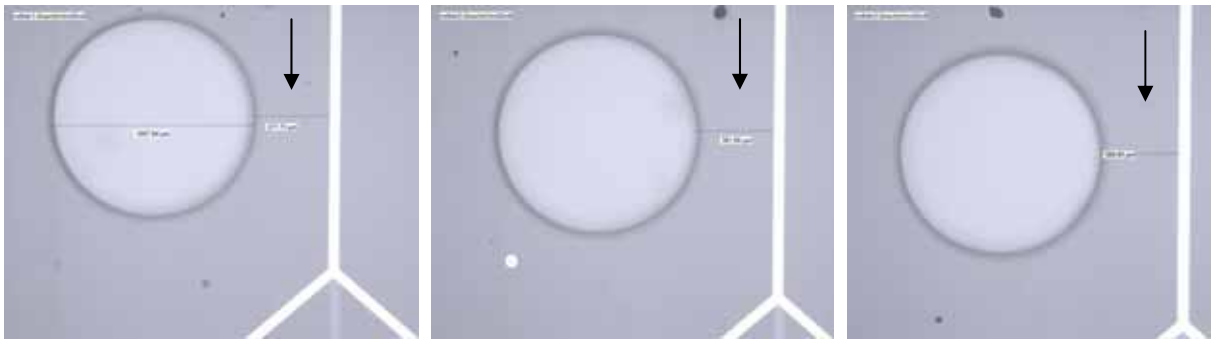

Fig.5.4.4. Alignment of PDMS using modified mould taking into account the shrinkage ratio.

Images of the figure 5.4.4 illustrate that by increasing the size of the master mould, we can compensate the shrinkage ratio for more that 92%. The first distance between the circle-shape patterns and the gold pattern, from the left, is 377 µm, the second is 381µm and the third is 388 µm. As in the case there was not size compensation in the mould, measures were taken in the 10 horizontal cells of the 4 in. wafer level. This variation is constant and it is the same in vertical way (10 cells too). This correction will enable to align precisely the inlet and outlet circle holes on the previous photoPDMS realisation on wafer level.

Seok Woo and Seung S. Lee have investigated certain parameters which modify the shrinkage of PDMS. They used one of the most common PDMS (Sylgard 184, Dow Conring Co.) and they found a shrinkage ratio in 4 in. wafer of 1.94% for a curing temperature of 100° C [1]. The PDMS film thickness they used was 1.2mm. On the contrary, in my experiences, I found 1% of shrinkage ratio for the same curing temperature and for 500 µm PDMS thickness.

However I used another PDMS, called RTV615 from GE Bayer silicones purchased from AB Chimie France. These two PDMS present slightly different electrical and physical properties. Table 5.4.1 summarises the principal characteristics of the two types of PDMS. From these experiments, I think that it is necessary to consider other parameters such as the coefficient of thermal conductivity of a specific PDMS to construct a more exact formula to calculate the shrinkage ratio. Note in the table, for example, that the tear strength value is different between the two PDMS. I think it is necessary to consider the differential equation of the law of heat conduction (Fourier's law) as well as other material parameters as the width of the PDMS film. Then, a deep mathematical model and simulation study are necessary.

Sylgard® 184

CTM*	ASTM*	Property	Unit	Value
		As supplied		
0050	D1084	Viscosity at 23°C (Base)[1]	mPa.s	5500
		Mixing ratio by weight (Base:Curing Agent)		10:1
0050	D1084	Viscosity at 23°C, immediately after mixing with Curing Agent	mPa.s	4000
0055	D1824	Pot life at 23°C[2]	hours	2
		Physical properties, cured 4 hours at 65°C		
0176		Color		Clear
0099	D2240	Durometer hardness, Shore A		50
0137A	D412	Tensile strength	MPa	7.1
0137A	D412	Elongation at break	%	140
0159A	D624	Tear strength - die B	kN/m	2.6
0022	D0792	Specific gravity at 23°C		1.05
		Volume coefficient of thermal expansion	1/K	$9.6x10^{-4}$
		Coefficient of thermal conductivity	W/(m.K)	0.17
		Electrical properties, cured 4 hours at 65°C		
0114	D149	Dielectric strength	kV/mm	21
0112	D150	Permittivity at 100Hz		2.75
0112	D150	Permittivity at 100kHz		2.75
0112	D150	Dissipation factor at 100Hz		0.001
0112	D150	Dissipation factor at 1kHz		0.001
0249	D257	Volume resistivity	Ohm.cm	$5x10^{14}$
		Comparative tracking index (IEC112)		600

1. Brookfield LVF, spindle #4 at 60rpm
2. Time required for catalysed viscosity to double at 23°C.
* CTM: Corporate Test Method, copies of CTMs are available on request.
ASTM: American Society for Testing and Materials.

RTV® 615

Uncured Properties		RTV615A	RTV615B	RTV655A	RTV655B
Colour		Clear, colourless	Clear, colourless	Clear, colourless	Clear, colourless
Consistency		Easily pourable	Easily pourable	Easily pourable	Easily pourable
Viscosity	mPa·s	4300	-	5700	-
Specific Gravity	g/cm³	1.02	-	1.04	-

Uncured properties with curing agent added		RTV615	RTV655
Mix ratio		10:1	10:1
Colour		Clear, colourless	Clear, colourless
Consistency		Easily pourable	Easily pourable
Viscosity	mPa·s	4000	5200
Work time @ 25 °C	hrs	4	4

Cured properties (Cured 1 hr @ 100 °C)			
Mechanical		**RTV615**	**RTV655**
Hardness	Shore A	44	45
Tensile strength	MPa	6.5	6.5
Elongation	%	120	120
Shrinkage	%	0.2	0.2
Refractive index		1.406	1.430
Dielectric strength	kV/mm	19.7	19.7
Electrical			
Dielectric constant @ 1 kHz		2.7	2.7
Dissipation factor @ 1 kHz		0.0006	0.0004
Volume resistivity	Ohm · cm	1.8×10^{15}	1.8×10^{15}
Thermal			
Useful temperature range	°C	-60 to 200	-115 to 200
Thermal conductivity	W/m · K	0.2	0.2
Coefficient of expansion	m/m · K	27×10^{-5}	33×10^{-5}
Specific heat	J/g · K	1.3	1.3

Table 5.4.1. comparison characteristics between sylgard 184 and RTV 615 from fabricant [2][3].

5.4.2 Conclusions and perspectives

In this part of this chapter we have compensated for the shrinkage involved in classical PDMS by increasing the size of the master mould used to fabricate the PDMS film (500µm thick). This film serves to encapsulate the photoPDMS-based microchannels like presented in this section of the chapter. Finally, this encapsulation has been engineered as follows: I have modified the size of the circle-shape hole diameter made of photoPDMS (first section of this chapter), this permit to fit with the interior diameter (I.D.=500µm) of the interconnecting tubes we use. Next modification consisted of making circle-shaped holes in the PDMS film (480 µm thick) to encapsulate the microfluidic system, thus circle-shaped holes have a diameter of 1mm corresponding to the outside diameter (OD) of each interconnecting tube.

Fig. 5.4.4 illustrates a final sealed encapsulation in one cell. In a device like this, interconnecting tubes (as presented in section 2) can be sealed. Complete integration of the nanodevices showing sealed tubes is presented in chapter 7.

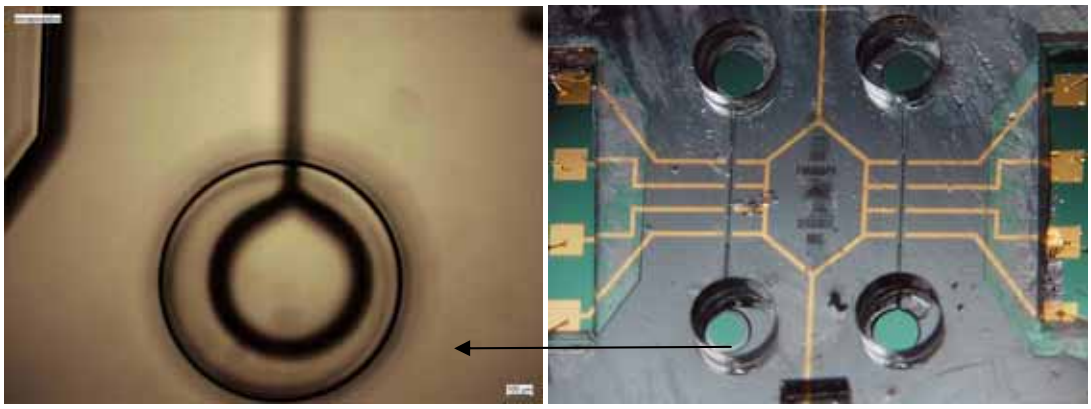

Fig.5.4.5. Final alignment and encapsulation using PDMS (480µm thick) onto PhotoPDMS-based microfluidic channels (26 µm thick).

5.4.3 References

[1] Seok Woo Lee. Seung S. Lee, "Shrinkage ratio of PDMS and its alignment method for the wafer level process", *Microsyst. Technol.*, 2008, 14: 205-208.

[2] Product information of Sylgard 184, Dow Conring Co.

[3] Product information of RTV615, GE Bayer silicones.

Chapter VI

Nanodevices integration with MEMS-based spotter (bioplumes) for multiplexed biological deposition

6.1 Introduction

Microarrays are microscope probe spots, or elements that recognise another element named target, using the methods described in the general introduction of this thesis, to immobilise the elements. Microarrays are suitable to analyse proteins (called proteins microarrays) or biomolecules such as DNA (called DNA microarrays). To elaborate these mentioned microarrays, several techniques have been proposed involving either *direct-contact methods* like dip-pen nanotechnology (DPN) [1], mechanical microspotting [2], or *not direct-contact methods* like ink-jet [3]. Otherwise; there is an important demand for microarrays based on micro and nanotechnologies. In this context, direct-contact methods seem to be the most adequate to deliver spots with submicrometer sizes or to elaborate picolitres droplets [4]. In this chapter we present a direct-contact device called *bioplume*. It is a patented cantilever-based spotter device that permits to deposit precisely liquid spots from picolitre to femtolitre range [5-6]. It was developed by our research staff (nanobiosystems) [7].

The objective of this short chapter is to present the so called bioplume device coupled with the nanobiosensor-based device we are presenting in this thesis. The purpose is to deposit the biomolecules as probes (single chain variable fragments (scFv)-F7N1N2 that recognise the active antigen form of RhoA presented in chapter 4) locally on the interdigitated nanoelectrodes devices (IND) avoiding cross contamination and using less analytes thereof. Indeed, depositions are intended to be conducted into the photoPDMS-based microchannels with the object of reaching locally the active zone of the IND. Moreover, before doing this, a study of the modification in the IND due to the bioplumes while depositing, is performed.

6.1.1 Bioplumes device fabrication and implementation

Fig.6.1 illustrates the typical technological methodology to realise the bioplumes. To know more exactly about their realisation, some publications can be consulted [8].

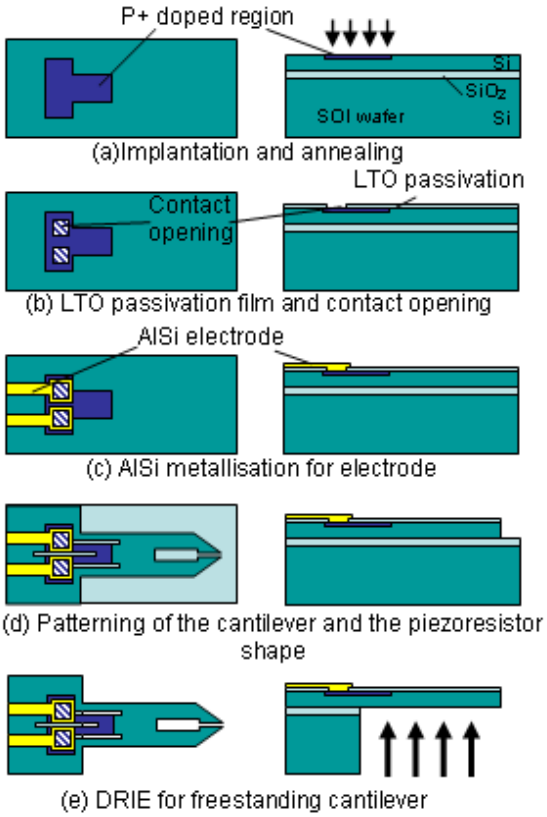

Fig.6.1. Fabrication process of the cantilever-based spotter device with metallic electrodes called *bioplumes*, picture from [10].

The devices consist in arrays of silicon cantilever that are integrated with channels in their tips for liquid loading and deposition. Furthermore each cantilever has a reservoir. The loading is made by simple capillarity, however if applying an electrostatic field, loading efficiency can increase, either by electrowetting because of the reduction of the contact angle or by dielectrophoresis because of the created electrostatic forces [4].

The cantilevers are 2 mm long, 120 µm wide and 5 µm thick, so each tip has a square section of 25 μm^2. Each cantilever is spaced of 360 µm to fit with our interdigitated nanoelectrodes devices (IND). Fig. 6.2 illustrates 4 cantilevers and one enlarged tip of one "bioplume".

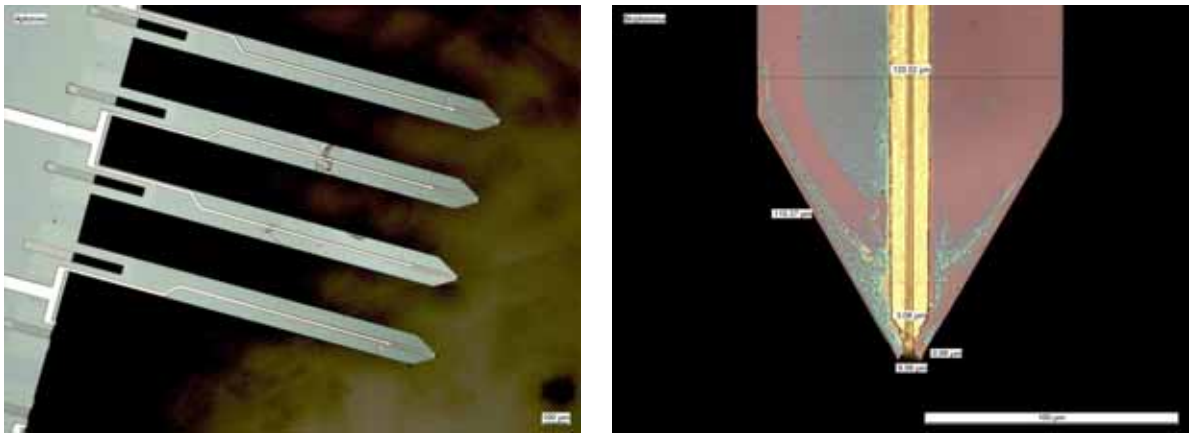

Fig.6.2. Optical images of an array of 4 cantilevers and one enlarged image of the tip.

One advantage of this kind of cantilever-based spotter device is that it can be easily cleaned and loaded with different analytes. Bioplumes have been used to deposit, for example, packed polystyrene (PS) nanobeads [9]. Fig. 6.3 (a) illustrates the full spotter system including the cantilever arrays, which has four alignment degrees in X, Y, Z and θ. One practical example of deposition is water-glycerol ratio droplets deposition as depicted in fig. 6.3 (b) [10].

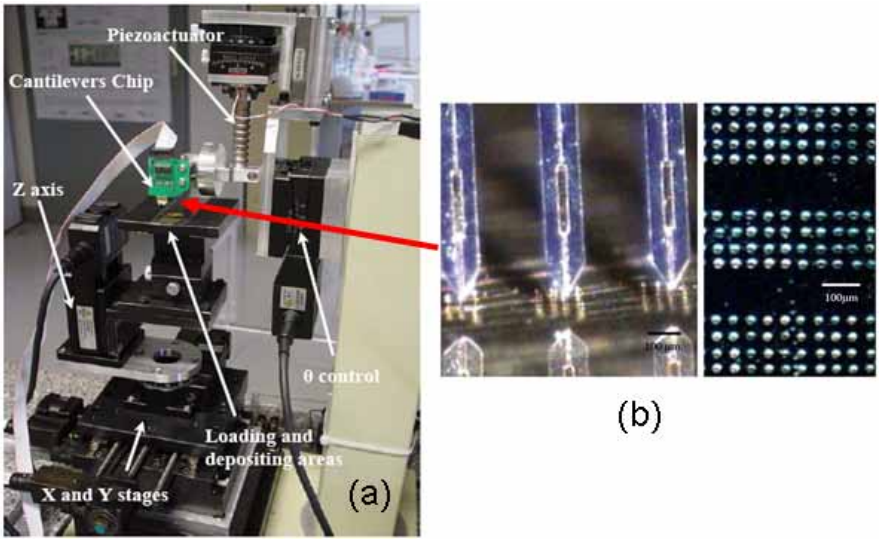

Fig. 6.3. (a) Complete spotter system with four alignment degrees, including the cantilevers arrays, (b) left: enlarged optical image of cantilevers and right: picture of spotted droplets (~10µm diameter). Pictures from [10].

6.1.2 Bioplumes coupled with nanodevices sensors

Originally, we designed each cell's interdigitated nanoelectrodes devices (IND) to fit with the space distance between each cantilever (320 µm). These devices were the first we elaborated, that is why the nano-electrodes we used in these experiments are not compensated for proximity effects (demonstrated in chapter 1).

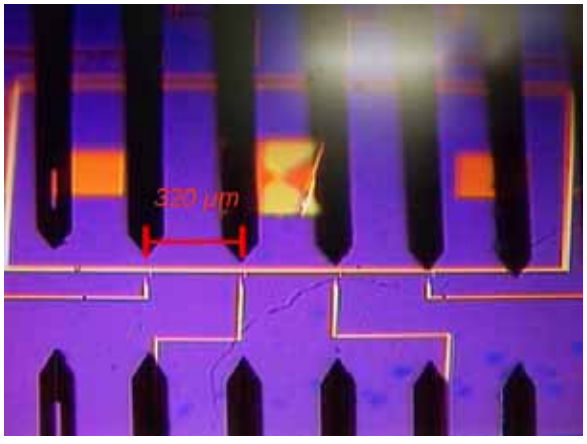

Fig. 6.4. Optical image of bioplumes showing their distance that fits with each IND of the two cell's columns.

Figure 6.4 illustrates the bioplumes approaching to four IND of one cell. It illustrates that the space between bioplumes fits with the space between each column of IND, permitting to depose locally the analyte (the probes). Reflected images of bioplumes, on the bottom, on the SiO_2 surfaces were useful to align precisely the microcantilevers.

6.2 Deposition on interdigitated nanoelectrodes devices (IND)

As mentioned, the objective of having these cantilevers compatible with our devices is to deposit in parallel fashion different biological compounds named probes.

We started the study by investigating the damage of the bioplumes to the IND. Firstly, we observed the IND before depositing on them (using an ultra-high resolution scanning transmission electronic microscopy FE-SEM Hitachi S-4800). Secondly, we used a compound mixture to observe the droplets thus we used water-glycerol ratio (40% v/v), the glycerol diminish the evaporation rate of the water and 20% of lysine. We also used a colorant that permitted us to observe the droplets shape in more detail. Fig. 6.5 illustrates a local deposition of this mentioned liquid mixture.

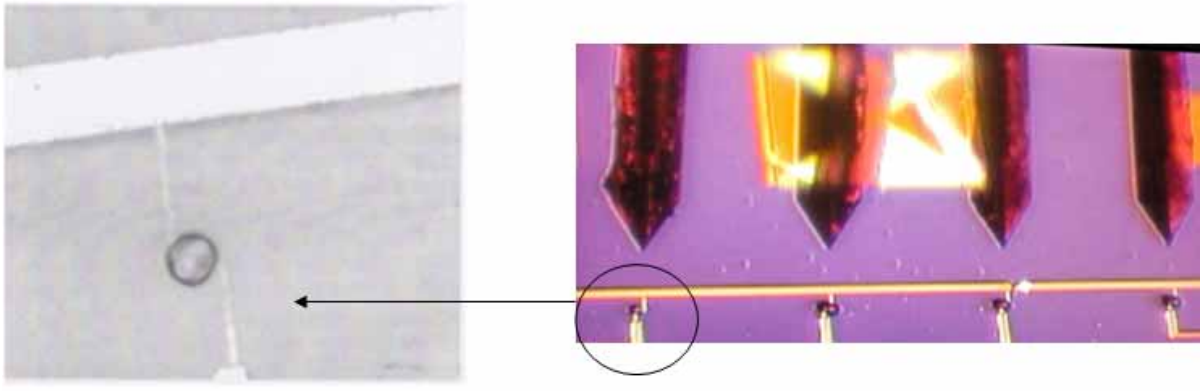

Fig. 6.5. Local deposition on the 4 IND of one cell's column, on the left: a ~10µm-diameter droplet.

Figure 6.6 compares two IND, before and after depositing the liquid mixture. The figure illustrates that some auto-organised nano-emulsions were formed (~60 nm diameter, certainly because of the mixture of glycerine and water) mainly between the nano-electrodes. The circles, on the pictures, illustrate that IND is the same, just before deposition (picture on the left) and after depositing (picture on the right).

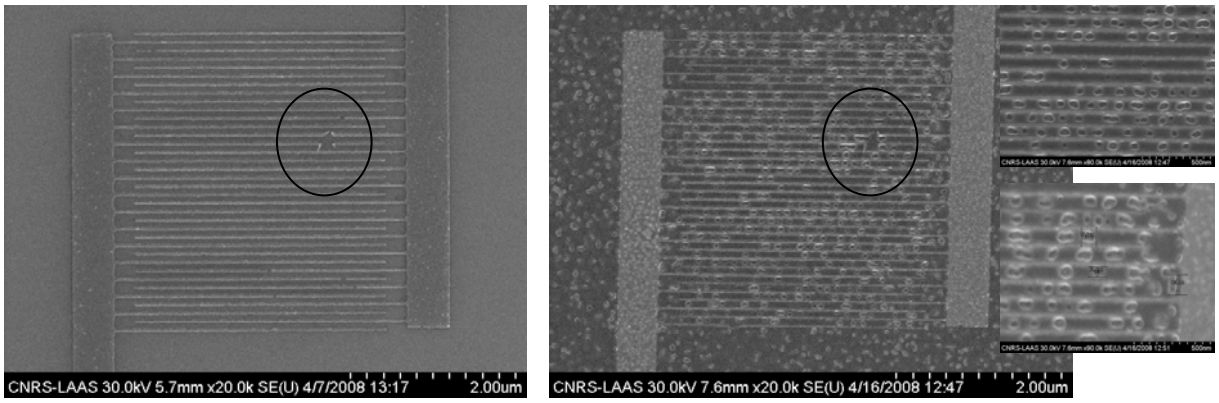

Fig.6.6. On the left an IND before liquid mixture deposition, on the right the same IND after depositing the liquid mixture showing some nano-emulsions.

Pictures of fig. 6.6 illustrate the case where there was no damage after bioplumes deposition. However the microcantilevers can damage the IND. Figure 6.7 depicts this case, on the right the nanoelectrodes are deformed due to the tip of one microcantilever.

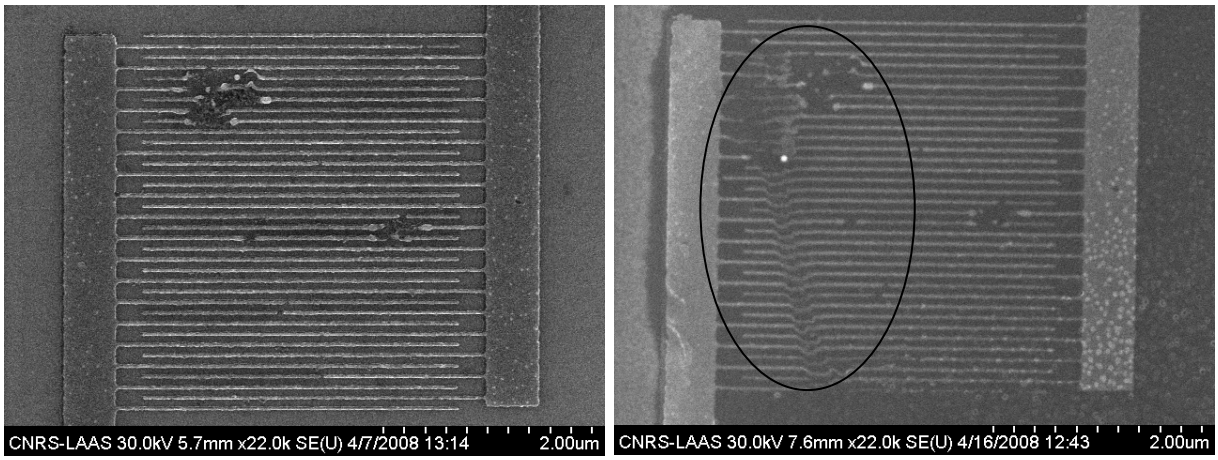

Fig.6.7. On the right an IND before liquid mixture deposition, on the left the same IND after depositing the liquid mixture clearly showing damages.

A good alignment is crucial as well as the force applied while depositing, to avoid damage in the IND. We obtained the best results by approaching the bioplumes until they almost touch the IND, thus depositing rapidly the biological compound (bioplumes have the advantage of permitting an easy adjustment since they have a graphical interface to do this task).

Otherwise, another parameter that is important to take into consideration is the degree of hydrophobicity or hydrophilicity of the surface. For example, if the surface is too hydrophilic, the shape and the size of the droplet change considerably.

A typical process to render the SiO_2 surfaces hydrophilic, a simple treatment by O_2 plasma (300W) for 30 s was applied by a Tepla model 300 plasma machine (without Faraday cage). See Fig. 6.8.

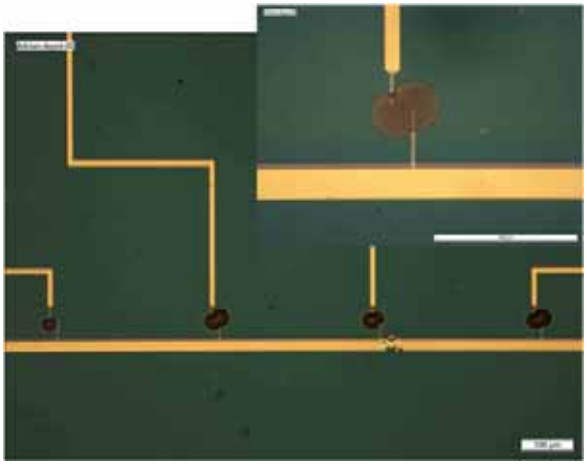

Fig. 6.8. Droplets deposition on hydrophilic surface (~40 µm diameter).

6.3 Deposition into photoPDMS-based microchannels and discussion

Previous study permitted us to know about deposition, using the bioplumes on the IND without microchannels, however microchannels are useful to transport the target biomulecules to be detected. Our objective was then, to deposit the probes in parallel and reproducible manner at wafer level, after elaborating the photoPDMS-based microchannels. By doing this methodology, even if the cantilevers were not right-directed onto the active zone, the flow could move into the microchannels to reach the active zone (this approach also allows us to avoid damaging the IND when performing the deposition). Last step was to encapsulate these microchannels with a PDMS film (480 µm thick), as demonstrated in section two of chapter 5. Fig. 6.9 demonstrates the compatibleness of the bioplumes with our nanobiosensors based devices, after elaborating the photoPDMS based microchannels, hence the bioplumes can enter into the microchannels.

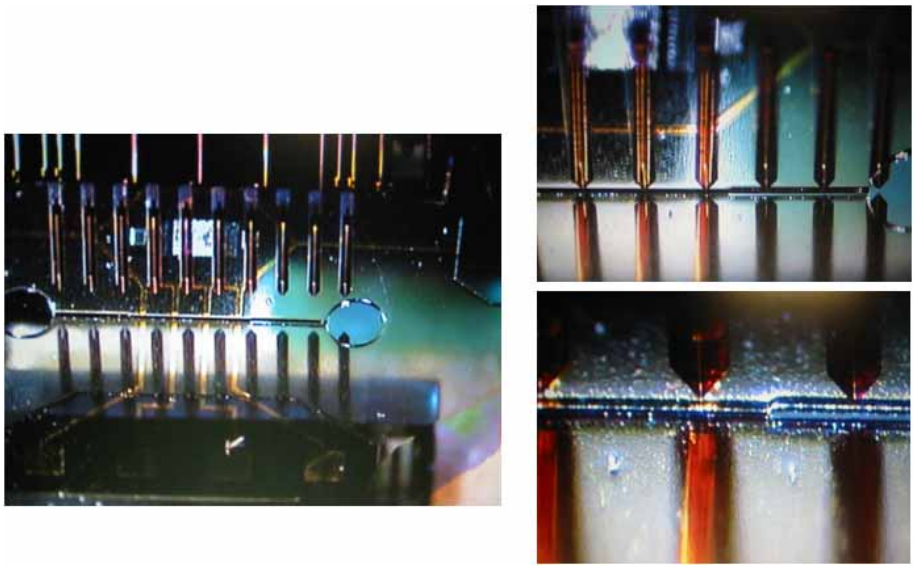

Fig.6.9. Deposition using bioplumes on part of the 4 in. wafer integration (on the left). Enlarged images of photoPDMS microchannels and bioplumes showing compatibility with our technological development (on the right).

6.4 Conclusions

In this short chapter we proposed the use of a microchannels-based system named “bioplume” combined with our nanotechnological development. The interest in using this system is to depose in parallel and locally the probes into the photoPDMS-based microchannels with the objective of reaching locally the active zone of the interdigitated nanoelectrodes devices (IND) without damaging the INDs. Depositions were expected to be conducted after different technological steps realised in the context of this research thesis. The sequence steps after depositing by *bioplumes* are: mix and match realisation (chapter 2), Ni nanoislands deposition and validation (chapter 3), surface chemistry and biology validation (chapter 4), and finally after photoPDMS-based microfluidic realisation (section one of chapter 5).

In the next and final chapter, we illustrate the full integration, which is expected to follow after probes deposition demonstrated in this chapter and if the probes are not possible to be injected into the interconnecting tubes as demonstrated in chapter 5. We will also demonstrate in next chapter the biomedical application we introduced in the general introduction of this research work.

6.5 References

[1] Demers L. M., Ginger D. S., Park S. J., Li Z., Chung S. W., Mirkin C. A., "Direct Patterning of Modified Oligonucleotides on Metals and Insulators by Dip-Pen Nanolithography", *Science*,**2002**, 296 (5574), p.1836-183.

[2] Schena M., Heller R. A., Theriault T. P., Konrad K., Lachenmeier E., R. W. Davis, "Microarrays: biotechnology's discovery platform for functional genomics", *Trends Biotechnol*. **1998**, 16, p. 301-306.

[3] Blanchard A. P., Kaiser R. J., Hood L. E., "High-density oligonucleotide arrays", *Biosens. Bioelectronics.*, **1996**, p. 687-690.

[4] Belaubre P., Guirardel M., Garcia G., Pourciel J. B., "Fabrication of biological microarrays using microcantilevers", *Appl. Phys. Lett.,* **2003**, 82, p.3122-3124.

[5] Belaubre Pascal Guirardel Matthieu, Leberre Véronique, Pourciel Jean-Bernard, Bergaud Christian, "Cantilever-based microsystem for contact and non-contact deposition of picoliter biological samples", *Sensor and actuators A: Physical*, **2004**, 110, p.130-135

[6] Belaubre, P., Guirardel, M., Leberre, V., Dagkessamanskaia, A., Trevisiol, E., Francois, J.-M., Pourciel, J.-B., Garcia, G., Bergaud, C., "Silicon-based microcantilevers for multiple biological sample deposition".,**2003**, *Conf: Transducers 03*, p.1816 -1819

[7] Bergaud C., Guirardel M., Belaubre P., Belier B., Pourciel J.B., "Device for the actively-controlled and localised deposition of at least one biological solution", *International Patent WO03097238*, **2003**.

[8] Leïchlé T., Saya, D., Pourciel J.B., Mathieu F., Bergaud C., Liviu Nicu, "Closed-loop MEMS-based Spotter Integrating Position Sensors with Nanometric Precision for the Control of Droplet Uniformity, Nano/Micro Engineered and Molecular Systems", **2006,** NEMS 06, p.730-733.

[9] Valsesia Andrea, Leïchlé T., Lacroix Lise Marie, Liviu Nicu, Bergaud Christian, "Deposition of Nanobead Hexagonal crystals using silicon microcantilivers", *Small*, **2006**,2, p.1-5.

[10] Leïchlé T., Saya, D., Pourciel J.B., Mathieu F., Liviu Nicu, Bergaud C., "Liquid loading of silicon-based cantilevers using electrowetting actuation for microspotting applications" *Sensor and actuators A: Physical*, **2006,**132 (2), p.590-596.

Chapter VII

Wafer scale integration of high sensitive electrical nanodevice for label-free cancer biomarkers detection

7.1 Introduction

The purpose of our research work has been the realisation of an innovative integrated nanobiosensor for detecting in label-free manner and high sensitivity biomolecules involved in tumorogenesis. Hence, in this chapter we demonstrate the complete integration of our nanobiosensor based devices, followed by characterising electrically the device in real time and continuous biological flow.

We had schematised the principle of our nanobiosensor in the general introduction of this thesis. This schema is presented once more in Fig.7.1.

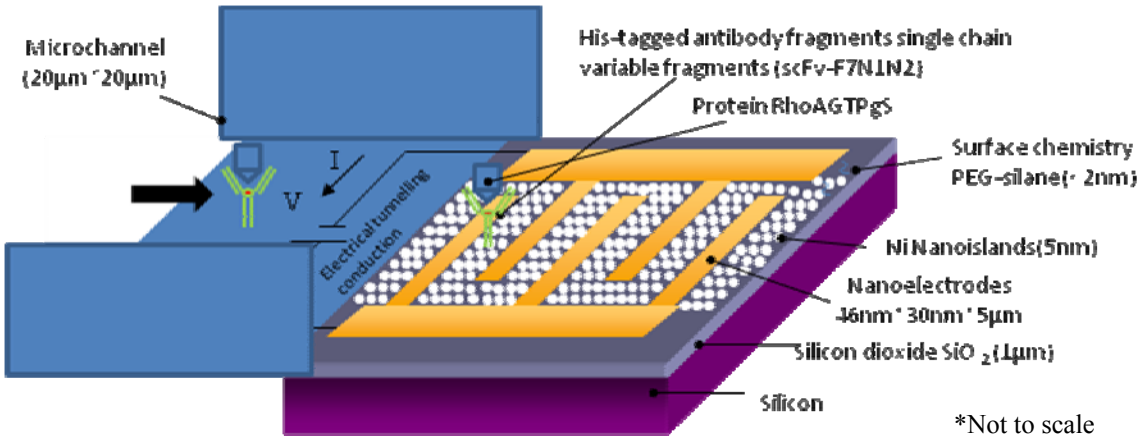

Fig.7.1. Schema illustrating the principle and integration of one nanobiosensor device.

We remember that the principle of the novel electrical nanobiosensor is based on the variation of electrical conductivity in the nanoelectrodes array due to the proteins adsorbed onto Ni nanoislands. Ni nanoilsands (~5nm diameter) are embedded into SiO_2 and placed between interdigitated nanoelectrodes devices (IND) of < 50nm width each electrode. Nanoislands are separated each other from ~2 nm. In these conditions, we obtain a nanotransducer, based on the variation of electrical tunnelling conductivity through metal nanoislands due to the quantum phenomenon called coulomb blockade at room temperature. Because of this phenomenon, these nanodevices are ultrasentive to any change that can affect the tunnelling conduction, for example, adsorption of proteins. Hence, his-tagged antibodies functioning as probe are linked, by coordinative bonds, to the Ni nanoislands, they recognise specifically the active RhoA form conformation which functions as target and discriminate against its inactive RhoA conformation. An innovative methodology to realise photoPDMS-based microchannels (20 µm diameter) was developed and integrated with IND on 4 inch wafer, see Fig. 7.1. Encapsulation with an etched PDMS-nanocomposite finalised the integration of the device.

Otherwise, to elaborate the different steps of the nanobiosensor integrations on wafer scale, we had proposed an organisation chart (organigram) in the general introduction. See Fig. 7.2.

We proposed two possible technological routes after PhotoPDMS based microchannels (chapter 5) to attain our purpose: once on the left containing the chapter 6 (bioplumes) and other route on the right of the organigram. Fig. 7.2 (next page) illustrates the selected route we used, by a continuous black row, to conduct the electrical and biological tests. We used this route since we have not tested yet the photoPDMS based microchannels encapsulation with the PDMS film (480µm thick, section 2 of chapter 5) after depositing biomolecules with bioplumes as demonstrated in chapter 6. However, it is possible to follow the not selected route for reaching full wafer scale integration and multiplexed biological deposition.

Finally, we did not use the bioplumes to depose the probes to conduct our final tests, but after encapsulating the microchannels we injected the biological flow (probes and targets) through the interconnecting tubes like in conventional QCM technology (see the continuous black row of the organigram).

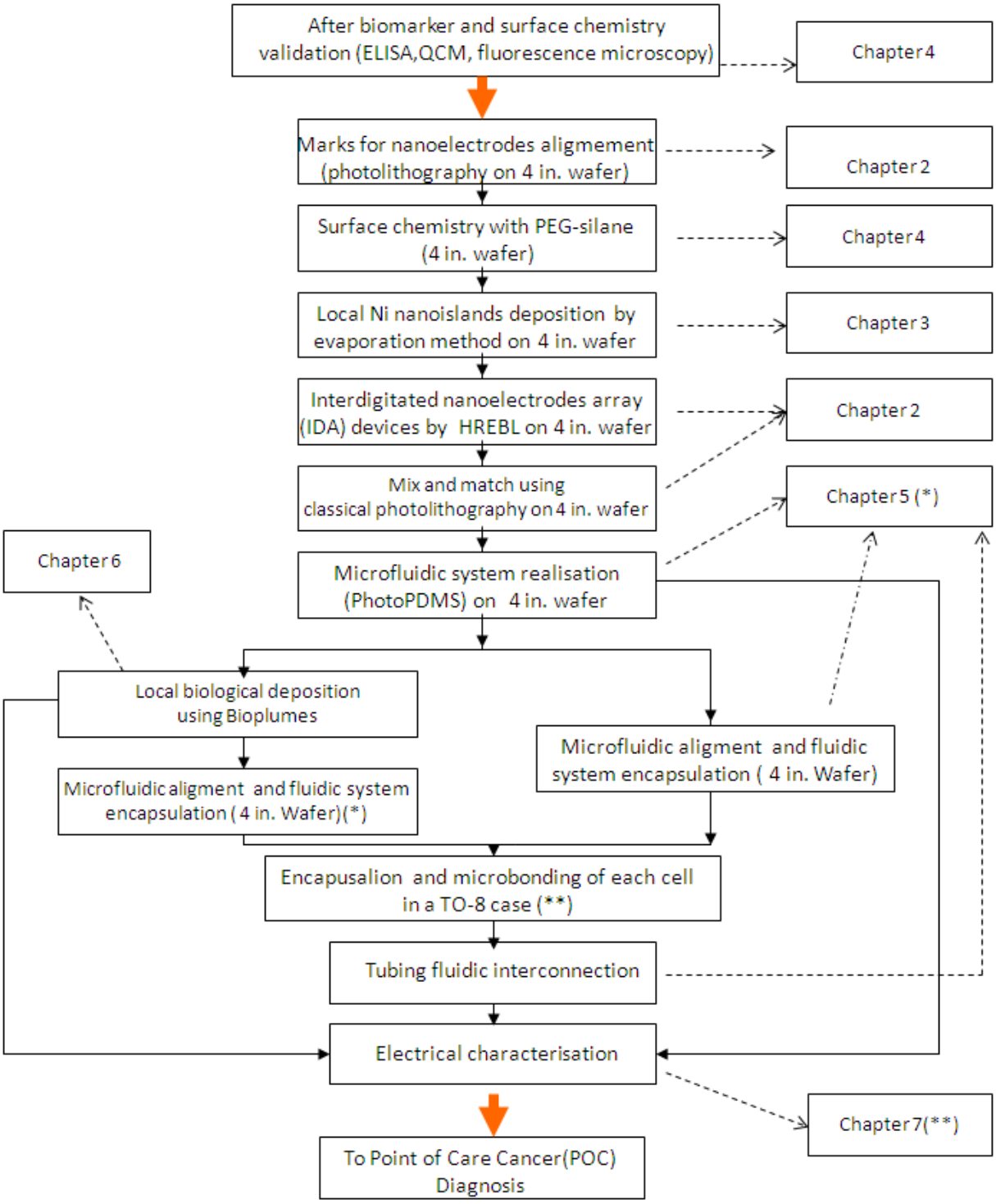

Fig.7.2. Orgranigram for elaborating the integrated devices and for presenting the research work in the different chapters. The row illustrates the selected route to conduct the biological tests, presented in this chapter.

All steps of the organigram, to achieve the integration, were demonstrated in previous chapters and all the parameters were given. Because of this reason, here I present all steps linked together, just mentioning the technological developments or the technological processes but without repeating the details but showing optical and electronic images of the different developments. In this context, the main purpose of this chapter is to present

electrical tests to detect selectively biomolecules which have been found as potential biomarkers in several cancers.

7.2 Nanobiosensors integration at wafer scale

To follow, exactly, the steps illustrated in the mentioned organigram, first 4 in. silicon wafers were thermally oxidised to obtain 1 µm of SiO_2. The choice of this was because the thickness is larger that the characteristic length of the active sensors (nanolectrodes) thus this diminishes the parasitic capacitance from the interdigitated nanoelectrode devices (IND) to the silicon [1] and also for keeping compatibleness with previous tests realised in quartz-SiO_2 (1 µm thick) for biological interactions and validation (chapter 4).

Several photomasks were produced to conduct the different steps of the organigram and some of them were used twice. The first technological step consisted of realising the marks patterns in wafer scale to align the nanostructures (to more details refer to chapter 2). To do this, we used the called here mask 1. Fig. 7.3 illustrates two marks after lift-off process (Ti/Au-10nm/20nm). A 4 in. wafer contains 1563 marks like these.

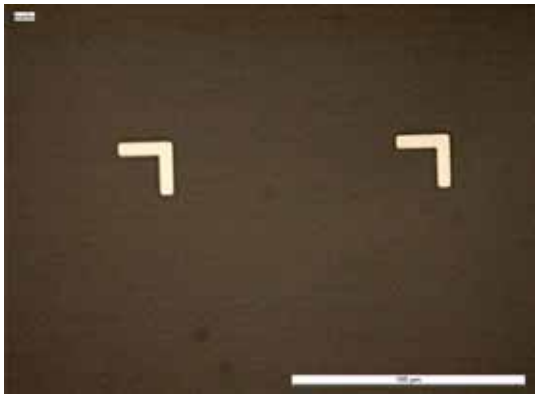

Fig.7.3. Two gold marks used to align nanoelectrodes at a wafer scale (there are 1532 marks in 4 inch wafer).

The second step was the realisation of the surface chemistry based on PEG-silane (refer to chapter 4, to more details). To do this, we used the photomask used in positive PhotoPDMS realisation. The reason is that, this mask (called here mask 5) permitted to realise channels-shape patterns in a positive resist (AZ1529), in such a way that the PEG-silane would pass into the patterns and be covalently bound on the SiO_2. Chemical compounds involved in preparing the PEG-silane did not remove the photoresist. Indeed a similar methodology was reported to realise PEG-passivated proteins microarrays in where some patterns were protected with photoresist [2]. The PEG-silane based surface chemistry serve, in our work, as anti-biofouling (as described in chapter 4). Indeed, as it is a hydrophilic surface (~37°) as demonstrated in chapter 4, it is useful to help in the transport of biological flow.

The subsequent step consisted of depositing the Ni nanoislands. To do this, 768 apertures in a reversible photoresist (AZ5214) were realised using the mask 2 which carried squares patterns of 10 µm X 10 µm. These patterns are aligned right in future interdigitated nanoelectrode devices (IND). See fig. 7.4.

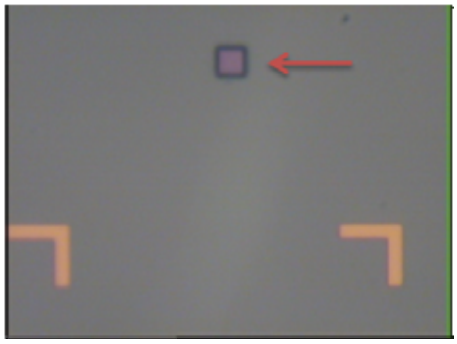

Fig.7.4. One opened-square shape pattern (10 µm X 10 µm) to depose Ni nanoislands. In a 4 in. wafer, there are 768 like this.

After spin-coating the electron-sensitive resist (PMMA) on the wafer, the interdigitated nanoelectrodes devices (IND) were realised by e-beam lithography, using the same parameters demonstrated in chapter 2. Fig. 7.5 (a) illustrates a typical optical image of IND after developing the PMMA (it is a useful optical image that permits us to infer from the successfulness of the IND, hence to observe if an electronic overdose or electronic underdose had been applied). Figure 7.5 (a) illustrates also a vertical and a horizontal line made by Raith 150 (see the rows on the marks) to find the centre of the gold marks and to align each IND as mentioned in chapter 2. Fig. 7.5 (b) illustrates a typical optical image after deposing Ti/Au-10nm/20nm, thus after lift-off process. This image illustrates a square spot (see the row) which corresponds to the nanometric Ni film deposition realised before the IND realisation. Finally the figure 7.6 illustrates a SEM image of the Ni depositions and IND.

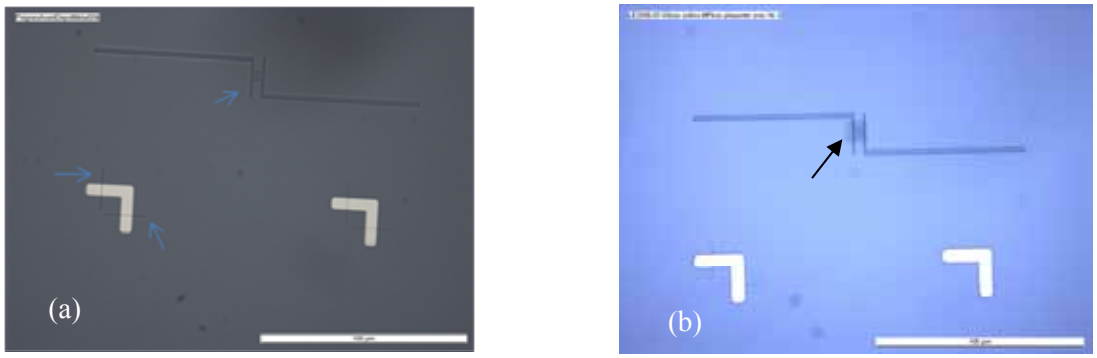

Fig.7.5. (a) Optical image of one IND after developing the PMMA, it illustrates the e-beam marks to align each IND, (b) typical image of IND after lift-off, illustrating the Ni nanoislands deposition with a row.

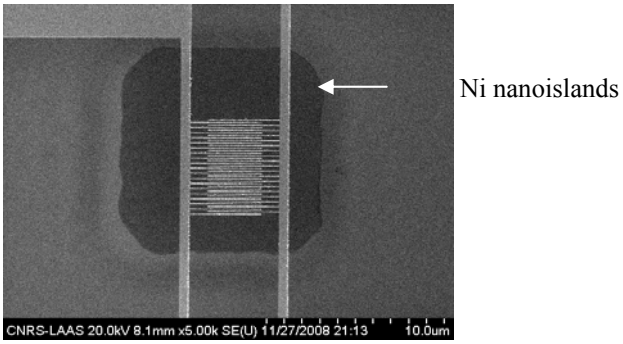

Fig.7.6. SEM image of the Ni nanoislands deposition in one (IND).

Next step consisted of using the mask 3 to realise the micropatterns which serve to connect the nanostructures. See Fig.7.7.

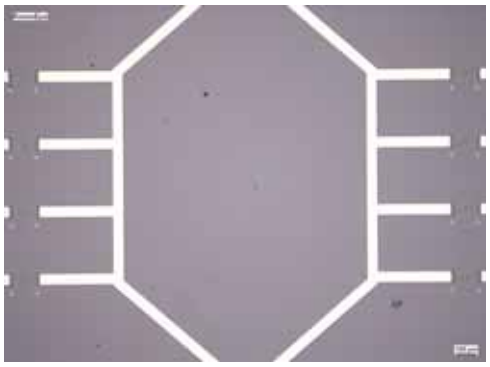

Fig.7. One cell illustrating the mix and match to connect the IND and to realise some micropads.

Finally the gold thickening, mentioned in chapter 2, was realised using mask 4. Fig 7.8 illustrates an Au thickening (1 μm thick) in one IND.

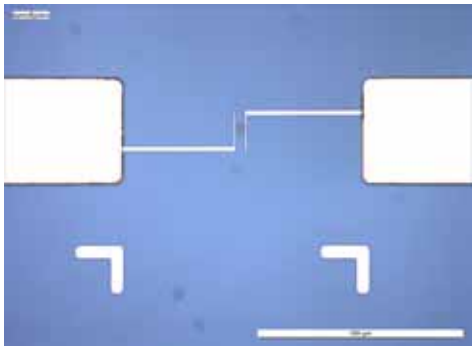

Fig.7.8. Gold thickening to realise microbondings.

Until here, the 4 in. wafer contains the nanodevices connected to several plots. Fig. 7.9 (a) illustrates an entire 4 in. wafer after mix and mach realisation as realised in chapter 2 (see the organigram of this thesis).

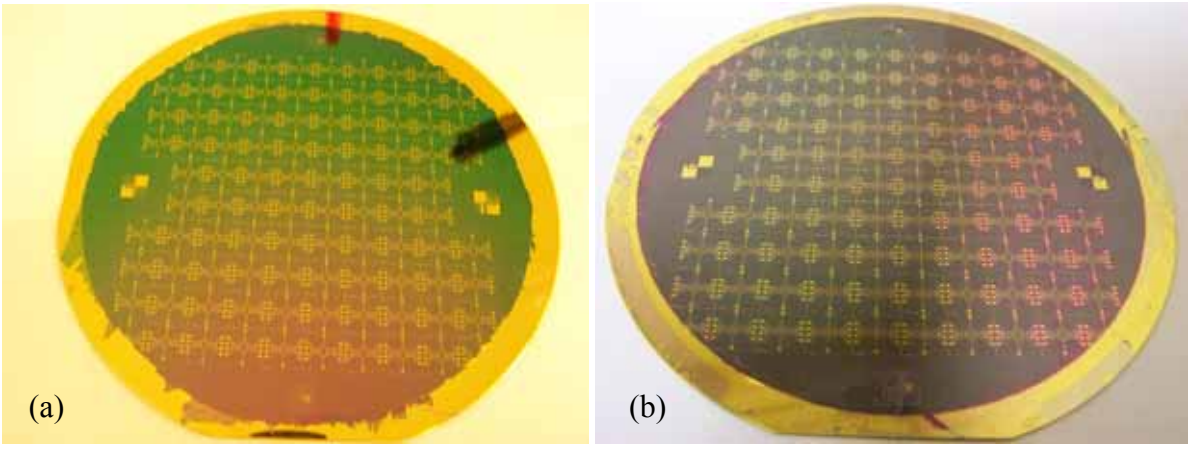

Fig.7.9. (a) Mix and match on 4 in. wafer level containing the nanoelectrodes and nanoislands, (b) photoPDMS based microchannels aligned on the 4 inch wafer of the Fig. 7.9(a).

The next step consisted of aligning and realising negative photoPDMS based microchannels in 4 in. wafer. The final process, at wafer level, is depicted in Fig. 7.9 (b).

Fig.7.10 (a) illustrates part of the 4 in. Wafer, demonstrating the alignment and realisation of negative photoPDMS based microchannles and Fig. 7.10 (b) depicts a close-up of a single cell.

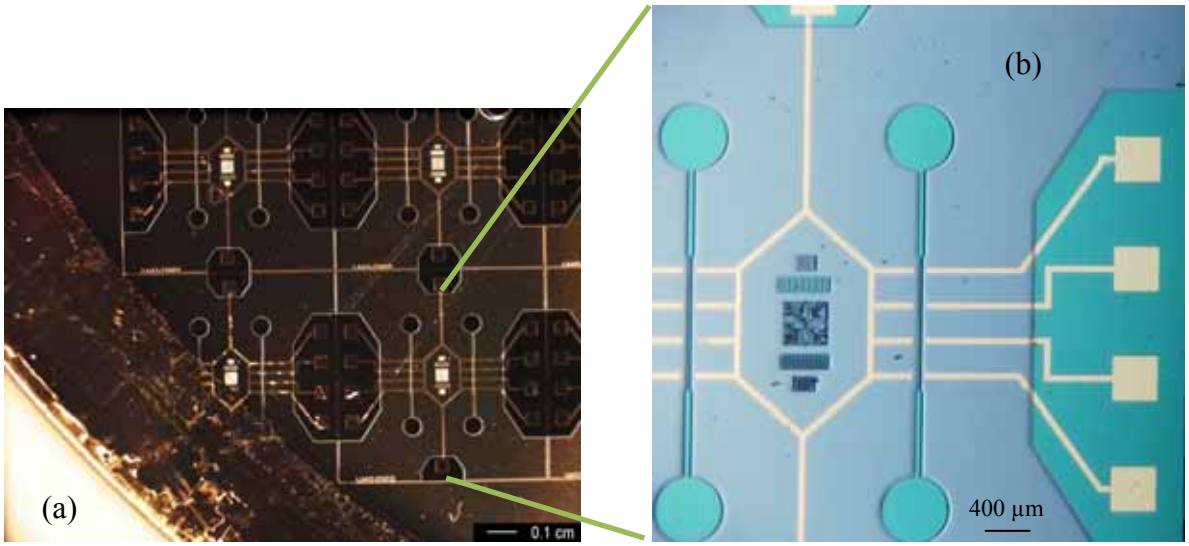

Fig.7.10. (a) Optical image of photoPDMS-based microchannels realisation on wafer scale (it is a part of the wafer), (b) Close-up of a single cell.

Our original objective was to encapsulate the photoPDMS based microchannels in wafer scale by using an etched PDMS nanocomposite (480 µm thick). Therefore we started testing the wafer scale encapsulation by using the nano-imprint lithography (NIL) tools of an EVG-620 machine. However, despite some results, we did not finish the final encapsulation of photoPDMS based microchannels. Then we decided to cut all the 98 cells of the previous wafer (after realising the photoPDMS based microchannels) and we encapsulated some cells into TO-8 cases, after realising the microbonding step. Fig.7.11 illustrates one encapsulated cell and an enlarged part of it, demonstrating successful microbondings. Note into the microchannels that there are IND.

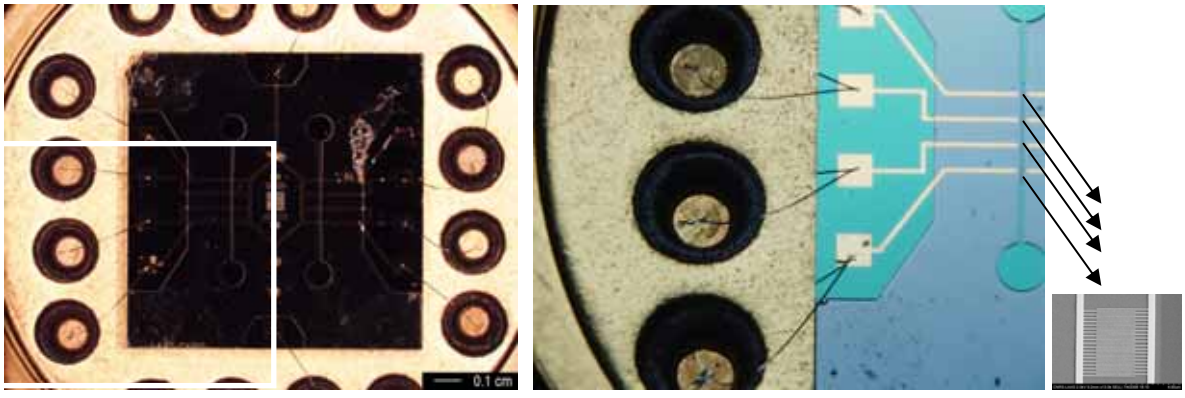

Fig.7.11. Left: one encapsulated cell in TO-8 case. Right: enlarged part of the TO-8 case, demonstrating successful microbonding into the photoPDMS patterns, this encapsulation contains 4 IND, into the two channels.

We encapsulated manually each cell (7 mm x 7 mm) containing two photoPDMS-based microchannels, with the objective of reaching the purpose of this thesis. We used the etched PDMS nanocomposite to encapsulate. Fig. 7.12 (a) pictures one cell encapsulated in a TO-8 case and Fig. 7.12 (b) and Fig. 7.13(c) picture, in different perspectives, the same cell in close-up.

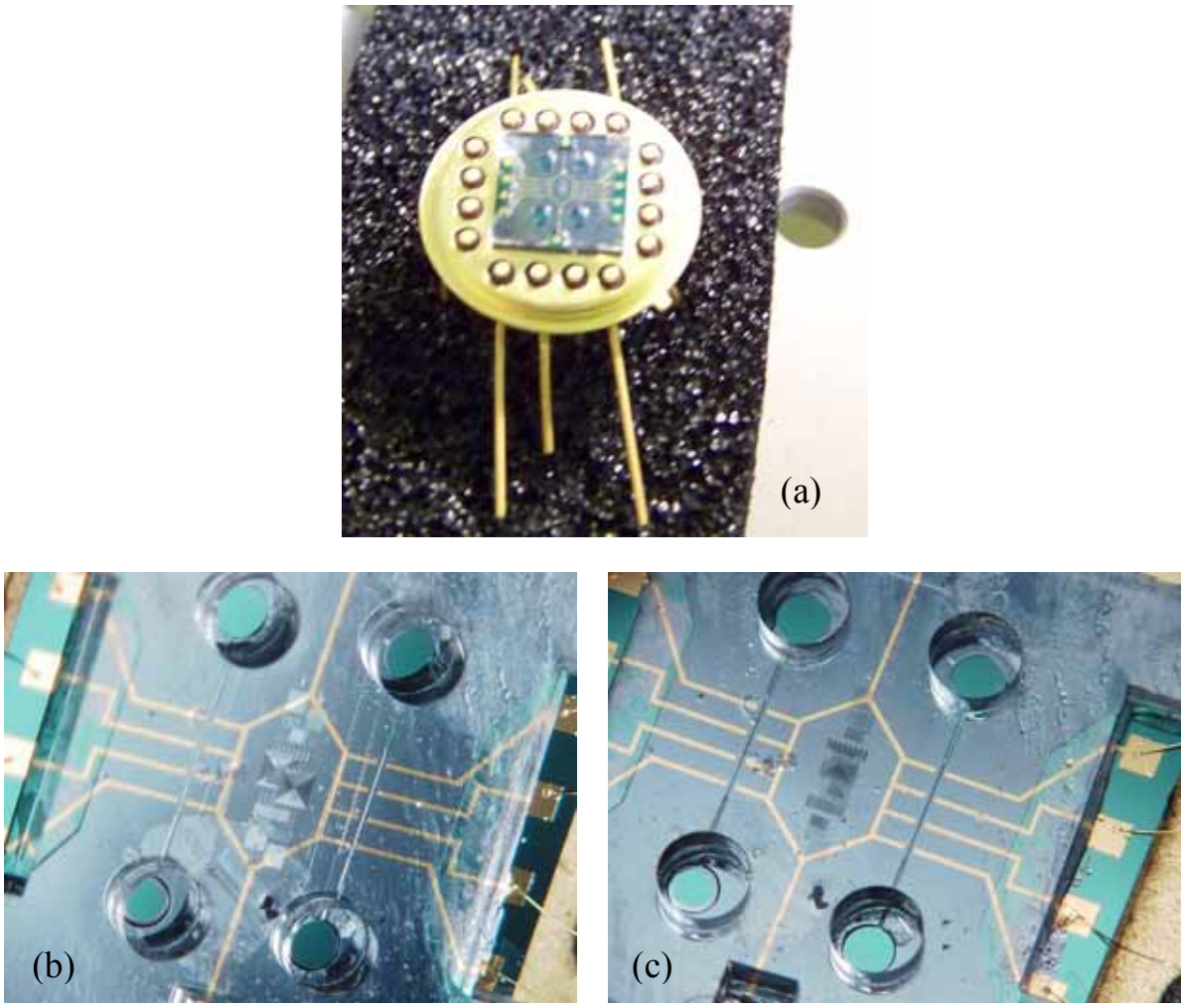

Fig.7.12. (a) An integrated device, encapsulated in TO-8 with the etch PDMS film (480 µm thick), (a)(b) Close-up, in different perspectives, of this successful encapsulation.

To seal the photoPDMS based microchannels with the etched PDMS film (480 µm thick), we used an epoxy resin: E501$^{(R)}$ model, purchased from Epotecny France. The choice was adopted after testing several models like E505 from Epotecny® France and the N-008 from Cluzeau info lab, however they did not work. It is a bicompound epoxy resin that polymerises at 65 C during 1 hour or at 25 C during 12h. The resin was applied manually thus a slight film was applied in all the 480 µm PDMS film to avoid filling the photoPDMS channels. In these devices the interconnecting tubes can be sealed into the circle shape patterns.

To seal four interconnecting tubes, we used the same piece presented in chapter 5 to seal, at same time, four tubes. See fig 7.13.

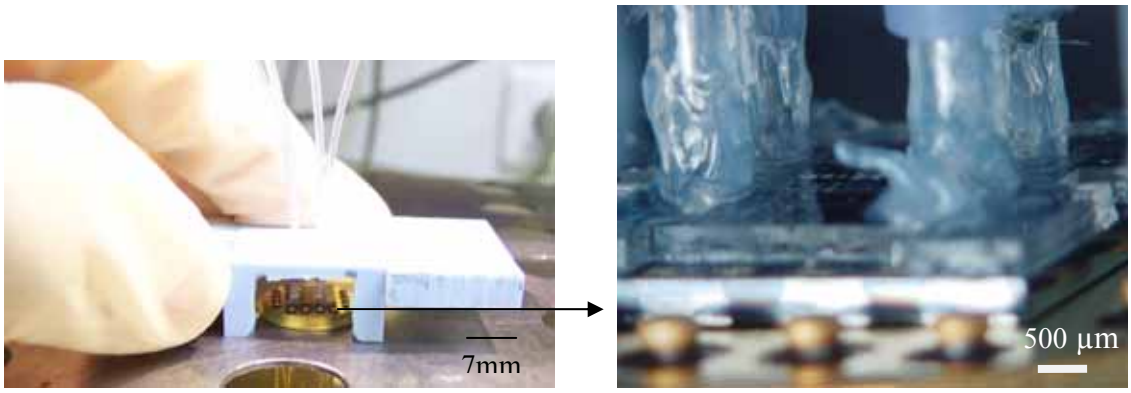

Fig.7.13. (a) Seal of four interconnecting tubes in one TO-8 case, using a polymeric piece. On the left, close-up of the same TO-8 illustrating the four tubes sealed into the circle-shape patterns of the PDMS film (480 µm).

To avoid leakage in the sealed tubes, it is critical to seal the tubes once they have well entered into the circle-shape opened patterns, furthermore it is important to use also a good adherent resist. Fig. 7.14 (a) depicts a good interconnecting tube sealed. Fig. 7.14 (b) depicts the PDMS film (480 µm), the Si/SiO_2, a microbonding and the adherent resist.

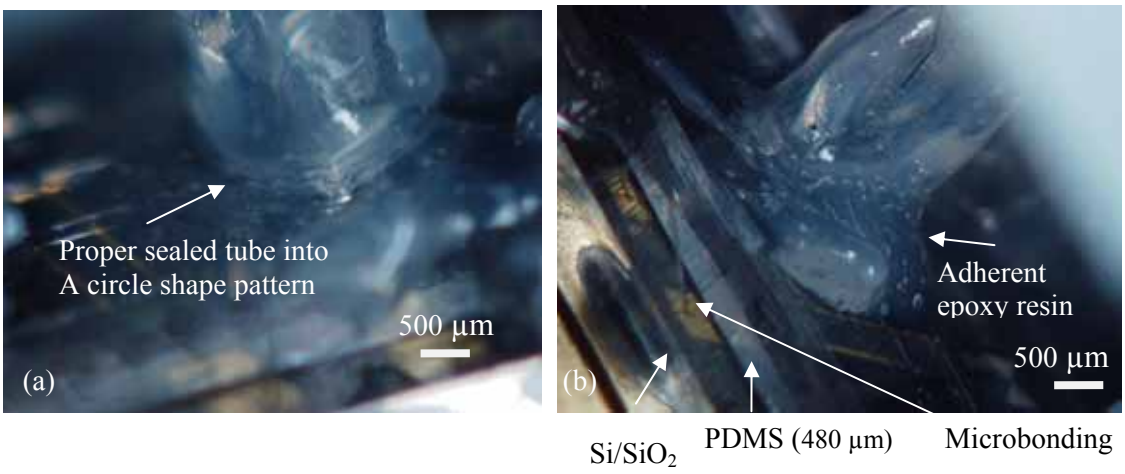

Fig.7.14. (a) An appropriate sealed tube into the circle-shape patterns, on the left, the tube showing the adherent resin used.

To do the electrical tests, we place placed one device in a faraday cup, made of metal to avoid electromagnetic noise and optical noise described in chapter 4. The piece, made of polymer, was used to guide and mainly to maintain the interconnecting tubes. The tubes were placed passing thought the metal case as we could to cover the faraday case. Finally the integrated device (TO-8 case) was soldered in a printed circuit to connect the electrical wires. We used a peristaltic pump to inject the flow. It is the peristaltic pump of the quartz crystal microbalance (QCM-D) used in chapter 4 to validate the bimolecular interaction. See Fig. 7.15 (a).

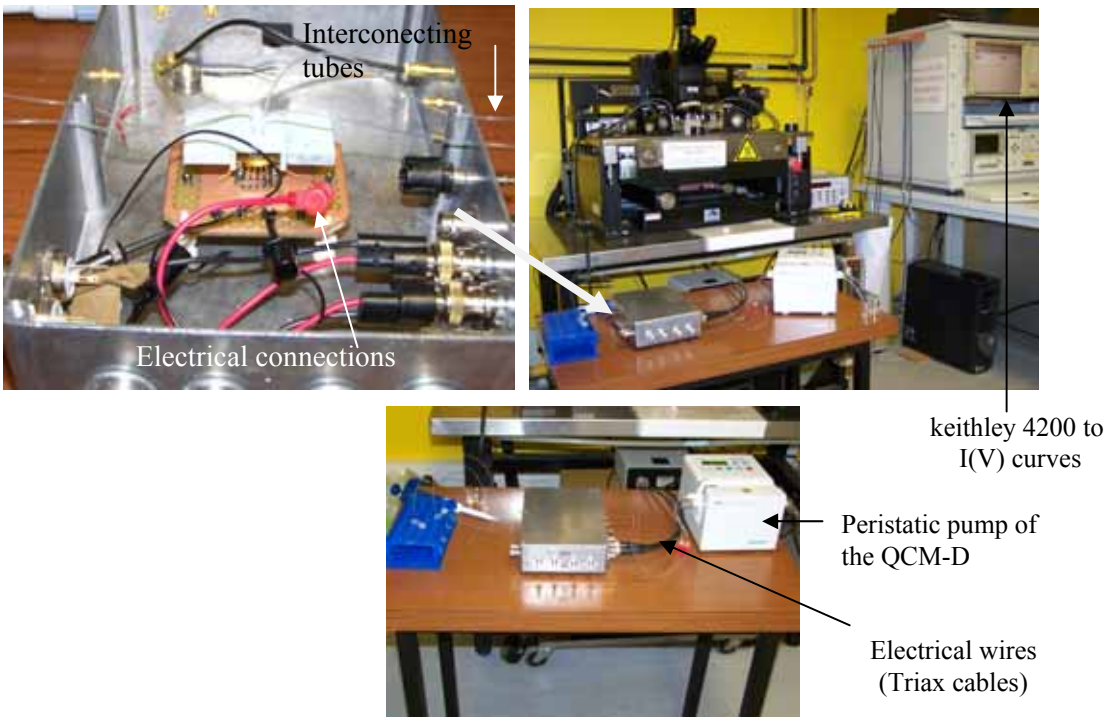

Fig.7.15. (a) Optical images of our soldered device in a printed circuit, placed into faraday cup to avoid electromagnetic and optical noise. The four interconnecting tubes go through the metal case. Images showing the connexion of electrical wires, and the Keithley 4200 to apply voltages and register the I(V) data and graphs.

7.3 Biological tests

Here, we present preliminary tests of biomolecule detection. We had never tested these kinds of Multitunnel Junction Devices (MTJ) coupled with biomolecules. Furthermore there are not works or papers in the specialised literature. Then, we decided in conjunction with physicists and biologists, to start our experiences by measuring the electrical response of our nanobiosensor based integrated devices (NID) after drying the antibodies and antigens. The principal reason, we thought, was that if doing the electrical tests in wet conditions (in aqueous solution thus in biological continuous flow) short circuit responses could be obtained. Clearly by doing this methodology, we can not be sure that the biomolecules keep their tertiary and quaternary structure (conformations) since they are in “dry” condition, otherwise perhaps some water molecules remained. This uncertain methodology is not realised in typical molecular biology tests such as enzyme-linked immunosorbent assay (ELISA). However, it was necessary to investigate our devices in these “dry” conditions, although in a second step a few electrical tests were realised in wet conditions (in aqueous solution so without drying the biomolecules).

Next graphs have been plotted, from the data files generated in Keithley 4200 machine, with origin-8 software.

7.3.1 Dry conditions

The methodology to realise the biological tests, in dry conditions, is as follows:

Note: We used for all tests, hepes buffer PH 7.5 with 5mM of $MgCl_2$ (to conserve the active or inactive conformation of RhoA when adsorbing the biomolecules) henceforth called hepes buffer solutions (HBS).

First, an injection of antibodies (scFv F7N1N2) at 40µg/ml in HBS was conducted (mass concentration similar to our QCM experiments of chapter four). Then, an "incubation" period for more than 40min was performed. Next step consisted of rinsing with HBS, finally rinse with de-ionised water. To dry the biomolecules, we used dry air during few seconds. After this methodology an I(V) measure was realised.

A) Results

Fig. 7.16 depicts the I(V) plot of the antibodies (scFv F7N1N2) response .

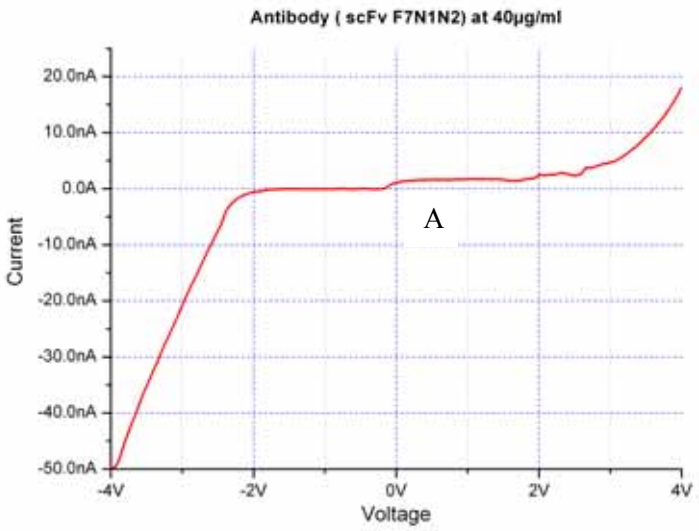

Fig.7.16. I(V) graph after antibodies (scFv F7N1N2) incubation and drying.

This graph (A) is a typical response of electrical tunnel conduction through the Ni nanoislands such as presented in chapter 3. However, here the curve is not symmetrical but not substantially noisy altogether. This asymmetrical shape can be due to the influence of biolomecules. Rather, despite this response shape, this graph can allow us to infer from the future adsorption of the subsequent biomolecules.

The mentioned adsorption is expected to change the shape of the curve, mainly change the coulomb gap. However we desired the inactive form of RhoA do not change significantly the curve of Fig. 7.16 but when the active form of RhoA were adsorbed, the same graph changed substantially. Next steps will consist of testing the inactive Rho A response and subsequently the active form of Rho A.

The antibodies GST-RhoA GDP (inactive form of RhoA) were prepared with HBS at 500ng/ml and they were injected. Next step was to rinse with HBS and finally rinse with deionised water. To dry the biomolecules we used dry air during few seconds. After this methodology an I(V) graph was plotted, by sweeping a voltage from -4 V to 4V. See Fig. 7.17.

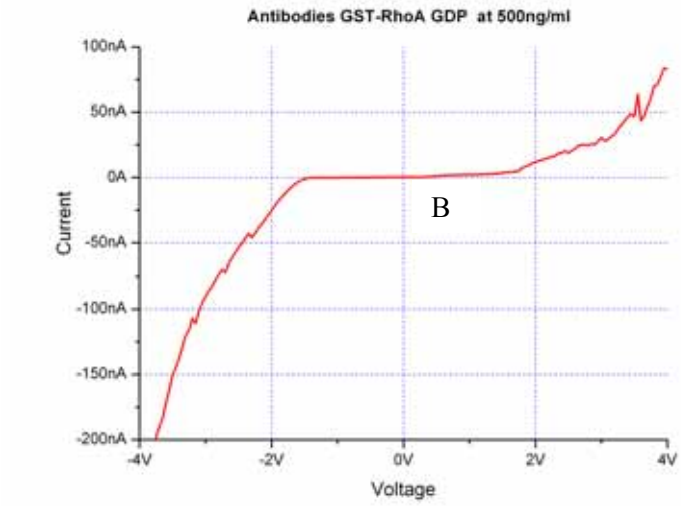

Fig.7.17. I(V) graph after antibodies incubation(scFv F7N1N2) and GST-RhoA GDP (inactive conformation) incubation and drying.

Slight variation can be observed in previous curve referring to the antibody´s curve of figure 7.16. Moreover what is observable is that more current pass through the device at a given voltage.

The antibodies GST-RhoA GTP (active form of RhoA) were prepared with HBS at 500ng/ml and they were injected. Next step was to rinse with HSB and finally rinse with deionised water. To dry the biomolecules we used dry air during few seconds. After this methodology an I(V) graph was plotted by sweeping a voltage from -4 V to 4V. See Fig. 7.18.

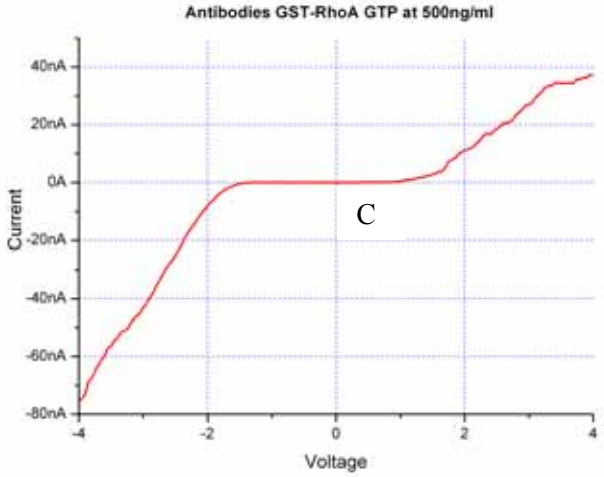

Fig.7.18. I(V) graph after antibodies (scFv F7N1N2) incubation and GST-RhoA GTP (active conformation) incubation and drying.

It is observable on Fig. 7.18 that less current passes through the device, however the curve shape has a behaviour resembling to such as of figure 7.17 (inactive form). Hence, no important noticeable coulomb gap variation is perceived thereof.

The different graphs can be superposed to observe clearly the expected variations. See Fig 7.19.

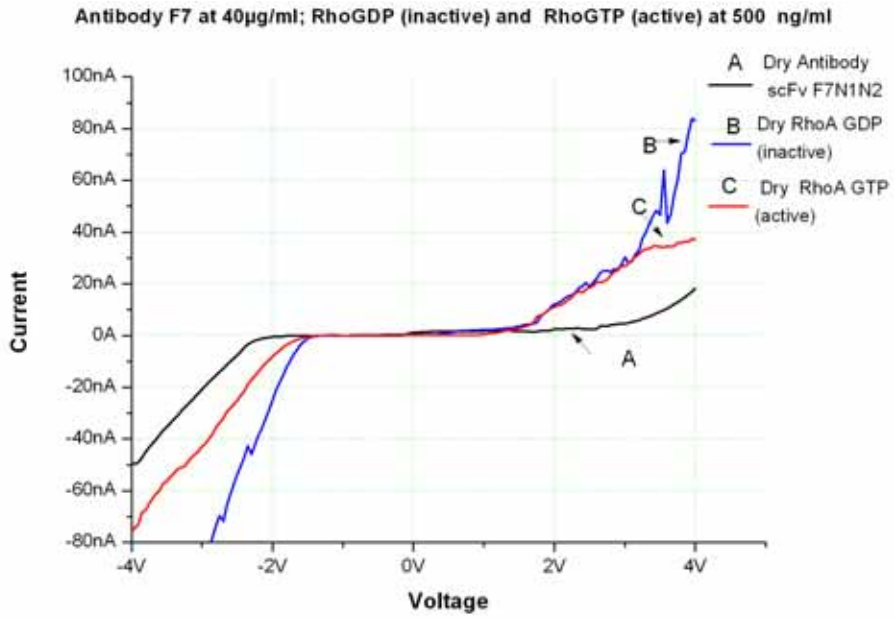

Fig.7.19. I(V) graphs of the antibodies GST-RhoA GDP and GST-RhoA GTP in dry conditions.

To observe if there is a variation of the coulomb gap in the I(V) graphs, due to the adsorption of the active form of RhoA, the conductance was traced (derivative dI/dV) similar to chapter 3. See Fig. 7.20.

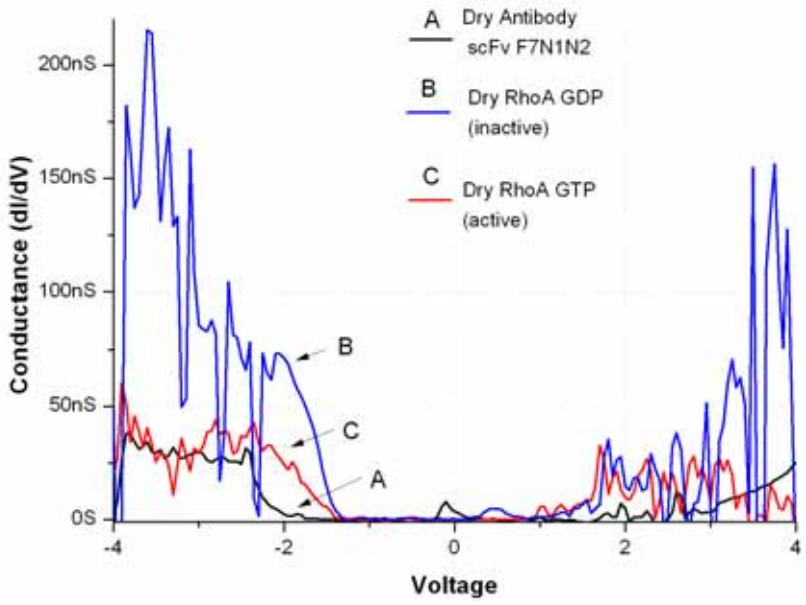

Fig. 7.20. Conductance of the I(V) graphs of Fig, 7.19, demonstrating coulomb blockade effects and the effect of the curve behaviour when absorbing the different biomolecules.

B) Discussions

The graphs of figure 7.19 have a typical comportment of electrical tunnel conductions, presenting coulomb blockade at room temperature. Hence, these multi tunnel junction devices (MTJ) have demonstrated electrical tunnel conductions also with biomolecules adsorption. However, these (MTJ) functioning with biomolecules at "dry conditions" did not clearly discriminate from the inactive form of RhoA (red curve: C), furthermore we did not see an important difference in the coulomb gap variation on the conductance graphs of figure 7.20. Otherwise, we noticed a higher passage of current when adsorbing the inactive form of RhoA, and a slight variation in its coulomb gap (blue curve), perhaps because of a change of conformation either in the first antibodies absorbed or the dried antigens we injected.

It is important to note that the inactive form of the RhoA can bind to the antibodies due to hydrophobic, hydrogen or other bonds but we must differentiate the electrical response from the inactive to active form, as in the case of typical detections method such as ELISA immunoassay. From these first experiments, we think that the biomolecules have lost their conformations while drying them, as hypothesised in the introduction section of the dry conditions tests. We decided to electrically experience the MTJ in wet conditions.

7.3.2 Wet conditions (in aqueous solution)

Here, we present some tests in wet conditions by omitting the dry part of the above protocols. These tests will permit us to demonstrate a better capability of our devices by discriminating between active and inactive form of RhoA biomolecules. The experiments have been realised in continuous biological (in aqueous solution) and in real time.

At the time we are writing this research work, we have detected 5 ng/ml thus 111pM if considering 45kD the molecular mass of GST-RhoA. Fig. 7.21 depicts a close up of the interconnecting tubes when the biological flow is passing through the interconnecting tubes. Some white spots are observable (in colour format).

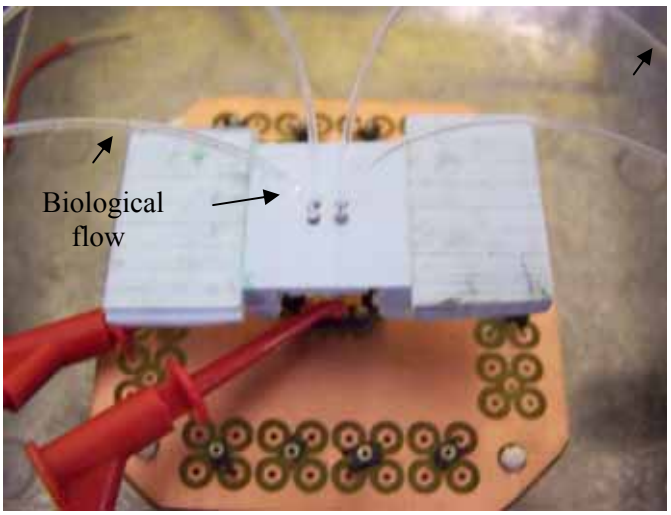

Fig.7.21. Close-up of our nanobiosensor based device (soldered in a printed circuit), the image demonstrates that some electrical tests were achieve in continuous biological flow (see the rows), consequently in real time.

A) Results

To conduct the electrical tests in wet conditions, an injection of antibodies (scFv F7N1N2) at 40µg/ml in HBS was conducted, then a voltage sweep was applied to plot an I(V) graph. Next 5ng/ml of GST-RhoA GDP (inactive) in HBS were injected and a subsequent voltage sweep was applied to plot an I(V) graph. Then, HBS was injected for few minutes to remove the no adsorbed biomolecules. Secondly, 5ng/ml of GST-RhoA GTP (active form) in HBS was injected, followed by applying a voltage sweep to plot a I(V) graph. See Fig 7.22.

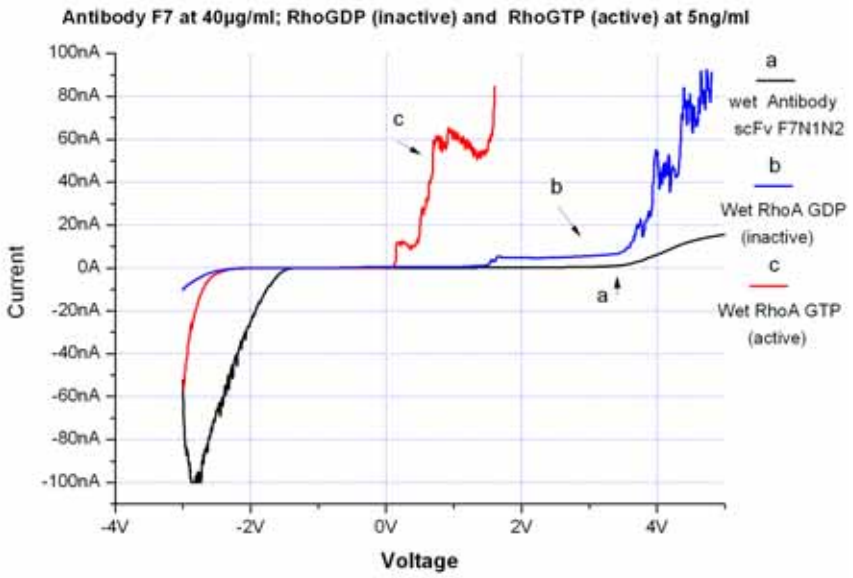

Fig.7.22. I(V) graphs of the GST-RhoA GDP and GST-RhoA GTP at wet conditions, responses of a continuous flow and real time.

The coulomb gaps of the previous graphs is clearly different, mainly in the positive values of voltage, being corroborated and plotted in the conductance graph (derivative dI/dV) of the Fig. 7.23.

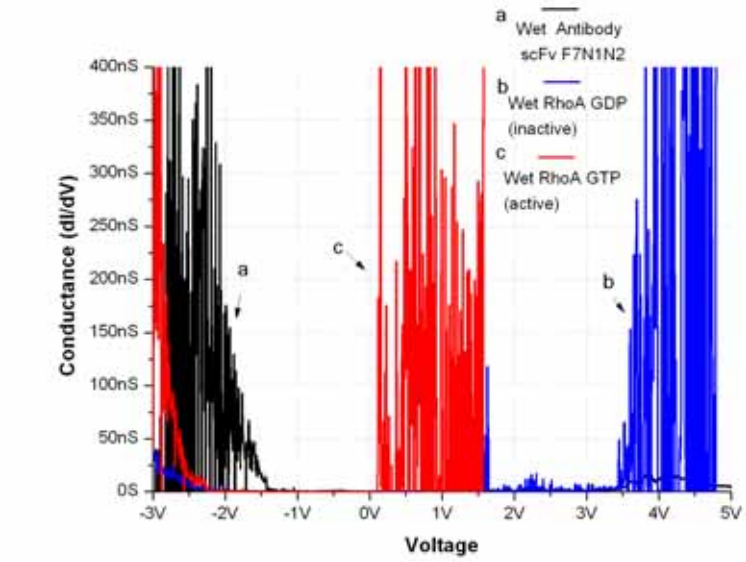

Fig.7.23. Conductance of the I(V) graphs of Fig, 7.22, demonstrating selectively a detection in wet conditions of the active form of RhoA, while discriminating from its inactive form of RhoA.

B) Discussions

In this case (wet conditions), our multi tunnel junction devices (MTJ) have demonstrated electrical tunnel conductions with biomolecules' adsorption in continuous biological flow, furthermore the MTJ have been characterised in real time. From the graphs of Fig. 7.22 and Fig. 7.23 we can infer from their behaviour, despite they are not symmetrical, that a detection of the active form of RhoA is well conducted (GST-RhoA GTP: red curve, referred as c) and that the MTJ device discriminates from the inactive form of RhoA (GST-RhoA GDP: blue curve, referred as b). Indeed, these graphs present some noisy responses and less current passes through the device while adsorbing RhoA active form.

Another important result is that, these kinds of multitunnel junction devices (MTJ) have rapid responses since the electrical responses have been generated in real time. As comparison, M. Lieber´s group reported, in the 2005 year, electrical detections of cancer biomarker through nanowires [3]. Although nanowires demonstrated high sensitivities (femtomolar level) one drawback (not mentioning the fact that nanowires are difficult to be positioned) is their high detection time because of the inefficient mass transport [4]. In the article of Lieber´s group, the detection time between different biomolecules was at least 25 min [3]. Otherwise our devices demonstrated higher detection time (few seconds to obtain I(V) graphs).

We observe that we have not obtained classical Coulomb blocakade reigimes, even though there is not conduction, near zero voltage. However, the asymmetrical behaviour is not well understood yet, perhaps the charges charges involved in biomolecules (mainly in the protein Rho,) are the origin of this depending of its ionised state. It is suitable to test the devices varying the pH ultil find its isolectric point and compare the different graphs.

Indeed, I hypothesise that the biomolecules linked with metal (histidine) could behave as electron transfer proteins thus when other biomolecules (targets) are specifically linked, the electrical tunnelling conduction is modified.

Finally, the device did not present significant hysteresis in both dry and wet conditions. Direct-plotted graph of Keithley 4200 corroborated this situation. Figure 7.24 (a) corresponds to the antibodies´ hysteresis in aqueous solution and (b) corresponds to the GST-RhoA GTP hysteric graph, in dry condition.

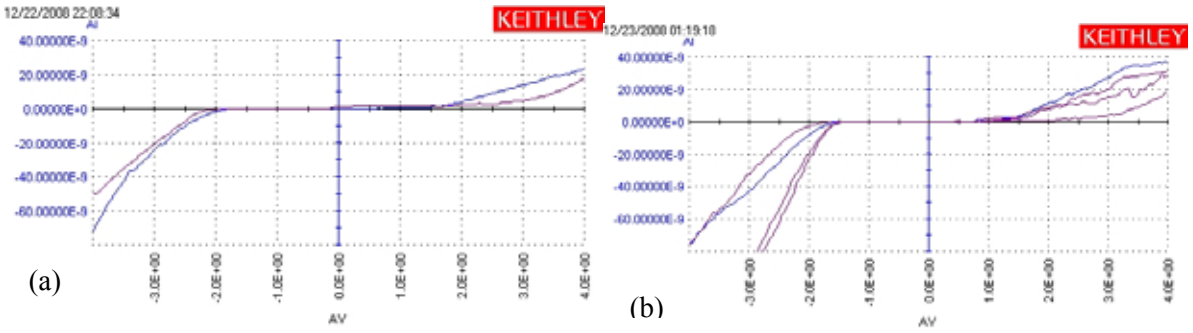

Fig.7.24. (a) no significant hysteric in I(V) graphs of the scFv F7N1N2 antibodies in aqueous solution, (b) no significant hysteric in I(V) graphs of the GST-RhoA GTP antigens in dry condition.

7.4 Conclusions

In this final chapter we have demonstrated the complete integration of our nanobiosensors which were based on intedigitated nanoelectrodes and Ni nanoislands serving as transducers. These mixed and matched devices, realised at wafer level, have been coupled with PhotoPDMS-based microchannels as an innovative microfluidic methodology realisation. The integration finalised by covering the microfluidic channels with etched PDMS nanocomposite. To inject biomolecules, interconnecting tubes has been sealed in a single cell, after encapsulating the cell in TO-8 cases.

An integrated device has been electrically tested after injecting some different concentration of biomolecules.

Our integrated device presented typical electrical tunnelling conduction when biomolecules were injected in dry condition and continuous biological flow. In dry condition we were not able to discriminate the RhoA in active conformation from the RhoA in inactive conformation. However, from our preliminary tests, this kind of device turned out to be sensitive with high time responses, to detect the active form of RhoA (potential biomarker) and discriminating from the inactive form of RhoA (as negative test) in aqueous solution. Finally, our devices did present significant hysteresis neither in dry nor in wet conditions.

These integrated devices are the basis of functional lab-on-chips devices with applications in biomedicine, since integration with a display and a measure system such as microcontroller is expected. Devices had been conceived aiming a contribution to the multidisciplinary approach named nanobiotechnology and specifically to its exciting application named nanomedicine. Hence, these kinds of devices are one the nanotechnological routes, from which the point of care cancer diagnostics and personalised medicine can be reached.

7.5 References

[1] Gerwen Peter Van, Laureyn Wim, Laureys Wim, "Nanoscale interdigitaed electrode arrays for biochemical sensors", *Sensor and Actuators B*, **1998**,49, p-73-80.

[2] Kannan Balaji, Castelino Kenneth, Chen Fanqing Frank, Majumdar Arum., "Lithographic techniques and surface chemistries for the fabrication of PEG-passivated protein microarrays", *Biosensors and Bioelectronics,* **2006**, 21, 1960-1967.

[3] Zheng Gengfeng, Patolsky Fernando,Cui Yi,et al., "Multiplexed electrical detection of cancer markers with nanowire sensor arrays", *Nat. Biotechnol.,* **2005**,23:10, p.1294-1301.

[4] Kim Rip Dong, Zheng Xiaolin, "Numerical characterization and optimization of the microfluidics for nanowires biosensors", *NanoLett.,* **2008**, *8* :10, p. 3233-3237

General conclusion and prospective outlook

In this research project (thesis) we aimed at realising a novel nanodevice capable of detecting, at high sensitivity and reliability, cancer biomarkers. It was originally conceived to be part of an integrated device as the basis of a functional lab-on-chip. We were able to reach, in great part, our purpose. However, the devices lack of integrability and reliability to be used, with the same efficiency as for example a typical glucometer. Rather, through the development of different processes, we found several technological drawbacks which are not generally described in detail in a thesis manuscript. Nevertheless, I consider that one on the principal drawbacks (outside technological problems) was to find time to discuss and to realise all technological processes with all the different partners of the project due to the high interdisciplinary character of this work. In this context, in nanotechnology developments, it is essential to be flexible yet able to stick to the plan that has been drawn by the all participants of the project (physicists, physicians, biologists, chemists, mechanical and electrical engineers, technicians and so on). On the other hand, as in nanotechnology, it is necessary to use a large variety of chemical, electronic, biological materials and other compounds; it was also decisive to plan in advance the time it takes for supplier companies to deliver compounds or equipments. Last but not least, one must consider the available functional equipment (and obviously to preview the out of functioning) in the clean room or technological central devoted to nanotechnological processes. Hence, it is important to take in consideration that it does not take the same time, for example to repair a machine, in a research laboratory or a factory.

Concerning purely technological situations, we encountered an important bottleneck mainly in the realisation of interdigitated nanoelectrodes devices at wafer level. Hence we devoted important time to find the optimum parameters to realise our devices at the level of a 4 inch wafer and the critical parameter was to find the optimum dose. We dedicated also a large amount of time to obtain devices functioning as multi tunnel junction devices. Here, it was necessary to experience with several thicknesses of Ni depositions layers to obtain electrical tunnel conduction, but mainly to conjugate the same thickness deposition with the intedigitated nanoelectrodes. Seeking the way of integrating our devices with realisable microfuidic devices, we were able to develop novel technologies based on photoPDMS thus novel methodological processes to implement microchannels. However, in the case of the positive photoPDMS, the crucial step was to find the best photoinhibitor, easily dissolved and mixed with typical PDMS but also the photoinhibitor which permitted us to reach a good resolution. I can say that the method of dissolving the chemical compound was essential. Concerning the negative photoPDMS which underwent a longer implementation, the key issue was to find a good resolution at the wafer level. The essential step was the properness of the surface chemistry to stick to the subsequent PDMS. Thanks to the good adherent resist, we found, we were able to properly seal the interconnecting tubes and inject the biological molecules. Finally, we were able to realise some preliminary biological tests with encouraging results. However, it is suitable to realise more tests in aqueous solution to improve the functionality of our devices. The last point, described in this perspective outlook, is a possible path to decreasing the cost of fabrications.

One of the possible technologies to be considered is nanoimprint lithography (NIL), all types such as thermoplastic nanoimprint lithography (T-NIL), or photo nanoimprint lithography (P-NIL) which can replace, in an industrial environment, the electron beam

lithography employed to fabricate our intedigitated nanoelectrodes devices (IND). The technique will permit to realise the same kinds of devices at a lower cost.

Through the development of our work, we have found a way to transfer metal patterns onto PDMS and it was named reverse soft lithography. It is suitable to test this technique first at submicrometer scale (~500nm) to subsequently experience at nanometer scale (a disadvantage would be the use of ebeam lithography to realise the patterns, to be transferred).

Once the technological process is lower, it is important to integrate the device with an electronic device to measure the current variations. The objective will be to reduce the size of the electronic measurement device, maintaining a measurable reliability.

Otherwise, I consider a priority to start mathematical simulations of the interaction biomolecules with metal molecules of the nanotransducer: Some parameters have to be considered, such as biological flow diffusivity, limit detection time.

It is important to note that nanoelectrodes based devices, we realised, can be applied to other technological domains such as in nano-electrochemistry, biomolecular electronics, spintronics or to detect several kinds of compounds such as gases.

Adrián Martínez Rivas
nanobiomex@hotmail.com

ANNEXE: Epistemological and ethical personal opinions in nanotechnology

I write here my philosophical and ethical attitudes towards nanotechnology. I would like philosophers who stated the basis of epistemology to excuse me because I am not a philosopher and I dared to think about this intellectual plane. The reason is that through the development of my research work, I was able to work in the scientific approach named nanotechnology and/or nanoscience (especially nanobiotechnology and nanomedicine) in which there are constant technological advances but also philosophical paradigms and ethical issues are constantly emerging.

Firstly, I analyse from a conceptual point of view the similitude and difference between science and philosophy, next a philosophical reflexion of the nanobiotechnology approach is performed. Finally, after introducing some thoughts, I describe concisely the ethical subject before giving my personal opinion.

In science we need to create concepts and hypothesis, to define what our senses perceive as results of what our current technological machines interpret and one of the purposes of philosophy is precisely to define concepts. Here the first correlation is found. Otherwise, following the existential phenomenological definition of German philosopher Martin Heidegger, philosophy can be conceived as an inexorable thought or source of thought which can not be undertaken immediately, similar to science I would say. In science, we need a reference, state a basis so we can follow a method either to create a theory, a device or a machine. French philosopher Gilles Deleuze stated that one of the differences between philosophy and science is that philosophy is performed with a plane of immanence or consistency and science with a plane of reference. In my opinion, it is like if science had a though stopped to an image or reference and philosophy had an image stopped to a though. Hence, the primary difference is the way science and philosophy face the constant chaos of our conscious external world and a similitude is that chaos is faced both by the science and philosophy; even more this chaos is well faced by art.

Nowadays, we have to admit the importance of philosophy in science and remember that in the 17^{th} and the 18^{th} centuries all scientists were also philosophers who performed important scientific advances really to society. It turns out that scientific researchers need following a kind of “philo-scientific method”. In the philosophic part of the method, it is necessary to acquire a reflexion with questions such as why and how, what is the purpose. In the scientific part of the same method, a comparison, a basis or evaluations are needed. However, the constraints are not the same in philosophy and science.

To create concepts, it is suitable to define what a thing is. Martin Heidegger analysed this ancient question in his book: Die frage nach dem Ding (also analysed by Emmanuel Kant). Heidegger postulated that space and time are essential to define a thing and there is space in the interior of the thing. He imagined a piece of chalk that is split in smaller pieces, he arrived to imagine a piece of chalk measuring till 4 microns because of mechanical difficulties, he wrote. He concluded that the differences between these pieces are the quantity but the essence of the thing does not change (the what). Nowadays with the developments issue from nanotechnology, it is possible to split the matter to a smaller “pieces”, to observe and manipulate this matter. Here, we find precisely a novel philosophical paradigm because we have observed, by experience, that matter ranging from nanometrical size (<100nm) to smaller size, experience other properties as if its essence had changed. Indeed, according to

Heidegger, to learn about a thing (as a condition to define a thing) it is necessary to appropriate this thing, to learn to know the thing, to learn the usage of this thing. For example, when we perceive a chair, we know about this thing because of its usage: to permit to people to sit on. If this chair does not have one or more legs, we continue knowing that it is a chair; furthermore a chair with arms is an armchair thus its essence does not change. On the other hand, in the nanoworld, if it is changed a part of the nanometric thing, its usage changes. What it is more, if it is changed the distance of two nanometric things, the ensemble of the thing does not have the same usage (it is valid for the atoms and bonds forming a molecule), for example if we modify the nanoislands distance of our devices (around 2 nm); the device is not more a multitunnel junction device (MTJ) but is what we know as resistance or insulator (we have demonstrated it, in this thesis). Hence, in nanometric size a thing become other thing without being other thing, because of this in nanotechnology the object and subject are intimately connected.

At the present time, human society is involved in the approach named nanotechnology but also in nanoscience (because of the above examples and other demonstrations not presented here), in which an inevitable confluence, at the molecular level, has occurred. As written, here the concepts of object and subject have close meaning. If comparing with the tunnel junction duality or wave particular duality explained in this thesis, it is like if the essence of nanoscience were based on the concept/subject duality, not exiting neither a subject nor a concept but both of them, without being both at the same time. Conceptions as the degree of electrical conduction in carbone nanotubes which depends on the arrangement of carbons atoms are examples of this. In this context, bifurcations to the plane of philosophy are created to conceive the electrical tunnel conduction (quantum phenomena) and specially the electron penetration into a higher potential barrier.

Throught scientific history, philosophical currents have appeared, one of them, thought as such that permits a progress through science, was coined firstly by Auguste Comte. He claimed, in 1829, the necessity to follow a more general science to reorganise society and avoid crisis in which the most civilised nations are involved (sociology basis). However at that time, the problem, he said, was the difference of science development rate. He thought that the natural philosophy or specifically positive philosophy, opposed to metaphysic, was the route that permitted to reach his purpose. Nowadays, human society is involved in nanoscience and nanotechnology in which most of the involved sciences are at the same development level. Concerning positivism, Max Planck, one of the founders of quantum physics which governs the phenomena encountered in nanometric scale, was in accordance with positivism to the fact that science progresses in relation with the improvement of measurement methods (specially what for Planck was the more exact science: physics). However Planck disagrees with Auguste´s positivism on the sensible impression measures, which are supposed to form the point of depart of all science. According to Planck, the measures have to be considered as final more of less complex results having an influence between the exterior world and the phenomena involved in our measurement instruments and in our sensorial organs. I think that with a kind of transdiciplinarity of several philosophical currents such as positivism (Comte), Cartesian current (Descartes), existentialism (Husserl, Heidegger), psychoanalysis of science, philosophy of science (Popper, Poincaré, Bachelard), philosophy of biology (Piaget) and so on, we can face the inevitable chaos in a coordinative philo-scientific ordinate and abscise being the bifurcations not so distant in the nanoscience and nanotechnology plane.

Concerning the nanobiotechnology relating to "natural" biology, the main difference is that the molecular biology face the chaos to maintain the human body functionality, while nanobiotechnology wants to face the chaos at the same degree of coordinates but having other objectives: In the best case, to enhance the human quality of life. Rather, society scares the unknown creating macro chaos. Even if in the most of the cases, the uncertainty is created because of lack of clear information the society receives, in other cases the fright is sustained. In this context, the personal ethic plays an essential role, because of the free will some researchers think to have in their laboratories and their countries. Unfortunately, I think that what slow the progress of (nano) science is the human vanity and its foolish behaviour, but mainly the stupidity of some governments to focus on nanotechnology and nanoscience as the opportunity to enhance the army and soldier capacities, for instance, to see farther, to create other kinds of biological bombs, under the pretext of defending "freedom", covering purely influenceable economic interests. In the same via, some movements such as transhumanism is currently appearing under the pretext of nanotechnology as point of departing to enhance the human qualities and permit the human being to live longer ("immortality"). Other "scientists" find in their thoughts incapacity to think, wanting to create a humanoid to satisfy the sexual desire in human or to implant a microsystem directly in a living insect to observe its comportment (this was presented in a prestigious international conference at Paris in 2007). Finally, extreme initiatives such as the so called NBIC which means nanotechnology, biotechnology, information and cognition having the objective of enhancing human performance have appeared. The term "convergence" was adopted from mathematics, to justify this transdisciplinarity. "Convergence" has been immeasurably popularised and adopted such as the term nano to attract investment (in some of the cases nanotechnogy is not even performed). However, it is not the essential problem, but the ethical problems, it gives rise. An international committee of UNESCO elaborated a report, in 2006, called: "*The ethics and politics of nanotechnology*". According to this report, even nanotechnology definition is not agreed and dozens definitions are found depending on the political or ethical context. Hence, definition depends on what politicians want the people worry about or believe but also the interests of nations, I would add that also that depends on what some demagogic television programs want, taking in consideration our consumer society. For UNESCO, even if some nations do not participate yet, directly, in nanotechnology, they have to elaborate the purpose of nanotechnology under ethics, justice, equity and fairness. In this context, UNESCO can be a mediator.

I do not know if nanotechnology will permit us to see outside the frontier of the "chaos", the society has created too, because what takes 5-10 years or more to be developed in research laboratories, some international companies modify genetically some ancient-edible mesoamerican products such as bean, maize, sunflower producing illnesses in few years. The same companies immeasurably pollute the rivers, the air and the natural world in which, finally, all people live. Foolishly, human produces most of its illnesses to in a second step search for a technology (currently using nanotechnology) to diagnose and treat the same illnesses. Lamentably I have entered in this inevitable vicious cycle.

I am convinced that nanoscience and nanotechnology can help in the techno-scientific progresses, almost all media tells us that, but what I do not know, and media does not tell, is if nanotechnology and nanoscience will create a progress in the mind society to be more rational and human.

Adrián Martínez Rivas (nanobiomex@hotmail.com)

Wafer scale integration of coulomb blockade-based nanobiosensors with microfluidic channels for label-free detection of cancer biomarkers

In this thesis we propose and implement the fabrication on 4 inch wafer of a novel type of nanobiosensor capable of high sensitivity detection. The principle of the nanobiosensor is based on the variation of electrical tunnelling conductivity through metal nanoislands due to the quantum phenomenon called "Coulomb blockade". Nickel nanoislands (~5nm diameter), are placed between interdigitated nanoelectrodes devices (IND) (width~45nm). Hence, the conductivity of these Multiple-Tunnel-Junction (MTJ) devices is modified by the adsorption of biomarkers involved in tumourigenesis. Oncologists have recently isolated and characterised a new conformational single chain variable fragment (scFv) which selectively recognises the active form of RhoA. This potential biomarker has been found overexpressed in various tumours. Antibodies fragments (scFv) are adsorbed through coordinative bonds onto nickel nanoislands. Hence the scFv are capable of recognising specifically the active RhoA conformation. We have investigated this biomarker and validated the nickel nanoilands based chemical construction for label-free biodetection using a quartz crystal microbalance (QCM) before implementing the methodology to our devices. An innovative methodology to realise photoPDMS-based microchannels was also developed. Encapsulation with an etched PDMS-nanocomposite finalised the integration of the devices. The final electrical characterisation of the integrated device was tested in real time and continuous biological flow. The active form of RhoA was discriminated against its inactive conformation. In annexe, I present my epistemological and ethical opinions in nanotechnology.

Keywords: Electric nanodetection, cancer biomarker, protein Rho, interdigitated nano-electrodes, nanoislands, coulomb blockade, photosensitive PDMS, microfluidic, packaging, quartz crystal microbalance.

Intégration à grande échelle de nanobiocapteurs basés sur le blocage de coulomb et de canaux microfluidiques, pour la détection directe de biomarqueurs cancéreux

Dans cette thèse, nous proposons et démontrons un nouveau type de nanobiocapteur pour la détection de biomolécules à haute sensibilité et leur intégration à grande échelle (plaquette de 4 pouces). Le principe du nouveau nanobiocapteur électrique est basé sur la variation de conductivité électrique à travers des nano-îlots grâce au phénomène quantique appelé « blocage de Coulomb ». Les nano-îlots de nickel (~5nm de diamètre) sont placés entre les nano-électrodes interdigitées (IND) (~45nm de largeur). La conductivité de ces dispositifs à Jonctions Tunnel Multiples (MTJ) est modifiée par l'adsorption de biomarqueurs impliqués dans la tumorogènese. Les oncologues ont récemment isolé et caractérisé un nouveau fragment d'anticorps à chaîne simple (scFv) qui reconnaît sélectivement la forme active de RhoA. Ce biomarqueur potentiel a été trouvé surexprimé dans diverses tumeurs. Les fragments d'anticorps ont été adsorbés, par des liaisons de coordination, sur les nano-îlots de nickel. Ces fragments sont capables de reconnaître spécifiquement la forme active de RhoA. Nous avons étudié ce biomarqueur et validé la chimie de surface à base de nano-'îlots de nickel pour la détection sans marquage, en utilisant une microbalance à quartz (QCM). Puis, nous avons mis au point et adapté à notre dispositif une méthodologie innovatrice pour réaliser, à l'échelle d'une plaquette, des microcanaux basés sur du photoPDMS. La caractérisation électrique finale des dispositifs intégrés a été testée en temps réel et à flux biologique continu. La forme active de RhoA a été détectée en discriminant la forme inactive. En annexe, je présente mon opinion épistémologique et éthique sur la nanotechnologie.

MOTS CLÉS: Nano-détection électrique, bio-marqueur cancéreux, protéine Rho, nano-électrodes interdigités, nano-îlots, blocage de coulomb, PDMS photosensible, micro-fluidique, encapsulation, microbalance à quartz.